NOVEL SYNTHESES AND APPLICATIONS OF LAYERED TRANSITION METAL HYDROXIDES

By

DEWAN RUSSEL RAHMAN

Bachelor of Science in Chemistry
University of Dhaka
Dhaka, Bangladesh
2012

Master of Science in Chemistry
University of Dhaka
Dhaka, Bangladesh
2014

Submitted to the Faculty of the
Graduate College of the
Oklahoma State University
in partial fulfillment of
the requirements for
the Degree of
DOCTOR OF PHILOSOPHY
July, 2022

NOVEL SYNTHESES AND APPLICATIONS OF

LAYERED TRANSTION METAL HYDROXIDES

Dissertation Approved:

Dr. Allen Apblett

Dissertation Adviser

Dr. Barry Lavine

Dr. Gabriel Cook

Dr. Yolanda Vasquez

Dr. Raman Pal Singh

ACKNOWLEDGEMENTS

First, I would like to thank the Chemistry Department of Oklahoma State University for giving me the chance to pursue a Ph.D. The most important person in my Ph.D. program was my advisor, Dr. Allen Ablett, as his continued guidance and support played a crucial role in completing the Ph.D. research successfully and becoming an independent and critical thinker in my field. His method of instruction for research was superb and suited me excellently. He provided me dedicated financial support during my Ph.D. study, besides the Chemistry Department. I would also like to thank XploSafe for its financial support and the opportunity to work with them during my Ph.D. research. Additionally, I would like to thank my committee members, Dr. Cook, Dr. Lavine, Dr. Materer, Dr. Vasquez, and Dr. Raman Pal Singh, for serving on my committee, for their feedback on the candidacy proposal, and for their time in the Ph.D. defense process.

When I look back on my undergraduate study at the University of Dhaka, Bangladesh, I realize that my undergraduate laboratory work made me love chemistry and facilitated serious motivation to pursue a Ph.D. in chemistry. Therefore, I would like to thank the Chemistry Department's undergraduate program at the University of Dhaka. Additionally, I would like to thank my M.S. advisor, Dr. Hosne Ara Begum, and co-advisor, Dr. Tanvir Muslim, at the University of Dhaka for their excellent support and guidance in my M.S. research, which, I believe, played a significant role in cementing my motivation for pursuing a Ph.D. and becoming a researcher.

Finally, I would like to thank my family – my mom, dad, brother, and wife for their constant support during my entire Ph.D. journey. I especially thank my wife, who almost single-handedly took care of our newborn baby during my dissertation writing.

Dewan Russel Rahman
Stillwater, Oklahoma, USA

Name: DEWAN RUSSEL RAHMAN

Date of Degree: JULY, 2022

Title of Study: NOVEL SYNTHESES AND APPLICATIONS OF LAYERED TRANSITION METAL HYDROXIDES

Major Field: CHEMISTRY

Abstract: The dissertation herein reports the serendipitous discovery of hydrolysis reactions of later 3d transition metal acetates that deposit nanostructured thin films of corresponding layered metal hydroxides, $M(OAc)_{2-x}(OH)_x \cdot nH_2O$ or metal hydroxides, $M(OH)_2$ (where M is Cu, Ni, Co, and Zn; and OAc is acetate, CH_3COO^-). At 90°C, aqueous copper acetate solutions deposited acetate-intercalated layered copper hydroxide that in 24 hours transformed into CuO films decorated with aggregated spherical particles. Using this reaction, it was possible to produce stoichiometric CuO on silica pellets and mesoporous silica after thermolysis of the deposited copper acetate hydroxide. While nickel acetate hydrolysis produced films consisting of web-like nanowalls of nickel acetate hydroxide. These could subsequently be converted by heating into NiO films while maintaining the same morphology. Interestingly, hydrolysis of cobalt and zinc acetates produced thin films of β-$Co(OH)_2$ and $ZnO/Zn(OH)_2$, respectively, that can easily be transformed into Co_3O_4 or CoOOH and ZnO films by pyrolysis. $ZnO/Zn(OH)_2$ was deposited as nanosphere-type particles almost uniformly distributed across the substrates, while β-$Co(OH)_2$ was grown as a dual nanomorphology – interconnected nanowalls forming a network-like structure and nanosphere-type particles. A solution growth process for deposition β-$Ni(OH)_2$ and α-$N(OH)_2$ using aqueous hexamine nickel(II) hydroxide, $Ni(NH_3)_6(OH)_2$ solutions were also investigated. Evaporation of ammonia from the solutions of $Ni(NH_3)_6(OH)_2$ deposited highly crystalline β-$Ni(OH)_2$ films. While the addition of sodium aluminate to the nickel-ammonia complex facilitated the growth of aluminum-substituted α-$Ni(OH)_2$ membranes with the formula $Ni_{0.74}Al_{0.26}(OH)_{2.26} \cdot 1.5H_2O$ at the solution/air interface.

Additionally, propylene oxide assisted-hydrolysis reactions of later 3d transition metals acetates were investigated to produce acetate-intercalated layered hydroxides (metal acetate hydroxides) in high yields. Hydrolysis of copper acetate aqueous solution with excess propylene oxide at 40°C produced crystalline copper acetate hydroxide, $Cu(OAc)_{0.44}(OH)_{1.56} \cdot 0.50H_2O$ with a yield of 100%. Zinc acetate aqueous solution generated zinc acetate hydroxide, $Zn(OAc)_{0.33}(OH)_{1.67} \cdot 0.50H_2O$ with a yield of 93.6%. However, nickel or cobalt acetate did not produce layered hydroxides; instead, they formed β-$Ni(OH)_2$ or β-$Co(OH)_2$. The uptake of phosphate and arsenate using layered zinc acetate hydroxide synthesized via the propylene oxide-assisted hydrolysis method was investigated. Zinc acetate hydroxide has an initial rapid uptake of phosphate from hydrogen phosphate solutions, corresponding to ion exchange of phosphate for acetate. Beyond this point, a slow acid-base reaction continued by which hydroxides were neutralized by hydrogen phosphate. This led to high phosphate uptake capacity of 259 mg/g after 7 days at room temperature and 356 mg/g after 7 days at 45 °C. Unlike phosphate, arsenate uptake was low 60 mg/g and appeared to be limited to surface adsorption.

TABLE OF CONTENTS

Chapter Page

Chapter Page

Chapter Page

LIST OF TABLES

Table Page

Chapter II

Table Page

Chapter III

Supporting Information Chapter III

Chapter IV

Table Page

Table Page

Chapter VA

Chapter VB

Table Page

Chapter VII

Chapter VIII

LIST OF SCHEMES

Scheme Page

Scheme Page

Chapter VA:

Chapter VB:

Chapter VI

Chapter VII

Chapter VIII

LIST OF FIGURES

Figure Page

Figure Page

Figure Page

Chapter III

Figure Page

Figure Page

Figure Page

Figure Page

Chapter VI

Chapter VII

Figure Page

Chapter VIII

CHAPTER I

Introduction

Layered hydroxides, hydroxides, and oxides of later 3d transition metals (cobalt, nickel, copper, and zinc) are valuable and essential materials for various existing and emerging technologies due to their rich chemistries and lattice structures. These materials deposited as nano-/micro-structures on substrates, support, porous materials, and as nano/micron size powder have been shown excellent performances and promise to be useful in the uptake of pollutants from water, electrodes materials for various types of batteries, electro/photocatalysis, catalysis, advanced oxidation process, sensors, fuel cells, electrochromic devices, electron/hole-type materials for perovskite solar cells, photovoltaics, transparent semiconductive materials, and other metal oxide-based semiconductor technologies (applications of later 3d transition metal layered hydroxides, hydroxides, and oxides are briefly included later). As a result, developing new processes or advancing existing routes for deposition of these materials as nanostructured films or membranes and their synthesis as powders have drawn significant attention and are one of the frontier research in inorganic synthesis and materials chemistry.

One of the aims of the dissertation herein was to develop straightforward, inexpensive, and green processes for deposition of nano-/micro-structured films, membranes, and decorated supports of acetate intercalated-layered metal hydroxides (LMHs) or hydroxides of later 3d transition metals.

To pursue the goal, the dissertation investigation led to the serendipitous discovery of a hydrolysis process to deposit layered metal hydroxides or metal hydroxides as nano-/micro-structured films and decorated support and porous materials. The discovery directed the research to an additional aim to develop a new hydrolysis route for synthesizing acetate-intercalated layered hydroxides and a bimetallic-hydroxide of the later 3d transition metals in high yields. The final goal of the dissertation research was to explore the interactions of phosphate and arsenate in water using one of the synthesized acetate-intercalated layered hydroxides due to its excellent anion exchange capability to uptake these pollutants from water.

The introduction of the dissertation briefly describes the difference between the structures of acetate-intercalated layered metal hydroxides and metal hydroxides of later 3d transition metals. It briefly discusses the thermal conversion of these hydroxides to corresponding metal oxides and a short review of the applications of these layered metal hydroxides, metal hydroxides, and metal oxides in various technologies. The introduction also includes a brief review of existing deposition and synthesis routes of later 3d transition metal layered hydroxides, hydroxides, and their oxides. Afterward, the scope of the present dissertation research is discussed, briefly stating the focus of the dissertation chapters and their accomplishments and findings.

Structures of acetate-intercalated layered hydroxides and hydroxides of later 3d transition metals:

Acetate-intercalated layered metal hydroxides (LMHs) are constituted by brucite-like layers of $M(OAc)_x(OH)_{5-x}$ octahedra (M is divalent metal, OAc is an acetate, CH_3COO^- group), where the acetate groups are intercalated in between the brucite like layers. Figure 1 showcases an acetate-intercalated layered copper hydroxide structure where copper acetate hydroxide is built by building block $Cu(OAc)(OH)_5$ octahedra.[1] Nickel acetate hydroxide is expected to have a similar layered structure to copper acetate hydroxide; however, the lattice unit cell differed. Because

depending on the metals, the layered structure adopts a hexagonal or monoclinic lattice structure. Copper acetate hydroxide in Figure 1 adopts a monoclinic structure,[1] while zinc or nickel acetate hydroxide adopts a hexagonal lattice phase.[2] Interestingly layered zinc hydroxide constituted by $Zn(OH)_6$ octahedra/$Zn(OH)_4$ tetrahedra.[3, 4] The acetate groups are coordinated with $Zn(OH)_4$ tetrahedra, making them $Zn(OAc)(OH)_3$ tetrahedra. The analogous crystal structure of zinc hydroxy nitrate is presented in Figure 2. Nevertheless, the layered structures have fascinating anion-exchange properties as the intercalated-acetate groups can be substituted for other anions. Also, the interlayer distance between two adjacent layers is often in the order of nanometers, making them excellent materials for adsorption and catalysis. The acetate-intercalated bimetallic layered double hydroxides of two different divalent metals have similar acetate-intercalated layered hydroxide structures involving two metal ions instead of one metal ion. While metal hydroxides are built by layers of $M(OH)_x$ polyhedra without anion intercalations, as presented in Figures 3 and 4.

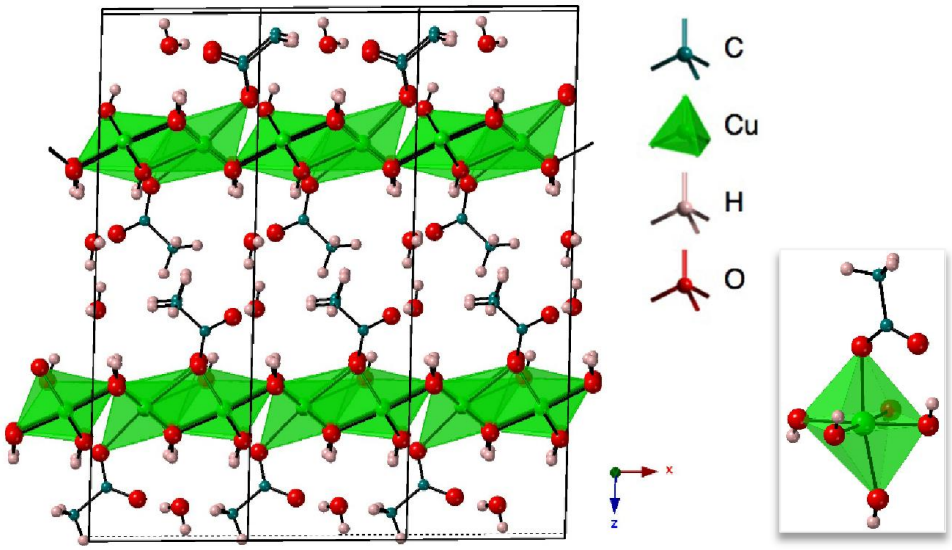

Figure 1: Layered structure of copper acetate hydroxide, $Cu_2(OAc)(OH)_3$. The crystal structure is redrawn using the published crystal structure by Švarcová *et al.*[1]

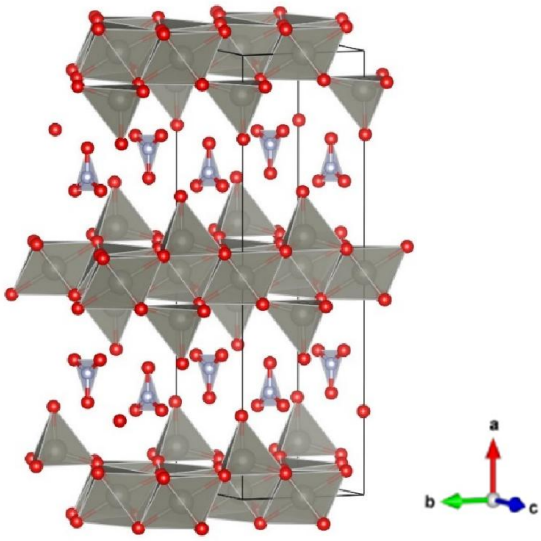

Figure 2: Crystal structure of zinc hydroxy nitrate, $Zn_5(OH)_8(NO_3)_2 \cdot 2H_2O$ without hydrogen atoms (CIF file #210–6442, crystallographic open database).[5] The structure is redrawn using the VESTA software. In the case of zinc acetate hydroxide, the acetate will be coordinated with the tetrahedral zinc.[3, 4]

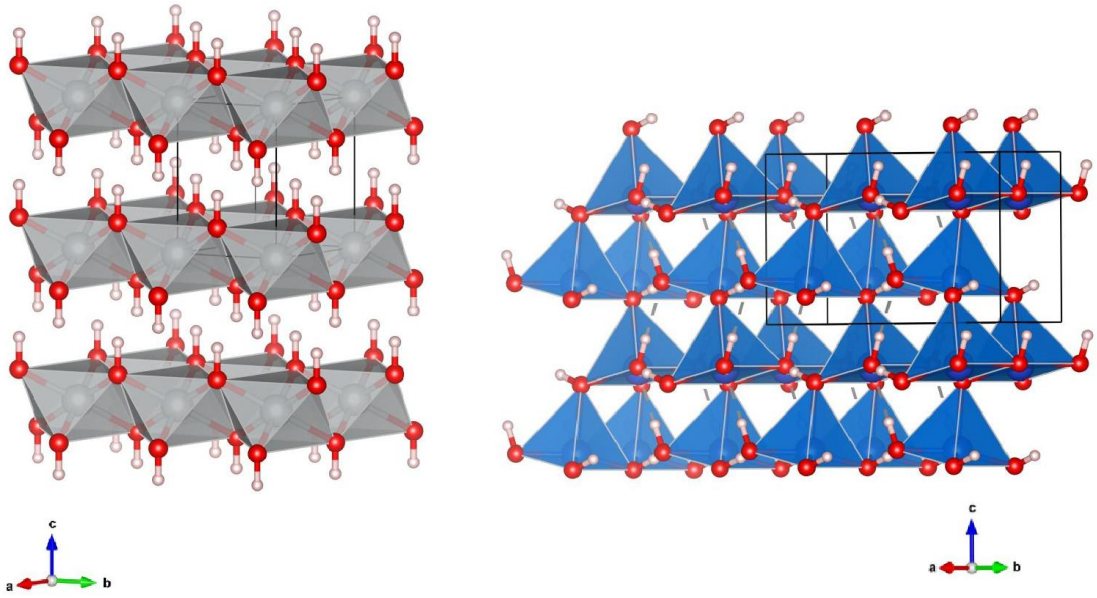

Figure 3: Nickel hydroxide is built up by $Ni(OH)_6$ octahedra (left), whereas copper hydroxide is constituted by $Cu(OH)_5$ pentahedra (right). Nickel hydroxide CIF file# mp-27912 and copper hydroxide CIF file# mp-505105.[6, 7]

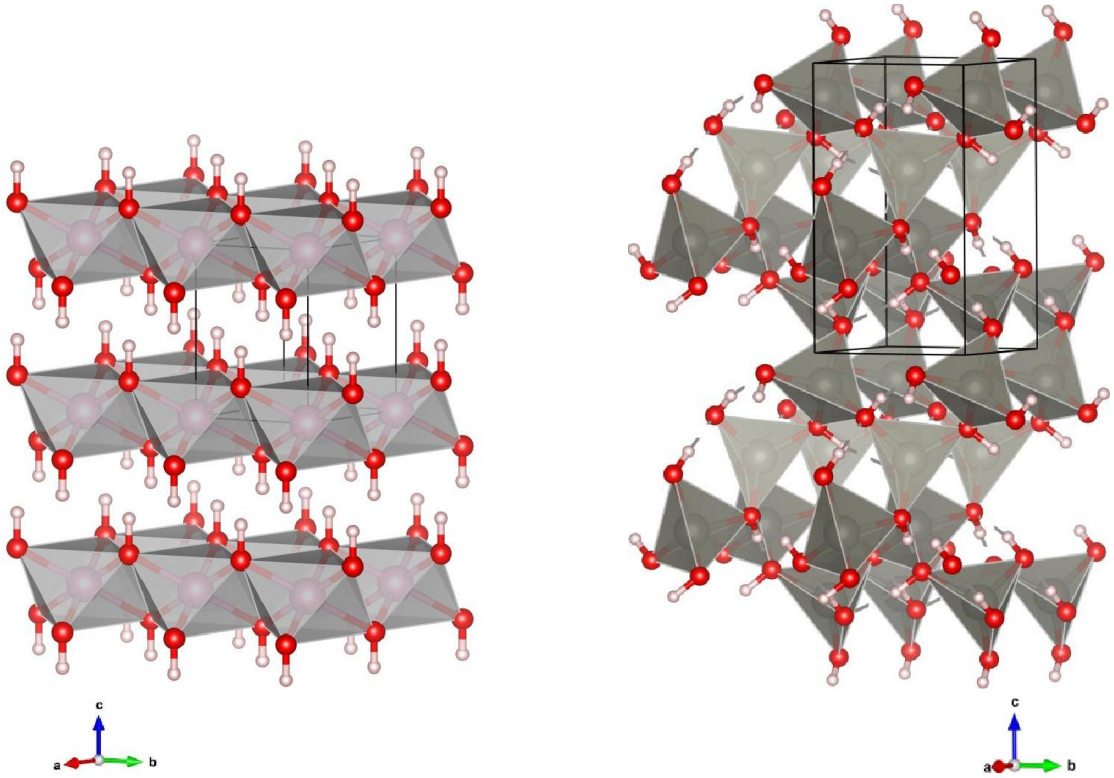

Figure 4: Cobalt hydroxide is built up by $Co(OH)_6$ (left), whereas zinc hydroxide is constituted by $Zn(OH)_4$ tetrahedra (right). Cobalt hydroxide CIF file# mp-24105 and zinc hydroxide CIF file# mp-625830.[8, 9]

Conversion of acetate-intercalated layered metal hydroxides and hydroxides to corresponding metal oxides:

Pyrolysis readily converts acetate-intercalated layered metal hydroxides and metal hydroxides into corresponding metal oxides. The thermochemistry involves in pyrolysis is straightforward. Upon heating, the metal acetate hydroxides will be dehydroxylated as water, and acetate will decompose as volatile/gaseous organics, which will leave only metal oxides. While metal hydroxides will also be directly converted to metal oxides by dehydroxylation. Nanostructured acetate-intercalated metal hydroxides or hydroxides are often transformed into metal oxides with identical nano-morphologies.[10-12] Therefore, nanostructures of metal acetate

hydroxides or metal hydroxides as films or decorated supports can be used to prepare corresponding nanostructured metal oxides decorated substrates/supports that are valuable in metal oxide based-applications. Likewise, nano-/micro-size powders of metal acetate hydroxides or metal hydroxides are excellent precursors for nano-/micro-size powders of metal oxides. While some metal hydroxides, such as nickel hydroxides, can be converted to nickel oxyhydroxide, NiOOH by chemical or electrochemical oxidation, and cobalt hydroxide can be transformed to cobalt oxyhydroxide, CoOOH simply by pyrolysis. Stochiometric bimetallic hydroxides and layered double hydroxides (LDHs) can be converted to bimetallic oxyhydroxides or bimetallic oxides as solid solutions depending on the lattice structures of the constituent metal oxyhydroxides/oxides. The thermal conversion of metal acetate hydroxides, metal hydroxides, and bimetallic hydroxides or LDHs to corresponding metal oxides and bimetallic oxides can be effortlessly achieved on large scales.

$$M(OAc)_x(OH)_{2-x}\cdot nH_2O\ (s) \longrightarrow M(OAc)_x(OH)_{2-x}\ (s) + nH_2O\ (g)$$

$$M(OAc)_x(OH)_{2-x}\ (s) \longrightarrow MO\ (s) + \tfrac{1}{2}x\ Ac_2O\ (g) + \tfrac{1}{2}(2-x)\ H_2O\ (g)$$

Scheme 1: Thermal conversion of acetate-intercalated layered hydroxide to corresponding metal oxides. Where M is divalent transition metals, OAc is acetate, and Ac_2O is acetic anhydride.

Notably, the thermochemistry of copper acetate hydroxide pyrolysis differs from other later 3d transition metal acetate hydroxides. During the decomposition of acetate (OAc^-) in the copper acetate hydroxide, OAc^- groups can reduce Cu^{2+} to Cu^+ in the solid phase leading to the formation of CuO/Cu_2O.[13] The thermal event in the case of copper acetate hydroxide is as follows.

$$Cu(OAc)_x(OH)_{2-x}\ (s) \longrightarrow Cu_2O/CuO\ (s) + \tfrac{1}{2}x\ C_2H_6\ (g) + 2xCO_2\ (g) + \tfrac{1}{2}(2-x)\ H_2O\ (g)$$

Scheme 2: Decomposition of copper acetate hydroxide, $Cu(OAc)_x(OH)_{2-x}$ to Cu_2O/CuO.

Applications of layered hydroxides, hydroxides, and oxides of later 3d transition metals in existing and emerging technologies:

Acetate-intercalated layered metal hydroxides (LMHs) or bimetallic layered double hydroxides (LDHs) of later 3d transition metals are best known for their anion exchangeability.[4, 14-16] The intercalated-acetate groups coordinated to $M(OH)_x$ polyhedra can undergo anion-exchange with various anions such as phosphate (PO_4^{3-}), arsenate (AsO_4^{3-}), arsenite (AsO_3^{3-}), selenate (SeO_4^{2-}), selenite (SeO_3^{2-}), antimonate (SbO_4^{3-}), chromate (CrO^{2-}), etc. Thus, acetate-intercalated layered metal hydroxides can be directly used as a sorbent to uptake the mentioned species from water to possibly recover them and prevent water pollution from these hazardous species for a safer water environment for human and aquatic species. Especially as layered zinc hydroxide is more benign than copper, nickel, and cobalt, it is an attractive material for real-world pollutants uptake applications. Additionally, Nuclear power plants release wastewater with radioactive technetium oxyanion, $TcO4^-$, which is difficult species to deal with due to high water solubility and a dangerous species since technetium-99 (^{99}Tc) is a β emitter with a lifetime of 2.13×10^5 years.[17, 18] Acetate-intercalated zinc acetate hydroxide will be a promising material to uptake these radioactive oxyanions for treating the nuclear power plant release water. Layered metal hydroxides can also potentially be employed to uptake volatile organics indoors in laboratories and chemical industries. While layered transition metal hydroxides as nano-powders, decorated substrates or supports, and films are promising materials for catalysis and sensors.[19, 20] Acetate or other carboxylates intercalated layered metal hydroxides decorated substrates, supports, and films are excellent precursors for nano- or micro-structured metal oxides decorated substrates or supports and metal oxide films. Due to the anionic exchangeability of layered metal hydroxides, they can be utilized to prepare Metal Organic Frameworks (MOFs) as recently, it was investigated that nitrate-intercalated layered zinc-copper hydroxides and acetate-intercalated layered zinc hydroxides generated MOFs with a few known organic linkers at room temperature.[21]

Hydroxides or oxides of later 3d transition metals (Ni, Co, Co, and Zn) are valuable materials for many essential and emerging technologies briefly discussed as follows.

Nickel hydroxide is best known for its application as electrode material in batteries due to well-known nickel-cadmium (Ni-Cd) and nickel-metal-hydride (NiMH) batteries.[22] Nickel hydroxide has also been used as positive electrodes for nickel-iron and nickel-zinc rechargeable batteries that pose a low environmental impact.[23-25] While aluminum substituted α-nickel hydroxide exhibit high lithium storage capacities; therefore, they are promising materials as electrodes in lithium-ion batteries.[26] Additionally, nickel hydroxides have the beneficial photo- and electrochemical properties that make them useful co-catalysts for photocatalytic hydrogen production from water,[27] excellent electrocatalysts for the oxygen evolution reaction,[28] and safer hydrogen generation from alkaline water.[29] While they can also be used for electrocatalysis of small molecules in fuel cells, energy storage, organic synthesis, and wastewater treatment.[30] Nickel hydroxides can be used as sensors for many analytes such as vitamins, hydrogen peroxide, and glucose due to their excellent electrochemical behavior.[31-34]

Cobalt hydroxide, $Co(OH)_2$ are also valuable materials as electrodes for batteries and supercapacitors.[35, 36] Another key aspect of cobalt hydroxide is that it can easily be transformed into cobalt oxyhydroxide (CoOOH) by heating under air. CoOOH has better conductivity than cobalt oxides or hydroxides, making it an attractive material for electrode applications for lithium-ion batteries.[37] Recently, nano-$Co(OH)_2$ was investigated as a promising bifunctional catalyst for oxygen evolution and oxygen reduction reactions that occur in rechargeable metal-air batteries.[38] Nanostructures of cobalt hydroxides can readily be converted into nanostructured cobalt oxide, Co_3O_4 that have been investigated as promising catalysts for the electro-/photo-catalytic splitting of water for H_2 generation[39, 40] and CO_2 electroreduction to formate.[41] Recently, it has been shown that Co_3O_4 decorated onto the outer surface of mesoporous silica particles can photo-reduce CO_2

to CO with 83% selectivity with an excellent conversion rate in a photosensitizer/aqueous-organic solvent system.[42]

NiO is an excellent p-type or hole-type semiconductive oxide material with a wide band gap of 3.15 – 4.3 eV [43] under ambient conditions. This makes nanostructured nickel oxide (NiO) as thin films or decorated supports valuable and promising materials in various important technologies such as a hole transport layer in perovskite solar cells, hole injection/transport layers in organic light-emitting diodes, photocatalysis, electrocatalytic water splitting, gas sensors, electrochromic glasses, transparent conductive oxides.[44-50] Copper oxides decorated substrates or supports and as powders have been the interest of many areas of research such as thermal-catalysis, photocatalytic reduction of CO_2, photoelectrodes for photoelectrochemical processes, electrocatalysis, gas sensors, hole transport layer in perovskite photovoltaics, degradations of organic pollutants from water by the advanced oxidation process, uptakes of volatile organics, antimicrobial surfaces, Hepatitis-B virus sensors (DNA biosensors).[51-60]

Zinc oxide, ZnO is a valuable and promising material in various well-established and emerging technologies. Recently, it was shown that nanostructured ZnO deposited onto fluorine-doped tin oxide substrates can efficiently electro-catalyze water to hydrogen peroxide.[61] Nano ZnO is an excellent photocatalyst to degrade organic pollutants from water and was proven to be a valuable catalyst for useful organic transformations.[62-65] While ZnO nanoparticles-loaded catalyst supports are promising materials for industrial catalytic applications such as biodiesel production.[66] Additionally, nano-/micro-structured ZnO films are up-and-coming materials in metal oxide semiconductor-based applications such as photovoltaics, field-effect transistors, biosensors, transparent (semi-)conductive glasses, electron-transport layers in perovskite solar cells, and piezoelectric devices. [67-72]

Applications of bimetallic nickel-cobalt hydroxides or oxyhydroxides and nickel cobaltite:

Bimetallic nickel-cobalt hydroxides can directly be used as catalysts for hydrogen evolution reaction (HER) from alcohols, electrooxidation of urea, and positive electrodes for supercapacitors.[73-75] While bimetallic nickel-cobalt hydroxides are excellent precursors for accessing nickel-cobalt oxyhydroxides. Nickel-cobalt oxyhydroxides can potentially be a promising catalyst for reducing CO_2 to value-added ethanol and Fischer-Tropsch hydrocarbon synthesis due to the bimetallic synergy of nickel and cobalt.[76-78] Additionally, nickel-cobalt oxyhydroxide can be employed as electrocatalysts for useful organic transformations and as electrodes for supercapacitors.[79-81] Whereas nickel cobaltite, $NiCo_2O_4$, can easily be prepared by pyrolysis of a corresponding stochiometric nickel-cobalt hydroxide. Nickel cobaltite is an up-and-coming material as electrodes for lithium-ion batteries, supercapacitors, and hybrid supercapacitors.[82, 83] Nickel cobaltite can electro-oxidize methanol efficiently with a better lifespan than NiO or Co_3O_4; therefore, it is a promising material for the direct methanol fuel cell.[84]

A short review of the hydrolysis route for deposition of layered hydroxides, hydroxides, and oxides of later 3*d* transition metals:

Hydrolysis (hydrothermal) reactions of metal salts are one of the widely used solution processes for accessing nanostructured films or decorated supports of layered metal hydroxides or metal hydroxides and their oxides. Hydrolysis reaction involves a metal salt and often an organic that can generate in situ OH^- ions. One of the well-known hydrolysis reactions involves heating aqueous solutions of metal salts with hexamethylenetetramine (HMTA) to deposit nanostructured metal hydroxides or oxide as films. For example, zinc or nickel nitrate aqueous solutions with hexamethylenetetramine were extensively investigated that produced films of nanostructured zinc oxide or nickel hydroxide films. A mixture of nickel nitrate and HMTA aqueous solutions at 100°C deposited films of β-nickel hydroxide as web-like interconnected nanowalls.[85] While films of ZnO

nanorods were produced from the aqueous solutions of zinc nitrate, $Zn(NO_3)_2$, and HMTA.[86] Cobalt nitrate and HMTA aqueous solution grew randomly ordered porous nanoflakes (web-like nanowalls) film of cobalt hydroxide $Co(OH)_2$.[87]

Besides hexamethylenetetramine, urea ($CO(NH_2)_2$) has also been studied with metal salts in hydrothermal conditions for nanostructured metal hydroxides or oxides deposition. For example, a mixture of nickel nitrate, urea, and ammonium fluoride in water at 105 °C in an autoclave produced layered nickel hydroxide carbonate, $Ni_2(OH)_2(CO_3)\cdot nH_2O$ as thin films, which after annealing at 300-450 °C were successfully yielded to NiO thin films consisted of interconnected-nanowalls.[88] While hydrolysis of zinc nitrate with urea produced randomly oriented porous ZnO nanowalls on silicon substrates.[89] Cobalt nitrate, urea, and ammonium fluoride in water at 100 °C and following annealing at 523 K produced Co_3O_4 interconnected nanosheets as films.[90] Although the study did not characterize it, the film that was generated before annealing should be cobalt hydroxide carbonate, $Co_2(OH)_2(CO_3)\cdot nH_2O$.[91]

The hydrothermal heating of metal acetates is rarely investigated in the literature to deposit films of acetate-intercalated layered metal hydroxides. One of the few examples is the hydrothermal heating of mixtures of later 3d transition metal acetates, such as a 1:10 mixture of nickel and zinc acetate aqueous solution at 150°C in autoclave generated web-like interconnected nanowalls of acetate-intercalated layered nickel-zinc hydroxide, $Ni_{0.78}Zn_{0.44}(OOCCH_3)_{0.44}(OH)_2\cdot H_2O$ as thin films.[92] While the suspension of a layered metal hydroxide can generate metal oxide films as copper hydroxy nitrate, $Cu_2(OAc)(OH)_3$ suspensions in water were reported to make CuO films on glass substrates at 200 °C in an autoclave.[93]

Other than hydrothermal or solvothermal processes, metal organic deposition followed by pyrolysis, SILAR (Successive Ion Layer Adsorption and Reaction), and electrochemical deposition

methods also have been widely used for preparing nanostructured films of transition metal oxides and hydroxides.[94-96]

A brief review of the existing synthesis routes for acetate-intercalated layered transition metal hydroxides:

Literature investigation reveals very few routes reported for synthesizing acetate-intercalated layered hydroxide of copper acetate hydroxide. Švarcová *et al.* synthesized copper acetate hydroxide, $Cu_2(OAc)(OH)_3$ single crystal by heating copper acetate aqueous solution at 60 °C under reflux.[1] However, the yield of the hydrolysis of copper acetate is very low, as investigated in Chapter III of the dissertation. The other investigated route employed titrimetric precipitation of aqueous solutions of copper acetate with dilute NaOH to pH 6.5 and subsequent hydrothermal heating at 40 °C that yielded acetate-intercalated copper hydroxide, $Cu_2(OAc)_{0.9}(OH)_{3.1}\cdot 0.7H_2O$.[97] While Masciocchi *et al*. prepared a copper acetate hydroxide phase, $Cu_2(CH_3COO)(OH)_3\cdot H_2O$, by slow titration of 0.1M copper acetate by 0.1M NaOH and by only heating of 0.01M – 0.18M aqueous copper acetate solutions (without base) at 50 – 75 °C.[98]

While zinc acetate hydroxide, $Zn_5(OH)_8(OCOCH_3)_2,2H_2O$ was often reported to produce by two reactions that are (i) precipitation of zinc acetate by NaOH,[99] and (ii) reaction of ZnO with zinc acetate aqueous solution at room temperature.[100-101] The latter route was developed and extensively investigated by Meyn and coworkers using metal oxides and aqueous solutions of corresponding nitrates.[102] Poul and coworkers developed polyol-mediated hydrolysis of zinc, nickel, or cobalt acetate that can produce corresponding metal acetate hydroxides at room temperature to 60 °C. They showed that the polyol process with zinc acetate generated $Zn(OH)_{1.58}(Ac)_{0.42}\cdot 0.31H_2O$.[2] While nickel acetate hydroxide, $Ni(OAc)_x(OH)_{2-x}\cdot nH_2O$ cannot be synthesized by the direct precipitation route like zinc or copper. Poul and coworkers showed that their polyol process generated $Ni(OH)_{1.60}(Ac)_{0.40}\cdot 0.63H_2O$.[2] Nishizawa and coworkers, during

investigating the hydrothermal reaction of nickel acetate to NiO via the formation β-$Ni(OH)_2$ in an autoclave, claimed that the hydrothermal reaction produced α-type nickel acetate hydroxide, $Ni_2(OH)_3(OAc)\cdot 1.4H_2O$ layered material at 160 °C.[103] These are the few synthesis routes reported in the literature that produce acetate-intercalated layered hydroxides of later 3d transition metals.

Phosphate and arsenic pollution:

Excess phosphate in water causes eutrophication (algal bloom) and aquatic plants on surface water as phosphate is food for algae, plants, and plant species. An algal bloom is a severe threat to the biodiversity of water bodies as it makes the water bodies inhibitable for aquatic life. Algal bloom pollution is the main culprit in creating "Dead Zones" in water bodies where aquatic species cannot survive due to the lack of dissolved oxygen.[104] While blue-green algae (cyanobacteria) bloom is known as harmful algal bloom since this type of algae impairs waterbodies by releasing toxins that are dangerous to humans, animals, and aquatic species.[104] Harmful algal bloom can also impact safer drinking water facilities. For example, in 2014, a massive bloom of cyanobacteria in Lake Erie closed drinking water facilities that served 500,000 people in Toledo, Ohio.[105] While an article published in ACS Environmental Science & Technology in 2009 calculated that economic loss in the U.S. due to eutrophication of freshwater is about $2.2 billion annually for combined value losses of recreational water usage, real estate waterfront, spending on recovery of threatened and endangered species, and drinking water.[106] In the U.S., ranchers and framers also encounter problems and economic loss for losing farmland pondwater essential for ranching and farming. Phosphate pollution is a global issue due to the loss of clean surface water, financial loss, and harmful effects on humans, birds, mammals, and water species.

Arsenic pollution in water is another critical issue since arsenic exposure to humans can cause serious health problems. One of such problems is chronic skin problems such as skin lesions, which may result in skin cancer.[107, 108] According to the Minnesota Department of Health,

prolonged exposure to low levels of arsenic in humans through drinking water may cause diabetes and increase the risk of cancer in the bladder, lungs, liver, and other organs.[109] While EPA has concluded that inorganic arsenic is carcinogenic to humans.[110] Another danger of arsenic water pollution is that arsenic species can be bioaccumulated in aquatic and marine species that end up in humans through diet.[111]

Unfortunately, besides natural sources, many anthropogenic sources in our current advanced era exist as necessary evils that cause phosphate and arsenic pollution in surface water and drinking water systems. Therefore, removing phosphate species from industrial wastewater, municipal wastewater, irrigation runoff from farms, etc., and arsenic species from arsenic-containing industrial release water and regular water for daily use and drinking are critical demands in our present time to have a safer water environment. Among many existing and emerging technologies, uptake of phosphate or arsenate from water using sorbent materials is one of the most inexpensive, attractive, and industrially scalable processes for remediation of these species from water and possibly recovering them for value-added materials or chemicals. Therefore, developing suitable materials that exhibit high uptake capacities, are inexpensive to synthesize, scalable, possible for recovery, and are environmentally benign is a critical need in our present time to deal with the phosphate and arsenate pollution and possibly recover them for reuse.

Scope of the dissertation research

Serendipitous discovery of the reaction of copper acetate and water at 90 °C (hydrolysis of copper acetate) that deposited CuO via formation of copper acetate hydroxide intermediate directed the dissertation research to extensively investigate the hydrolysis of later 3d transition metals – Cu, Co, Ni, and Zn. Therefore, one of the goals of the dissertation was to explore the hydrolysis reactions of these metal acetates to develop straightforward routes for the deposition of acetate-intercalated layered metal hydroxides or hydroxides of these transition metals.

Chapter II investigated nickel acetate hydrolysis, while Chapter III explored copper acetate and copper formate hydrolysis. Nickel acetate produced thin films decorated with web-like interconnect nanowalls of layered nickel hydroxide (nickel acetate hydroxide) on glass substrates. These films were readily transformed into NiO films with identical nanostructure by pyrolysis. Copper acetate generated spere-type microparticles decorated copper oxides via deposition of crystalline copper acetate hydroxide, which was the acetate-intercalated layered copper hydroxide. Further, copper acetate hydrolysis reactions with silica pellets and mesoporous silica followed by ex-situ pyrolysis were investigated, presenting a novel and simple way to prepare CuO decorated support or porous materials. While copper formate interestingly produced copper(I) oxide/copper formate hydroxide as nano/-micro size octahedron-rectangular-type particles deposited on glass substrates.

The findings of nickel acetate and copper acetate hydrolysis prompted the dissertation research to investigate the hydrolysis reactions of nickel and copper acetate mixtures, as covered in Chapter IV. The hydrolysis reactions produced powders of nickel-copper acetate hydroxides that are novel bimetallic nickel-copper layered double hydroxides (LDHs). The investigation of a series of the hydrolysis reaction of nickel and copper acetate mixtures at various ratios led to the discovery of an unusual dependency of nickel-copper contents in the LDHs to the ratios of nickel and copper ions in the initial reaction solution. The LDHs are copper-rich within the 1:1 to 6:1 nickel to copper ions, while ratios higher than 7:1 of nickel to copper ions generated nickel-rich LDHs. A hypothesis of copper-rich nucleation followed by an ion-exchange process during the growth of LDH particles was proposed for the observed unusual trends of nickel-copper contents in the LDHs. The morphologies of two of the LDHs were nano-/micro size square-type plates.

Chapter VA and VB include the investigation of the hydrolysis of zinc acetate and cobalt acetate aqueous solutions, respectively. The goals of the chapters were to explore the hydrolyses to find out if these reactions could deposit layered hydroxides or hydroxides of the corresponding

metals and what nanostructures they would generate. Interestingly, unlike nickel or copper, the zinc acetate produced ZnO/$Zn(OH)_2$ sphere-type particles deposited as films on glass and gold-palladium coated glass substrates. While cobalt acetate grew a dual nanomorphology – interconnected nanowalls and nanosphere-type particles as films on glass substrates. These nanostructured films were effortlessly converted to zinc oxide (ZnO) and cobalt oxyhydroxide (CoOOH) or cobalt oxide (Co_3O_4) films upon pyrolysis. Additionally, cobalt acetate hydrolysis with macroporous silica gel and silica pellets showed that the process can functionalize these materials with cobalt hydroxide and cobalt oxides after pyrolysis.

Therefore, Chapters II, III, and V of the present study have established a new straightforward route for preparing nano/micro-structured layered hydroxides or hydroxides and corresponding oxides of later 3d transition metals (Ni, Co, Cu, and Zn) as films and decorated supports/porous materials. While Chapter IV has advanced a simple synthesis route for novel acetate-intercalated bimetallic nickel-copper LDHs and has opened the door to exploring the hydrolysis reaction of mixtures of other transition metal acetates.

The present dissertation also pioneered a novel process for converting commercial nickel hydroxide powder into nickel hydroxide films and membranes, as presented in Chapter VI. The investigation exploited the solubility of nickel hydroxide in concentrated aqueous ammonia that produced hexamine nickel(II) hydroxide, $Ni(NH_3)_6(OH)_2$ complex. The release of ammonia from the complex in open chemical bath systems was explored, which deposited highly crystalline β-$Ni(OH)_2$ films. While the addition of sodium aluminate, $NaAl(OH)_4$ to the $Ni(NH_3)_6(OH)_2$ complex was investigated to develop aluminum substituted α-$Ni(OH)_2$ films as aluminum can replace nickel during the growth of nickel hydroxide and produce a stable α-type $Ni(OH)_2$. Interestingly, the addition of $NaAl(OH)_4$ generated free-standing membranes of aluminum substituted α-$Ni(OH)_2$ instead of deposited films on substrates. The developed solution growth method using nickel-ammonia complex does not leave any chemical waste, making it a green process.[112]

Additionally, the dissertation aimed to develop a hydrolysis route to synthesize acetate-intercalated layered hydroxides of later 3d transition metals in high yields. This led the dissertation research to explore the hydrolysis of the metal acetates in the presence of propylene oxide in water. Since propylene oxide can react with a hexaaqua metal complex $[M(H_2O)_6]^{2+}$ to generate $[M(OH)(H_2O)]^{+}$, that is the key species to form acetate-intercalated layered metal hydroxides and metal hydroxides depending on the metals. Therefore, Chapter VII presents the exploration of propylene oxide-assisted hydrolysis of later 3d transition metal acetates in water. It turned out the hydrolysis of cooper acetate produced crystalline copper acetate hydroxide, $Cu(OAc)_{0.0.44}(OH)_{1.56}\cdot 0.40H_2O$ in 100% yield while zinc acetate generated zinc acetate hydroxide, $Zn(OAc)_{0.33}(OH)_{1.67}\cdot 0.50H_2O$ with ~94% yield. While the reaction of 1:2 nickel acetate to cobalt acetate produced a stochiometric nickel-cobalt hydroxide, which is an excellent precursor for nickel-cobalt oxyhydroxide, $NiCo_2O_x(OH)_{6-2x}$ and nickel cobaltite, $NiCo_2O_4$. Notably, the hydrolysis of later 3d transition metals acetates with propylene oxide in water was not explored before; as a result, the developed hydrolysis route is a development of a novel synthesis route for accessing acetate-intercalated copper or zinc acetate hydroxide and a stoichiometric nickel-cobalt hydroxide.

Zinc acetate hydroxide, $Zn(OAc)_{0.33}(OH)_{1.67}\cdot 0.50H_2O$ is a promising material for uptake of phosphate or arsenate due to its anion exchangeability as the intercalated-acetate groups can be replaced by phosphate (PO_4^{3-}) and arsenate (AsO_4^{3-}). Theoretically, if all the acetate groups of the zinc acetate hydroxide are replaced by phosphate or arsenate, that would offer excellent uptake capacities for these hazardous species from water. Therefore, as presented in Chapter VIII, the dissertation research was promoted to investigate phosphate and arsenate uptake using zinc acetate hydroxide synthesized by the propylene oxide-assisted hydrolysis method. The investigation found that prolonged interaction of a high ppm hydrogen phosphate (HPO_4^{2-}) involved an initial acetate (anion) exchange followed by a slow acid-base reaction with the zinc acetate hydroxide. The reaction stage led to a superior phosphate uptake capacity compared to other layered hydroxides,

hydroxides, porous metal oxides, and even some metal-organic frameworks. While, unlike phosphate, arsenate interaction is limited to adsorption, which might accompany a minimal acetate exchange. This resulted in a lower arsenate uptake capacity than phosphate by the zinc acetate hydroxide but better or comparable in terms of arsenate uptake using metal oxides, metal hydroxides, and layered double hydroxides.

References:

(1) Švarcová, S.; Klementová, M.; Bezdička, P.; Łasocha, W.; Dušek, M.; Hradil, D., Synthesis and characterization of single crystals of the layered copper hydroxide acetate $Cu_2(OH)_3(CH_3COO)\cdot H_2O$. *Crystal Research and Technology* **2011,** 46, (10), 1051-1057.

(2) Poul, L.; Jouini, N.; Fiévet, F., Layered Hydroxide Metal Acetates (Metal = Zinc, Cobalt, and Nickel): Elaboration via Hydrolysis in Polyol Medium and Comparative Study. *Chemistry of Materials* **2000,** 12, (10), 3123-3132.

(3) Miao, J.; Xue, M.; Itoh, H.; Feng, Q., Hydrothermal synthesis of layered hydroxide zinc benzoate compounds and their exfoliation reactions. *J. Mater. Chem.* **2006,** 16, (5), 474-480.

(4) Kandare, E.; Hossenlopp, J. M., Hydroxy Double Salt Anion Exchange Kinetics: Effects of Precursor Structure and Anion Size. *The Journal of Physical Chemistry B* **2005,** 109, (17), 8469-8475.

(5) Moezzi, A.; Lee, P.-S.; McDonagh, A. M.; Cortie, M. B., On the thermal decomposition of zinc hydroxide nitrate, $Zn_5(OH)_8(NO_3)_2\cdot 2H_2O$. *Journal of Solid State Chemistry* **2020,** 286.

(6) The Materials Project; $Ni(OH)_2$, https://materialsproject.org/materials/mp-32403/.

(7) The Materials Porject; $Cu(OH)_2$ https://doi.org/10.17188/1262260.

(8) The Materials Project; $Co(OH)_2$, https://materialsproject.org/materials/mp-25489/.

(9) The Materials Project; $Zn(OH)_2$, https://doi.org/10.17188/1278479.

(10) Dewan Russel Rahman. Novel Syntheses and Applications of Layered Transition Metal Hydroxides, *Chapter II*. Ph.D. Dissertation, Oklahoma State University, 2022.

(11) Ganga, B. G.; Santhosh, P. N., Facile synthesis of porous copper oxide nanostructure using copper hydroxide acetate precursor. *Materials Letters* **2015,** 138, 113-115.

(12) Yang, L. X.; Zhu, Y. J.; Li, L.; Zhang, L.; Tong, H.; Wang, W. W.; Cheng, G. F.; Zhu, J. F., A Facile Hydrothermal Route to Flower-Like Cobalt Hydroxide and Oxide. *European Journal of Inorganic Chemistry* **2006,** 2006, (23), 4787-4792.

(13) Dewan Russel Rahman. Novel Syntheses and Applications of Layered Transition Metal Hydroxides, *Chapter VII*. Ph.D. Dissertation, Oklahoma State University, 2022.

(14) Rabu, P.; Delahaye, E.; Rogez, G., Hybrid interfaces in layered hydroxides: magnetic and multifunctional superstructures by design. *Nanotechnology Reviews* **2015,** 4, (6).

(15) Kozai, N.; Mitamura, H.; Fukuyama, H.; Esaka, F.; Komarneni, S., Synthesis and Characterization of Copper Hydroxide Acetate With a Layered Discoid Crystal. *Journal of Materials Research* **2011,** 20, (11), 2997-3003.

(16) Kozai, N.; Mitamura, H.; Fukuyama, H.; Esaka, F.; Komarneni, S., Synthesis and characterization of nickel–copper hydroxide acetate, $NiCu(OH)_{3.1}(OCOCH3)_{0.9}\cdot 0.9H_2O$. *Microporous and Mesoporous Materials* **2006,** 89, (1-3), 123-131.

(17) Liang, L.; Gu, B.; Yin, X., Removal of technetium-99 from contaminated groundwater with sorbents and reductive materials. *Separations Technology* **1996,** 6, (2), 111-122.

(18) Li, J.; Dai, X.; Zhu, L.; Xu, C.; Zhang, D.; Silver, M. A.; Li, P.; Chen, L.; Li, Y.; Zuo, D.; Zhang, H.; Xiao, C.; Chen, J.; Diwu, J.; Farha, O. K.; Albrecht-Schmitt, T. E.; Chai, Z.; Wang, S., $(99)TcO_4(-)$ remediation by a cationic polymeric network. *Nat Commun* **2018,** 9, (1), 3007.

(19) Kim, A.; Varga, I.; Adhikari, A.; Patel, R., Recent Advances in Layered Double Hydroxide-Based Electrochemical and Optical Sensors. *Nanomaterials (Basel)* **2021,** 11, (11).

(20) Xu, M.; Wei, M., Layered Double Hydroxide-Based Catalysts: Recent Advances in Preparation, Structure, and Applications. *Advanced Functional Materials* **2018,** 28, (47).

(21) Zhao, J.; Nunn, W. T.; Lemaire, P. C.; Lin, Y.; Dickey, M. D.; Oldham, C. J.; Walls, H. J.; Peterson, G. W.; Losego, M. D.; Parsons, G. N., Facile Conversion of Hydroxy Double Salts to Metal–Organic Frameworks Using Metal Oxide Particles and Atomic Layer Deposition Thin-Film Templates. *Journal of the American Chemical Society* **2015,** 137, (43), 13756-13759.

(22) J. McBreen, Nickel Hydroxides, Handbook of Battery Materials, 2nd ed., J.O. Besenhard and C. Daniel, Ed., Verlag GmbH, Wiley-VCH, 2011, p 149–168.

(23) Chakkaravarthy, C.; Periasamy, P.; Jegannathan, S.; Vasu, K. I., The nickel/iron battery. *Journal of Power Sources* **1991,** 35, (1), 21-35.

(24) Shukla, A. K.; Ravikumar, M. K.; Balasubramanian, T. S., Nickel/iron batteries. *Journal of Power Sources* **1994,** 51, (1), 29-36.

(25) Kimmel, S. W.; Hopkins, B. J.; Chervin, C. N.; Skeele, N. L.; Ko, J. S.; DeBlock, R. H.; Long, J. W.; Parker, J. F.; Hudak, B. M.; Stroud, R. M.; Rolison, D. R.; Rhodes, C. P., Capacity and phase stability of metal-substituted α-$Ni(OH)_2$ nanosheets in aqueous Ni–Zn batteries. *Materials Advances* **2021,** 2, (9), 3060-3074.

(26) Li, Y.; Pan, G.; Xu, W.; Yao, J.; Zhang, L., Effect of Al substitution on the microstructure and lithium storage performance of nickel hydroxide. *Journal of Power Sources* **2016,** 307, 114-121.

(27) Xie, L.; Hao, J.-G.; Chen, H.-Q.; Li, Z.-X.; Ge, S.-Y.; Mi, Y.; Yang, K.; Lu, K.-Q., Recent advances of nickel hydroxide-based cocatalysts in heterogeneous photocatalysis. *Catalysis Communications* **2022,** 162.

(28) Gao, M.; Sheng, W.; Zhuang, Z.; Fang, Q.; Gu, S.; Jiang, J.; Yan, Y., Efficient water oxidation using nanostructured alpha-nickel-hydroxide as an electrocatalyst. *J Am Chem Soc* **2014,** 136, (19), 7077-84.

(29) Chen, L.; Dong, X.; Wang, Y.; Xia, Y., Separating hydrogen and oxygen evolution in alkaline water electrolysis using nickel hydroxide. *Nat Commun* **2016,** 7, 11741.

(30) Miao, Y.; Ouyang, L.; Zhou, S.; Xu, L.; Yang, Z.; Xiao, M.; Ouyang, R., Electrocatalysis and electroanalysis of nickel, its oxides, hydroxides and oxyhydroxides toward small molecules. *Biosens Bioelectron* **2014,** 53, 428-39.

(31) Yang, H.; Gao, G.; Teng, F.; Liu, W.; Chen, S.; Ge, Z., Nickel Hydroxide Nanoflowers for a Nonenzymatic Electrochemical Glucose Sensor. *Journal of The Electrochemical Society* **2014,** 161, (10), B216-B219.

(32) Xia, K.; Yang, C.; Chen, Y.; Tian, L.; Su, Y.; Wang, J.; Li, L., In situ fabrication of $Ni(OH)_2$ flakes on Ni foam through electrochemical corrosion as high sensitive and stable binder-free electrode for glucose sensing. *Sensors and Actuators B: Chemical* **2017,** 240, 979-987.

(33) Canevari, T. C.; Cincotto, F. H.; Landers, R.; Machado, S. A. S., Synthesis and characterization of α-nickel (II) hydroxide particles on organic-inorganic matrix and its application in a sensitive electrochemical sensor for vitamin D determination. *Electrochimica Acta* **2014,** 147, 688-695.

(34) Fang, B.; Gu, A.; Wang, G.; Li, B.; Zhang, C.; Fang, Y.; Zhang, X., Synthesis hexagonal ß-$Ni(OH)_2$ nanosheets for use in electrochemistry sensors. *Microchimica Acta* **2009,** 167, (1-2), 47-52.

(35) Gao, X.-P.; Yao, S.-M.; Yan, T.-Y.; Zhou, Z., Alkaline rechargeable Ni/Co batteries: Cobalt hydroxides as negative electrode materials. *Energy & Environmental Science* **2009,** 2, (5).

(36) Deng, T.; Zhang, W.; Arcelus, O.; Kim, J. G.; Carrasco, J.; Yoo, S. J.; Zheng, W.; Wang, J.; Tian, H.; Zhang, H.; Cui, X.; Rojo, T., Atomic-level energy storage mechanism of cobalt hydroxide electrode for pseudocapacitors. *Nat Commun* **2017,** 8, 15194.

(37) Fu, Y.; Li, L.; Ye, S.; Yang, P.; Liao, P.; Ren, X.; He, C.; Zhang, Q.; Liu, J., Construction of cobalt oxyhydroxide nanosheets with rich oxygen vacancies as high-performance lithium-ion battery anodes. *Journal of Materials Chemistry A* **2021,** 9, (1), 453-462.

(38) Zhan, Y.; Du, G.; Yang, S.; Xu, C.; Lu, M.; Liu, Z.; Lee, J. Y., Development of Cobalt Hydroxide as a Bifunctional Catalyst for Oxygen Electrocatalysis in Alkaline Solution. *ACS Appl Mater Interfaces* **2015,** 7, (23), 12930-6.

(39) Gupta, S.; Yadav, A.; Bhartiya, S.; Singh, M. K.; Miotello, A.; Sarkar, A.; Patel, N., Co oxide nanostructures for electrocatalytic water-oxidation: effects of dimensionality and related properties. *Nanoscale* **2018,** 10, (18), 8806-8819.

(40) Moridon, S. N. F.; Salehmin, M. I.; Mohamed, M. A.; Arifin, K.; Minggu, L. J.; Kassim, M. B., Cobalt oxide as photocatalyst for water splitting: Temperature-dependent phase structures. *International Journal of Hydrogen Energy* **2019,** 44, (47), 25495-25504.

(41) Gao, S.; Jiao, X.; Sun, Z.; Zhang, W.; Sun, Y.; Wang, C.; Hu, Q.; Zu, X.; Yang, F.; Yang, S.; Liang, L.; Wu, J.; Xie, Y., Ultrathin Co_3O_4 Layers Realizing Optimized CO_2 Electroreduction to Formate. *Angew Chem Int Ed Engl* **2016,** 55, (2), 698-702.

(42) Fu, Z. C.; Moore, J. T.; Liang, F.; Fu, W. F., Highly efficient photocatalytic reduction of CO_2 to CO using cobalt oxide-coated spherical mesoporous silica particles as catalysts. *Chem Commun (Camb)* **2019,** 55, (77), 11523-11526.

(43) Pintor-Monroy, M. I.; Barrera, D.; Murillo-Borjas, B. L.; Ochoa-Estrella, F. J.; Hsu, J. W. P.; Quevedo-Lopez, M. A., Tunable Electrical and Optical Properties of Nickel Oxide (NiO_x) Thin Films for Fully Transparent NiO_x-Ga_2O_3 p-n Junction Diodes. *ACS Appl Mater Interfaces* **2018,** 10, (44), 38159-38165.

(44) Zhu, Z.; Bai, Y.; Zhang, T.; Liu, Z.; Long, X.; Wei, Z.; Wang, Z.; Zhang, L.; Wang, J.; Yan, F.; Yang, S., High-performance hole-extraction layer of sol-gel-processed NiO nanocrystals for inverted planar perovskite solar cells. *Angewandte Chemie (International ed. in English)* **2014,** 53, (46), 12571-5.

(45) Liu, S.; Liu, R.; Chen, Y.; Ho, S.; Kim, J. H.; So, F., Nickel Oxide Hole Injection/Transport Layers for Efficient Solution-Processed Organic Light-Emitting Diodes. *Chemistry of Materials* **2014,** 26, (15), 4528-4534.

(46) Tian, F.; Liu, S.; Tian, H.; Dong, R.; Zhang, Y.; Wei, D.; Ye, L.; Whitmore, L., Growth and Photocatalytic Properties of NiO Nanostructures Prepared in Acidic and Alkaline Solutions with Same Reagents. *The Journal of Physical Chemistry C* **2018,** 123, (1), 504-510.

(47) Zhao, Y.; Jia, X.; Chen, G.; Shang, L.; Waterhouse, G. I. N.; Wu, L.-Z.; Tung, C.-H.; O'Hare, D.; Zhang, T., Ultrafine NiO Nanosheets Stabilized by TiO_2 from Monolayer NiTi-LDH Precursors: An Active Water Oxidation Electrocatalyst. *Journal of the American Chemical Society* **2016,** 138, (20), 6517-6524.

(48) Soleimanpour, A. M.; Khare, S. V.; Jayatissa, A. H., Enhancement of hydrogen gas sensing of nanocrystalline nickel oxide by pulsed-laser irradiation. *ACS Appl Mater Interfaces* **2012,** 4, (9), 4651-7.

(49) Guillemot, T.; Schneider, N.; Loones, N.; Javier Ramos, F.; Rousset, J., Electrochromic nickel oxide thin films by a simple solution process: Influence of post-treatments on growth and properties. *Thin Solid Films* **2018,** 661, 143-149.

(50) Zhai, P.; Yi, Q.; Jian, J.; Wang, H.; Song, P.; Dong, C.; Lu, X.; Sun, Y.; Zhao, J.; Dai, X.; Lou, Y.; Yang, H.; Zou, G., Transparent p-type epitaxial thin films of nickel oxide. *Chem Commun (Camb)* **2014,** 50, (15), 1854-6.

(51) Primo, A.; Esteve-Adell, I.; Blandez, J. F.; Dhakshinamoorthy, A.; Alvaro, M.; Candu, N.; Coman, S. M.; Parvulescu, V. I.; Garcia, H., High catalytic activity of oriented 2.0.0 copper(I) oxide grown on graphene film. *Nat Commun* **2015,** 6, 8561.

(52) Wang, W.; Deng, C.; Xie, S.; Li, Y.; Zhang, W.; Sheng, H.; Chen, C.; Zhao, J., Photocatalytic C-C Coupling from Carbon Dioxide Reduction on Copper Oxide with Mixed-Valence Copper(I)/Copper(II). *J Am Chem Soc* **2021,** 143, (7), 2984-2993.

(53) Aktar, A.; Ahmmed, S.; Hossain, J.; Ismail, A. B. M., Solution-Processed Synthesis of Copper Oxide (Cu_xO) Thin Films for Efficient Photocatalytic Solar Water Splitting. *ACS Omega* **2020,** 5, (39), 25125-25134.

(54) Yu, F.; Li, F.; Zhang, B.; Li, H.; Sun, L., Efficient Electrocatalytic Water Oxidation by a Copper Oxide Thin Film in Borate Buffer. *ACS Catalysis* **2014,** 5, (2), 627-630.

(55) Lupan, O.; Ababii, N.; Mishra, A. K.; Gronenberg, O.; Vahl, A.; Schurmann, U.; Duppel, V.; Kruger, H.; Chow, L.; Kienle, L.; Faupel, F.; Adelung, R.; de Leeuw, N. H.; Hansen, S., Single CuO/Cu_2O/Cu Microwire Covered by a Nanowire Network as a Gas Sensor for the Detection of Battery Hazards. *ACS Appl Mater Interfaces* **2020,** 12, (37), 42248-42263.

(56) Zuo, C.; Ding, L., Solution-Processed Cu_2O and CuO as Hole Transport Materials for Efficient Perovskite Solar Cells. *Small* **2015,** 11, (41), 5528-32.

(57) Dasineh Khiavi, N.; Katal, R.; Kholghi Eshkalak, S.; Masudy-Panah, S.; Ramakrishna, S.; Jiangyong, H., Visible Light Driven Heterojunction Photocatalyst of CuO-Cu_2O Thin Films for Photocatalytic Degradation of Organic Pollutants. *Nanomaterials (Basel)* **2019,** 9, (7).

(58) Huang, Y.-C.; Luo, C.-H.; Yang, S.; Lin, Y.-C.; Chuang, C.-Y., Improved Removal of Indoor Volatile Organic Compounds by Activated Carbon Fiber Filters Calcined with Copper Oxide Catalyst. *CLEAN - Soil, Air, Water* **2010,** 38, (11), 993-997.

(59) Hassan, I. A.; Parkin, I. P.; Nair, S. P.; Carmalt, C. J., Antimicrobial activity of copper and copper(i) oxide thin films deposited via aerosol-assisted CVD. *J Mater Chem B* **2014,** 2, (19), 2855-2860.

(60) Zhu, H.; Wang, J.; Xu, G., Fast Synthesis of Cu_2O Hollow Microspheres and Their Application in DNA Biosensor of Hepatitis B Virus. *Crystal Growth & Design* **2009,** 9, (1), 633-638.

(61) Kelly, S. R.; Shi, X.; Back, S.; Vallez, L.; Park, S. Y.; Siahrostami, S.; Zheng, X.; Nørskov, J. K., ZnO As an Active and Selective Catalyst for Electrochemical Water Oxidation to Hydrogen Peroxide. *ACS Catalysis* **2019,** 9, (5), 4593-4599.

(62) Chen, X.; Wu, Z.; Liu, D.; Gao, Z., Preparation of ZnO Photocatalyst for the Efficient and Rapid Photocatalytic Degradation of Azo Dyes. *Nanoscale Res Lett* **2017,** 12, (1), 143.

(63) Kumar, B. V.; Naik, H. S. B.; Girija, D.; Kumar, B. V., ZnO nanoparticle as catalyst for efficient green one-pot synthesis of coumarins through Knoevenagel condensation. *Journal of Chemical Sciences* **2011,** 123, (5), 615-621.

(64) Sarvari, M. H.; Sharghi, H., Reactions on a Solid Surface. A Simple, Economical and Efficient Friedel−Crafts Acylation Reaction over Zinc Oxide (ZnO) as a New Catalyst. *The Journal of Organic Chemistry* **2004,** 69, (20), 6953-6956.

(65) Kim, Y. J.; Varma, R. S., Microwave-assisted preparation of cyclic ureas from diamines in the presence of ZnO. *Tetrahedron Letters* **2004,** 45, (39), 7205-7208.

(66) Wang, A.; Quan, W.; Zhang, H.; Li, H.; Yang, S., Heterogeneous ZnO-containing catalysts for efficient biodiesel production. *RSC Advances* **2021,** 11, (33), 20465-20478.

(67) Wibowo, A.; Marsudi, M. A.; Amal, M. I.; Ananda, M. B.; Stephanie, R.; Ardy, H.; Diguna, L. J., ZnO nanostructured materials for emerging solar cell applications. *RSC Advances* **2020,** 10, (70), 42838-42859.

(68) Hoffmann, R. C.; Sanctis, S.; Schneider, J. J., Molecular Precursors for ZnO Nanoparticles: Field-Assisted Synthesis, Electrophoretic Deposition, and Field-Effect Transistor Device Performance. *Inorg Chem* **2017,** 56, (13), 7550-7557.

(69) Ahmad, M.; Zhu, J., ZnO based advanced functional nanostructures: synthesis, properties and applications. *J. Mater. Chem.* **2011,** 21, (3), 599-614.

(70) Özgür, Ü.; Hofstetter, D.; Morkoç, H., ZnO Devices and Applications: A Review of Current Status and Future Prospects. *Proceedings of the IEEE* **2010,** 98, (7), 1255-1268.

(71) Liu, C.; Wu, W.; Zhang, D.; Li, Z.; Ren, G.; Han, W.; Guo, W., Effective stability enhancement in ZnO-based perovskite solar cells by MACl modification. *Journal of Materials Chemistry A* **2021,** 9, (20), 12161-12168.

(72) Garcia-Farrera, B.; Velasquez-Garcia, L. F., Ultrathin Ceramic Piezoelectric Films via Room-Temperature Electrospray Deposition of ZnO Nanoparticles for Printed GHz Devices. *ACS Appl Mater Interfaces* **2019,** 11, (32), 29167-29176.

(73) Baranton, S.; Coutanceau, C., Nickel cobalt hydroxide nanoflakes as catalysts for the hydrogen evolution reaction. *Applied Catalysis B: Environmental* **2013,** 136-137, 1-8.

(74) Yan, W.; Wang, D.; Botte, G. G., Nickel and cobalt bimetallic hydroxide catalysts for urea electro-oxidation. *Electrochimica Acta* **2012,** 61, 25-30.

(75) Vidhya, M. S.; Ravi, G.; Yuvakkumar, R.; Velauthapillai, D.; Thambidurai, M.; Dang, C.; Saravanakumar, B., Nickel–cobalt hydroxide: a positive electrode for supercapacitor applications. *RSC Advances* **2020,** 10, (33), 19410-19418.

(76) Wang, L.; He, S.; Wang, L.; Lei, Y.; Meng, X.; Xiao, F.-S., Cobalt–Nickel Catalysts for Selective Hydrogenation of Carbon Dioxide into Ethanol. *ACS Catalysis* **2019,** 9, (12), 11335-11340.

(77) Li, X.; Almkhelfe, H.; Bedford, N. M.; Back, T. C.; Hohn, K. L.; Amama, P. B., Characterization and catalytic behavior of Fischer–Tropsch catalysts derived from different cobalt precursors. *Catalysis Today* **2019,** 338, 40-51.

(78) Casci, J. L.; Lok, C. M.; Shannon, M. D., Fischer–Tropsch catalysis: The basis for an emerging industry with origins in the early 20th Century. *Catalysis Today* **2009,** 145, (1-2), 38-44.

(79) Taitt, B. J.; Nam, D.-H.; Choi, K.-S., A Comparative Study of Nickel, Cobalt, and Iron Oxyhydroxide Anodes for the Electrochemical Oxidation of 5-Hydroxymethylfurfural to 2,5-Furandicarboxylic Acid. *ACS Catalysis* **2018,** 9, (1), 660-670.

(80) Zhou, H.; Li, Z.; Xu, S. M.; Lu, L.; Xu, M.; Ji, K.; Ge, R.; Yan, Y.; Ma, L.; Kong, X.; Zheng, L.; Duan, H., Selectively Upgrading Lignin Derivatives to Carboxylates through Electrochemical Oxidative C(OH)-C Bond Cleavage by a Mn-Doped Cobalt Oxyhydroxide Catalyst. *Angew Chem Int Ed Engl* **2021,** 60, (16), 8976-8982.

(81) Gao, M.; Li, Y.; Yang, J.; Liu, Y.; Liu, Y.; Zhang, X.; Wu, S.; Cai, K., Nickel-cobalt (oxy)hydroxide battery-type supercapacitor electrode with high mass loading. *Chemical Engineering Journal* **2022,** 429.

(82) Chen, Y.; Qu, B.; Hu, L.; Xu, Z.; Li, Q.; Wang, T., High-performance supercapacitor and lithium-ion battery based on 3D hierarchical NH_4F-induced nickel cobaltate nanosheet-nanowire cluster arrays as self-supported electrodes. *Nanoscale* **2013,** 5, (20), 9812-20.

(83) Mahadik, S. M.; Chodankar, N. R.; Han, Y. K.; Dubal, D. P.; Patil, S., Nickel Cobaltite: A Positive Electrode Material for Hybrid Supercapacitors. *ChemSusChem* **2021,** 14, (24), 5384-5398.

(84) Liu, S.; Hu, L.; Xu, X.; Al-Ghamdi, A. A.; Fang, X., Nickel Cobaltite Nanostructures for Photoelectric and Catalytic Applications. *Small* **2015,** 11, (34), 4267-83.

(85) Lu, Z.; Chang, Z.; Zhu, W.; Sun, X., Beta-phased $Ni(OH)_2$ nanowall film with reversible capacitance higher than theoretical Faradic capacitance. *Chem Commun (Camb)* **2011,** 47, (34), 9651-3.

(86) Strano, V.; Urso, R. G.; Scuderi, M.; Iwu, K. O.; Simone, F.; Ciliberto, E.; Spinella, C.; Mirabella, S., Double Role of HMTA in ZnO Nanorods Grown by Chemical Bath Deposition. *The Journal of Physical Chemistry C* **2014,** 118, (48), 28189-28195.

(87) Zhang, Y.; Xia, X.; Kang, J.; Tu, J., Hydrothermal synthesized porous $Co(OH)_2$ nanoflake film for supercapacitor application. *Chinese Science Bulletin* **2012,** 57, (32), 4215-4219.

(88) Chen, Z.; Xiao, A.; Chen, Y.; Zuo, C.; Zhou, S.; Li, L., Highly porous nickel oxide thin films prepared by a hydrothermal synthesis method for electrochromic application. *Journal of Physics and Chemistry of Solids* **2013,** 74, (11), 1522-1526.

(89) Husairi, F. S.; Ali, S. M.; Azlinda, A.; Rusop, M.; Abdullah, S., Special Effect of Urea as a Stabilizer in Thermal Immersion Method to Synthesis Porous Zinc Oxide Nanostructures. *Journal of Nanomaterials* **2013,** 2013, 1-7.

(90) Yang, Q.; Lu, Z.; Chang, Z.; Zhu, W.; Sun, J.; Liu, J.; Sun, X.; Duan, X., Hierarchical Co_3O_4nanosheet@nanowire arrays with enhanced pseudocapacitive performance. *RSC Adv.* **2012,** 2, (4), 1663-1668.

(91) Lin, X.; Li, H.; Musharavati, F.; Zalnezhad, E.; Bae, S.; Cho, B.-Y.; Hui, O. K. S., Synthesis and characterization of cobalt hydroxide carbonate nanostructures. *RSC Adv.* **2017,** 7, (74), 46925-46931.

(92) Nishizawa, H.; Yuasa, K., Preparation of Anion Exchangeable Layered Mixed Basic Salt $Ni_{1-x}Zn_{2x}(OH)_2(OCOCH_3)_{2x}\cdot nH_2O$ Thin Film under Hydrothermal Conditions. *Journal of Solid State Chemistry* **1998,** 141, (1), 229-234.

(93) Ghotbi, M. Y.; Rahmati, Z., Nanostructured copper and copper oxide thin films fabricated by hydrothermal treatment of copper hydroxide nitrate. *Materials & Design* **2015,** 85, 719-723.

(94) Karakawa, M.; Sugahara, T.; Hirose, Y.; Suganuma, K.; Aso, Y., Thin Film of Amorphous Zinc Hydroxide Semiconductor for Optical Devices with an Energy-Efficient Beneficial Coating by Metal Organic Decomposition Process. *Sci Rep* **2018,** 8, (1), 10839.

(95) Ratnayake, S. P.; Ren, J.; Colusso, E.; Guglielmi, M.; Martucci, A.; Della Gaspera, E., SILAR Deposition of Metal Oxide Nanostructured Films. *Small* **2021,** 17, (49), 2101666.

(96) Nguyen, T.; Boudard, M.; Carmezim, M. J.; Montemor, M. F., Layered $Ni(OH)_2$-$Co(OH)_2$ films prepared by electrodeposition as charge storage electrodes for hybrid supercapacitors. *Sci Rep* **2017,** 7, 39980.

(97) Kozai, N.; Mitamura, H.; Fukuyama, H.; Esaka, F.; Komarneni, S., Synthesis and characterization of copper hydroxide acetate with a layered discoid crystal. *Journal of Materials Research* **2005,** 20, (11), 2997-3003.

(98) Masciocchi, N.; Corradi, E.; Sironi, A.; Moretti, G.; Minelli, G.; Porta, P., Preparation, Characterization, and ab initio X-Ray Powder Diffraction Study of $Cu_2(OH)_3(CH_3COO)\cdot H_2O$. *Journal of Solid State Chemistry* **1997,** 131, (2), 252-262.

(99) Moezzi, A.; McDonagh, A.; Dowd, A.; Cortie, M., Zinc hydroxyacetate and its transformation to nanocrystalline zinc oxide. *Inorg Chem* **2013,** 52, (1), 95-102.

(100) Morioka, H.; Tagaya, H.; Karasu, M.; Kadokawa, J.-i.; Chiba, K., Effects of Zinc on the New Preparation Method of Hydroxy Double Salts. *Inorganic Chemistry* **1999,** 38, (19), 4211-4216.

(101) Kandare, E.; Hossenlopp, J. M., Thermal Degradation of Acetate-Intercalated Hydroxy Double and Layered Hydroxy Salts. *Inorganic Chemistry* **2006,** 45, (9), 3766-3773.

(102) Meyn, M.; Beneke, K.; Lagaly, G., Anion-exchange reactions of hydroxy double salts. *Inorganic Chemistry* **1993,** 32, (7), 1209-1215.

(103) Nishizawa, H.; Kishikawa, T.; Minami, H., Formation of α,β-Type Hydroxides and Second-Stage Intermediate in Hydrothermal Decomposition of Nickel Acetate. *Journal of Solid State Chemistry* **1999,** 146, (1), 39-46.

(104) EPA; The Effects: Dead Zones and Harmful Algal Blooms. https://www.epa.gov/nutrientpollution/effects-dead-zones-and-harmful-algal-blooms

(105) EPA *A Compilation of Cost Data Associated with the Impacts and Control of Nutrient Pollution*; https://www.epa.gov/sites/default/files/2015-04/documents/nutrient-economics-report-2015.pdf.

(106) Dodds, W. K.; Bouska, W. W.; Eitzmann, J. L.; Pilger, T. J.; Pitts, K. L.; Riley, A. J.; Schloesser, J. T.; Thornbrugh, D. J., Eutrophication of U.S. Freshwaters: Analysis of Potential Economic Damages. *Environmental Science & Technology* **2009,** 43, (1), 12-19.

(107) Kapaj, S.; Peterson, H.; Liber, K.; Bhattacharya, P., Human health effects from chronic arsenic poisoning--a review. *J Environ Sci Health A Tox Hazard Subst Environ Eng* **2006,** 41, (10), 2399-428.

(108) Karagas, M. R.; Gossai, A.; Pierce, B.; Ahsan, H., Drinking Water Arsenic Contamination, Skin Lesions, and Malignancies: A Systematic Review of the Global Evidence. *Curr Environ Health Rep* **2015,** 2, (1), 52-68.

(109) Minnesota Department of Health; Arsenic in Drinking Water. https://www.health.state.mn.us/communities/environment/water/contaminants/arsenic.html#HeatlhEffects

(110) EPA;, Arsenic Compounds. In https://www.epa.gov/sites/default/files/2021-04/documents/arsenic_april_2021.pdf.

(111) Pei, J.; Zuo, J.; Wang, X.; Yin, J.; Liu, L.; Fan, W., The Bioaccumulation and Tissue Distribution of Arsenic Species in Tilapia. *Int J Environ Res Public Health* **2019,** 16, (5).

(112) ACS 12 Principles of Green Chemistry. https://www.acs.org/content/acs/en/greenchemistry/principles/12-principles-of-green-chemistry.html

CHAPTER II

Hydrolysis of Nickel Acetate: Deposition of Web-Like Nanowalls of Nickel Acetate Hydroxide as Thin Films for Nickel Oxide

■ Introduction:

Nanostructured nickel oxide (NiO) as thin films have excellent and promising applications in various essential technologies such as a hole transport layer in perovskite solar cells,[1] hole injection/transport layers in organic light-emitting diodes,[2] photocatalysis,[3] electrocatalytic water splitting,[4] gas sensors,[5] electrochromic glasses,[6] transparent conductive oxides,[7] etc. NiO is a semi-conductive oxide material of a wide band gap in the order of 3.15 to 4.3 eV.[8] In such wide band gap oxide as NiO, the primarily formed Ni^{2+} vacancies or holes (major intrinsic defects) facilitate the hopping migration of small polaronic charges across the oxide material at the ambient condition,[9] which renders the NiO an excellent p-type or hole-type oxide material. Moreover, nanostructured NiO can be fabricated as high-quality thin films on different substrates such as glass, indium tin oxide coated glass, fluorine-doped tin oxide coated glass, flexible substrates, graphene, carbon cloth, metals, metal oxides, etc.[10-18] As a result, nanostructured NiO thin films are desirable and promising materials in various technologies mentioned above. Due to the broad range of applications of nanostructured NiO as thin films, it has been a great interest in the scientific community to fabricate thin films of NiO nanostructures using facile, cost-effective, and lesser chemical involving methods.

Hydrothermal deposition is an appealing solution growth process for depositing thin films of nanostructured metal oxides as it is a simple, large substrate-area scalable, and cheaper process. One of the well-studied hydrothermal deposition processes for NiO thin films involves aqueous solutions of nickel nitrate, $Ni(NO_3)_2$ and hexamethylenetetramine (HMTA) as precursor solutions in a closed reaction vessel. For example, F. Cao and his co-workers reported a 1:2 mixture of nickel nitrate and HMTA aqueous solution at 105 °C in an autoclave produced an intermediate film, which converted to mesoporous NiO films with nanomorphology of interconnected web-like nanowalls after pyrolysis.[11] Whereas W. K. Chan *et al.* found a 1:1 mixture at 90 °C in a closed vial generated a thin film, which produced NiO having a network-like nanostructure upon pyrolysis.[15] These hydrothermal reactions to produce NiO films are similar to the well-known hydrothermal synthesis of thin films of ZnO nanorods from the aqueous solutions of zinc nitrate, $Zn(NO_3)_2$, and HMTA.[19] Other than HMTA, urea ($CO(NH_2)_2$) has also been studied with nickel nitrate in hydrothermal reactions. Z. Chen *et al.* reported that a mixture of nickel nitrate, urea, and ammonium fluoride in water at 105 °C in an autoclave produces layered nickel hydroxide carbonate, $Ni_2(OH)_2CO_3 \cdot nH_2O$ as thin films, which after annealing at 300-450 °C were successfully yielded to NiO thin films consisted of interconnected-nanowalls.[20]

Hydrolysis of transition metal acetates in organic solvents such as polyols was also studied as a hydrothermal method for synthesizing metal acetate hydroxides as precursors for metal oxides. One such study was reported by L. Poul and co-workers as they explored the hydrothermal reaction of zinc, nickel, and cobalt acetates separately in polyols (diethylene glycol and 1, 2-propanediol) solvents. They found that the polyol-mediated hydrolysis of metal acetates produced layered materials of metal acetate hydroxides, $M(OH)_{2-x}(CH_3COO)_x \cdot nH_2O$ (where M= Zn, Ni, and Co).[21] However, the study did not mention the generation of thin films of the corresponding metal acetate hydroxides. Studies on hydrolysis of aqueous solutions of metal acetates without any organic solvent or reactant are found to be very few. Nishizawa and co-workers studied hydrolysis of only

nickel acetate aqueous solution in an autoclave up to 350 °C and 16 MPa pressure and then rapid cooling to room temperature.[22] The autoclave with nickel acetate solution was heated at a ramp of 4 °C per minute. They claimed the hydrothermal reaction yields nickel oxide in a few steps – firstly, at 160 °C, the solution produces α-type nickel acetate hydroxide, $Ni_2(OH)_3(OAc)\cdot 1.4H_2O$ layered material, then secondly, at 320 °C, nickel acetate hydroxide decomposes to β-$Ni(OH)_2$ by losing acetate. Upon further heating (above 340 °C), the β-$Ni(OH)_2$ converts to NiO. The study also did not report the formation of films of nickel acetate hydroxide or nickel oxide. Nishizawa also studied hydrolysis of aqueous solutions zinc acetate and nickel acetate mixtures in an autoclave up to 300 °C, which reported a 1:10 mixture of zinc and nickel acetate aqueous solution at 150 °C produced a thin film of $Ni_{0.78}Zn_{0.44}(OH)_2(OAc)_{0.44}\cdot nH_2O$.[23] Without knowing anybody's work, we independently and serendipitously found that hydrolysis of only an aqueous solution of copper acetate at a low temperature of 90 °C in a closed pyrex bottle in 24 hours can produce aggregates of copper (II) oxide, CuO on glass substrates (presented later in Chapter III). Motivated by the finding, we explored the hydrolysis of pure nickel acetate aqueous solution at 90 °C. To our surprise, at that low temperature, the hydrolysis reaction produced excellent-quality thin films of web-like nanostructured nickel acetate hydroxide, which is an acetate-intercalated layered nickel hydroxide. Literature investigation revealed that low-temperature hydrolysis of only aqueous solutions of nickel acetate to deposit nanostructured thin films of acetate-intercalated layered nickel hydroxide has not been reported yet.

Herein, as a result, we report the discovery of straightforward hydrolysis (hydrothermal) reaction of nickel acetate aqueous solutions without an additional reactant or an organic solvent that deposited nickel acetate hydroxide, $Ni(OAc)_{0.28}(OH)_{1.72}\cdot 0.25H_2O$ as nanostructured thin film-precursor for corresponding nanostructured NiO thin films. The hydrolysis reaction required nickel acetate as a starting material and water, where water plays the role of a solvent as well as a reactant. The nickel acetate hydroxide films were deposited as a web-like network structure of nanowalls on

glass substrates. These thin films of nickel acetate hydroxide were excellent precursors for producing NiO thin films since, upon pyrolysis at 425 °C, the thin films of nickel acetate hydroxide were readily converted to NiO thin films by maintaining the same web-like network morphology of the nanowalls. The deposition process for web-like nanostructured NiO as thin films reported here is facile, inexpensive, and found to be excellently reproducible.

■ Experimental

Thin films of web-like nanostructured nickel acetate hydroxide, $Ni(OAc)_{0.28}(OH)_{1.72}\cdot 0.25H_2O$ were deposited on microscope-glass substrates. The glass substrates were first cleaned by soaking them in soap water, washed thoroughly in hot water, and deionized water. Finally, acetone rinse was employed to remove any remaining organics from the glass substrates. For a typical hydrolysis reaction, 10 mmol nickel acetate tetrahydrate, $Ni(OOCCH_3)_2\cdot 4H_2O$ (Fisher Scientific) without further purification was dissolved in 50 mL of deionized water. The solution was then heated at 90 °C for 24 hours with a pre-cleaned glass substrate (vertically placed) in a closed Pyrex bottle as depicted in Scheme 1. A very light-green-colored material as a thin film was deposited on the glass substrate. The film was first washed by dipping it in deionized water and then dried at room temperature under air. Upon pyrolysis at 425°C, the thin film of nickel acetate hydroxide, $Ni(OAc)_{0.28}(OH)_{1.72}\cdot 0.25H_2O$ was converted to the thin film of nickel oxide, NiO. The deposited thin films of nickel acetate hydroxide, $Ni(OAc)_{0.28}(OH)_{1.72}\cdot 0.25H_2O$ and their pyrolysis to the thin films of NiO were found to be produced with excellent reproducibility.

The thin films of nickel acetate hydroxide and their pyrolyzed thin films of NiO were directly studied for characterization using Thermo Fisher Nicolet iS50 attenuated total reflectance-FTIR spectrophotometer, Bruker D8 Advance X-ray Diffractometer, and FEI Quanta 600 field emission gun ESEM instrument. For obtaining XRD patterns, Cu K_α (λ=1.54056Å) radiation was employed. SEM images of nickel acetate hydroxide thin films were taken at 15 kV, whereas the

pictures of NiO thin films were taken at 20kV. The thickness of the films was determined by using Bruker DektakXT profilometer. UV-Visible spectroscopy of both thin films was performed in Varian Cary 100 UV-Visible Spectrophotometer. The nickel acetate hydroxide grown in the reaction solution was collected by centrifugation and washed thoroughly with DI water to remove surface adsorbed acetate. Washing was continued until the rinse water read close to zero μScm^{-1} in a conductometer. The material was then vacuum dried and used for Elemental Analysis, Microwave Plasma Atomic Emission Spectroscopy (MP-AES), and Thermogravimetric Analysis (TGA). Agilent 4200 MP-AES instrument was used for estimating the nickel content. While the elemental analysis was executed in a LECO CHN 628 analyzer to determine carbon and nitrogen content. The thermogravimetric analysis (TGA) of the nickel acetate hydroxide was performed using a Mettler Toledo TGA instrument. Particle size distributions of a reaction solution were obtained by a Malvern HPPS particle size analyzer.

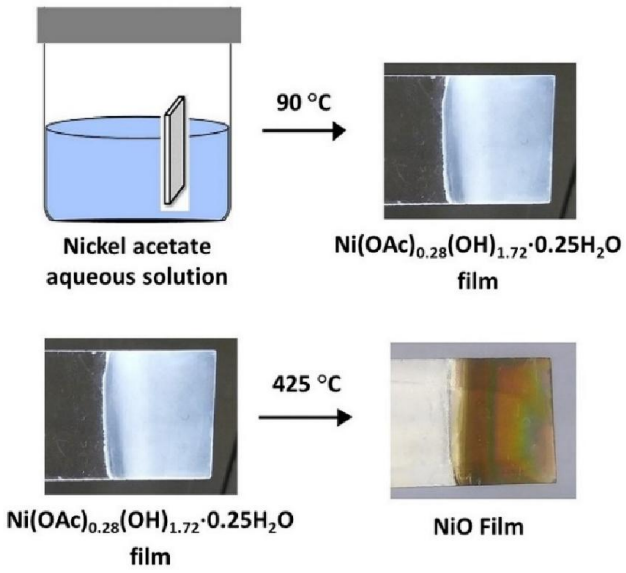

Scheme 1: Hydrolysis of nickel acetate aqueous solution at 90 °C to deposit a thin film of nickel acetate hydroxide, $Ni(OAc)_{0.28}(OH)_{1.72}\cdot 0.25H_2O$ followed by thermal decomposition of the deposited thin film at 425 °C to yield a NiO thin film.

■ **Results and Discussion:**

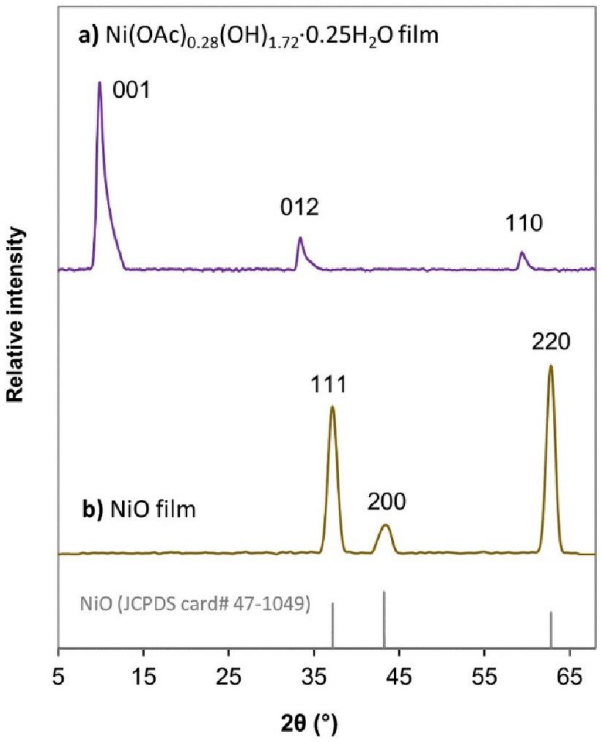

Figure 1: The XRD pattern of (a) a web-like nanostructured thin film of nickel acetate hydroxide, $Ni(OAc)_{0.28}(OH)_{1.72}\cdot 0.25H_2O$, and (b) a thin film of identical nanostructured NiO prepared by pyrolysis of the nickel acetate film at 425°C. At the bottom of the figure, the XRD pattern represents NiO from JCPDS card# 47-1049.[24]

Thin films of web-like nanostructured nickel acetate hydroxide, $Ni(OAc)_{0.28}(OH)_{1.72}\cdot 0.25H_2O$ and nickel oxide, NiO were directly run in the Bruker Discover D8 X-ray diffractometer by employing Cu Kα (λ= 1.54056Å) radiation for acquiring their XRD patterns. Figure 1 presents the smoothed and backgrounds subtracted XRD patterns of both films. The XRD pattern of the film of nickel acetate hydroxide (Figure 1(a)) shows three peaks at 9.90°, 33.40°, and 59.39°. The peaks can be well indexed as (001), (012), and (110) lattice planes, respectively, corresponding to a hexagonal lattice phase. The XRD peaks are in close agreement with other acetate-intercalated

nickel hydroxides such as $Ni(OH)_{1.60}(OAc)_{0.40}\cdot 0.63H_2O$ and $Ni_2(OH)_3(OAc)\cdot 1.4H_2O$.[21, 22] The acetate-intercalated nickel hydroxides are layered metal hydroxides (LMHs) that adopt a hexagonal lattice phase forming a brucite type layered structure.[21, 25] Also, the XRD pattern of nickel acetate hydroxide, $Ni(OAc)_{0.28}(OH)_{1.72}\cdot 0.25H_2O$ has sharp peaks at a smaller Bragg angle, and broad asymmetric peaks at the higher angles may indicate the turbostratic feature of the layered structure.[21] The d-spacings of (001), (012), and (110) planes and the lattice parameters were determined from the XRD pattern as shown in Table 1. The strong intensity of the (001) planes indicates a preferential growth of the layered structure along the c-axis of a lattice. This is, indeed, consistent with the SEM images of the thin film of nickel acetate hydroxide (Figure 4), as they reveal that the deposited film material was grown as a web-like network structure of interconnected nanowalls across the substrate (along a- and b- axes of a lattice). While the thickness of the thin film (height of the nanowalls) was estimated as 400 nm by a profilometer (Table 6), which indicates the interconnected nanowalls are grown vertically along the substrate that is along the c-axis of a lattice. The (001) planes (c-parameter of the lattice, the first (*00l*) reflection) also represent the distance of two adjacent layers (interlayer spacing) along the c-axis of a layered hydroxide lattice structure.[21, 26] Notably, the interlayer spacing of the thin film of the nickel acetate hydroxide (d_{001} = 8.92Å) of this work is smaller than the other reported nickel acetate hydroxides of $Ni(OH)_{1.60}(OAc)_{0.40}\cdot 0.63H_2O$[21] and $Ni_2(OH)_3(OAc)\cdot 1.4H_2O$[22] as compared in Table 2. Whereas the d_{001} spacing of the nickel acetate hydroxide deposited as film (this work) is larger than the aluminum substituted α-nickel hydroxide, $Ni_{0.74}Al_{0.26}(OH)_{2.26}\cdot 1.5H_2O$ membrane (the first d_{00l} spacing = 7.37 Å) that we published in our other work[27] where the membrane was prepared by a facile evaporation method from an aqueous solution of a mixture of sodium aluminate, $NaAl(OH)_4$ and nickel ammonia hydroxide, $Ni(NH_3)_6(OH)_2$. A schematic structural model of the layered structure of the nickel acetate hydroxide, $Ni(OAc)_{0.28}(OH)_{1.72}\cdot 0.25H_2O$ of this work is presented in Figure 9 (right).

The XRD pattern of the web-like nanostructured NiO film is presented in Figure 1(b), which exhibits peaks at 37.15, 43.05°, and 62.80°. The peaks correspond to (111), (200), and (220) lattice planes, respectively, of a cubic lattice system. The d-spacings of the lattice planes are tabulated in Table 1. The positions (2θ) of the XRD peaks of the prepared NiO film are matched up with the peaks corresponding to a cubic lattice system of NiO (JCPDS card# 47-1049[24]) which confirms that the film of nickel acetate hydroxide, $Ni(OAc)_{0.28}(OH)_{1.72}\cdot 0.25H_2O$ was successfully converted to the film of NiO upon pyrolysis at 425°C. The sharp (111) lattice planes indicate that the web-like nanostructured NiO has vertically grown planes along the c-axis of a cubic lattice. While smaller and significantly broader (200) planes specify the diffraction of x-rays by a smaller number of lattice planes (nano-thickness) along the a- or b-axis of the lattice. These observations of the XRD pattern are, indeed, very consistent with the SEM image of the NiO film (Figure 5), as it evidentially shows that the web-like interconnected nanowalls of NiO have nano-thickness across the substrate (a- or b-axis of a lattice) while they have grown vertically on the substrate (c-axis of a lattice). The XRD peaks of both films of nickel acetate hydroxide and NiO are broad that also indicative of the fact that the deposited nickel acetate hydroxide and NiO materials have nano-dimensions.[28, 29]

Table 1: Miller indices, their d-spacings, and lattice parameters of thin films of web-like nanostructured nickel acetate hydroxide and nickel oxide

Film	2θ	hkl	d (Å)	Lattice parameters (Å)
$Ni(OAc)_{0.28}(OH)_{1.72}\cdot 0.25H_2O$	9.90	001	8.92	a = 3.10 c = 8.92
	33.40	012	2.68	
	59.39	110	1.55	
NiO	37.17	111	2.42	a = 4.18
	43.30	200	2.09	
	62.78	220	1.48	

Table 2: Comparison of d-spacings of the first (*00l*) planes (interlayer distance) of the thin film of web-like nanostructured nickel acetate hydroxide (of this work) with other reported nickel acetate hydroxides and a membrane of α-type nickel hydroxide (where X-ray sources for diffraction angles were CuK_{α}, λ=1.54056Å)

Nickel hydroxides	**Interlayer distance (*d*-spacing of the first (*00l*) planes) (Å)**	***a* parameter (Å)**	**References**
$Ni(OAc)_{0.28}(OH)_{1.72}\cdot 0.25H_2O$	8.92	3.09	This work
$Ni(OH)_{1.60}(OAc)_{0.40}\cdot 0.63H_2O$	10.64	3.11	Reference 21
$Ni_2(OH)_3(OAc)\cdot 1.4\ H_2O$	9.44	3.10	Reference 22
$\alpha\text{-}Ni_{0.74}Al_{0.26}(OH)_{2.26}\cdot 1.5H_2O$	7.37	3.06	Reference 29

A thin film of nickel acetate hydroxide, $Ni(OAc)_{0.28}(OH)_{1.72}\cdot 0.25H_2O$, and a thin film of NiO were directly run in the attenuated total reflectance-FTIR instruments, and the spectra are presented in Figure 2. FTIR spectrum of the thin film of nickel acetate hydroxide showed peaks for acetate (CH_3COO^-) at 1375 and 1586 cm^{-1} (Figure 2(a)). The 1375 cm^{-1} peak represents the -COO symmetric stretching mode, whereas 1586 cm^{-1} indicates the -COO asymmetric stretching mode. The difference between the two peaks is in the order of 211 cm^{-1}, which suggests that the acetates have uni-coordination with nickel.[22] The peak at 1321 cm^{-1} (just before the -COO symmetric stretching mode) indicates the CH_3 deformation of the acetate (CH_3-COO^-) groups.[21] The peaks of acetates in our study are found to be in good agreement with other nickel acetate hydroxides reported in the works of L. Poul[21] and H. Nishizawa[22] that are compared in Table 3**.** The intense peak at 606 to 636 cm^{-1} must be due to Ni-OH bending vibration mode. The strong band at 606-636 cm^{-1} also indicates that the hydroxyl groups of the deposited nickel acetate hydroxide are connected by hydrogen bonding to interlayer water molecules.[22] While a sharp peak at 3641 cm^{-1}

establishes Ni-OH starching modes. The broad peak at 3417 cm^{-1}, just before the sharp peak at 3641 cm^{-1}, confirms that the material contains the H-bonded interaction of the hydroxyl groups to interlayer water molecules.

Pyrolysis at 425 °C converted the thin films of nickel acetate hydroxide to the thin films of NiO. Figure 2(b) presents an FTIR spectrum from 525 to 700 cm^{-1}, and Figure S1 in supporting information shows a full range (525 to 4000 cm^{-1}) FTIR spectrum of such a typical NiO thin film. As in the full range FTIR spectrum of the NiO thin film, no peaks for acetate are observed, confirming that the acetate groups were completely decomposed at 425°C. Intense peaks at the range of 529-550 cm^{-1} in the spectrum must be due to the Ni-O lattice vibrations and infrared active surface modes of NiO.[30, 31] The surface modes (polaritons) of NiO nanoparticles in IR spectra have been reported at the range of 525-560 cm^{-1}.[31] The FTIR spectrum of a pyrolyzed film of nickel acetate hydroxide, alongside the XRD pattern and TGA experiment (discussed later), confirms that the films of nickel acetate hydroxide were successfully converted to the films of NiO upon pyrolysis.

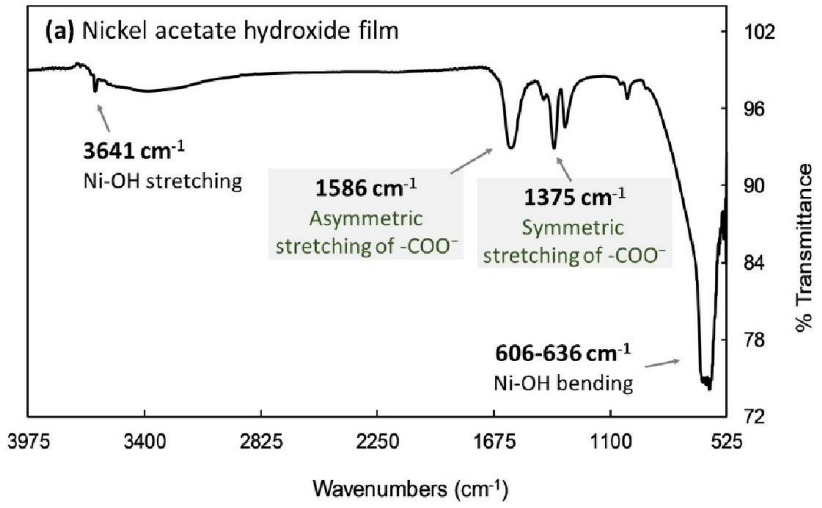

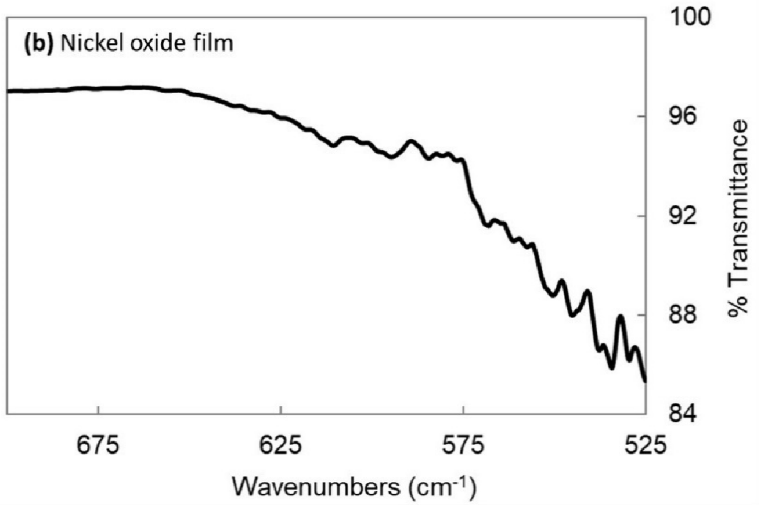

Figure 2: FT-IR spectra of (a) thin film of nickel acetate hydroxide, $Ni(OAc)_{0.28}(OH)_{1.72}\cdot 0.25H_2O$, and (b) thin film of NiO prepared by pyrolysis of the nickel acetate hydroxide thin film at 425 °C.

Table 3: Comparison of symmetric and asymmetric stretching bands of -COO of acetate group of nickel acetate hydroxides in FT-IR spectroscopy

Nickel Acetate Hydroxides	**Symmetric stretching of -COO (cm^{-1})**	**Asymmetric stretching of -COO (cm^{-1})**	**References**
$Ni(OAc)_{0.28}(OH)_{1.72}\cdot 0.25H_2O$	1375	1586	This work
$Ni(OH)_{1.60}(OAc)_{0.40}\cdot 0.63H_2O$	1380	1609	Reference 21
$Ni_2(OH)_3(OAc)\cdot 1.4H_2O$	1385	1593	Reference 22

The vacuum dried nickel acetate hydroxide (collected from the reaction solution) was used for elemental analysis, Microwave Atomic Emission Spectroscopy (MP-AES), and thermogravimetric analysis. The elemental analysis confirmed the presence of 5.98% of carbon, while the MP-AES analysis determined the nickel content as 52.9%. Table S1 of the supporting information presents the MP-AES analysis data for determining nickel content. The nickel content

estimated from the thermogravimetric analysis closely agrees with the MP-AES analysis, as shown in Table 4.

Table 4: Nickel and carbon contents of nickel acetate hydroxide, $Ni(OAc)_{0.28}(OH)_{1.72}\cdot 0.25H_2O$ from MP-AES, thermogravimetric, and elemental analysis

Ni content from MP-AES (%)	Ni content from TGA (%)	Carbon Content from elemental analysis (%)
52.9±0.8	53.85[a]	5.98

a. The amount of Ni was estimated using the ceramic yield of NiO from the TGA plot (Figure 3). The ceramic yield is 68.53%, which determines the amount of nickel as 53.85%.

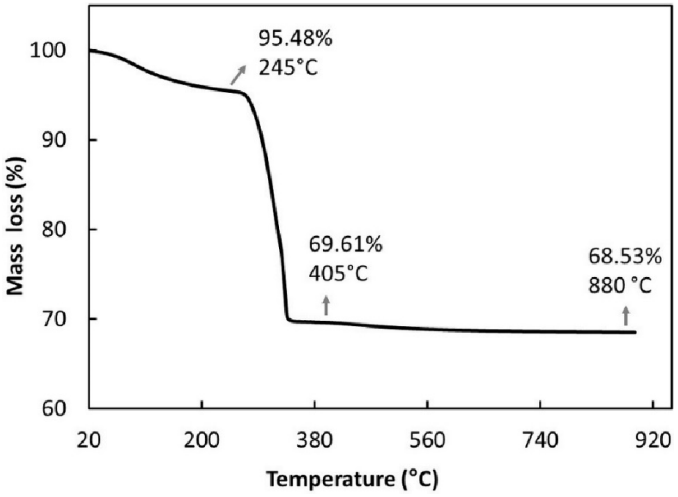

Figure 3: Thermogravimetric analysis of nickel acetate hydroxide, $Ni(OAc)_{0.28}(OH)_{1.72}\cdot 0.25H_2O$.

The thermogravimetric analysis (TGA) plot of nickel acetate hydroxide is presented in Figure 3, and a DTG (differential thermogravimetric) plot derived from the TGA experiment is added in the supporting information (Figure S2). The TGA experiment was performed under air at a heating ramp of 20°C/minute. The amount of sample for the experiment was 19.116 mg. In the

TGA plot, the first mass loss from around 50 to 245 °C represents the loss of interlayer water, determined as 4.52%. The rest of the mass loss up to 370 °C must be due to the dehydroxylation of hydroxyl groups and decomposition of acetate groups to yield the ceramic product of NiO. The losses of mass in the TGA plot are consistent with other reported layered basic nickel acetates,[21, 22] where the losses of mass were confirmed by a TGA-mass spectrophotometer instrument.[21] After 405 °C, the ceramic product of NiO is still losing a little bit of its mass which can be attributed to the following – (i) desorption of excessive oxygen bound to the Ni^{3+} sites (that generated due to cation vacancies) of the ceramic product of NiO,[32] and/or (ii) dehydroxylation of a minimal amount of undecomposed surface hydroxyl groups. These surface hydroxyl groups need to migrate across the surface to come close to each other to decompose as water, which renders the dehydroxylation of the surface hydroxyl groups to occur at higher temperatures above 405 °C. Based on the TGA experiment, the carbon content from elemental analysis, and the nickel content from MP-AES analysis, the formula of nickel acetate hydroxide was determined as $Ni(OAc)_{0.28}(OH)_{1.72}\cdot 0.25H_2O$. Table S2 in the supporting information includes the enumeration of the formula of nickel acetate hydroxide.

The thin film of nickel acetate hydroxide, $Ni(OAc)_{0.28}(OH)_{1.72}\cdot 0.25H_2O$, was deposited as interconnected nanowalls forming a web-like network structure across the glass substrate (Figure 4). After the pyrolysis of the thin films of nickel acetate hydroxide to the thin films of NiO, the web-like network morphology of the interconnected nanowalls retained the structure on the substrate (Figure 5). This shows that the thermal decomposition of the thin film material of nickel acetate hydroxide does not destroy the starting morphology of the web-like nanowalls while converting to NiO. This is an important finding as it shows that nanostructures of nickel acetate hydroxides are excellent precursors to access similar nanostructured NiO. Layered hydroxides of other metals such as copper acetate hydroxide and cobalt dodecyl sulfate hydroxide have also been reported to produce corresponding nanostructured oxides upon pyrolysis by adopting their starting

morphologies.[33, 34] The web-like morphology of NiO nanowalls as thin films has also been reported in other hydrothermal and non-hydrothermal synthetic routes.[10-12, 15, 20] Compared to the other works, our study does not require any second reactant or organic solvent in depositing the thin films of nickel acetate hydroxide as a precursor for thin films of NiO. It renders the hydrothermal reaction of our study as an excellent lesser chemical involving process.

The interconnected nanowalls of the web-like morphology of NiO have open spaces among the walls that were estimated by ImageJ software. Figure 6(a) presents a schematic drawing of the open spaces, while Figure 6(b) presents a distribution plot of the areas of the open spaces. The areas of the open spaces are dominantly in the order of 25-100 nm^2 since 50% of the open spaces have areas in this range. The second dominant open spaces are 101-5000 nm^2, constituting 21% of the open spaces. If the web-like interconnected NiO nanowalls decorated substrates/supports were employed in the thermal-, photo- and electro-catalysis, gas or electrochemical sensors, adsorptive removal of organic or inorganic pollutants, etc. The open areas between the nanowalls would play a crucial role in such applications. Since these open spaces surrounded by NiO nanowalls formed a pore-like structure that would be available for adsorption of reactant molecules to be catalyzed, gases or analytes to be detected, and organic or inorganic pollutants to be removed.

Distribution plots of the thicknesses of the interconnected nanowalls of both films are also presented in Figure 7, where the thicknesses of the nanowalls of both films were estimated from randomly selected two hundred nanowalls. The average thickness of the nanowalls of nickel acetate hydroxide was determined as 66±11 nm, while after pyrolysis, the thickness of NiO nanowalls was estimated as 35±7 nm (Table 5). The lower thickness of NiO nanowalls than the nickel acetate hydroxide was expected as the nickel acetate hydroxide is a layered material that adopts a brucite type layered structure that adopts a hexagonal lattice phase. [21, 25] While NiO adopts a rock salt structure that is consisted of a cubic lattice structure.

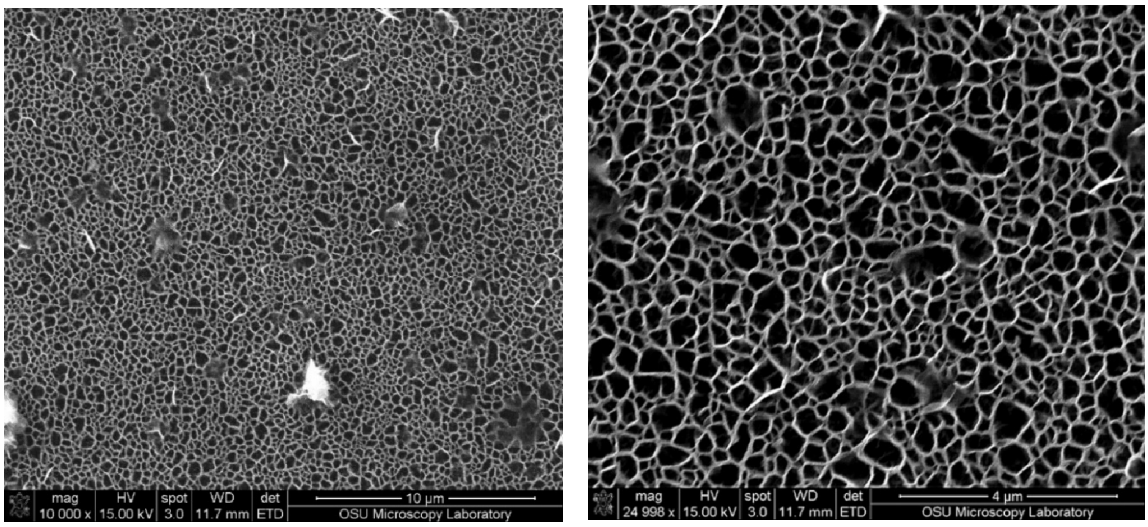

(a) (b)

Figure 4: SEM images of a thin film of web-like nanostructured nickel acetate hydroxide deposited on a glass substrate. Magnifications: (a) 10,000x and (b) ~25,000x.

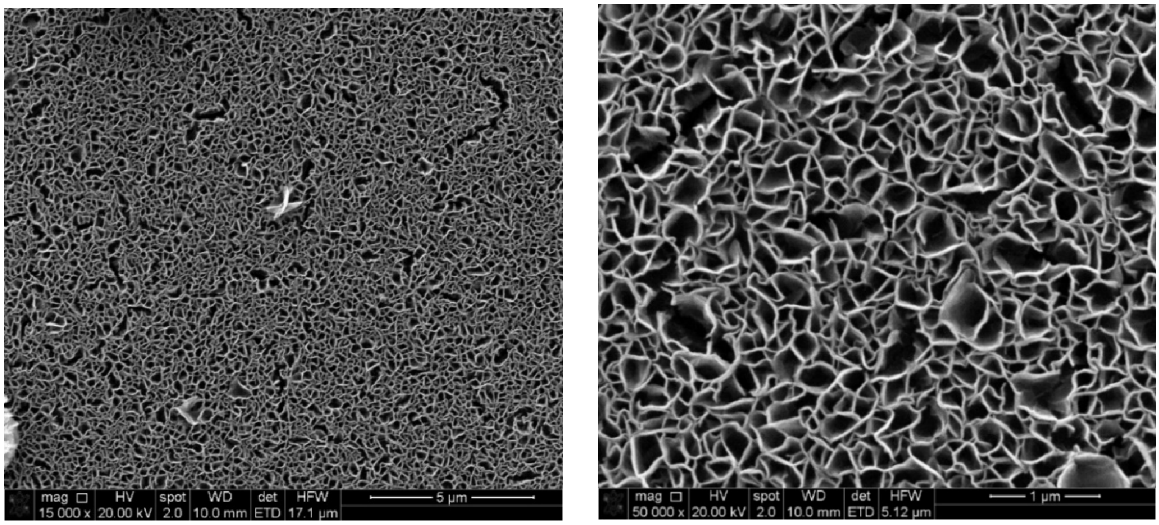

(a) (b)

Figure 5: SEM images of web-like nanostructured NiO thin film prepared by pyrolysis of a nickel acetate hydroxide thin film. Magnifications: (a) 15,000x and (b) 50,000x.

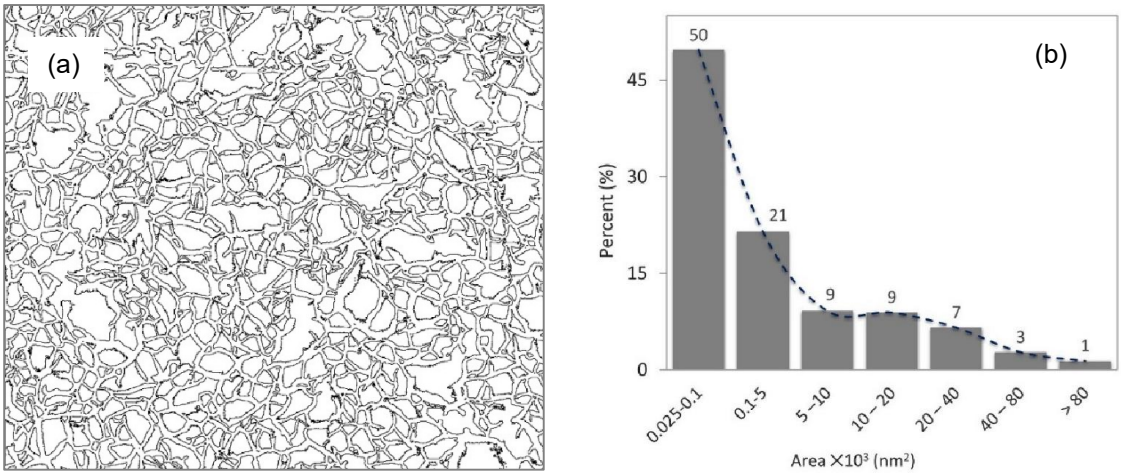

Figure 6: Schematic drawing of the open spaces among the web-like nanowalls of a nickel oxide film and (b) distribution of areas of open spaces (percent vs. nm^2) among the nanowalls. SEM image Figure 5(b) of the nickel oxide film and ImageJ software were used to develop the schematic drawing and estimate the areas of open spaces.

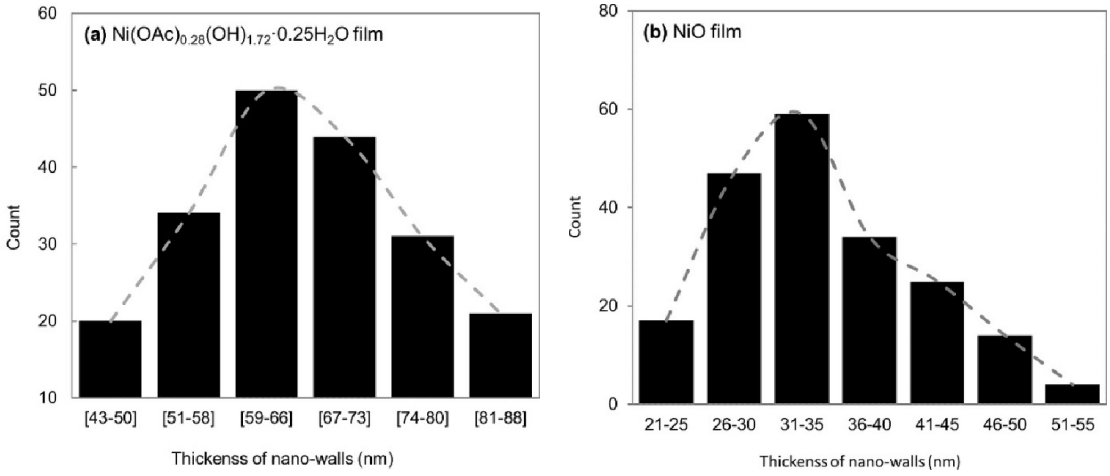

Figure 7: Distribution of thicknesses of the web-like nanowalls of the thin films of (a) nickel acetate hydroxide and (b) nickel oxide. The thicknesses were estimated using the SEM images in Figures 4(b) and 5(b).

Table 5: Average thicknesses of the web-like nanowalls of nickel acetate hydroxide and nickel oxide determined from randomly selected two hundred nanowalls using the SEM images presented in Figures 4(b) and 5(b)

Thin Films	Average Thickness of nano-walls (nm)
$Ni(OAc)_{0.28}(OH)_{1.72}\cdot 0.25H_2O$	66±11
NiO	35±7

The thicknesses (heights) of typical web-like nanostructured films of nickel acetate hydroxide and NiO were determined by employing a calibrated Bruker DektakXT profilometer. The experiments were performed with a 2 μm stylus under a standard scan setting. Their average thicknesses from five scans for each film are tabulated in Table 6. The average thickness of the film of nickel acetate hydroxide was estimated as 400 nm, confirming that the hydrothermal reaction deposited "thin films" that are less than 1 micrometer thick. While thin films of nickel acetate yielded NiO thin films of lower thickness. The average thickness of a thin film of NiO was measured as 320 nm.

Table 6: Thicknesses (heights) of the thin films of nickel acetate hydroxide and nickel oxide determined using a profilometer

Thin films	Thickness (heights) of the thin films (nm)
$Ni(OAc)_{0.28}(OH)_{1.72}\cdot 0.25H_2O$	400±10
NiO	320±10

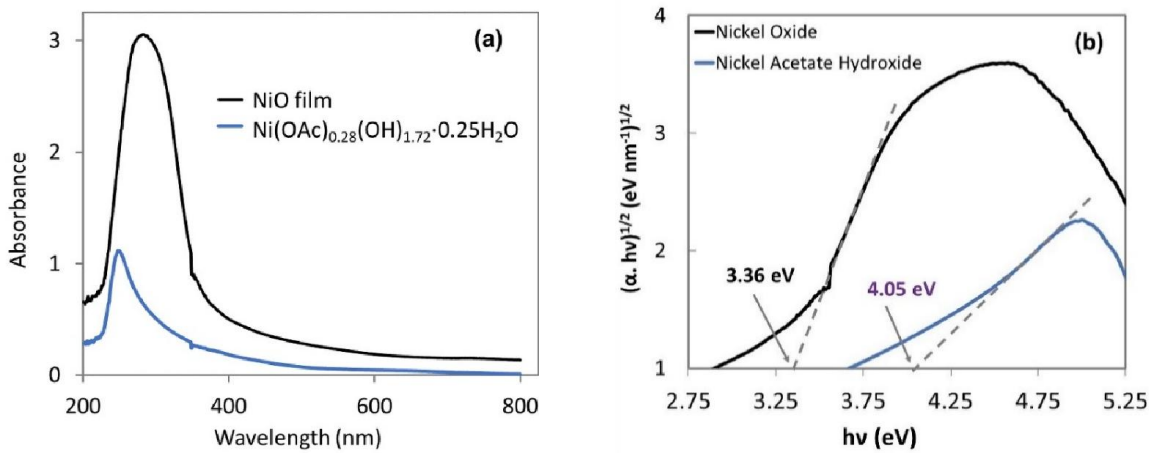

Figure 8: (a) UV-Visible absorption spectra of web-like nanostructured thin films of nickel acetate hydroxide and nickel oxide. (b) Tauc's plot for calculating the band gap of the thin films.

UV-Visible absorption spectra of typical thin films of nickel acetate hydroxide and NiO were also investigated. Figure 8(a) presents the absorption spectra of both films from 800 to 200 nm, where the spectra clearly show absorption discontinuity at 350 nm due to the light source changeover of the UV-Visible instrument. The NiO thin film exhibits strong UV region absorption and weak absorption of visible light. This suggests that the NiO film has a wide optical band gap.[35] Whereas the thin film of nickel acetate hydroxide shows lower absorption of the UV-Visible light than that of NiO film. The λ_{max} of the nickel acetate hydroxide thin film is 253 nm, whereas for NiO thin film is 283 nm. These indicate that the band gap of the nickel acetate hydroxide film is higher than the NiO film. For estimating the optical band gap of the thin films from the UV-Visible absorption spectra, the Tauc's equation was employed.[35] The Tauc's equation can be presented as by the following expression (1), [35, 36]

$$(\alpha.h\nu)^{1/\gamma} = B(h\nu - E_g) \qquad (1)$$

Where α is the absorption coefficient, h is the Plank's constant, ν is the frequency of the photon, E_g is the optical band gap, and B is a constant. The factor γ is related to the nature of the electronic

transition from the valence band to the conduction band. For direct band gap semiconductors, γ is equal to ½, whereas for indirect band gap semiconductors, γ is equal to 2. As α is directly proportional to absorbance and NiO is an indirect band gap semiconductor (γ is equal to 2), the absorption spectrum of the NiO film was used to plot the Tauc's relationship by employing the equation (1). Figure 8(b) presents the Tauc's plot of both nickel acetate hydroxide and NiO thin films, where the optical band gaps of the films were determined as 4.05 and 3.36 eV, respectively. The optical band gap of the thin film of NiO here in the study is lower than often reported values of 3.5-3.8 eV. [2, 37, 38] Nevertheless, thin films of NiO with a lower optical band gap than 3.5 eV (in the order of 3.1-3.4 eV) prepared by solution casting followed by pyrolysis of different nickel-precursors were also reported. [39-41]

Figure 9 represents the proposed reactions involved in the hydrothermal reaction of only aqueous nickel acetate solution in a closed system for deposition of thin films of nickel acetate hydroxide, $Ni(OAc)_{0.28}(OH)_{1.72}\cdot 0.25H_2O$. Nickel acetate ($N(OOCCH_3)_2\cdot 4H_2O$), when dissolved in water, produced nickel (Ni^{2+}) and acetate ($CH3COO^-$) ions. The acetate ions in water maintain an equilibrium, $CH_3COO^- + H_2O \rightleftharpoons CH_3COOH + OH^-$, which at the reaction temperature of 90 °C shifted to the right to produce more acetic acid (CH_3COOH) and hydroxide (OH^-) ions. Therefore, the reaction solution at 90 °C contained nickel (Ni^{2+}), hydroxide (OH^-), and acetates (CH_3COO^-) ions. These ions at the hydrothermal condition may nucleate to solid-phase particles of nickel acetate hydroxide, $Ni(OAc)_x(OH)_{2-x}\cdot nH_2O$.

$CH_3COO^-_{(aq)} + H_2O_{(l)} \rightleftharpoons CH_3COOH_{(l)} + OH^-_{(aq)}$

$Ni[(H_2O)_6]^{2+}_{(aq)} + OH^-_{(aq)} \rightleftharpoons [Ni(OH)(H_2O)_5]^+_{(aq)}$

$[Ni(OH)(H_2O)_5]^+_{(aq)} + CH_3COO^-_{(aq)} + OH^-_{(aq)} \longrightarrow Ni(CH_3COO)_x(OH)_{2-x}\cdot nH_2O_{(s)}$ [Nucleation]

$Ni(CH_3COO)_x(OH)_{2-x}\cdot nH_2O_{(s)} \longrightarrow Ni(CH_3COO)_{0.28}(OH)_{1.78}\cdot 0.25H_2O_{(s)}$ [Growth]

Scheme 2: Proposed reactions in the hydrolysis of nickel acetate aqueous solution.

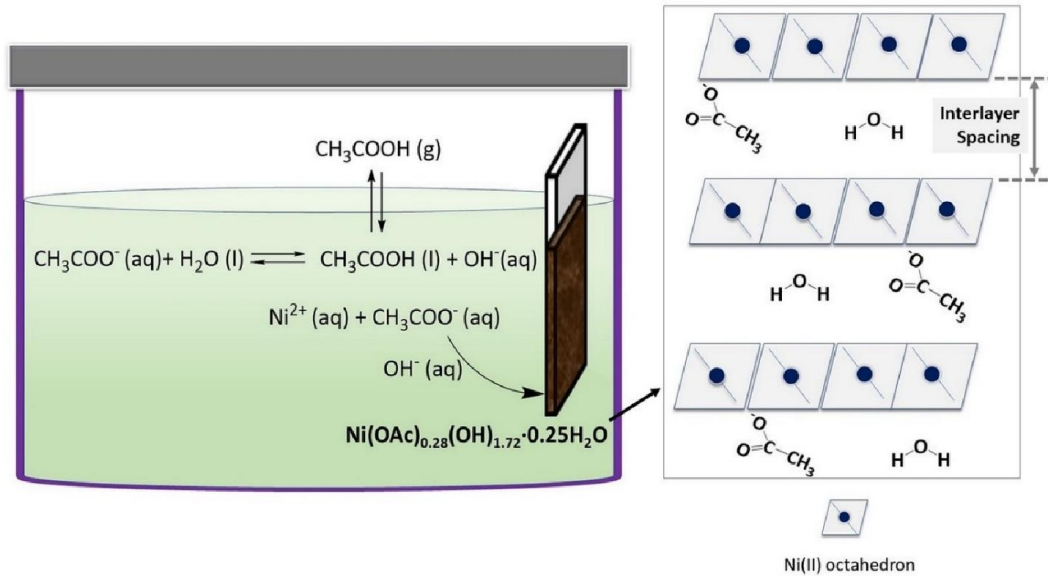

Figure 9: Proposed reaction scheme for the deposition of $Ni(OAc)_{0.28}(OH)_{1.72}\cdot 0.25H_2O$ as thin film by the hydrothermal (hydrolysis) reaction of nickel acetate aqueous solution (left) and a schematic structural model of the layered structure of $Ni(OAc)_{0.28}(OH)_{1.72}\cdot 0.25H_2O$ (right)

Table 7: Initial and final pH of ~ 0.2M nickel acetate aqueous solutions in the hydrothermal reaction for deposition of thin films of $Ni(OAc)_{0.28}(OH)_{1.72}\cdot 0.25H_2O$.

Initial pH	Final pH
6.8±0.1	6.1±0.1

The pH change of the reaction solution also supports the proposed reactions discussed above. The initial pH of the reaction solution was 6.8, while after the reaction, the pH was measured as 6.1 (Table 7). Consumption of the in situ generated OH^- to produce nickel acetate hydroxide renders shifting the equilibrium between acetate ions and water ($CH_3COO^- + H_2O \rightleftharpoons CH_3COOH + OH^-$) to the right, which yields more acetic acid and hydroxide ions. The increasing production of acetic acid during the hydrolysis reaction is very likely the reason for lowering the pH of the solution. The produced acetic acid in water at 90 °C also generates acetic acid vapor in the reaction

system. The smell of acetic acid was observed while opening the reaction vessel at the end of the reaction, further confirming the acetic acid production from the reaction solution at 90 °C.

Particle size distributions of a typical hydrothermal reaction of ~ 0.2M nickel acetate aqueous solution were acquired by employing Dynamic Light Scattering (DLS) experiments. Figure 10(a) presents the volume distributions of the hydrodynamic size of the particles with time. It was evident from the volume distribution plot that the growth of particle size in the reaction increases with time. The average particle sizes were estimated from the volume distributions and plotted against time, as presented in Figure 10(b). The average particle size vs. time plot reveals that the growth of $Ni(OAc)_{0.28}(OH)_{1.72}\cdot 0.25H_2O$ particles involves two steps – (i) an initial incubation period for the nucleation of solid particles of nickel acetate hydroxide and then (ii) rapid growth of the nucleated particles. The hydrothermal reaction solution was clear at 15-20 minutes and became cloudier at 30-35 minutes. This also confirms that the reaction involves an initial incubation period for hydrothermal nucleation. The two steps of the particle growth mechanism – the initial slow nucleation step for growing a critical size of particles and then autocatalytic surface growth of the nucleated particles were introduced and discussed by Watzky and Finke.[42, 43] SEM images of the deposited nickel acetate hydroxide thin film show that the growth of interconnected web-like nanowalls on the substrate has a thickness of 66±11 nm and height of 400±10. Whereas DLS experiments of the reaction solution reveal that the average size of the particles reached ~5 μm after 75 minutes of the reaction. This indicates that the growth of particles in the solution is different from that on the substrate. Likely, the initially formed nucleated particles after deposition were preferentially grown vertically of the substrate, developing interconnected nanowalls having open spaces among the walls. Whereas in the solution, the nucleated particles agglomerate to become larger particles, that is, grow as particles constituted by the aggregated nanowalls that were spread out in space three-dimensionally resulting in bigger particle sizes in solution.

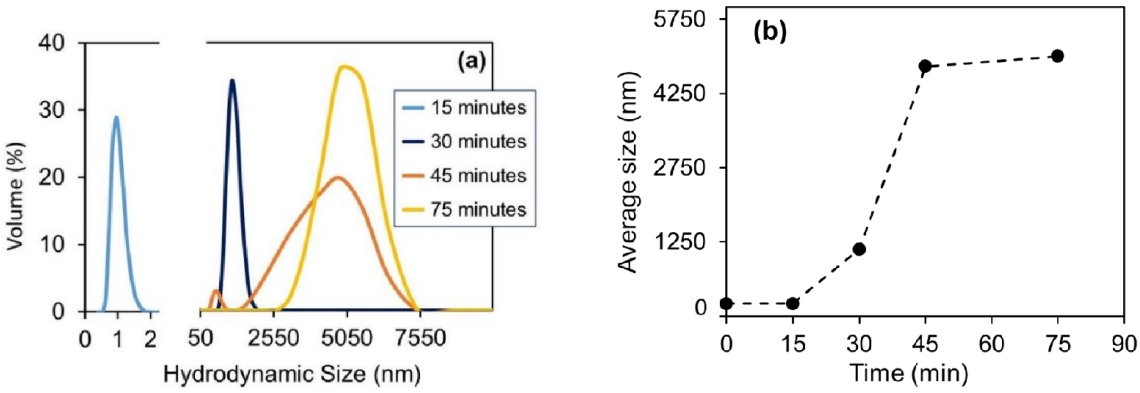

Figure 10: Particle size distribution analysis of a hydrothermal reaction of ~ 0.2M nickel acetate aqueous solution acquired by DLS experiments – (a) volume distribution of the hydrodynamic size of the grown particles in the reaction with time and (b) the average size of the particle vs. time.

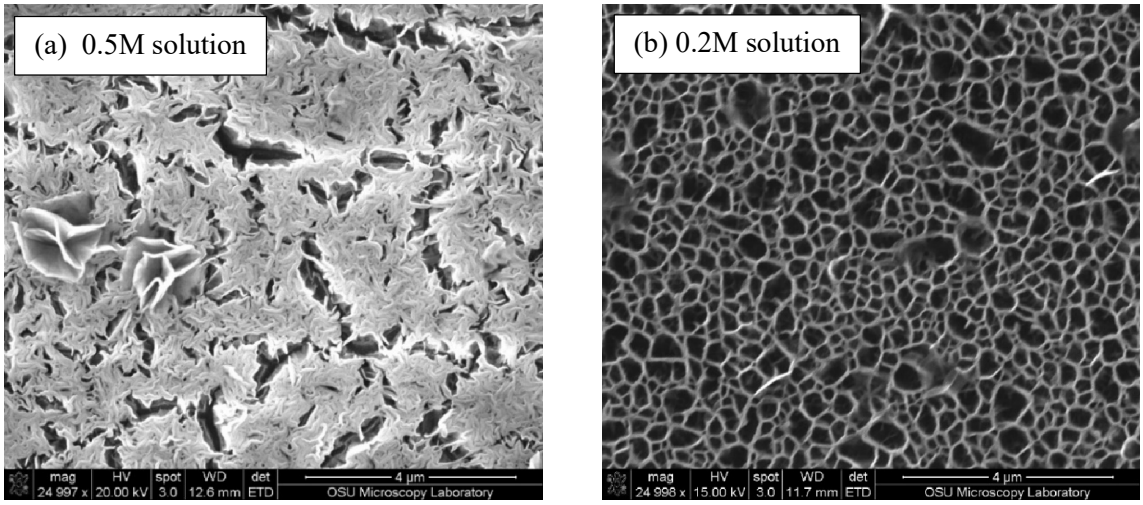

Figure 11: Comparison of the thin films of nickel acetate hydroxide prepared from the hydrolysis reactions of 0.5 M 50 g and 0.2 M 50 g of nickel acetate aqueous solutions at 90 °C in 24 hours.

The effect of nickel acetate concentration in the hydrothermal (hydrolysis) reaction was found to impact the web-like network structure of the nanowalls of nickel acetate hydroxide. Figure 11 shows SEM images of the thin films of nickel acetate hydroxide prepared from 0.5M and 0.2M aqueous solutions of nickel acetate. It is evidently clear from the SEM images that at a higher concentration of 0.5M, the open spaces among the web-like network structure of interconnected

nanowalls are occupied by more nanowalls. As a result, the 0.5M nickel acetate hydrothermal reaction generated a web-like network structure with almost no open spaces among the nanowalls.

The hydrothermal reaction of nickel acetate aqueous solution was excellently reproducible to produce the web-like morphology of nickel acetate hydroxide. Figure 12 represents the SEM images of two films generated from two separate reactions with the same concentration (0.2M) of nickel acetate aqueous solutions. The SEM images clearly show that both reactions deposited an identical web-like structure of interconnected nanowalls of nickel acetate hydroxide as thin films.

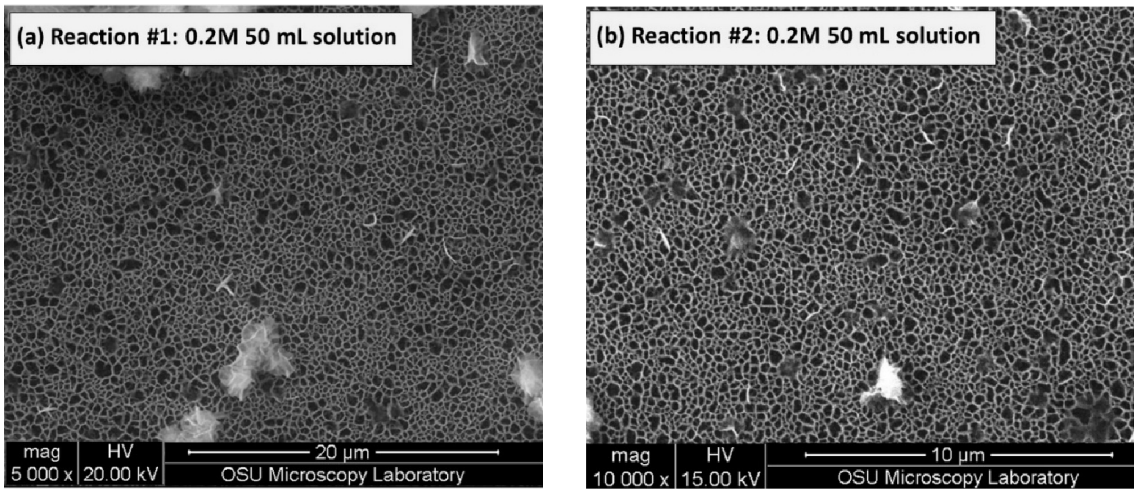

Figure 12: Comparison of nickel acetate hydroxide thin films deposited from two separate hydrothermal reactions of 0.2M 50g nickel acetate aqueous solutions at 90 °C in 24 hours.

The success of the hydrolysis reaction of only nickel acetate aqueous solution to deposit web-like nanostructured nickel acetate hydroxide as thin films encouraged us to investigate the reaction with support materials such as silica pellets. A reaction of 0.255M (6.402 g in 98.2 g water) nickel acetate aqueous solution with 10.048 g of silica pellets was tested at 120 °C for 24 hours. The reaction turned the white pellets into green pellets (Figure 13), confirming the reaction deposed nickel acetate hydroxide onto the pellets. While elemental analysis of the green pellets for nickel (5.81%) and carbon (0.36%) confirmed that the deposited material is $Ni(OAc)_{0.16}(OH)_{1.84}\cdot xH_2O$.

The mass of the green pellets (after drying in an oven at 100 °C) was 11.651 g which determined the deposition was 16.0 % (w/w). The green silica pellets were readily converted to NiO decorated silica pellets after pyrolysis at 400 °C, which transformed the green pellets into brownish-black pellets.

Figure 13: Nickel acetate hydroxide decorated silica pellets, prepared by hydrolysis of nickel acetate aqueous solution and silica pellets.

■ Conclusion:

This investigation presents a discovery of hydrothermal (hydrolysis) reaction of only nickel acetate aqueous solution at a low temperature of 90 °C that deposited web-like interconnected nanowalls of acetate-intercalated layered nickel hydroxide, $Ni(OAc)_{0.28}(OH)_{1.72}\cdot 0.25H_2O$ as thin films. These thin films were readily converted to NiO by pyrolysis at 425 °C. As the prepared NiO thin films retained the web-like morphology of the interconnected nanowalls, the discovered hydrothermal reaction is an inexpensive and facile mothed for depositing thin films of web-like nanostructured NiO. The hydrothermal reaction for depositing web-like nanostructured nickel acetate hydroxide, $Ni(OAc)_{0.28}(OH)_{1.72}\cdot 0.25H_2O$ as thin films does not require any second reactant or organic solvent that also makes the hydrothermal reaction as an excellent lesser chemical

involving process for accessing nanostructured NiO as films. Additionally, the hydrolysis reaction was readily employed for functionalizing silica supports with nickel acetate hydroxide and NiO. Notably, nickel acetate hydroxide and NiO nanostructured thin films deposited substrates, and their decorated supports were robust, which is an essential feature for thin films and supported materials to be employed in real-world applications. Therefore, the hydrolysis reaction of nickel acetate has opened a new straightforward route for preparing nanostructured layered nickel hydroxide- and NiO-supported substrates or supports for various necessary nickel hydroxide/oxide decorated substrates/supports based technologies.

■ Supporting Information

Table S1: MP-AES analysis data and calculation for determination of nickel content of nickel acetate hydroxide

Mass of nickel acetate hydroxide was taken for digestion 9.1 mg and the mass of the digested solution was 9.3617 g

Analysis #	Initial mass of the digested solution (g)	Final mass the of digested solution after dilution (g)	MP-AES reading (ppm)	ppm of Ni in the digested solution	Amount of Ni (mg)	% Ni	Average % Ni
1	0.2174	11.1347	10.10	517.30	4.84	53.2	53±0.8
2	0.2172	11.1349	10.15	520.35	4.87	53.5	
3	0.2499	10.8629	11.65	506.41	4.74	52.1	

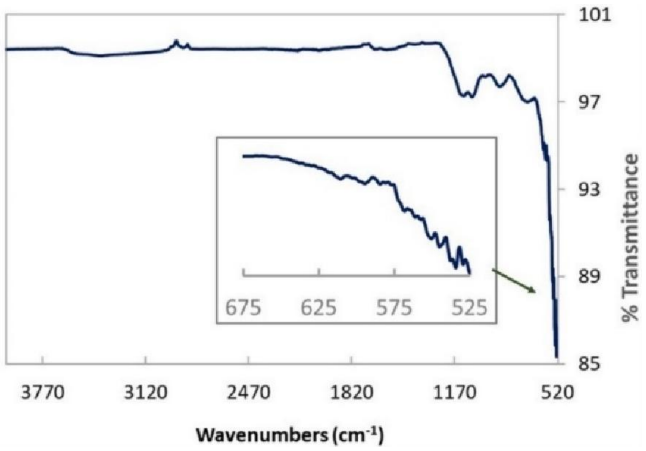

Figure S1: ATR-FTIR spectrum of a NiO film prepared by pyrolysis of a nickel acetate hydroxide. The inset image is the zoom-in of the spectrum from 525 to 675 cm^{-1}.

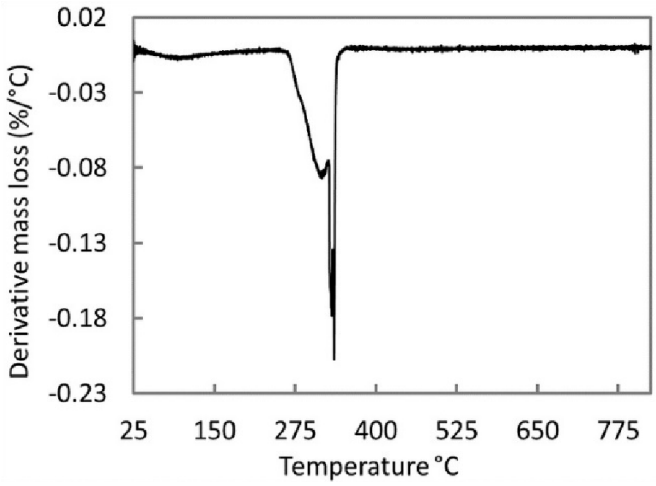

Figure S2: DTG (differential thermogravimetric) plot derived from the TGA experiment of nickel acetate hydroxide, $Ni(OAc)_{0.28}(OH)_{1.72}\cdot 0.25H_2O$.

Table S2: Determination of the molecular formula of nickel acetate hydroxide

Species	% mass	% mass/ molar mass	Mole ratio	Molar mass of the precursor from the TGA plot (g mol^{-1})	Molecular Formula
Ni	52.9[a]	0.901	1.0	108.99[e]	$Ni(OAc)_{0.28}(OH)_{1.72}\cdot 0.25H_2O$ (Formula Mass = 108.97 $gmol^{-1}$)
Acetate	14.7[b]	0.249	0.28		
Hydroxide	26.4 [c]	1.55	1.72		
Water	4.5[d]	0.25			

a. Estimated from MP-AES analysis

b. Carbon content from the elemental analysis was 5.98% which represents 14.7% of acetate.

c. As the mole ratio of acetate for one mole of nickel is 0.28, the mole ratio of hydroxide for one mole of nickel must equal to 2-0.28 = 1.72. The mole ratio of 1.72 of hydroxide represents 26.4% of hydroxide.

d. Estimated from TGA

e. The molar mass of the precursor from the TGA plot

$$\frac{\text{Molar mass of NiO}}{\text{ceramic yield}/100} = \frac{74.69}{0.6853} = 108.99\ \text{gmol}^{-1}$$

Table S3: Comparison of calculated and experimental nickel and carbon contents of nickel acetate hydroxide

	Experimental	Calculated
Nickel content (%)	52.9±0.8	53.86
Carbon content (%)	5.98	6.17

Table S4: MP-AES analysis for determining nickel concentrations of ~ 0.2M nickel acetate reaction solution (initial and after reaction) in a hydrolysis reaction.

Initial Ni^{2+} concentration of the reaction solution (ppm)	Final Ni^{2+} concentration of the reaction solution (after reaction, 24 hours) (ppm)
$(10.9 \pm 0.03) \times 10^3$	$(10.4 \pm 0.1) \times 10^3$

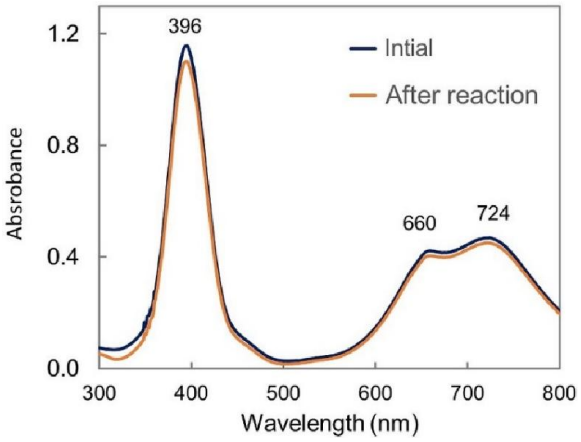

Figure S3: UV-visible spectra of reaction solution (initial and after reaction) of a hydrolysis reaction of ~ 0.2M nickel acetate aqueous solution

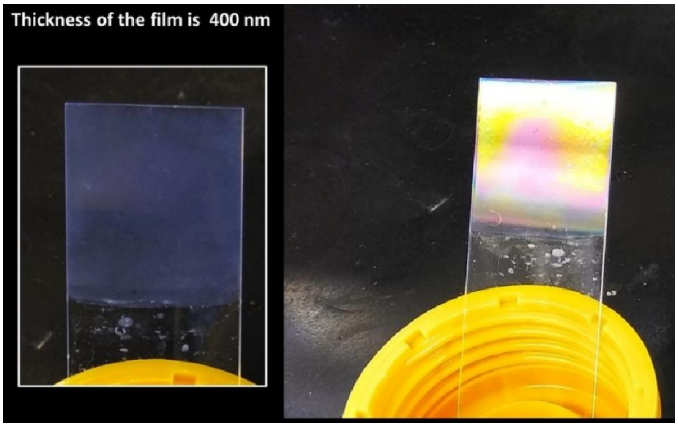

Figure S4: Interference of visible light on a nickel acetate hydroxide thin film.

Figure S5: Interference of visible light on a nickel oxide (NiO) film. The film was prepared by pyrolysis of a nickel acetate hydroxide film.

■ References:

(1) Zhu, Z.; Bai, Y.; Zhang, T.; Liu, Z.; Long, X.; Wei, Z.; Wang, Z.; Zhang, L.; Wang, J.; Yan, F.; Yang, S., High-performance hole-extraction layer of sol-gel-processed NiO nanocrystals for inverted planar perovskite solar cells. *Angewandte Chemie (International ed. in English)* **2014,** 53, (46), 12571-5.

(2) Liu, S.; Liu, R.; Chen, Y.; Ho, S.; Kim, J. H.; So, F., Nickel Oxide Hole Injection/Transport Layers for Efficient Solution-Processed Organic Light-Emitting Diodes. *Chemistry of Materials* **2014,** 26, (15), 4528-4534.

(3) Tian, F.; Liu, S.; Tian, H.; Dong, R.; Zhang, Y.; Wei, D.; Ye, L.; Whitmore, L., Growth and Photocatalytic Properties of NiO Nanostructures Prepared in Acidic and Alkaline Solutions with Same Reagents. *The Journal of Physical Chemistry C* **2018,** 123, (1), 504-510.

(4) Zhao, Y.; Jia, X.; Chen, G.; Shang, L.; Waterhouse, G. I. N.; Wu, L.-Z.; Tung, C.-H.; O'Hare, D.; Zhang, T., Ultrafine NiO Nanosheets Stabilized by TiO2 from Monolayer NiTi-LDH Precursors: An Active Water Oxidation Electrocatalyst. *Journal of the American Chemical Society* **2016,** 138, (20), 6517-6524.

(5) Soleimanpour, A. M.; Khare, S. V.; Jayatissa, A. H., Enhancement of hydrogen gas sensing of nanocrystalline nickel oxide by pulsed-laser irradiation. *ACS Appl Mater Interfaces* **2012,** 4, (9), 4651-7.

(6) Guillemot, T.; Schneider, N.; Loones, N.; Javier Ramos, F.; Rousset, J., Electrochromic nickel oxide thin films by a simple solution process: Influence of post-treatments on growth and properties. *Thin Solid Films* **2018,** 661, 143-149.

(7) Zhai, P.; Yi, Q.; Jian, J.; Wang, H.; Song, P.; Dong, C.; Lu, X.; Sun, Y.; Zhao, J.; Dai, X.; Lou, Y.; Yang, H.; Zou, G., Transparent p-type epitaxial thin films of nickel oxide. *Chem Commun (Camb)* **2014,** 50, (15), 1854-6.

(8) Pintor-Monroy, M. I.; Barrera, D.; Murillo-Borjas, B. L.; Ochoa-Estrella, F. J.; Hsu, J. W. P.; Quevedo-Lopez, M. A., Tunable Electrical and Optical Properties of Nickel Oxide (NiO x) Thin Films for Fully Transparent NiO x-Ga2O3 p-n Junction Diodes. *ACS Appl Mater Interfaces* **2018,** 10, (44), 38159-38165.

(9) Yu, J.; Rosso, K. M.; Bruemmer, S. M., Charge and Ion Transport in NiO and Aspects of Ni Oxidation from First Principles. *The Journal of Physical Chemistry C* **2012,** 116, (2), 1948-1954.

(10) Sialvi, M. Z.; Mortimer, R. J.; Wilcox, G. D.; Teridi, A. M.; Varley, T. S.; Wijayantha, K. G.; Kirk, C. A., Electrochromic and colorimetric properties of nickel(II) oxide thin films prepared by aerosol-assisted chemical vapor deposition. *ACS Appl Mater Interfaces* **2013,** 5, (12), 5675-82.

(11) Cao, F.; Pan, G. X.; Xia, X. H.; Tang, P. S.; Chen, H. F., Hydrothermal-synthesized mesoporous nickel oxide nanowall arrays with enhanced electrochromic application. *Electrochimica Acta* **2013,** 111, 86-91.

(12) Han, S. Y.; Lee, D. H.; Chang, Y. J.; Ryu, S. O.; Lee, T. J.; Chang, C. H., The Growth Mechanism of Nickel Oxide Thin Films by Room-Temperature Chemical Bath Deposition. *Journal of The Electrochemical Society* **2006,** 153, (6).

(13) He, Q.; Yao, K.; Wang, X.; Xia, X.; Leng, S.; Li, F., Room-Temperature and Solution-Processable Cu-Doped Nickel Oxide Nanoparticles for Efficient Hole-Transport Layers of Flexible Large-Area Perovskite Solar Cells. *ACS Applied Materials & Interfaces* **2017,** 9, (48), 41887-41897.

(14) Zeng, G.; Li, W.; Ci, S.; Jia, J.; Wen, Z., Highly Dispersed NiO Nanoparticles Decorating graphene Nanosheets for Non-enzymatic Glucose Sensor and Biofuel Cell. *Scientific Reports* **2016,** 6, 36454.

(15) Y. Y. Xi, D. L., A. B. Djurišić, M. H. Xie, K. Y. K. Man, and W. K. Chan, Hydrothermal Synthesis vs Electrodeposition for High Specific Capacitance Nanostructured NiO Films. *Electrochemical and Solid-State Letters* **2008,** 11, 56-59.

(16) Luan, F.; Wang, G.; Ling, Y.; Lu, X.; Wang, H.; Tong, Y.; Liu, X.-X.; Li, Y., High energy density asymmetric supercapacitors with a nickel oxide nanoflake cathode and a 3D reduced graphene oxide anode. *Nanoscale* **2013,** 5, (17), 7984-7990.

(17) Gomaa, M. M.; Boshta, M.; Farag, B. S.; Osman, M. B. S., Structural and optical properties of nickel oxide thin films prepared by chemical bath deposition and by spray pyrolysis techniques. *Journal of Materials Science: Materials in Electronics* **2016,** 27, (1), 711-717.

(18) Jao, M.-H.; Cheng, C.-C.; Lu, C.-F.; Hsiao, K.-C.; Su, W.-F., Low temperature and rapid formation of high quality metal oxide thin film via a hydroxide-assisted energy conservation strategy. *Journal of Materials Chemistry C* **2018,** 6, (37), 9941-9949.

(19) Strano, V.; Urso, R. G.; Scuderi, M.; Iwu, K. O.; Simone, F.; Ciliberto, E.; Spinella, C.; Mirabella, S., Double Role of HMTA in ZnO Nanorods Grown by Chemical Bath Deposition. *The Journal of Physical Chemistry C* **2014,** 118, (48), 28189-28195.

(20) Chen, Z.; Xiao, A.; Chen, Y.; Zuo, C.; Zhou, S.; Li, L., Highly porous nickel oxide thin films prepared by a hydrothermal synthesis method for electrochromic application. *Journal of Physics and Chemistry of Solids* **2013,** 74, (11), 1522-1526.

(21) Poul, L.; Jouini, N.; Fiévet, F., Layered Hydroxide Metal Acetates (Metal = Zinc, Cobalt, and Nickel): Elaboration via Hydrolysis in Polyol Medium and Comparative Study. *Chemistry of Materials* **2000,** 12, (10), 3123-3132.

(22) H. Nishizawa, T. K., and H. Minami, Formation of α, β -Type Hydroxides and Second-Stage Intermediate in Hydrothermal Decomposition of Nickel Acetate. *Journal of Solid State Chemistry* **1999,** 146, 39-46.

(23) Yuasa, H. N. a. K., Preparation of Anion Exchangeable Layered Mixed Basic Salt Ni1–xZn2x(OH)2(OCOCH3)2·nH2O Thin Film under Hydrothermal Condition. *Journal of Solid State Chemistry* **1998,** 141, 229-234.

(24) Yan, H.; Zhang, D.; Xu, J.; Lu, Y.; Liu, Y.; Qiu, K.; Zhang, Y.; Luo, Y., Solution growth of NiO nanosheets supported on Ni foam as high-performance electrodes for supercapacitors. *Nanoscale Research Letters* **2014,** 9, (1), 424.

(25) Evans, D. G.; Slade, R. C. T., Structural Aspects of Layered Double Hydroxides. In *Layered Double Hydroxides*, Duan, X.; Evans, D. G., Eds. Springer Berlin Heidelberg: Berlin, Heidelberg, 2006; pp 1-87.

(26) Hall, D. S.; Lockwood, D. J.; Bock, C.; MacDougall, B. R., Nickel hydroxides and related materials: a review of their structures, synthesis and properties. *Proc Math Phys Eng Sci* **2015,** 471, (2174), 20140792.

(27) Vecoven, A.; Rahman, D. R.; Apblett, A. W., Green Process for Preparation of Nickel Hydroxide Films and Membranes. *Journal of Materials Engineering and Performance* **2020,** 29, (9), 5602-5608.

(28) Holder, C. F.; Schaak, R. E., Tutorial on Powder X-ray Diffraction for Characterizing Nanoscale Materials. *ACS Nano* **2019,** 13, (7), 7359-7365.

(29) Peck, M. A.; Langell, M. A., Comparison of Nanoscaled and Bulk NiO Structural and Environmental Characteristics by XRD, XAFS, and XPS. *Chemistry of Materials* **2012,** 24, (23), 4483-4490.

(30) Yu, P. C.; Lampert, C. M., In-situ spectroscopic studies of electrochromic hydrated nickel oxide films. *Solar Energy Materials* **1989,** 19, (1), 1-16.

(31) Biju, V.; Abdul Khadar, M., Fourier transform infrared spectroscopy study of nanostructured nickel oxide. *Spectrochimica Acta Part A: Molecular and Biomolecular Spectroscopy* **2003,** 59, (1), 121-134.

(32) Dubey, P.; Kaurav, N.; Devan, R. S.; Okram, G. S.; Kuo, Y. K., The effect of stoichiometry on the structural, thermal and electronic properties of thermally decomposed nickel oxide. *RSC Advances* **2018,** 8, (11), 5882-5890.

(33) Švarcová, S.; Klementová, M.; Bezdička, P.; Łasocha, W.; Dušek, M.; Hradil, D., Synthesis and characterization of single crystals of the layered copper hydroxide acetate Cu2(OH)3(CH3COO)·H2O. *Crystal Research and Technology* **2011,** 46, (10), 1051-1057.

(34) Liu, X.; Ma, R.; Bando, Y.; Sasaki, T., Layered cobalt hydroxide nanocones: microwave-assisted synthesis, exfoliation, and structural modification. *Angewandte Chemie (International ed. in English)* **2010,** 49, (44), 8253-6.

(35) Gao, Y.; Xu, J.; Shi, S.; Dong, H.; Cheng, Y.; Wei, C.; Zhang, X.; Yin, S.; Li, L., TiO2 Nanorod Arrays Based Self-Powered UV Photodetector: Heterojunction with NiO Nanoflakes and Enhanced UV Photoresponse. *ACS Appl Mater Interfaces* **2018,** 10, (13), 11269-11279.

(36) Makula, P.; Pacia, M.; Macyk, W., How To Correctly Determine the Band Gap Energy of Modified Semiconductor Photocatalysts Based on UV-Vis Spectra. *J Phys Chem Lett* **2018,** 9, (23), 6814-6817.

(37) Ganapathi, S. K.; Kaur, M.; Singh, R.; Singh, V. I.; Debnath, A. K.; Muthe, K. P.; Gadkari, S. C., Anomalous Sensing Response of NiO Nanoparticulate Films toward H2S. *ACS Applied Nano Materials* **2019,** 2, (10), 6726-6737.

(38) Holden, K. E. K.; Dezelah, C. L.; Conley, J. F., Jr., Atomic Layer Deposition of Transparent p-Type Semiconducting Nickel Oxide Using Ni((tBu2)DAD)2 and Ozone. *ACS Appl Mater Interfaces* **2019,** 11, (33), 30437-30445.

(39) Yadav, A. A.; Chavan, U. J., Influence of substrate temperature on electrochemical supercapacitive performance of spray deposited nickel oxide thin films. *Journal of Electroanalytical Chemistry* **2016,** 782, 36-42.

(40) Farhadi, S.; Roostaei-Zaniyani, Z., Simple and low-temperature synthesis of NiO nanoparticles through solid-state thermal decomposition of the hexa(ammine)Ni(II) nitrate, [Ni(NH3)6](NO3)2, complex. *Polyhedron* **2011,** 30, (7), 1244-1249.

(41) Hosny, N. M., Synthesis, characterization and optical band gap of NiO nanoparticles derived from anthranilic acid precursors via a thermal decomposition route. *Polyhedron* **2011,** 30, (3), 470-476.

(42) Whitehead, C. B.; Özkar, S.; Finke, R. G., LaMer's 1950 Model for Particle Formation of Instantaneous Nucleation and Diffusion-Controlled Growth: A Historical Look at the Model's Origins, Assumptions, Equations, and Underlying Sulfur Sol Formation Kinetics Data. *Chemistry of Materials* **2019,** 31, (18), 7116-7132.

(43) Watzky, M. A.; Finke, R. G., Transition Metal Nanocluster Formation Kinetic and Mechanistic Studies. A New Mechanism When Hydrogen Is the Reductant: Slow, Continuous Nucleation and Fast Autocatalytic Surface Growth. *Journal of the American Chemical Society* **1997,** 119, (43), 10382-10400.

CHAPTER III

Deposition of Copper Oxides and Layered Copper Hydroxides by Hydrolysis of Copper Acetate and Copper Formate Aqueous Solutions

■ Introduction

Deposition of copper oxides on substrates or supports has been the interest of many areas of research such as thermal-catalysis,[1] photocatalytic reduction of CO_2,[2] photoelectrodes for photoelectrochemical processes,[3] electrocatalysis,[4] hole transport layer in perovskite photovoltaics,[5] gas sensors,[6] degradations of organic pollutants from water by the advanced oxidation process,[7] uptakes of volatile organics,[8] antimicrobial surfaces,[9] Hepatitis-B virus sensors (DNA biosensors).[10] While layered copper hydroxides, $Cu_x(A)_{2x-y}(OH)_y \cdot nH_2O$ (where A is a univalent anion) decorated substrates or supports and films potentially can directly be used for uptake of volatile organics, catalysis, and sensors. Also, layered copper hydroxides decorated substrates/supports and films are excellent precursors for nano- or micro-structured copper oxides decorated substrates/supports and copper oxide films. Due to the versatile uses of copper oxides (CuO and Cu_2O) and layered copper hydroxides, $Cu_x(A)_{2x-y}(OH)_y \cdot nH_2O$ (where A is a univalent anion), deposition of nano- or micro-structured copper oxides and layered hydroxides on substrates and supports using facile and inexpensive routes are very important to develop in our present-day technology-dependent era.

Hydrothermal deposition routes using copper salts have been widely used to deposit nano- and micro-structured copper oxide on various substrates. Very often reported hydrothermal reactions involve copper salts and a second reactant that is usually a base (low-temperature heating of copper salts in basic conditions), for example – copper acetate and NaOH,[11] copper sulfate and ammonium hydroxide with a capping agent,[12] copper chloride and excess ammonium hydroxide at pH 10 with and without sodium lactate,[13] etc. Other reported interesting methods for accessing Cu_xO and Cu_2O films are the reaction of a copper iodide film with NaOH[3] and hydrothermal treatment of metallic copper foils in aqueous copper chloride or nitrate or sulfate solutions at 100 – 180°C.[14] While layered copper hydroxides, $Cu_x(A)_{2x-y}(OH)_y \cdot nH_2O$ (where A is a univalent anion), have been widely prepared using well-studied precipitation reactions or titrations of aqueous solutions of copper salts with a base followed by hydrothermal aging of the precipitates or reaction solutions. For example – titration of aqueous solutions of copper acetate with dilute NaOH to pH 6.5 and subsequent hydrothermal heating at 40 °C yielded acetate-intercalated layered copper hydroxide, $Cu_2(OAc)_{0.9}(OH)_{3.1} \cdot 0.7H_2O$.[15] Another study showed the direct formation of copper hydroxy nitrate, $Cu_2(OH)_3(NO_3) \cdot nH_2O$ just by precipitation (without hydrothermal heating) of copper nitrate by NaOH under a nitrogen atmosphere.[16] The study also showed that aqueous dispersions of the prepared copper hydroxy nitrate powder deposited copper oxide (CuO) films on glass substrates under hydrothermal heating at 200 °C. Notably, articles on the synthesis of formate-intercalated layered copper hydroxide, $Cu_z(OOCH)_x(OH)_{2z-x}$ are found to be very few. One report by Wasuke and coworkers showed that hydrolysis of copper formate in water at 60-70°C produced Cu(OOCH)(OH) blue prismatic crystals. Further heating of Cu(OOCH)(OH) crystals in 1:1 methanol and water at 60-70°C yielded bright green crystalline powder of $Cu_2(OOCH)(OH)_3$.[17]

Hydrolysis (hydrothermal) reactions of copper acetate and copper formate is a very facile route for deposition of layered copper acetate hydroxide, $Cu(OAc)_{2-x}(OH)_x \cdot nH_2O$ and formate hydroxide, $Cu(CHOO)_{2-x}(OH)_x \cdot nH_2O$, respectively. These layered hydroxides are excellent

precursors for copper oxides since the carboxylate groups (acetate or formate) readily decompose as organics and CO_2, and hydroxyl groups dehydroxylate as water vapor upon pyrolysis. Therefore, deposition of nano- or micro-structured copper acetate hydroxide or copper formate hydroxide on supports or substrates is a promising as well as an inexpensive process for accessing nano- or micro-structured copper oxides decorated supports or high-quality films. In the previous chapter (Chapter II), we showed that thermal decomposition of web-like nanostructured nickel acetate hydroxide, $Ni(OAc)_{0.28}(OH)_{1.72}\cdot 0.25H_2O$ as thin films on glass substrates produced identical nanostructured NiO thin films. Masciocchi *et al*. investigated the precipitation of a copper acetate hydroxide phase, $Cu_2(CH_3COO)(OH)_3\cdot H_2O$, by slow titration of 0.1M copper acetate by 0.1M NaOH as well as by only heating of 0.01M – 0.18M aqueous copper acetate solution (without base) at 50 – 75 °C.[18] The later reaction might deposit copper acetate hydroxide as films on the reaction container; however, they did not report any deposition or formation of films. Disk-shaped copper acetate hydroxide was prepared by simply precipitation reaction (with continuous stirring) of copper acetate and NaOH. Ex-situ thermal decomposition of the prepared disk-shaped copper acetate hydroxide interestingly produced porous copper(II) oxide, CuO, by maintaining the starting disk-shaped morphology.[19] Synthesis of various phases of copper acetate hydroxides (as powders) using aqueous ammonia were extensively investigated by Bette *et al*.[20] They showed using TGA and ex-situ XRD experiments that thermal decomposition of $Cu_3(CH_3COO)_2(OH)_4$ phase initially produced a mixture of copper oxides, Cu_2O/CuO around 250 °C. While further heating oxidized Cu_2O to CuO, which resulted in a pure CuO phase. These are a few of the studies in the literature which showed the deposition or synthesis of copper acetate hydroxides and their conversion to copper oxides. Nevertheless, the literature review reveals that the direct deposition of nano-/micro-structured copper(II) oxide and copper(I) oxide/copper formate hydroxide on substrates using only copper acetate and copper formate aqueous solutions, respectively, (without a second reactant) have never been reported. Additionally, deposition of copper acetate hydroxide onto silica support and mesoporous silica by hydrolysis of copper acetate has not been found in the literature.

Independently and serendipitously, we discovered that heating copper acetate aqueous solutions without any second reactant or organic solvent at 90° C directly deposited black films of copper(II) oxide, CuO, in 24 hours. While the reaction after three hours deposited bluish-green crystalline particles characterized as copper acetate hydroxide, $Cu(OAc)_{0.41}(OH)_{1.59}\cdot 0.40H_2O$, which shows that CuO formation in 24 hours occurred via copper acetate hydroxide formation. The finding motivated us to also investigate the hydrothermal reaction of only copper formate aqueous solution. Interestingly, unlike copper acetate reaction, hydrolysis of only copper formate aqueous solutions deposited dark-green crystalline particles in 48 hours on glass substrates. The dark-green crystalline product in the reaction was found to be a two-phase material of copper(I) oxide/copper formate hydroxide, $(Cu_2O)_{0.25}/(Cu_2(OOCH)(OH)_3)_{0.25}$.

Additionally, the hydrolysis reaction of only copper acetate aqueous solutions with catalyst supports or mesoporous materials such as silica pellets and mesoporous silica (OSU-6) showed that the reaction deposits copper acetate hydroxide onto these materials. Pyrolysis readily converted the copper acetate hydroxide deposited silica pellets, and mesoporous silica into copper oxide supported silica pallets and mesoporous silica.

■ Experimental:

All the experiments were performed using copper acetate monohydrate, $Cu(OOCCH_3)_2\cdot H_2O$ (Baker Analyzed™ Reagent), copper formate tetrahydrate, $Cu(OOCH)_2\cdot 4H_2O$ (Alfa Aesar), and deionized water as solvent.

Hydrolysis of copper acetate aqueous solution for deposition of CuO: For a typical deposition process of CuO particles, 10.0 mmol copper acetate hydroxide dissolved in 50. g of deionized water in a 100 mL screw-cap Pyrex bottle. A precleaned microscope glass slide was vertically immersed in the copper acetate solution **(**Figure 1**)**. After closing the bottle with a cap, it was heated in an oven at 90 °C for 24 hours. That produced a black coating on the glass slide, as

shown in Figure 1. Next, the coated substrate was dipped in DI water to wash it thoroughly. To wash out surface adsorbed acetate completely, dipping of the coated substrate was continued with fresh DI water a few times until the wash solution's conductivity became zero. XRD pattern **(**Figure 5**)** confirmed that the deposited black material on the glass substrate is copper(II) oxide, CuO.

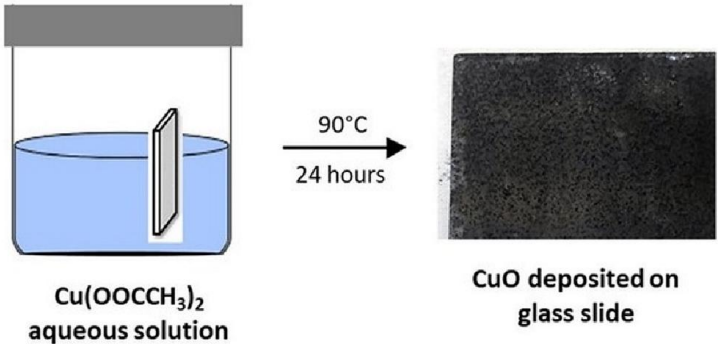

Figure 1: Reaction schematic of copper acetate hydrolysis with a vertically placed glass substrate for deposition of CuO particles (left). Camera picture of a prepared CuO decorated glass substrate (right).

Isolation of initially formed product in the hydrolysis of copper acetate at 90°C: The hydrolysis reaction of copper acetate aqueous solution initially deposited bluish-green crystalline material **(**Figure 2**)**. Prolonged heating (24 hours) in the hydrothermal condition at 90°C directly converted the bluish-green materials into black copper(II) oxide, CuO. For isolating the bluish-green material, a reaction of 10.0 mmol copper acetate in 50.0 g of water was performed at 90 °C for 3 hours instead of 24 hours. The isolated bluish-green material was washed thoroughly (confirmed by conductivity reading) on a glass-fritted filter and dried overnight at 60 °C. The amount of the green crystalline product was 0.204 g and characterized as an acetate-intercalated layered double hydroxide of copper, $Cu(OAc)_{0.41}(OH)_{1.59}\cdot 40H_2O$ by ATR-FTIR spectroscopy, TGA, and elemental analysis.

Figure 2: Initially formed bluish-green crystalline product in the hydrolysis of only copper acetate at 90 °C (10.0 mmol copper acetate in 50 g of water, after 3 hours).

Hydrothermal growth of crystalline copper(I) oxide/copper formate hydroxide, $Cu_2O/Cu_2(OOCH)(OH)_3$ from only copper formate aqueous solution: 10.0 mmol (2.26 g) of copper formate tetrahydrate was dissolved in 50.0 g of DI water for the hydrolysis reaction. It turned out the purchased copper formate tetrahydrate contained insoluble solid residue, which was separated by filtration. After washing, the vacuum dried-insoluble residue was weighted. The amount of dissolved copper formate was determined as 9.80 mmol. After filtration, the clear copper formate solution was heated in a 100 mL pyrex bottle at 90 °C for 48 hours with a precleaned microscope glass slide. Dark green crystalline particles were produced. The crystalline product decorated glass slide, the product from the reaction solution, and the product deposited on the reaction container were washed thoroughly until the rinse water read zero in a conductivity meter. All of them dried at 60 °C overnight and were collected for analysis. XRD pattern, TGA, and elemental analysis confirmed the product is a mixture of copper (I) oxide and copper formate hydroxide, $Cu_2O/Cu_2(OOCH)(OH)_3$. Figure 3 presents a camera picture and a low magnification SEM image of a copper(I) oxide/copper formate hydroxide decorated glass slide.

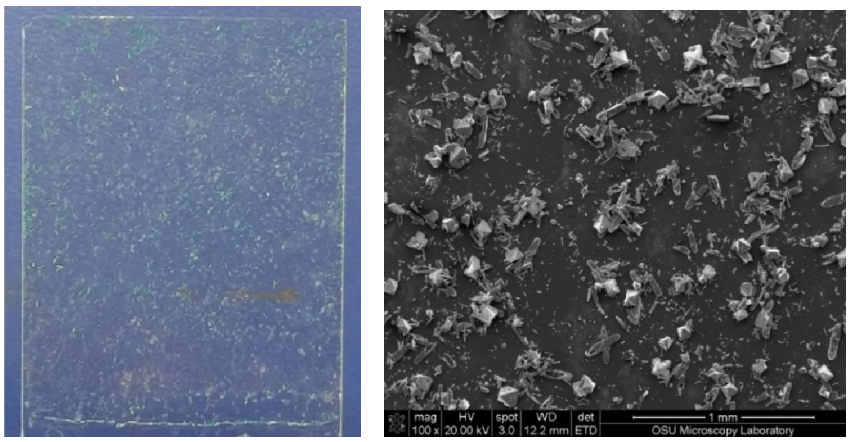

Figure 3: Camera picture of copper(I) oxide/copper formate hydroxide decorated glass slide (left) and low magnification (100x) SEM image of such a typical slide (right)

Hydrolysis of copper formate for deposition of Cu_2O/CuO: Hydrolysis reactions using 25.0 mmol (5.64 g) copper formate tetrahydrate dissolved in 50.0 g of water were also performed separately for 48 hours. After separating the insoluble residue, the concentration of the solution was 0.49 M. Heating 50.0 g of the solution at 90 °C with a precleaned glass slide for 48 hours deposited a very dark green crystalline particles on the glass slide. Figure 4 presents the camera picture of such a film. In this case, it turned out that a Cu_2O/CuO decorated film was produced.

Figure 4: Cu_2O/CuO decorated glass substrates prepared by hydrolysis of 0.49 M aqueous solution of copper formate at 90 °C for 48 hours.

Characterization/Instruments:

FTIR Spectroscopy: Attenuated total reflectance FTIR spectra of the CuO decorated glass substrate and $Cu_2O/Cu_2(OOCH)(OH)_3$ particles were collected using a Nicolet iS50 instrument. A diamond crystal was used for the FTIR experiments.

X-Ray Diffraction (XRD): The XRD patterns in this chapter were collected using Bruker D8 Advance X-ray Diffractometer at Helmrich Research Center, Tulsa, Oklahoma. Copper oxide (CuO) and copper formate hydroxide/copper(I) oxide, $Cu_2O/Cu_2(OOCH)(OH)_3$ decorated glass substrates were directly employed for acquiring their XRD patterns. The operating condition was 40kV power, and the X-Ray source was Cu Kα (λ=1.54056Å) radiation. 2θ range was 5° to 70° with an interval of 0.01°. The XRD pattern of CuO film was smoothed, and the background was subtracted using Qualx software. In the case of the XRD pattern of $Cu_2O/Cu_2(OOCH)(OH)_3$ crystalline particles, the background was low and was not subtracted.

SEM: A CuO decorated substrate was sputter-coated with an ultra-thin film coating of gold-palladium for acquiring SEM images. The coating was necessary to avoid the charging effect while collecting SEM images of the CuO decorated substrate. An operation voltage of 20kV was used for acquiring the SEM Images at various magnifications in an FEI Quanta 600 field emission gun ESEM instrument. ImageJ software was used to estimate the particle size of CuO from an SEM image of the CuO decorated substrate. The same SEM instrument and condition were also employed to collect SEM images of the $Cu_2O/Cu_2(OOCH)(OH)_3$ decorated glass slide.

Thermogravimetric Analysis (TGA) and Particle Size Distribution analysis: All TGA experiments were performed in a Perkin Elmer TGA4000 instrument under air at a heating rate of 10°C per minute. Malvern HPPS instrument was employed to investigate the particle size distributions vs. time of a hydrolysis reaction of 0.2 M copper acetate aqueous solution.

■ **Results and Discussion:**

Characterization of CuO decorated glass substrates:

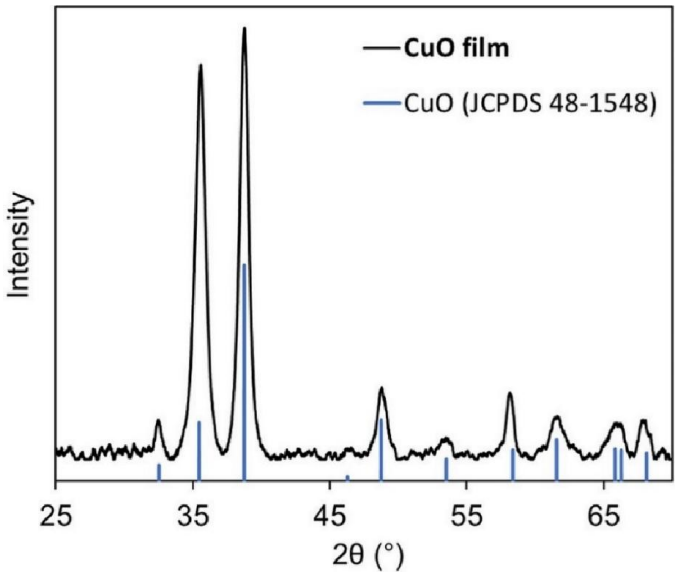

Figure 5: XRD pattern of a CuO deposited glass substrate prepared by the hydrolysis of only copper acetate aqueous solution (without any base or second reactant).

XRD pattern of a typical black material decorated substrate matched with copper (II) oxide, CuO (JCPDS: 48-1548[21]) as presented in Figure 5. The 2θ values of the XRD peaks and their d-spacing are tabulated in Table 1. The matched copper (II) oxide phase adopts a monoclinic lattice structure, and its lattice parameters are a = 4.6883 Å, b = 3.4229 Å, c = 5.1319 Å, and β = 99.506° (JCPDS: 48-1548). A lattice structure of CuO is drawn by the VESTA software and presented in Figure 6. The XRD peaks are broad, which indicates the CuO particles are constituted by nano-crystallites. Miler indices of 002 at 35.57° are very tall, indicating that the particles were grown along with the c- axis of a lattice, i.e., particles were grown vertically on the substrate. While the sharp 111 reflection at 38.77° indicates the growth of the particles along the a-axis and b-axis of a lattice, suggesting the particles were grown across the substrate. Alternatively, it can be described that the particles deposited on the substrate were grown three-dimensionally. The SEM images

(Figures 9 and 10) of a typical CuO decorated substrate show that CuO particles were, in fact, deposited as the sphere-type particles grown three-dimensionally.

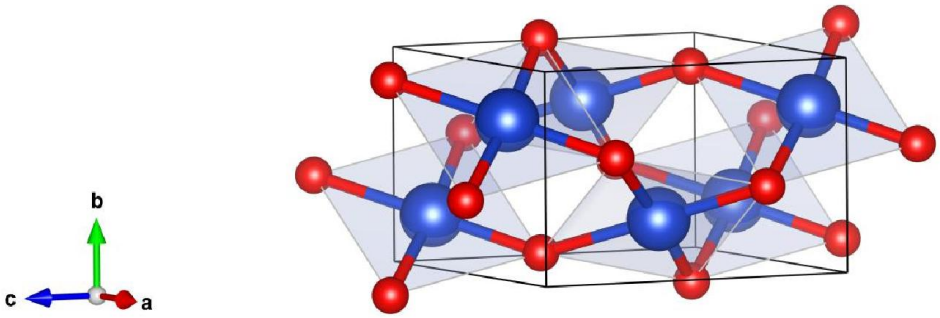

Figure 6: Lattice structure of copper (II) oxide, CuO (blue spheres are copper atoms and red spheres are oxygen atoms).

Table 1: The 2θs of the XRD peaks, their Miler indices, and their d-spacings of CuO decorated glass substrate's XRD pattern

2θ	**hkl**	**d (Å)**
32.47	1 1 0	2.76
35.57	0 0 2	2.53
38.77	2 0 0	2.32
46.30	1 1 -2	1.96
48.79	-2 0 2	1.86
53.49	2 0 2	1.71
58.14	-1 1 3	1.57
61.60	-3 1 1	1.50
65.79	1 1 3	1.42
66.26	3 1 1	1.41
67.88	0 0 4	1.38

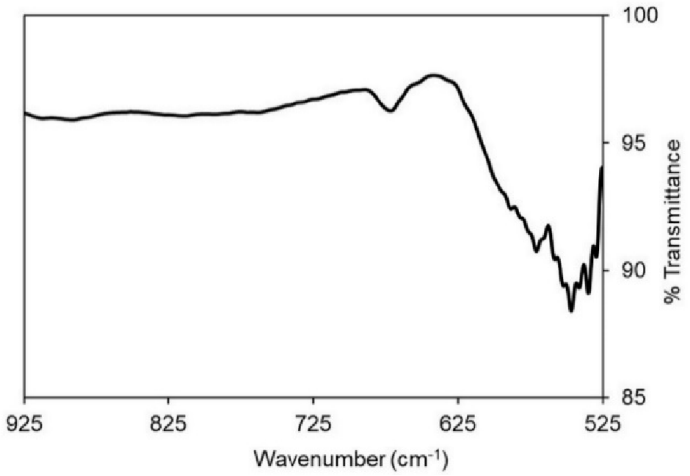

Figure 7: Attenuated total reflectance FTIR spectrum of a CuO decorated glass slide prepared by hydrolysis of copper acetate aqueous solution.

Figure 7 presents a typical CuO film's attenuated total reflectance FTIR (ATR-FTR) spectrum. The IR absorption bands at 535, 547, and 571 cm^{-1} should be due to the different Cu-O vibrational modes. G Kliche extensively studied far-infrared reflection spectra of polycrystalline CuO and observed six lattice vibrational modes at 300K.[22] One of the vibrational modes reported in that study was 533 cm^{-1}, which very closely agrees with the 535 cm^{-1} of this study. The other vibrational modes of Cu-O that are below 535 cm^{-1} were not detected by the FT-IR instrument in this study as the instrument could not operate at frequencies lower than 525 cm^{-1}. Vibrational bands close to 547 and 571 cm^{-1} were also reported for a CuO film deposited on a silicon substrate.[23] The peak at the higher frequency of 671cm^{-1} may be generated due to Cu-O-Cu bending mode.

Figures 9 and 10 present the SEM images of a typical CuO decorated substrate that shows that the CuO particles were grown as agglomerates of sphere-type particles. The sphere-type particles are constructed by hemispheres or trientspheres (two or three sphere-type grains) visible by the connection lines or grain boundaries (Figure 10a). More than three grains were also found in a few particles (Figure 9b). Another SEM image (Figure 10b) shows visible grains that are not yet fully developed into the final sphere-type particles. Therefore, it can be assumed that the

initially nucleated nanoparticles deposited or grown on the substrate later expanded to bigger size particles with time. The mechanism of the growth of the CuO particles on the substrate can be considered a complex process since it involves –

(i) the deposition of the initial nucleated particles that are copper acetate hydroxide, $Cu(OAc)_{2-x}(OH)_x \cdot nH_2O$,

(ii) hydrothermal growth of the deposited particles, and

(iii) hydrothermal decomposition of $Cu(OAc)_{2-x}(OH)_x \cdot nH_2O$ to CuO.

To answer why CuO is grown as sphere-type particles – it can be assumed that the initial nucleated particles may be deposited as sphere-type particles or deposited nucleated particles transformed into that shape during the hydrothermal growth. The intriguing question is why the nucleated particles are deposited as or changed into sphere-type particles during the hydrothermal process – at this moment, we do not know the exact reason for that.

A reaction product after three hours of the hydrolysis reaction was isolated and found to be copper acetate hydroxide, $Cu(OAc)_{0.41}(OH)_{1.59} \cdot 0.40H_2O$, a layered copper hydroxide (details characterization is discussed later). This confirms the initial nucleation, growth, and deposition on the substrate occurred as copper acetate hydroxide, $Cu(OAc)_{2-x}(OH)_x \cdot nH_2O$ particles. The grown copper acetate hydroxide started decomposing after a particular time of the hydrothermal reaction and transformed entirely into copper(II) oxide in 24 hours. This is quite like copper(II) hydroxide, $Cu(OH)_2$, which is not hydrothermally stable since it decomposed to copper(II) oxide at relatively low temperatures of 50-80°C under basic conditions.[24, 25] Another study showed (by following a patent application) that copper acetate aqueous solution under basic conditions at 90±5 °C produced copper (II) oxide films.[11] Very likely in that study, the film initially was grown as copper acetate hydroxide and then decomposed to CuO films. However, in this study, we found that copper acetate

hydroxide can be decomposed into copper (II) oxide under an acidic condition since the initial pH of the reaction solution was 5.3, which changed to 4.8 after 24 hours of the reaction (Table 3).

The size (diameter) of CuO sphere-type particles was determined using the ImageJ software from Figure 9a. The average size of the sphere-type CuO particles from randomly selected 50 particles was determined as 3.28 ± 0.85 µm. While the range of the size of the particles was found to be between 1.76 to 5.81 µm. The distribution of the sizes of CuO particles is showcased in Figure 8. The estimated size of XRD crystallites using Scherrer equation[26] was 119 ± 28 nm (calculations are in Supporting Table S1), which is smaller than the size of copper oxide's visible grains (hemispheres or trientspheres) particles. These crystallites are the constituents of the grains and are not visible in the SEM since an SEM cannot see crystallites; rather, it can only see the morphology of particles.

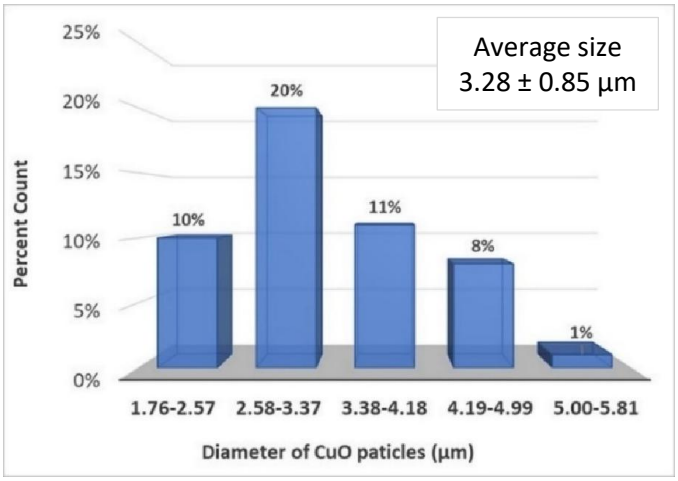

Figure 8: Distribution of sizes of CuO particles determined from an SEM image (Figure 9a). The average size of CuO particles is 3.28 ± 0.85 µm.

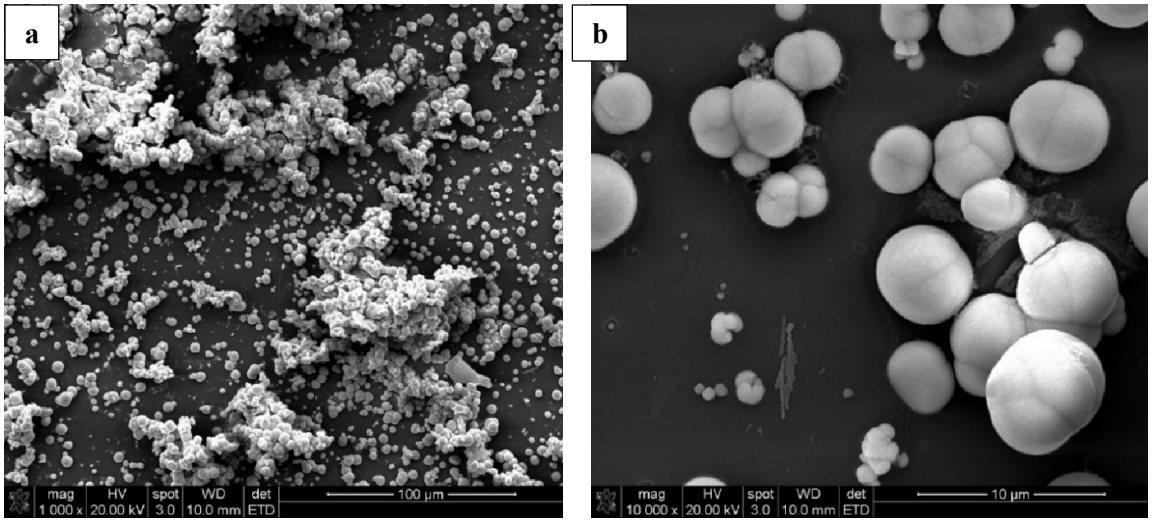

Figure 9: SEM images of CuO film at different magnifications (a) 1000x and (b) 10,000x

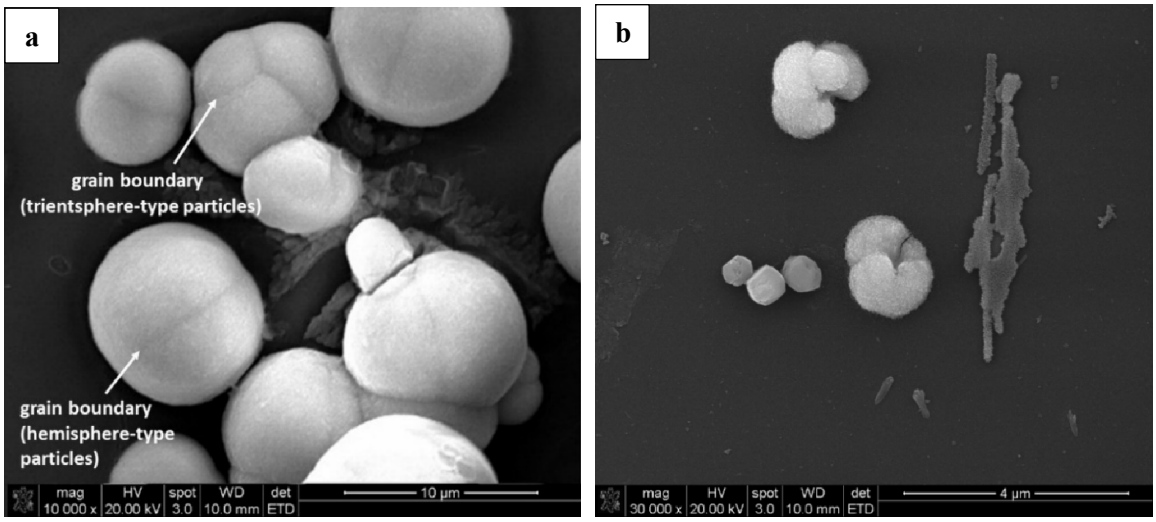

Figure 10: (a) Visible grain boundaries of a hemisphere- and trientsphere-type particles that made up the complete sphere-type particles (b) CuO particles clearly show the crystallites or grains that are yet to be grown as a complete sphere-type particle.

Initially formed crystalline product in the hydrolysis of only copper acetate at 90 °C:

The hydrothermal reaction of copper acetate aqueous solution without any second reactant or organic solvent produced CuO films in 24 hours. However, the reaction initially generated a

green-colored crystalline material, as presented in Figure 11. The material was isolated after three hours of the reaction and characterized. An Attenuated Total Reflectance-FTIR (ATR-FTIR) spectrum (Figure 11 (right)) and a TGA plot (Figure 12) of the isolated material confirm that it is an acetate-intercalated layered double hydroxide of copper, $Cu(OAc)_{0.41}(OH)_{1.59}\cdot 0.40H_2O$. The FTIR bands at 1341 cm^{-1} (–CH_2– starching), 1405 cm^{-1} (symmetric stretching of -COO^-), and 1543 cm^{-1} (asymmetric stretching of -COO^-) confirms the presence of acetate (CH_3-COO^-) in the green crystalline product.[18] The absorption at 787 cm^{-1} and the strong absorption at 647 cm^{-1} indicate the Cu-O-H deformation modes.[27] Also, the small sharp bands at 3607, 3573, and 3518 cm^{-1} can be assigned to the -O-H (coordinated to Cu) stretching modes that may suggest three distinct hydroxyl groups in the layered structure.[18, 27] While the broad peak at 3231 cm^{-1} (-O-H stretching mode due to H-bonding with water molecules) and the small peaks at 1666 and 1693 cm^{-1} (H-O-H bending/scissoring modes of water molecules) confirms the presence of interlayer water molecules in the layered structure. The two bending/scissoring bands of water may indicate the presence of two types of hydrogen-bonded water molecules. Notably, our ATR-FTIR investigation of the layered copper hydroxide, $Cu(OAc)_{0.41}(OH)_{1.59}\cdot 0.40H_2O$ exhibited water scissoring vibrational modes at 1666 and 1693 cm^{-1} that are not buried by the asymmetric starching of acetate groups. However, studies on acetate-intercalated layered copper hydroxides often did not either observe or describe the bending/scissoring vibrational modes of interlayer water molecules.[18, 20] A TGA experiment (Figure 12) determined the amount of interlayer water as 5.89% from the first decomposition step from 90 – 150 °C. The mass loss from 150 to 283 °C was due to the decomposition of acetate as ethane and carbon dioxide and hydroxyl groups as water. TGA ceramic yield of 65.30% (850 °C) for copper(II) oxide estimated the molecular mass of the green crystalline product as 121.82 $gmol^{-1}$. The calculated amount of copper was 52.12%, acetate groups 21.30%, and hydroxyl groups 21.75%. Therefore, the product's formula was enumerated as $Cu(OAc)_{0.41}(OH)_{1.59}\cdot 0.40H_2O$. Calculation S1 in the supplementary information presents the calculations for determining the formula of the green crystalline product from the TGA experiment.

While the elemental analysis for carbon was found as 9.90% excellently agrees with the enumerated formula.

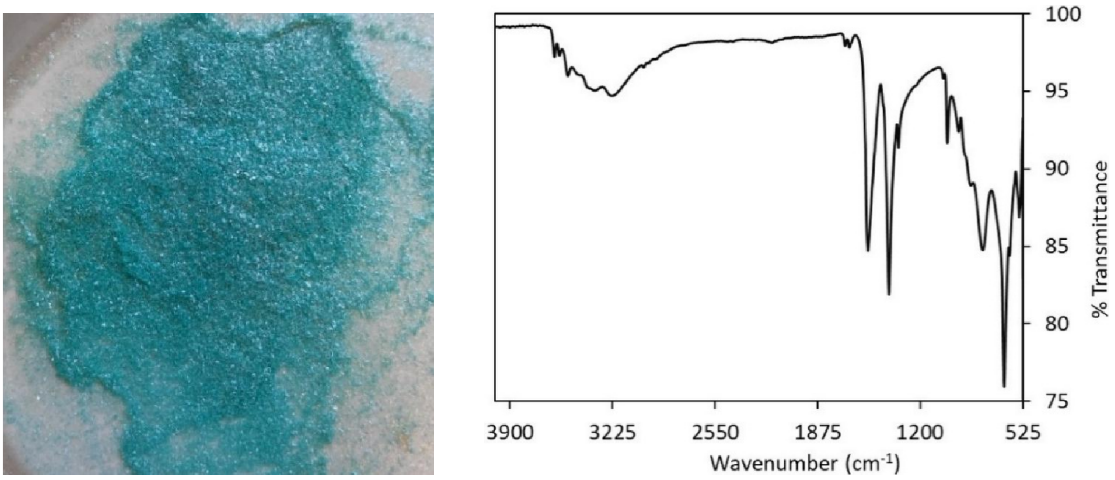

Figure 11: Initially formed bluish-green crystalline product, copper acetate hydroxide, $Cu(OAc)_{0.41}(OH)_{1.59}\cdot 0.40H_2O$ (left) in the hydrolysis reaction of only copper acetate aqueous solution (after 3 hours of reaction). ATR-FTIR spectrum of the product (right).

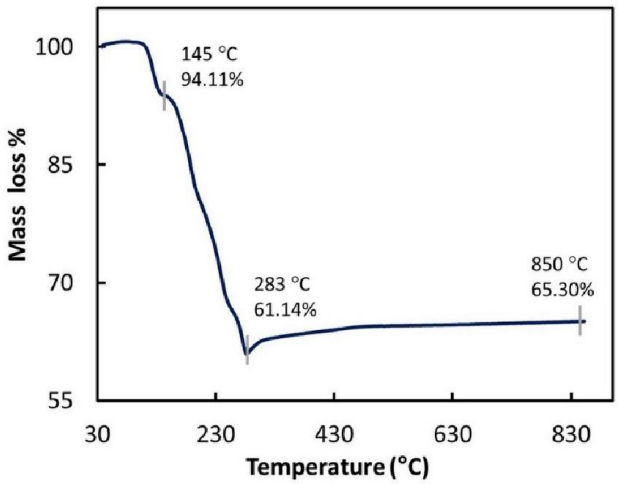

Figure 12: TGA plot of the bluish-green crystalline product isolated at 3 hours of the hydrolysis reaction of aqueous copper acetate.

Table 2: Copper and carbon contents of initially formed green crystalline product in the hydrolysis of copper acetate at 90 °C, determined from TGA and elemental analysis, respectively.

Copper content (%)	Carbon content (%)
52.12	9.90

Chemistry of copper acetate and water at 90°C: Proposed reactions for the deposition of copper(II) oxide from hydrolysis of copper acetate:

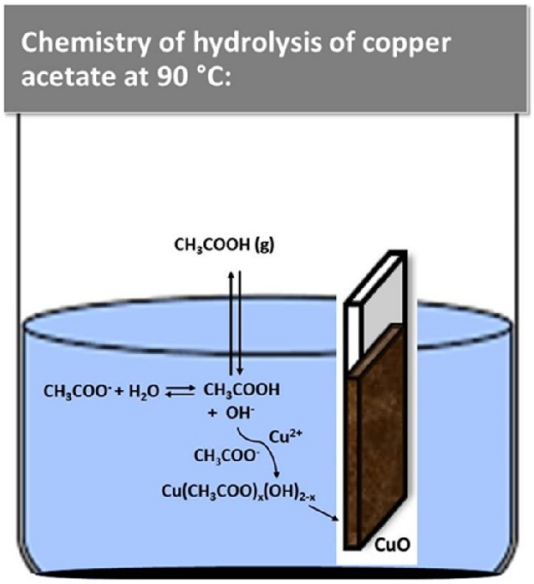

Figure 13: Possible reactions in the hydrolysis of copper acetate aqueous solution at 90 °C in a closed system that deposits CuO

Figure 13 depicts the possible hydrolysis reactions of only copper acetate that deposited copper oxide on a glass substrate. First, acetate ions, OAc^- (CH_3COO^-), react with the water molecules and produce hydroxide ions (OH^-) and acetic acid (HOAc). The hydroxide ions immediately start reacting with the copper ions (Cu^{2+}) that may begin the nucleation step since OH^-, Cu^{2+}, and OAc^- ions would likely generate an insoluble solid phase of copper acetate hydroxide,

$Cu(OAc)_{2-y}(OH)_y \cdot nH_2O$. The formation of green crystalline copper acetate hydroxide, $Cu(OAc)_{0.41}(OH)_{1.59} \cdot 0.40H_2O$ within the first three hours of the hydrolysis reaction, as discussed earlier, establishes the fact that the initial nucleated particles are a phase of copper acetate hydroxide, $Cu(OAc)_{2-y}(OH)_y \cdot nH_2O$. Therefore, the following reactions (Scheme 1) may involve generating the initial nucleated solid phase.

$$OAc^-_{(aq)} + H_2O_{(l)} \rightleftharpoons HOAc_{(l)} + OH^-_{(aq)}$$

$$[Cu(H_2O)_6]^{2+}_{(aq)} + OH^-_{(aq)} \longrightarrow [Cu(OH^-)(H_2O)_5]^{2+}_{(aq)}$$

$$[Cu(OH^-)(H_2O)_5]^{2+}_{(aq)} \xrightarrow[\text{Nucleation}]{OAc^-_{(aq)},\ OH^-_{(aq)}} Cu(OAc)_y(OH)_{2-y} \cdot nH_2O_{(s)}$$

Scheme 1: Proposed reactions that may start nucleation for the deposition of acetate-intercalated layered copper hydroxide, where $Cu(OAc)_y(OH)_{2-y} \cdot nH_2O$ represents the nucleated phase

In Reaction Scheme 1, $[Cu(H_2O)_6]^{2+}$ reacts with in situ formed OH^- ions that generate $[Cu(OH)(H_2O)_6]^+$ complex. The $[Cu(OH)(H_2O)_6]^+$ complex is considered as the precursor (pre-complex) for precipitation or deposition of $Cu(OH)_2$ when it undergoes a second attack of OH^-. However, as the hydrolysis reaction solution has both OAc^- and OH^- ions, the $[Cu(OH)(H_2O)_6]^+$ complex very likely nucleates as an acetate-intercalated layered copper hydroxide, $Cu(OAc)_{2-y}(OH)_y \cdot nH_2O$. The nucleated copper acetate hydroxide eventually grows to a particular phase with time when acetate ions in the solid and in the solution very likely reach an equilibrium. The grown-phase starts decomposing to CuO after a certain time under the hydrothermal condition and is ultimately converted to CuO after 24 hours. The decomposition of a grown-phase of copper acetate hydroxide to CuO can be expressed as follows.

$$Cu(OAc)_x(OH)_{2-x} \cdot nH_2O_{(s)} \xrightarrow{90\ ^\circ C} CuO_{(s)} + x\ OAc^-_{(aq)} + [\tfrac{1}{2}(2-x)+n]\ H_2O_{(l)}$$

Scheme 2: Decomposition of copper acetate hydroxide to copper(II) oxide, CuO, during hydrolysis reaction. Where $Cu(OAc)_{2-x}(OH)_x \cdot nH_2O$ presents the grown phase of copper acetate hydroxide that decomposes to CuO.

Table 3: Initial and final pH of 0.2M copper acetate aqueous solution used in a hydrothermal reaction for deposition of CuO.

Initial pH	Final pH
5.3	4.8

The pH change of the reaction solution from 5.3 (initial) to 4.8 (after reaction) of copper acetate supports the formation of acetic acid from the reaction between acetate ions and water, as shown in Reaction Scheme 1. Besides pH change, a pungent smell of acetic acid was observed at the end of the reaction, confirming the formation of acetic acid. The generation of acetic acid from acetate also produces hydroxide ions (OH^-). These OH^- are ions consumed immediately in nucleation, deposition, and growth of the layered copper hydroxide. This in-situ generation of OH^- ions renders the hydrolysis process working without any extra precipitating reactant or organic solvent (that generates in-situ OH^-). Therefore, in the hydrolysis reaction, water plays the role of the solvent and the reactant, making the process an excellent lesser chemical consuming process for deposition of copper acetate hydroxide and copper oxide.

The particle size distribution (PSD) against the time of a typical hydrolysis reaction was investigated as presented in Figure 14**.** The plot shows that the hydrolysis reaction involves an initial incubation period for the homogenous nucleation step. After nucleation, the nucleated particles were grown into bigger particles rapidly. The rapid growth of particles after nucleation often occurs in hydrothermal processes since the nucleated particles act as heterogeneous growth sites. The development of particles may follow the Finke-Watzky two-step growth model that

involves slow nucleation followed by autocatalytic surface growth.[28] The initial deposition of the particles on the substrate may occur in one of the following ways–

(i) the initial nucleated particles (0-30 minutes) in the solution deposit on the substrate, or

(ii) (ii) the nucleation occurs directly at the substrate if $[Cu(OH)(H_2O)]^+$ complex adsorbed at the surface.

While particle growth at the substrate is likely to follow the same trend as the solution. Therefore, after the initial nucleation or deposition of particles on the substrate, they grow bigger with time and reach a mean-steady size.

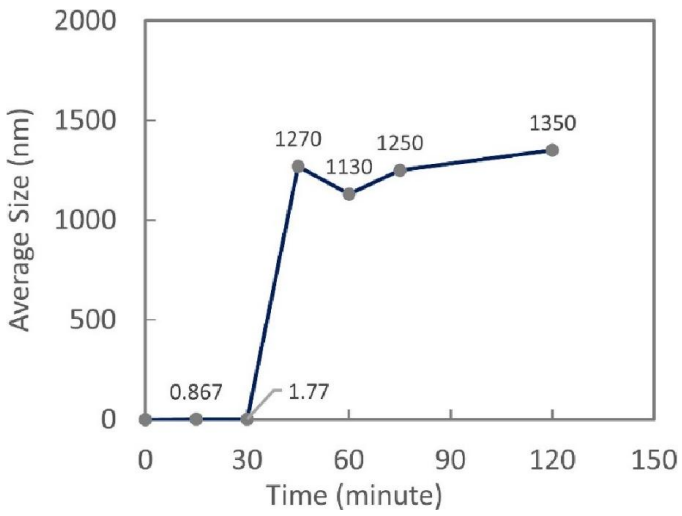

Figure 14: Average size vs. time of copper acetate hydroxide particles during hydrolysis reaction of 0.2M copper acetate solution without any second reactant.

Characterization of products from hydrolysis of copper formate:

Copper(I) oxide/copper formate hydroxide, $Cu_2O/Cu_2(OOCH)(OH)_3$: Hydrolysis of only copper formate aqueous solutions (9.80 mmol in 50 g water) deposited dark green crystalline materials onto glass slides. XRD pattern of the deposited dark-green crystalline materials exhibited two phases of materials – copper(I) oxide and copper formate hydroxide, $Cu_2O/Cu_2(OOCH)(OH)_3$.

The peaks at 36.48°, 42.42°, 52.55°, and 61.61° were matched up with copper(I) oxide, Cu_2O phase (Crystallographic Open Database, COD File# 00-101-0963). The rest of the peaks have a sharp peak at a lower angle (13.16°) and smaller peaks at higher angles (26.82°, 40.68°, and 55.28°) – this confirms that the material is also constituted by a layered structure.[29] Therefore, the remaining peaks can be attributed to the layered copper formate hydroxide $Cu_2(OOCH)(OH)_3$. Moreover, besides the XRD pattern analysis, TGA, FTIR, and elemental analysis (discussed later) established that the second phase of the material was formate intercalated copper hydroxide, $Cu_2(OOCH)(OH)_3$. All the reflections are sharp in nature in the XRD pattern, indicating the particles are polycrystalline.[26] Crystallite size was estimated using the Scherrer equation, which also confirmed the polycrystallinity of the particles since the estimated average crystallite size of Cu_2O was 549 ± 74 nm (supporting Table S2). While for $Cu_2(OOCH)(OH)_3$ estimated crystallite size was 472 ± 108 nm (supporting Table S3). The XRD corresponding to $Cu_2(OOCH)(OH)_3$ did not match any known copper compounds in the database, suggesting that the copper formate hydroxide phase has not been indexed or reported yet. Wasuke and co-workers investigated magnetic susceptibilities of basic copper(II) formates and reported the synthesis of $Cu(OOCH)(OH)$ and $Cu_2(OOCH)(OH)_3$; however, they did not show any XRD of their products.[17]

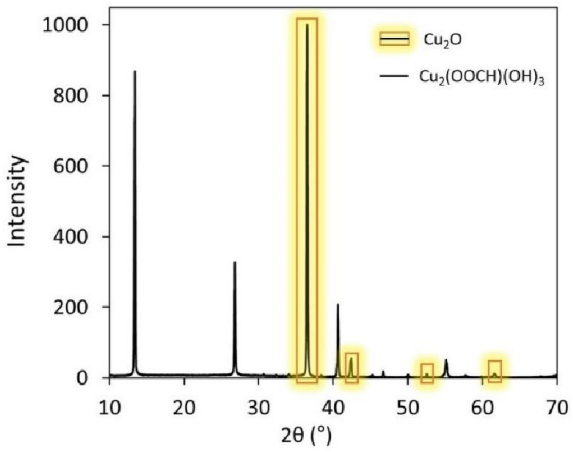

Figure 15: XRD of the dark green crystalline product of hydrolysis of copper formate aqueous solution (9.80 mmol copper formate in 50 g water) without any second reactant.

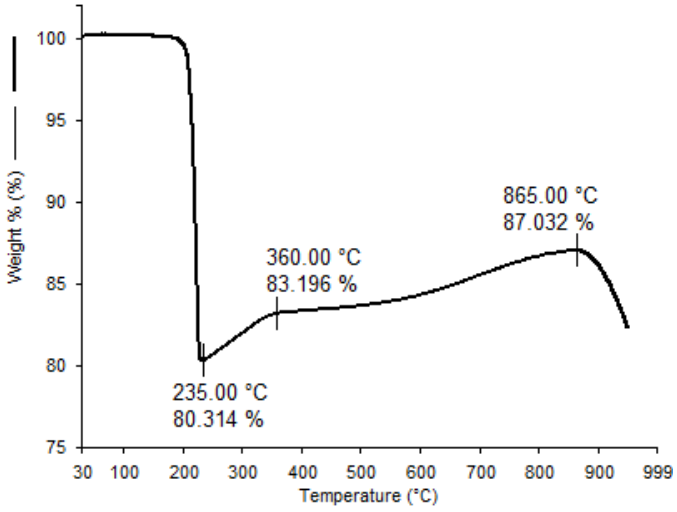

Figure 16: TGA of the hydrolysis product of copper formate aqueous solution. The formula of the product was determined as $(Cu_2O)_{0.25}/(Cu_2(OOCH)(OH)_3)_{0.25}$.

Figure 16 presents the TGA of copper(I) oxide/copper formate hydroxide. The first mass loss from 180 to 235 °C must be due to the decomposition of formate ($OOCH^-$) as CO_2 and dehydroxylation of hydroxide (OH^-) groups as water. The formate decomposition step also involves reducing Cu^{2+} likely to metallic copper (Cu^0) since formate ($OOCH^-$) generates HCOȮ radical by reducing Cu^{2+} to Cu^0 before decomposition as CO_2 and H_2O.[30] Therefore, at 235 °C, the materials can be attributed to Cu/Cu_2O. From 235 to 360°C, the increased mass indicates oxidation of metallic to Cu_2O alongside Cu_2O oxidation to CuO. The rest of the increase of mass from 360 to 865 °C corresponds to the completion of oxidation of Cu_2O to CuO. While CuO can be decomposed metallic Cu via copper(I) oxide, Cu_2O at a higher temperature,[31] Therefore, the mass loss from 865 to 950 °C stands for CuO decomposition to metallic Cu. Using the ceramic yield as 87.03% for CuO at 865 °C, the estimated amount of copper in the starting material is 69.53%, and the carbon content was determined as 3.28% from the elemental analysis. TGA and elemental analysis together determine the formula of the green crystalline material as $(Cu_2O)_{0.25}/(Cu_2(OOCH)(OH)_3)_{0.25}$. Supporting Calculation S2 presents the detailed enumeration for determining the formula. From

the formula, the calculated amount of mass loss due to formate decomposition should be 12.29%, and dehydroxylation of two equivalents of hydroxides as water should be 6.97%. The total of these two mass losses equals 19.26%, excellently agreeing with the TGA mass loss (19.69%) from 180 to 235 °C. This agreement further confirms the determined formula of the material.

Table 4: Copper and carbon contents of the dark green crystalline product prepared from the hydrolysis of 9.80 mmol copper formate in 50 g water.

Copper content (%)	Carbon content (%)
69.57[a]	3.28[b]

a. TGA
b. Elemental Analysis

Attenuated total reflectance FT-IR (Figure 17) of the hydrolysis product of copper formate also confirms the presence of formate, $HCOO^-$. The FT-IR spectrum showcases bands at 1558 and 1370 cm^{-1} that arise due to asymmetric and symmetric stretching, respectively, for -COO of formate (HCOO-), while the 1345 cm^{-1} peak states the C-H stretching of the formate. The difference between the symmetric and asymmetric bands is less than 200 cm^{-1}, which may indicate bidentate co-ordination of formate with copper similar to hydrated or anhydrous copper formate, $Cu(OOCH)_2 \cdot 4H_2O$ or $Cu(OOCH)_2$.[32] The out of plane deformation of OCO is also detected by the 1044 cm^{-1} band while the band at 844 cm^{-1} may suggest symmetric bending mode of OCO.[33] The sharp bands at 708, 756, and 788 cm^{-1} can be attributed to different Cu-OH vibration modes where the three bands may suggest that $Cu\text{-}(OH)_{2-x}$ (where x = number of formate, $HCOO^-$) groups are in three distinct chemical environments in the lattice of copper(I) oxide/copper formate hydroxide.

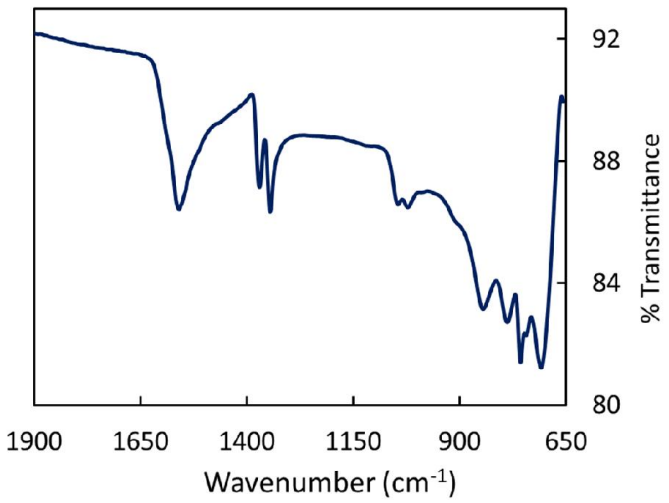

Figure 17: Attenuated Total Reflectance (ATR)-FTIR spectrum of copper(I) oxide/copper formate hydroxide.

Two shapes of particles – octahedron and rectangular-type bars, were deposited by the hydrolysis reaction of only copper formate. The shapes of particles are also indicative of the fact that the reaction produced a two-phase material. At this moment, we do not have sufficient characterization of the SEM to assign what shape is copper(I) oxide, Cu_2O, or copper formate hydroxide $Cu_2(OOCH)(OH)_3$. However, the stacking of sheets is visible at the edge of a rectangular-type particle in the SEM image Figure 18d. Since $Cu_2(OOCH)(OH)_3$ is a layered material; presumably, it grows as layers; hence, it will likely have stacking faults or stacking defects. As a result, the rectangular-type particle particles may represent $Cu_2(OOCH)(OH)_3$. While the octahedron-type particles may represent Cu_2O. Zhao and coworkers reported a synthesis of octahedron-type Cu_2O micro-crystals using copper nitrate and formic acid.[34] Since, in our study, formate ions can react with water and produce formic acid in situ (Scheme 3), the formation of Cu_2O may be facilitated by the in situ formed formic acid, similar to the hydrothermal reaction of copper nitrate and formic acid. The two shapes of the particle also suggest that the growth of Cu_2O is different than $Cu_2(OOCH)(OH)_3$. Therefore, it is very likely that the nucleation of Cu_2O and $Cu_2(OOCH)(OH)_3$ are separate events. Scheme 3 depicts the possible reactions that may involve in

the hydrothermal process of pure copper formate aqueous solution. In the hydrothermal reaction, formate ions react with water and produce hydroxide and formic acid in situ. The hydroxide ions (OH^-) facilitated the formation of $Cu(OOCH)_x(OH)_{2-x}$ as nucleated particles that further grow as $Cu_2(OOCH)(OH)_3$. While the formic acid reacts with $[Cu(H_2O)_6]^{2+}$ and generates Cu_2O particles. The initial pH of the reaction solution was 4.65; at the end of the reaction, it became 3.90. The pH change confirms the generation of H^+ in the reaction and supports the proposed reactions presented in Scheme 3.

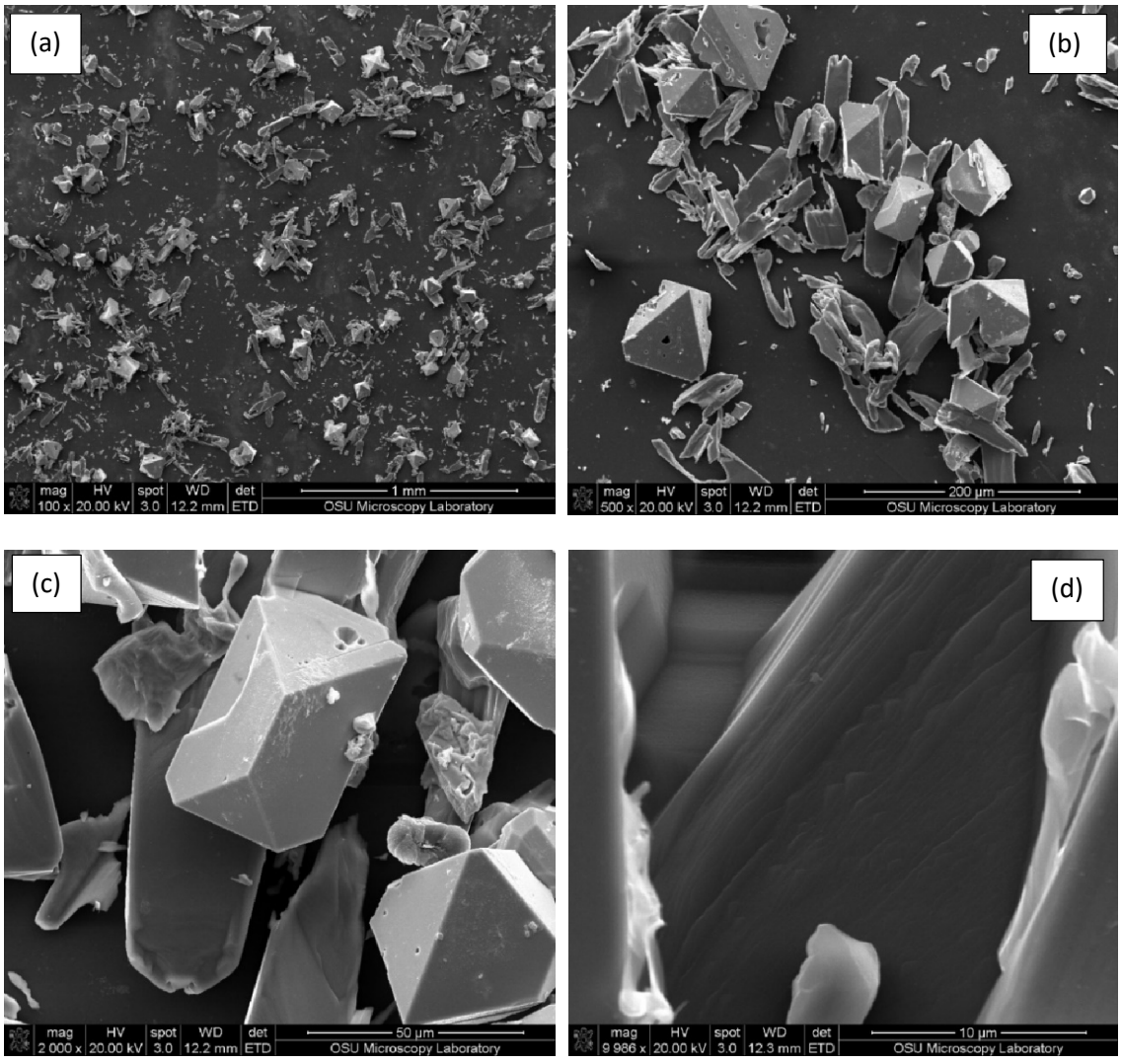

Figure 18: SEM images of copper(I) oxide/copper formate hydroxide, $Cu_2O/Cu_2(OOCH)(OH)_3$.

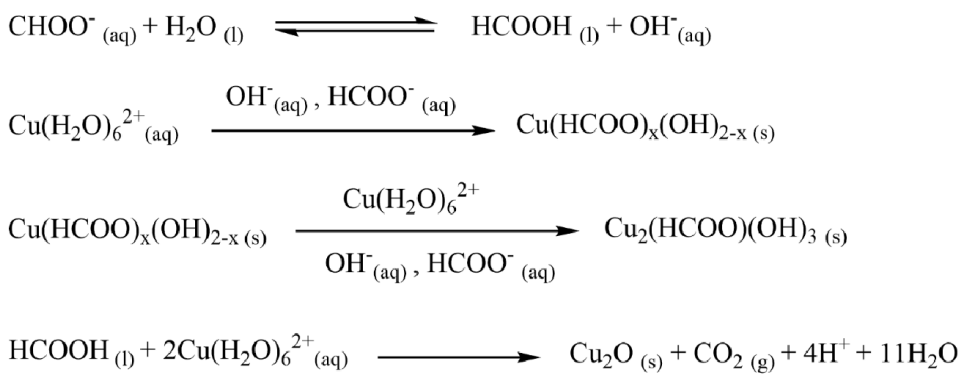

Scheme 3: Proposed reactions in the hydrolysis of pure copper formate aqueous solution.

Table 5: Initial and final pH in a hydrothermal reaction of ~ 0.2M copper formate aqueous solution to deposit copper(I) oxide/copper formate hydroxide.

Initial pH	Final pH
4.65	3.90

Deposition of copper(I) oxide/copper(II) oxide by hydrolysis of copper formate

Interestingly, hydrolysis of 0.49M 50 g copper formate aqueous solution deposited crystalline copper(I) oxide/copper(II) oxide, Cu_2O/CuO on glass slides as films. The color of the product was dark/blackish-green. FTIR experiment of the product (Supporting Figure S3) did not show any peaks for the formate, confirming no presence of copper formate hydroxide phase. While the TGA experiment of the product under air (Figure 19) exhibited no mass loss. Instead, an increase of mass up to 870°C was observed, confirming the oxidation of Cu_2O to CuO. In the TGA experiment, the total mass increase was 5.099% which enumerates the product's formula as $(Cu_2O)_{0.32}/(CuO)_{0.36}$.

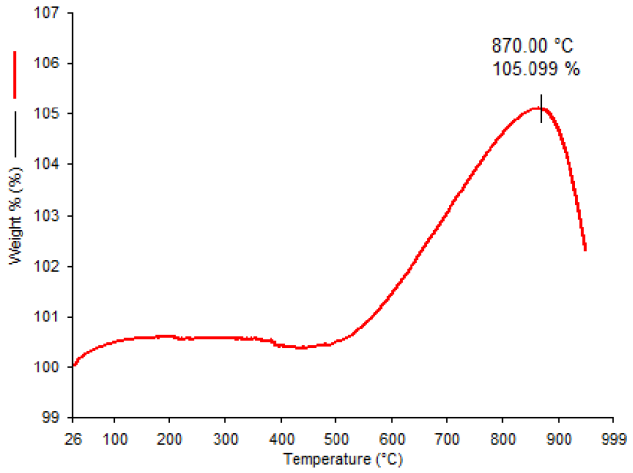

Figure 19: TGA plot of crystalline Cu_2O/CuO, the product from the hydrolysis of 0.49 M copper formate aqueous solution.

Hydrolysis of copper acetate with silica pellets and mesoporous silica:

The hydrolysis reaction of copper acetate and silica pellets was also investigated to see what material it can deposit onto the pellets. A reaction of 0.2M 50.0 g copper acetate aqueous solution was heated with 5.110 g silica pellets at 90 °C. After 48 hours, the reaction was stopped, and it turned out that the reaction generated blue-colored silica pellets (Figure 20a). Notably, the blue color is uniformly distributed in the silica pellets suggesting a homogenous deposition. The deposited blue material is copper hydroxide with a small amount of acetate intercalation, $Cu(OAc)_{0.04}(OH)_{1.96}\cdot nH_2O$, as determined from the elemental analysis of the blue pellets (copper 5.44% and carbon 0.09%). Upon pyrolysis at 400 °C, the blue silica pellets converted to green silica pellets with a uniformly distributed green color (Figure 20b). The color change confirms that pyrolysis converted the copper acetate hydroxide deposited silica pellets to CuO deposited silica pellets. The copper acetate hydroxide deposition onto the pellets was 8.02% (w/w). After pyrolysis, the copper oxide deposition on the pellets was determined as 5.35% (w/w).

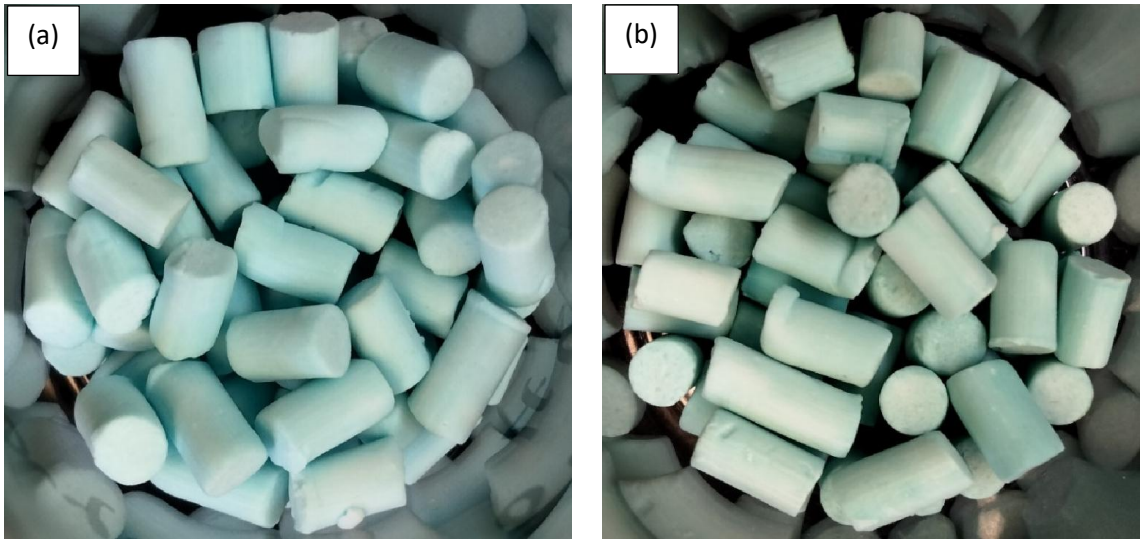

Figure 20: (a) copper acetate hydroxide deposited silica pellets, prepared by hydrolysis of copper acetate and silica pellets, (b) CuO deposited silica pellets, prepared by pyrolysis of the blue pellets.

Table 6: Deposition amount (w/w %) of copper acetate hydroxide and copper oxide onto silica pellets.

Copper acetate hydroxide deposition on silica pellets (w/w %)	Copper oxide deposition on silica pellets after pyrolysis (w/w %)
8.02	5.35

Hydrolysis of copper acetate was also investigated with porous materials such as mesoporous silica OSU-6 (synthesized and commercialized by XploSafe, Stillwater, Oklahoma). A reaction of 0.1506 g OSU-6 with 16.6925 g of 0.125M copper acetate aqueous solution at 80°C generated blue OSU-6. After washing and drying mass of blue SOU-6 was 0.5454 g. The blue color confirmed the deposition of copper acetate hydroxide onto OSU-6. After pyrolysis at 400 °C, the blue OSU-6 turned into green OSU-6 (Figure 21), confirming the transformation of copper acetate hydroxide to CuO. The percent deposition of copper oxide onto OSU-6 was 5.56%.

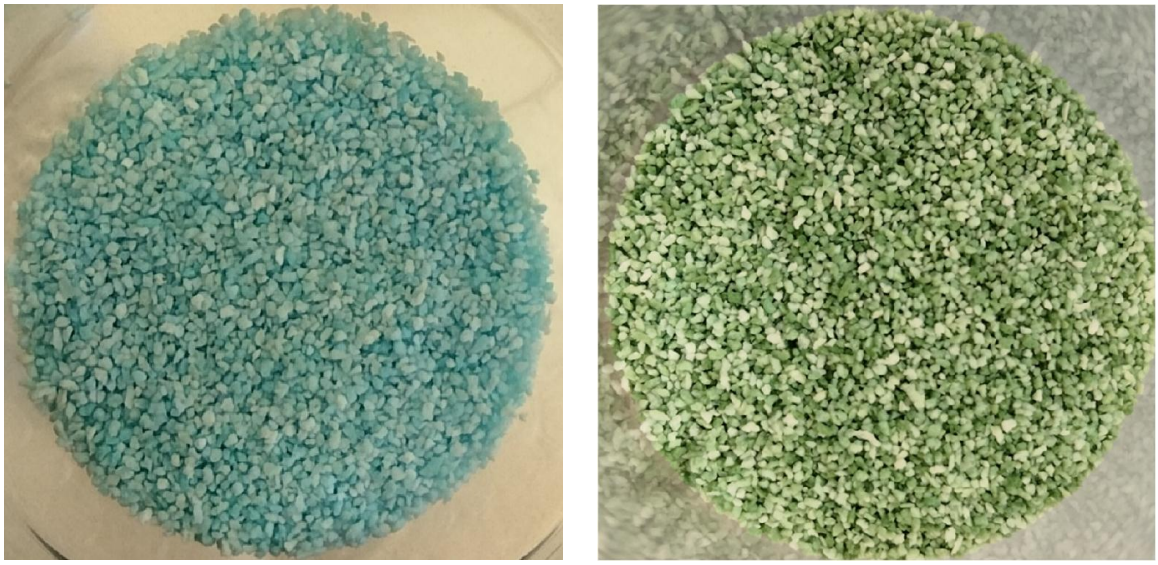

Figure 21: Copper acetate hydroxide (blue) and copper oxide (green) deposited OSU-6.

Table 7: Percent deposition (w/w %) of copper acetate hydroxide and copper oxide on OSU-6 (mesoporous silica)

Copper acetate hydroxide deposition (w/w %)	Copper oxide deposition after pyrolysis (w/w %)
7.70	5.56

■ Conclusion:

The chapter shows that hydrolysis of 0.20M copper acetate aqueous solution without any second reactant or organic reagent at 90°C directly deposited copper (II) oxide, CuO particles on glass substrates in 24 hours. The deposited CuO particles have sphere-type shapes (hemispheres and trientspheres) with an average size of 3.28±0.85 μm. Investigation of the reaction product during the initial hours proves that CuO deposits via an intermediate compound of copper acetate hydroxide, $Cu(OAc)_{0.41}(OH)_{1.59}\cdot 0.40H_2O$. While hydrolysis of only copper formate with a concentration of ~ 0.2M deposited copper(I) oxide/copper formate hydroxide, $Cu_2O/Cu_2(OOCH)$

$(OH)_3$. The morphologies of the $Cu_2O/Cu_2(OOCH)(OH)_3$ phases are octahedron- and rectangular-type particles. However, 0.49M copper formate solution deposited copper(I) oxide/copper(II) oxide, Cu_2O/CuO. The hydrolysis reactions of copper acetate and copper formate described in this work are a facile and inexpensive method for deposition of nano- or micro-size particles of copper oxides and layered copper hydroxides. Additionally, the hydrolysis reaction of copper acetate with silica pellets and mesoporous silica (OSU-6) also showed that it deposited copper acetate hydroxide onto silica pellets that were effortlessly converted to CuO deposited silica pellets and mesoporous silica by pyrolysis. The process is expected to easily be exploited to deposit copper oxides and acetate- or formate- intercalated copper layered hydroxides on other substrates, catalyst supports, and porous materials for various important applications. Therefore, the hydrolysis (hydrothermal) process developed in the present investigation has established a new straightforward route for accessing nano-/micro-structured copper oxides and layered copper hydroxides supported substrates, supports, and porous materials.

- **Future work:**

Proposed future work for a novel synthesis of Cu_2O from $Cu_2(OOCH)(OH)_3$:

The finding of copper formate hydrolysis that can generate $Cu_2O/Cu_2(OOCH)(OH)_3$ has motivated the idea of developing a route for synthesizing pure Cu_2O from $Cu_2(OOCH)(OH)_3$ by a hydrothermal or solvothermal method. It is hypothesized that low-temperature heating of $Cu_2(OOCH)(OH)_3$ solid using organic or aqua-organic solvents such as alcohols-formic acid or deoxygenated water-formic acid will convert the $Cu_2(OOCH)(OH)_3$ to Cu_2O. To investigate the idea, ex-situ prepared $Cu_2(OOCH)(OH)_3$ solid phase will be heated (50-60°C) in ethanol- or propanol-formic acid or deoxygenated water-formic acid solvent. While for large-scale ex-situ synthesis of a $Cu_2(OOCH)(OH)_3$ two approaches can be used – (i) a proton scavenger (such as propylene oxide) in the hydrolysis copper formate solution at 40-60° or at room temperature, and

(ii) direct precipitation of copper formate using NaOH followed by the aging of the precipitate at 40-60°. If the proposed solvothermal or hydrothermal treatment, as mentioned above, can transform $Cu_2(OOCH)(OH)_3$ directly to Cu_2O, it would be an inexpensive and straightforward process for the large-scale synthesis of Cu_2O.

■ Supporting Information

Equation S1: Scherrer equation to determine crystallite size.[26]

$$D = \frac{K\lambda}{\beta \cos\theta} \qquad (1)$$

Where D is crystallite size, K Scherrer's constant, θ is a diffraction angle, and β is the full width of a peak at half of its maximum (FWHM).

Table S1: Crystallite size estimation of CuO particles of a CuO decorated glass substrate using Scherrer equation.

2θ	FWHM (β)	β (radians)	Cos θ (radians)	D (nm)	Average D (nm)
32.47	0.5400	0.009425	0.9601	153.2	119 ± 28
35.57	0.8800	0.01536	0.9522	94.8	
38.77	0.7700	0.01344	0.9433	109.4	
48.79	0.8000	0.01396	0.9107	109.0	
58.14	0.5900	0.01030	0.8740	154.1	
61.60	0.9800	0.01710	0.8590	94.3	

Table S2: Crystallite size estimation of Cu_2O particles of a Cu_2O/ $Cu_2(OOCH)(OH)_3$ decorated glass slide using Scherrer equation.

2θ	FWHM (β)	β (radians)	Cosθ (radians)	D(nm)	Average D (nm)
36.48	0.140	0.002443	0.9498	597.5	549±74
42.42	0.150	0.002618	0.9323	568.1	
52.61	0.150	0.002618	0.8964	590.8	
61.61	0.210	0.003665	0.8589	440.4	

Table S3: Crystallite size estimation of $Cu_2(OOCH)(OH)_3$ particles of a $Cu_2O/Cu_2(OOCH)(OH)_3$ decorated glass slide using Scherrer equation.

2θ	FWHM (β)	β (radians)	Cosθ (radians)	D (nm)	Average D (nm)
13.36	0.1500	0.002618	0.9932	533.2	**472±108**
26.79	0.1600	0.002793	0.9728	510.4	
40.62	0.1600	0.002793	0.9378	529.4	
46.68	0.1700	0.002967	0.9182	509.0	
55.12	0.3200	0.005585	0.8865	280.0	

Calculation S1: Analysis of TGA plot of the bluish-green crystalline product (copper acetate hydroxide) for estimating the copper content and enumerating the product's formula.

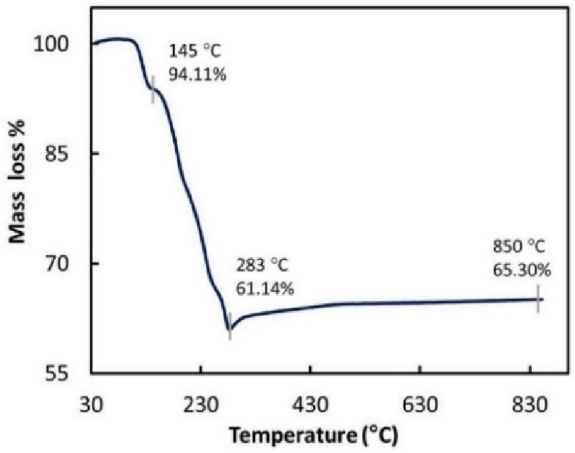

Figure S1: TGA of bluish-green crystalline product, copper acetate hydroxide, isolated after three hours in hydrolysis of copper acetate aqueous solution.

(i) Estimation of copper content: Ceramic yield (CuO at 850°C) = 65.30%

Percent copper in the ceramic product = (65.30/79.55) = 0.821* 63.55 = 52.17

Hence, copper content in the bluish-green crystalline product = 52.17%

(ii) Enumeration of the formula of the product, copper acetate hydroxide:

Ceramic yield (CuO at 850°C) = 65.30%. Therefore, molecular mass of the green crystalline product = 79.55/0.6530 = 121.82 g/mol

The general formula of copper acetate hydroxide is $Cu(OAc)_{2-x}(OH)_x \cdot nH_2O$. Therefore, $Cu(OAc)_{2-x}(OH)_x \cdot nH_2O$ must be equal to 121.82 g/mol. As the copper and water content can be determined from the ceramic yield and the first mass loss from the TGA experiment, then x in the general formula of $Cu(OAc)_{2-x}(OH)_x \cdot nH_2O$ can be solved as follows.

$Cu(OAc)_{2-x}(OH)_x \cdot nH_2O$ =121.82

63.55 + (2-x)59.044 + 17.008x + 7.19 = 121.82 [nH_2O = amount of water = 5.89%* 121.82 = 7.19 g]

x = 1.59

Therefore, the contents of hydroxyl groups (OH^-) and acetate groups (OAc^-) in green crystalline product, $Cu(OAc)_{2-x}(OH)_x \cdot nH_2O$, are

OH = 1.59 (21.75%)

OAc = 2-1.59 = 0.41 (21.30%)

Hence, the formula of the product is $Cu(OAc)_{0.41}(OH)_{1.59} \cdot 0.40H_2O$

Calculation S2: Analysis of the TGA plot of the dark-green crystalline product (copper(I) oxide/copper formate hydroxide) to estimate the copper content and enumerate the product's formula.

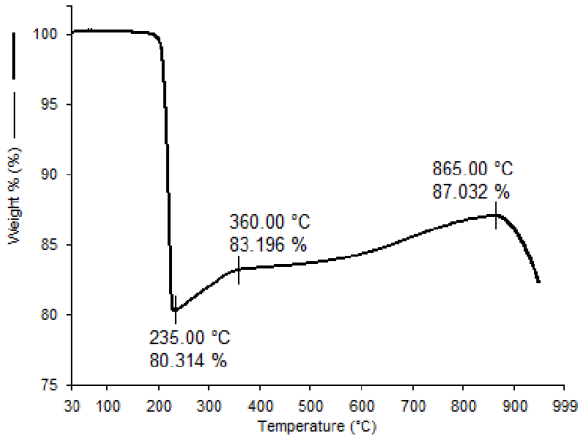

Figure S2: TGA of the dark-green crystalline product, copper(I) oxide/copper formate hydroxide

(i). Estimation of copper content:

Ceramic yield (CuO at 865°C) = 87.032%. Percent of copper in the ceramic product = (87.032/79.55) = 1.094* 63.55 = 69.53%

Hence, copper content in the dark green crystalline product = 69.53%

(ii). Enumeration of the formula of the dark green crystalline product (copper(I) oxide/copper formate hydroxide):

The general formula of copper formate hydroxide is $Cu_z(OOCH)_x(OH)_{2z-x}$ (TGA shows that there is no mass loss step for intercalated water molecules).

The material has two phases, copper(I) oxide and copper formate hydroxide (Figure 15, XRD pattern). Therefore, the formula of the materials is $(Cu_2O)_y/Cu_z(OOCH)_x(OH)_{2z-x}$

The experimental elemental analysis for carbon was 3.28%. Therefore, the ratio of copper and carbon in the product is as follows.

Elements	content (%)	ratio 1	ratio 2
Copper	69.52	1.09	1.0
Carbon	3.28	0.273	0.25

As 1 mole carbon is equivalent to 1 mole of formate, the formula of copper formate hydroxide must be $Cu_z(OOCH)_{0.25}(OH)_{2z-0.25}$. Mass loss due to decomposition of formate and hydroxyl groups is 19.87% (from TGA mass loss from 180 to 235°C).

$(OOCH)_{0.25} + (OH)_z = 19.87$

$11.25 + 17.008(z) = 19.87$

$z = \sim 0.50$

Hence, the formula of copper formate hydroxide is $Cu_{0.50}(OOCH)_{0.25}(OH)_{0.75}$. To have integers for all the species in the formula, it can be written as $(Cu_2(OOCH)(OH)_3)_{0.25}$

Now, the ceramic yield for CuO at 865°C is 87.032%. Therefore, the molecular mass of the dark green crystalline product should be 79.55/0.8703 = 91.41 g/mol.

Hence, $(Cu_2O)_y/Cu_z(OOCH)_x(OH)_{2z-x}$ must be equal to 91.41 g/mol. The y in the formula $(Cu_2O)_y/(Cu_2(OOCH)(OH)_3)_{0.25}$ can be solved as follows.

$(Cu_2O)_y/(Cu_2(OOCH)(OH)_3)_{0.25} = 91.41$

$143.09y + (127.1 + 45.017 + 51.024)0.25 = 91.41$

$143.09y + 55.79 = 91.41$

$y = 0.25$

Therefore, the formula of the product is $(Cu_2O)_{0.25}/(Cu_2(OOCH)(OH)_3)_{0.25}$

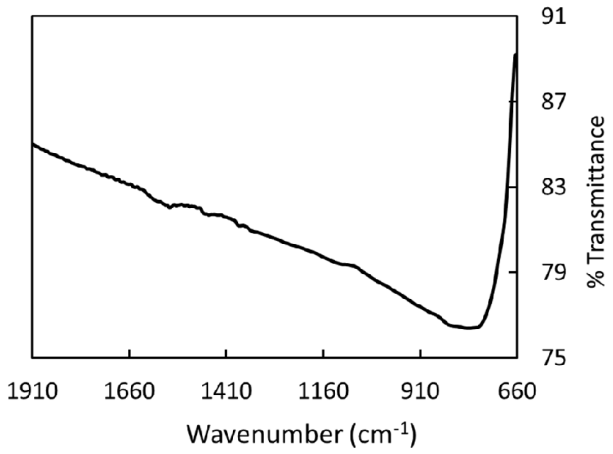

Figure S3: ATR-FTIR of the product (Cu_2O/CuO) deposited from the hydrolysis of 0.49M 50g aqueous solution of copper formate. The spectrum shows no peaks for formate in the range of 1350 to 1650 cm^{-1}.

Table S4: Copper content determination of copper acetate hydroxide deposited silica pellets (blue pellets)

Mass of blue pellets for digestion (g)	mass of the digested solution (g)	Dilution		MP-AES reading for Cu (ppm)	ppm of Cu in the digested solution	% Cu in the blue pellets
		m_1 (g)	m_2 (g)			
0.2198	20.0690	0.2050	21.2239	5.76	596	5.44

■ References:

(1) Primo, A.; Esteve-Adell, I.; Blandez, J. F.; Dhakshinamoorthy, A.; Alvaro, M.; Candu, N.; Coman, S. M.; Parvulescu, V. I.; Garcia, H., High catalytic activity of oriented 2.0.0 copper(I) oxide grown on graphene film. *Nat Commun* **2015,** 6, 8561.

(2) Wang, W.; Deng, C.; Xie, S.; Li, Y.; Zhang, W.; Sheng, H.; Chen, C.; Zhao, J., Photocatalytic C-C Coupling from Carbon Dioxide Reduction on Copper Oxide with Mixed-Valence Copper(I)/Copper(II). *J Am Chem Soc* **2021,** 143, (7), 2984-2993.

(3) Aktar, A.; Ahmmed, S.; Hossain, J.; Ismail, A. B. M., Solution-Processed Synthesis of Copper Oxide (Cu x O) Thin Films for Efficient Photocatalytic Solar Water Splitting. *ACS Omega* **2020,** 5, (39), 25125-25134.

(4) Yu, F.; Li, F.; Zhang, B.; Li, H.; Sun, L., Efficient Electrocatalytic Water Oxidation by a Copper Oxide Thin Film in Borate Buffer. *ACS Catalysis* **2014,** 5, (2), 627-630.

(5) Zuo, C.; Ding, L., Solution-Processed Cu2O and CuO as Hole Transport Materials for Efficient Perovskite Solar Cells. *Small* **2015,** 11, (41), 5528-32.

(6) Lupan, O.; Ababii, N.; Mishra, A. K.; Gronenberg, O.; Vahl, A.; Schurmann, U.; Duppel, V.; Kruger, H.; Chow, L.; Kienle, L.; Faupel, F.; Adelung, R.; de Leeuw, N. H.; Hansen, S., Single CuO/Cu2O/Cu Microwire Covered by a Nanowire Network as a Gas Sensor for the Detection of Battery Hazards. *ACS Appl Mater Interfaces* **2020,** 12, (37), 42248-42263.

(7) Dasineh Khiavi, N.; Katal, R.; Kholghi Eshkalak, S.; Masudy-Panah, S.; Ramakrishna, S.; Jiangyong, H., Visible Light Driven Heterojunction Photocatalyst of CuO-Cu2O Thin Films for Photocatalytic Degradation of Organic Pollutants. *Nanomaterials (Basel)* **2019,** 9, (7).

(8) Huang, Y.-C.; Luo, C.-H.; Yang, S.; Lin, Y.-C.; Chuang, C.-Y., Improved Removal of Indoor Volatile Organic Compounds by Activated Carbon Fiber Filters Calcined with Copper Oxide Catalyst. *CLEAN - Soil, Air, Water* **2010,** 38, (11), 993-997.

(9) Hassan, I. A.; Parkin, I. P.; Nair, S. P.; Carmalt, C. J., Antimicrobial activity of copper and copper(i) oxide thin films deposited via aerosol-assisted CVD. *J Mater Chem B* **2014,** 2, (19), 2855-2860.

(10) Zhu, H.; Wang, J.; Xu, G., Fast Synthesis of Cu2O Hollow Microspheres and Their Application in DNA Biosensor of Hepatitis B Virus. *Crystal Growth & Design* **2009,** 9, (1), 633-638.

(11) Ozga, M.; Kaszewski, J.; Seweryn, A.; Sybilski, P.; Godlewski, M.; Witkowski, B. S., Ultra-fast growth of copper oxide (II) thin films using hydrothermal method. *Materials Science in Semiconductor Processing* **2020,** 120.

(12) Teli, A. M.; Navathe, G. J.; Patil, D. S.; Jadhav, P. R.; Patil, S. B.; Dongale, T. D.; Karanjkar, M. M.; Shin, J. C.; Patil, P. S., TOPO mediated rapid hydrothermal synthesis and study of electrochemical performance of nano-structured copper oxide thin films. *Sustainable Energy & Fuels* **2017,** 1, (2), 377-386.

(13) Zhu, C.; Panzer, M. J., Seed Layer-Assisted Chemical Bath Deposition of CuO Films on ITO-Coated Glass Substrates with Tunable Crystallinity and Morphology. *Chemistry of Materials* **2014,** 26, (9), 2960-2966.

(14) Pan, L.; Zou, J.-J.; Zhang, T.; Wang, S.; Li, Z.; Wang, L.; Zhang, X., Cu2O Film via Hydrothermal Redox Approach: Morphology and Photocatalytic Performance. *The Journal of Physical Chemistry C* **2013,** 118, (30), 16335-16343.

(15) Kozai, N.; Mitamura, H.; Fukuyama, H.; Esaka, F.; Komarneni, S., Synthesis and Characterization of Copper Hydroxide Acetate With a Layered Discoid Crystal. *Journal of Materials Research* **2005,** 20, (11), 2997-3003.

(16) Ghotbi, M. Y.; Rahmati, Z., Nanostructured copper and copper oxide thin films fabricated by hydrothermal treatment of copper hydroxide nitrate. *Materials & Design* **2015,** 85, 719-723.

(17) Mori, W.; Kishita, M.; Inoue, M., Magnetic susceptibility and PMR spectrum of new basic copper(II) formates Cu3(HCOO)2(OH)4 and Cu(HCOO)(OH). *Inorganica Chimica Acta* **1980,** 42, 11-15.

(18) Masciocchi, N.; Corradi, E.; Sironi, A.; Moretti, G.; Minelli, G.; Porta, P., Preparation, Characterization, andab initioX-Ray Powder Diffraction Study of Cu2(OH)3(CH3COO)·H2O. *Journal of Solid State Chemistry* **1997,** 131, (2), 252-262.

(19) Ganga, B. G.; Santhosh, P. N., Facile synthesis of porous copper oxide nanostructure using copper hydroxide acetate precursor. *Materials Letters* **2015,** 138, 113-115.

(20) Bette, S.; Kremer, R. K.; Eggert, G.; Tang, C. C.; Dinnebier, R. E., On verdigris, part I: synthesis, crystal structure solution and characterisation of the 1-2-0 phase (Cu3(CH3COO)2(OH)4). *Dalton Trans* **2017,** 46, (43), 14847-14858.

(21) Volanti, D. P.; Orlandi, M. O.; Andrés, J.; Longo, E., Efficient microwave-assisted hydrothermal synthesis of CuO sea urchin-like architectures via a mesoscale self-assembly. *CrystEngComm* **2010,** 12, (6), 1696-1699.

(22) Kliche, G.; Popovic, Z. V., Far-infrared spectroscopic investigations on CuO. *Phys Rev B Condens Matter* **1990,** 42, (16), 10060-10066.

(23) Balamurugan, B.; Mehta, B. R., Optical and structural properties of nanocrystalline copper oxide thin films prepared by activated reactive evaporation. *Thin Solid Films* **2001,** 396, (1), 90-96.

(24) Singh, D. P.; Ojha, A. K.; Srivastava, O. N., Synthesis of Different Cu(OH)2 and CuO (Nanowires, Rectangles, Seed-, Belt-, and Sheetlike) Nanostructures by Simple Wet Chemical Route. *The Journal of Physical Chemistry C* **2009,** 113, (9), 3409-3418.

(25) Rangel, W. M.; Boca Santa, R. A. A.; Riella, H. G., A facile method for synthesis of nanostructured copper (II) oxide by coprecipitation. *Journal of Materials Research and Technology* **2020,** 9, (1), 994-1004.

(26) Holder, C. F.; Schaak, R. E., Tutorial on Powder X-ray Diffraction for Characterizing Nanoscale Materials. *ACS Nano* **2019,** 13, (7), 7359-7365.

(27) Secco, E. A.; Worth, G. G., Infrared spectra of unannealed and of annealed Cu4(OH)6(NO3)2. *Canadian Journal of Chemistry* **1987,** 65, (10), 2504-2508.

(28) Thanh, N. T.; Maclean, N.; Mahiddine, S., Mechanisms of nucleation and growth of nanoparticles in solution. *Chem Rev* **2014,** 114, (15), 7610-30.

(29) Poul, L.; Jouini, N.; Fiévet, F., Layered Hydroxide Metal Acetates (Metal = Zinc, Cobalt, and Nickel): Elaboration via Hydrolysis in Polyol Medium and Comparative Study. *Chemistry of Materials* **2000,** 12, (10), 3123-3132.

(30) Farraj, Y.; Grouchko, M.; Magdassi, S., Self-reduction of a copper complex MOD ink for inkjet printing conductive patterns on plastics. *Chem Commun (Camb)* **2015,** 51, (9), 1587-90.

(31) Yi, F.; DeLisio, J. B.; Nguyen, N.; Zachariah, M. R.; LaVan, D. A., High heating rate decomposition dynamics of copper oxide by nanocalorimetry-coupled time-of-flight mass spectrometry. *Chemical Physics Letters* **2017,** 689, 26-29.

(32) Carter, R. O.; Poindexter, B. D.; Weber, W. H., Vibrational spectra of copper formate tetrahydrate, copper formate dihydrate and three anhydrous forms of copper formate. *Vibrational Spectroscopy* **1991,** 2, (2), 125-134.

(33) Krishnan, B. S.; Ramanujam, P. S., Raman and infrared spectra of copper formate tetrahydrate. *Spectrochimica Acta Part A: Molecular Spectroscopy* **1972,** 28, (11), 2227-2231.

(34) Zhao, H. Y.; Wang, Y. F.; Zeng, J. H., Hydrothermal Synthesis of Uniform Cuprous Oxide Microcrystals with Controlled Morphology. *Crystal Growth & Design* **2008,** 8, (10), 3731-3734.

CHAPTER IV

Synthesis of Acetate-Intercalated Nickel-Copper Layered Double Hydroxides

■ Introduction

The findings of the hydrolysis reactions of only nickel acetate and copper acetate at 90 °C that produced nickel acetate hydroxide and copper oxide via copper acetate hydroxide, respectively (as discussed in Chapters II and III) made us motivated to investigate the reactions of nickel acetate and copper acetate mixtures in water. Herein, therefore, the chapter presents hydrolysis reactions of nickel acetate and copper acetate mixtures at various ratios at 90 °C without any second reactant or reagent such as bases or organics. It turned out that the reactions produced acetate-intercalated nickel-copper layered double hydroxides, $Ni_xCu_{1-x}(OAc)_{2-y}(OH)_y \cdot nH_2O$. The reactions up to the ratios of 6Ni:1Cu produced nickel-copper layered double hydroxides that were markedly copper-rich. While ratios higher than 7Ni:1Cu generated nickel-rich products. The significance of the hydrolysis reactions is that they were achieved without a second reactant or an organic solvent where water plays a role of a solvent and a reactant. Literature investigation reveals that low-temperature hydrolysis reactions of mixtures of copper acetate and nickel acetate without a second reactant or reagent can generate pure acetate-intercalated bimetallic nickel-copper layered double hydroxides (without formation of copper oxides) have not been published, so far.

The important feature of bimetallic layered double hydroxides, $M_1M_2(A)_{2-x}(OH)_x \cdot nH_2O$ (where M_1 and M_2 are metals and A is an anion) is that they are excellent precursors for bimetallic oxides that are valuable for catalysis.[1] The bimetallic layered double hydroxides can be used directly as catalysts such as electrocatalysts for water splitting,[2] In addition, due to their anion exchange properties, they can be used to remove pollutants from water such as arsenate, phosphate, antimonate, and other heavy metal oxyanions. For instance, nickel-copper acetate hydroxide, $NiCu(OAc)_{0.9}(OH)_{3.1} \cdot 0.09H_2O$ showed high anion exchangeability with PO_4^{3-}, AsO_4^{3-}, and SeO_3^{2-}.[3] Bimetallic nickel-cooper acetate hydroxide's anion-exchange property can also be exploited for removing radioactive pollutants such as TcO_4^- from water; hence, they can be proven promising materials for treating nuclear wastewater of nuclear power plants.

Synthesis of bimetallic layered double hydroxides, $M_1M_2(A)_{2-x}(OH)_x \cdot nH_2O$ was first reported by Boehm, H. P *et al.*[4]. They described the reaction of ZnO with chromium nitrate aqueous solution produced $Zn_2Cr(NO_3)(OH)_6 \cdot 2H_2O$. Martina and co-workers investigated the *Boehm* synthesis extensively and advanced the process for several bimetallic layered double hydroxides.[4] Out of several syntheses Martina studied, two reactions were – (i) CuO in nickel nitrate aqueous solution produced was nickel-copper layered hydroxide, $CuNi(OH)_3(NO_3) \cdot nH_2O$ at room temperature around two weeks (however, they separated the product after 4 months), and (ii) NiO in copper nitrate solution generated $NiCu(OH)_3(NO_3) \cdot nH_2O$ at room temperature in three weeks. Although Martina advanced the *Boehm* process for accessing several 3*d* transition metal layered double hydroxides, it is a time-consuming process since it takes weeks to a month to produce a desired bimetallic layered double hydroxide.

Direct hydrolysis or hydrothermal reactions of mixtures of nickel acetate and a second divalent metal acetate such as zinc or copper acetate without any second reactant or organic solvents are found to be very few in the literature. The few studied reactions of mixtures of nickel acetate and zinc acetate without any second reactant in an autoclave at a relatively higher temperature (200

– 300 °C) produced nickel-zinc acetate hydroxides, $Ni_xZn_{1-x}(OAc)_x(OH)_{2-x}\cdot nH_2O$,[5, 6] that are acetate-intercalated nickel-zinc layered double hydroxides. Also, a microwave hydrothermal process was found to be produced nickel-zinc acetate hydroxides.[7] Other than the above reactions, hydrolysis reactions of nickel nitrate and manganese nitrate mixtures with urea were investigated that produced carbonate-intercalated nickel-manganese layered double hydroxides.[8]

Interestingly, the literature review shows that only one synthesis was reported for accessing nickel-copper acetate hydroxides by Koazi et al.[3] They claimed to prepare $NiCu(OAc)_{0.9}(OH)_{3.1}\cdot 0.09H_2O$ from hydrothermal reactions of a mixture of nickel acetate and copper acetate and hydrogen peroxide. They investigated the hydrothermal reactions with and without H_2O_2 in an autoclave at 125 °C; however, they could not get pure phases of nickel-copper layered double hydroxides. Since the reactions produced either Cu_2O or CuO alongside the nickel-copper layered double hydroxides. In addition, in the previous chapter (Chapter III), we show that copper acetate hydrolysis at 90 °C in simple a screw cap pyrex-jar can produce copper acetate hydroxide that decomposed to CuO under hydrothermal conditions. Hence, at 125 °C in an autoclave, the formation of CuO or Cu_2O phases beside nickel-copper acetate hydroxide is unavoidable in the hydrolysis of a mixture of nickel acetate and copper acetate, even the addition of H_2O_2 may not stop the formation of copper oxides. While Martina and co-workers reported a synthesis of nickel-copper hydroxy nitrate.[4] As mentioned earlier, Martina employed the *Boehm* process, which is a time-consuming method – if that method is adopted for preparing nickel-copper acetate hydroxide, it would likely require weeks to prepare a nickel-copper acetate hydroxide.

Therefore, there is a need to develop new synthesis routes or advance the existing routes for preparing nickel-copper layered double hydroxides, $Ni_xCu_{1-x}(OAc)x(OH)_{2-x}\cdot nH_2O$. The present work addresses the need since it presents a straightforward and inexpensive route for synthesizing pure phases of acetate-intercalated nickel-copper layered double hydroxides. In the current work, hydrolysis reactions of only mixtures of nickel acetate and copper acetate (without any second

reactant) involved a low temperature of 90 °C that generated nickel-copper acetate hydroxides. The low temperature facilitates avoiding the formation of copper oxides in the hydrothermal process, which addresses the issue faced by Koazi et al.[3] Additionally, the present investigation discloses a discovery of unusual dependencies of nickel to copper contents (Ni_xCu_{1-x}) in the produced nickel-copper acetate hydroxides to the starting ratios of the reactants (nickel acetate and copper acetate) in hydrolysis reactions. The equimolar ratio (1:1) of nickel to copper acetate produced copper-rich products. Even higher nickel to copper acetate ratios such as 6:1, 4:1, 3:1, and 2:1 interestingly generated copper-rich products. While a ratio 7Ni:1Cu generated almost 1:1 nickel-copper product and ratios higher than 7Ni:1Cu such as 9Ni:1Cu and 50Ni:1Cu produced nickel-rich products. Further, investigating the hydrolysis reaction of a nickel and copper acetate mixture with silica pellets catalysts-supports showed that the hydrolysis process deposited a nickel-copper acetate hydroxide onto silica catalysts-supports. The nickel-copper acetate hydroxide decorated catalysts-supports can readily be converted to a corresponding two-phasic nickel oxide-copper oxides, NiO-CuO decorated silica catalyst-supports upon pyrolysis.

■ Experimental

Nickel acetate tetrahydrate, $Ni(OAc)_2 \cdot 4H_2O$ (Fisher Scientific), and copper acetate monohydrate, $Cu(OAc)_2 \cdot H_2O$ (Baker Analyzed reagent) were used directly without further purification (where OAc stands for acetate, CH_3COO^-). Deionized water (DI) was used as a solvent for all the reactions. Mixtures of nickel acetate and copper acetate (as mentioned in Table 1) were dissolved in 50g of deionized water in 100 mL screw-cap Pyrex bottles and heated in an oven at 90 °C. Total mmol of nickel acetate and copper acetate in all the reactions were the same. For all reactions, the products started appearing within one hour. After 24 hours, the reactions were stopped, and the products were isolated and washed thoroughly by deionized until the wash water read zero in a conductivity meter. Supporting Figures S1 presents camera pictures of the products that show their colors. ATR-FTIR spectroscopy, Thermogravimetric, Elemental, and X-ray powder

diffraction analysis characterized all the reaction products. Scheme 1 is the general reaction for hydrolysis of nickel acetate and copper acetate mixtures to synthesize nickel-copper acetate hydroxide. Information on the reactions and their products is tabulated in Table 1.

$$a\ Ni(OAc)_{2\,(aq)} + b\ Cu(OAc)_{2\,(aq)} \longrightarrow Ni_xCu_{1-x}(OAc)_y(OH)_{2-y}\cdot nH_2O_{\,(s)}$$

Scheme 1: Hydrolysis reaction of nickel and copper acetates without additional reactant or reagent. Where a and b stand for moles of nickel acetate and copper acetate, respectively.

Table 1: Hydrolysis reactions of various mixtures of nickel acetate and copper acetate at 90 °C for 24 hours and their products

Ratio of the Reactants (Ni : Cu)	a (mmol of nickel)	b (mmol of copper)	Products	Mass of the products (g)
1:9	2.25	20.25	$Ni_{0.04}Cu_{0.96}(OAc)_{0.51}(OH)_{1.49}\cdot 0.54H_2O$	0.301
1:3	5.63	16.87	$Ni_{0.10}Cu_{0.90}(OAc)_{0.51}(OH)_{1.49}\cdot 0.40H_2O$	0.420
1:2	7.5	15	$Ni_{0.13}Cu_{0.87}(OAc)_{0.50}(OH)_{1.50}\cdot 0.20H_2O$	0.343
1:1	11.25	11.25	$Ni_{0.22}Cu_{0.78}\,(OAc)_{0.51}\,(OH)_{1.49}\cdot 0.43H_2O$	0.521
2:1	15	7.5	$Ni_{0.33}Cu_{0.67}(OAc)_{0.51}(OH)_{1.49}\cdot 0.43H_2O$	0.565
3:1	16.87	5.63	$Ni_{0.39}Cu_{0.61}(OAc)_{0.50}(OH)_{1.50}\cdot 0.33H_2O$	0.593
4:1	18.00	4.50	$Ni_{0.42}Cu_{0.58}(OAc)_{0.52}(OH)_{1.48}\cdot 0.31H_2O$	0.329
6:1	19.29	3.21	$Ni_{0.46}Cu_{0.54}(OAc)_{0.47}(OH)_{1.53}\cdot 0.24H_2O$	0.348
7:1	19.69	2.81	$Ni_{0.51}Cu_{0.49}(OAc)_{0.44}(OH)_{1.56}\cdot 0.28H_2O$	0.368
9:1	22.25	2.25	$Ni_{0.59}Cu_{0.41}(OAc)_{0.51}(OH)_{1.49}\cdot 0.48H_2O$	0.343
50:1	22.055	0.456	$Ni_{0.78}Cu_{0.22}(OAc)_{0.47}(OH)_{1.53}\cdot 0.45H_2O$	0.147

Table 2: Following names for all the synthesized products will be used in the chapter for simplicity

Products	Name
$Ni_{0.04}Cu_{0.96}(OAc)_{0.51}(OH)_{1.49}\cdot 0.54H_2O$	$Ni_{0.04}Cu_{0.96}$ acetate hydroxide
$Ni_{0.10}Cu_{0.90}(OAc)_{0.51}(OH)_{1.49}\cdot 0.40H_2O$	$Ni_{0.10}Cu_{0.90}$ acetate hydroxide
$Ni_{0.13}Cu_{0.87}(OAc)_{0.50}(OH)_{1.50}\cdot 0.20H_2O$	$Ni_{0.13}Cu_{0.87}$ acetate hydroxide
$Ni_{0.22}Cu_{0.78}(OAc)_{0.51}(OH)_{1.49}\cdot 0.43H_2O$	$Ni_{0.22}Cu_{0.78}$ acetate hydroxide
$Ni_{0.33}Cu_{0.67}(OAc)_{0.51}(OH)_{1.49}\cdot 0.43H_2O$	$Ni_{0.33}Cu_{0.67}$ acetate hydroxide
$Ni_{0.39}Cu_{0.61}(OAc)_{0.50}(OH)_{1.50}\cdot 0.33H_2O$	$Ni_{0.39}Cu_{0.61}$ acetate hydroxide
$Ni_{0.42}Cu_{0.58}(OAc)_{0.52}(OH)_{1.48}\cdot 0.31H_2O$	$Ni_{0.42}Cu_{0.58}$ acetate hydroxide
$Ni_{0.46}Cu_{0.54}(OAc)_{0.47}(OH)_{1.53}\cdot 0.24H_2O$	$Ni_{0.46}Cu_{0.54}$ acetate hydroxide
$Ni_{0.51}Cu_{0.49}(OAc)_{0.44}(OH)_{1.56}\cdot 0.28H_2O$	$Ni_{0.51}Cu_{0.49}$ acetate hydroxide
$Ni_{0.59}Cu_{0.41}(OAc)_{0.51}(OH)_{1.49}\cdot 0.48H_2O$	$Ni_{0.59}Cu_{0.41}$ acetate hydroxide
$Ni_{0.78}Cu_{0.22}(OAc)_{0.47}(OH)_{1.53}\cdot 0.45H_2O$	$Ni_{0.78}Cu_{0.22}$ acetate hydroxide

Hydrolysis of $2Ni(OAc)_2$ and $1Cu(OAc)_2$ with silica pellets:

15.01 mmol (3.842 g) of hydrated nickel acetate, $Ni(OAc)_2\cdot 4.4H_2O$ (Alfa Aesar), and 7.508 mmol (1.499 g) of copper acetate monohydrate, $Cu(OAc)_2\cdot H_2O$ (Baker Analyzed) were dissolved in 50.024 g of water. 10.044 g silica pellets (Alfa Aesar) were introduced to the above solution. The solution with silica pellets was heated at 90 °C, which converted the white silica pellets into bluish-green colored silica pellets (Figure 21). After drying at 90 °C, the mass of the bluish-green silica pellets was 10.872 g. The deposited bluish-green material is a nickel-copper acetate hydroxide with the formula of $Ni_{0.55}Cu_{0.45}(OAc)_{0.30}(OH)_{1.70}\cdot nH_2O$ confirmed by the Microwave Plasma Atomic Emission Spectroscopy (MP-AES) experiment for nickel and copper and elemental analysis for carbon.

Characterization:

Microwave Plasma Atomic Emission Spectroscopy (MP-AES): All the reaction products were digested in concentrated HCl and diluted. Agilent 4200 MP-AES instrument was used to acquire the nickel and copper content of the products. The MP-AES experimental results for all the hydrolysis products are presented in Table S4(a) – S4(k) in the Supporting Information.

Elemental Analysis for Carbon: The hydrolysis products were analyzed for carbon by a LECO CN 628 instrument at the Soil, Water, and Forage Analytical Laboratory, Oklahoma State University, Stillwater, Oklahoma.

Attenuated Total Reflectance FTIR (ATR-FTIR): ATR-FTIR spectra of the hydrolysis products were collected using a Nicolet iS50. The range of the spectra was 525 to 4000cm^{-1}.

Thermogravimetric Analysis (TGA): TGA of all the products was performed using a Perkins Elmer TGA 4000 instrument. All TGA experiments were done under air at a heating rate of 5 °C/ min.

Differential Scanning Calorimeter (DSC): A Pekins Elmer DSC 4000 instrument was used for the DSC experiments. All the experiments were done at a 5 °C/min heating rate from 30 to 425 °C. Aluminum pans were used for the experiments.

X-ray powder diffraction (XRD): XRD patterns were collected using a Bruker Discover 8 instrument at Helmrich Research Center, Tulsa, Oklahoma. The Brag angles for all the experiments were 10° to 70° with intervals of 0.01°. The operating setting of the instrument was 40kV and 40mA. The X-ray source was copper K_{α}, 1.5406 Å.

Particle size distribution (PSD) analysis: Particle size distribution analysis during the hydrolysis reactions was explored using a Malvern HPPS instrument. The reaction solutions were

collected in polystyrene cuvettes, and the PSD experiments were performed at 25 °C. PSD analysis reveals the hydrodynamic sizes of the particles.

Scanning Electron Microscopy (SEM): SEM pictures were acquired using an FEI Quanta 600 field emission gun ESEM instrument at the Microscopy Lab, Oklahoma State University, Stillwater, Oklahoma. The SEM images were acquired at 20 to 25 kV at various magnifications.

■ Results and Discussion

The hydrolysis reactions of nickel and copper acetate mixtures showed interesting and unusual trends of nickel-copper contents (Ni_xCu_{1-x}) in products to nickel acetate and copper acetate ratios as reactants (Figure 1). An equimolar reaction (1:1) and even nickel-rich reactions such as 6:1, 4:1, 3:1, and 2:1 of nickel acetate to copper acetate produced copper-rich products. The copper-rich products showed liner dependency (navy blue line) to the mole fractions of copper acetate as reactants. Theoretically, if we solved the navy blue line ($y=0.608x+0.461$) for $y<0.461$, the x value would be negative, which is practically impossible. In other words, theoretically, nickel-rich products (higher nickel content than $Ni_{0.53}Cu_{0.47}$) should not be possible by the hydrolysis reactions if they follow the linear trend (navy blue line). However, experimentally, it turned out that there is a breakthrough point in the linearity (navy blue line) after 6Ni:1Cu and started a new liner dependency (dark green line) of Ni:Cu content in the products to the ratio of the reactants. At 7Ni:1Cu, the hydrolysis reaction produced almost 1Ni:1Cu nickel-copper acetate hydroxide ($Ni_{0.51}Cu_{0.49}$ acetate hydroxide). While ratios higher than 7Ni:1Cu generated nickel-rich products, such as the 9Ni:1Cu reaction produced $Ni_{0.59}Cu_{0.41}$ acetate hydroxide and the 50Ni:1Cu reaction generated $Ni_{0.78}Cu_{0.22}$ acetate hydroxide. Interestingly, the breakthrough point (connection point of the two lines) is at the 7Ni:1Cu reaction, where the nickel composition to copper is $Ni_{0.51}Cu_{0.49}$. This suggests a new phase of the nickel-copper acetate hydroxides started to form at a nickel-rich

composition. In other words, the two-liner dependencies may indicate the formation of two distinct phases of nickel-copper acetate hydroxides.

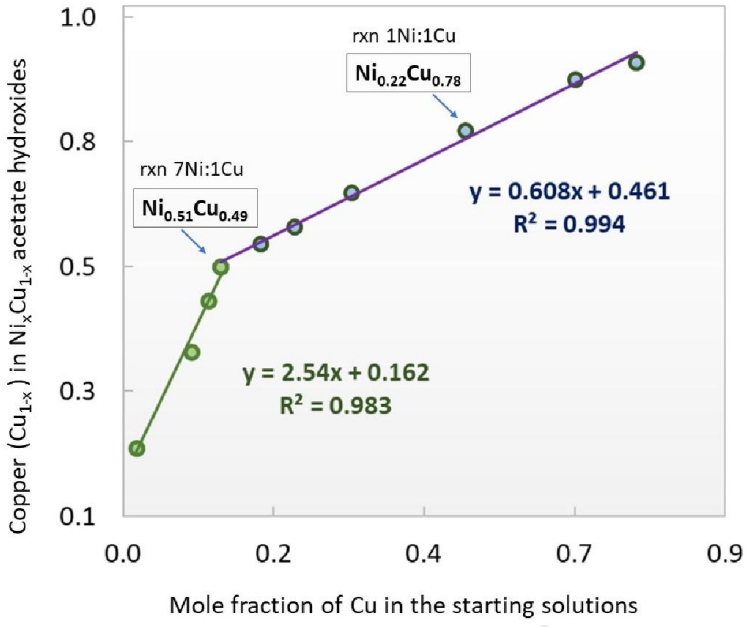

Figure 1: Copper (Cu_{1-x}) in the Ni_xCu_{1-x} acetate hydroxides against the mole fraction of copper in the reaction solutions of hydrolysis of nickel acetate and copper acetate mixtures at various ratios.

$$OAc^-_{(aq)} + H_2O \rightleftharpoons OAcH + OH^-_{(aq)}$$

$$Ni(H_2O)_6^{2+}{}_{(aq)} + Cu(H_2O)_6^{2+}{}_{(aq)} \xrightarrow[OAc^-,\ OH^-]{90^oC} Ni_zCu_{1-z}(OAc)_{2-b}(OH)_b \cdot aH_2O\ _{(s)}$$

(Nucleated Particles)

$$Ni_zCu_{1-z}(OAc)_{2-b}(OH)_b \cdot aH_2O\ _{(s)} \underset{Ni^{2+},\ Cu^{2+}}{\overset{90^oC,\ 24\ h}{\rightleftharpoons}} Ni_xCu_{1-x}(OAc)_{2-y}(OH)_y \cdot nH_2O\ _{(s)}$$

(Nucleated Particles) (Products)

Scheme 2: Possible reactions involved in the hydrolysis of nickel acetate and copper acetate mixtures at 90 °C.

To understand the unusual trends mentioned above, we should look at the reactions involving the hydrolysis reactions of nickel acetate and copper acetate mixtures at 90 °C. The possible reactions involved in the hydrolysis reactions can be expressed in Scheme 2.

Firstly, acetate ions with water reach an equilibrium that shifts to the right at 90°C, which results in the formation of OH^- ions. The in-situ generated OH^- ions are immediately consumed by $Ni(H_2O)_6^{2+}$ and $Cu(H_2O)_6^{2+}$ that start nucleation and generate nucleated particles. The nucleated particles, $Ni_zCu_{1-z}(OAc)_{2-b}(OH)_b \cdot aH_2O$, eventually grow to the respective final products depending on the starting ratio of the nickel to copper acetate. The particle size analysis (discussed later, Figure 17) and observations of the reactions confirm that the reaction solution remains clear within the first 20-25 minutes. After 20-25 minutes, the reaction solutions were getting cloudier, supporting the initial nucleation and growth of the nucleated particles to final products. The growth of the nucleated particles to the final products very likely involves two processes simultaneously – (i) autocatalytic rapid growth of nucleated particles and (ii) ion exchange of Ni^{2+}/Cu^{2+} with the growing particles.

Now let's look at the critical questions – (i) why the reactions (copper-rich, equimolar, and nickel-rich reactions up to 6Ni:1Cu) do produce copper-rich products, and (ii) while at very high ratios of Ni:Cu, the reactions produced nickel rich products. There may be a few possible reasons for the trends of Ni:Cu in the products to the ratio of the reactants.

(i) *Copper ions are more acidic than nickel:* The pKa of hexaaqua copper(II) ions, $Cu(H_2O)_6^{2+}$ is 7.5 while for hexaaqua nickel(II) ions is $Ni(H_2O)_6^{2+}$ is 9.9.[9] This means that $Cu(H_2O)_6^{2+}$ ions are more acidic than $Ni(H_2O)_6^{2+}$ ions. Therefore, as the copper ions are more acidic than nickel ions, the nucleation step (Scheme 2) consumes the in-situ formed OH^- ions and generates copper-rich nucleated particles. Experimentally we found that direct precipitation of 1:1 nickel acetate and copper acetate with 1 equivalent NaOH produced copper-rich products,

$Cu_{0.95}Ni_{0.05}(OAc)_x(OH)_{2-x}\cdot nH_2O$ (MP-AES analysis, TGA plot, and FTIR spectrum are at Supporting Table S2 and Figure S2). This experiment also supports the concept of the formation of copper-rich nucleated particles in hydrolysis reactions.

(ii) *Ion exchange of copper/nickel ions with the nickel/copper ions of the growing particles:* The copper-rich nucleated particles eventually grow as copper-rich products (up to 6Ni:1Cu reaction) and nickel-rich products (7Ni:1Cu and higher ratios than 7Ni:1Cu). It is very likely that the growth step simultaneously involves growth and the ion exchange process (Ni^{2+}/Cu^{2+} in solution with the Cu^{2+}/Ni^{2+} of growing solid phase) as presented in Scheme 3. The ion exchange process reaches an equilibrium that yields the final products. Therefore, the hydrolysis reactions generate thermodynamic products.

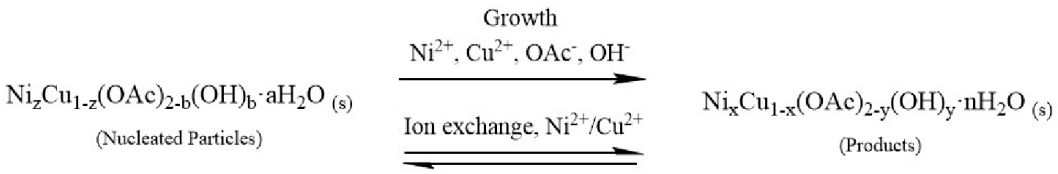

Scheme 3: Simultaneous growth and ion exchange process during the growth of nucleated particles to the final products of nickel-copper acetate hydroxides.

The copper-rich reactions such as 1Ni:2Cu and 1Ni:3Cu produce $Ni_{0.13}Cu_{0.87}$ and $Ni_{0.10}Cu_{0.90}$ acetate hydroxide, respectively. The products have very high copper contents to the ratios of copper to nickel acetate as reactants. This is due to the synergy of copper-rich nucleated particles formation and ion exchange of Cu^{2+} in reaction solution with Ni^{2+} of the growing-solid phase. Since the copper-rich reaction solutions have a higher amount of Cu^{2+} than Ni^{2+}, the ion exchange during the growth step results in a very high content of copper in the products. While in nickel-rich reactions, with the increasing ratios of nickel to copper acetate in the reactions, besides the formation of increasing nickel content nucleated particles, the ion exchange equilibria during the growth step facilitate the generation of growing nickel content products. However, the nickel-

rich reactions' products are still copper-rich within the reactant ratios from 1Ni:1Cu to 6Ni:1Cu. For example, the 2Ni:1Cu and 6Ni:1Cu reactions produce $Ni_{0.33}Cu_{0.67}$ and $Ni_{0.46}Cu_{0.54}$ acetate hydroxide, respectively.

Higher ratios than 6Ni:1Cu reaction, such as reaction 7Ni:1Cu generate almost 1:1 nickel to copper product and 9Ni:1Cu and 50Ni:1Cu produced nickel-rich products. This can also be explained in terms of nucleation and growth of nucleated particles accompanying the ion exchange process, as discussed above. In the cases of high and very ratios (7:1 or 9:1 and 50:1) of nickel acetate to copper acetate reactions – (i) the nucleated particles have much higher nickel content (i.e., critical content of nickel for nickel-rich products) compared to the other reactions of 1Ni:1Cu up to 6Ni:1Cu, and (ii) simultaneous ion exchange favor the exchange of Ni^{2+} ions in the reaction solutions (that are very much excess in the reaction solutions) with Cu^{2+} of nucleated/growing solid phase. Therefore, since the nucleated particles have the critical nickel content for nickel-rich products and the reaction solutions have excess Ni^{2+}, ion exchange results in nickel-rich products. As a result, the high and very high ratios of nickel to copper (7Ni:1Cu, 9Ni:1Cu, and 50Ni:1Cu) produced nickel-rich products that follow a new linear trend to ratios of the reactants, as shown by the green linear line in Figure 1.

To support the ion exchange mechanism during the growth of the nucleated particles to the final products, we performed ex-situ ion exchange experiments with pure nickel acetate hydroxide, $Ni(OAc)_{0.28}(OH)_{1.72}\cdot 0.25H_2O$ (solid phase) with an aqueous solution of Cu^{2+} (copper acetate). The ion exchange experiments (Supporting Table S1(a-b)) confirm that Cu^{2+} ions undergo ion exchange with Ni^{2+} of the solid nickel acetate hydroxide. Like the nickel acetate hydroxide phase, it is expected pure copper acetate hydroxide, $Cu(OAc)_x(OH)_{2-x}\cdot nH_2O$ will involve in the ion exchange process with aqueous Ni^{2+} ions, and a nickel-copper acetate hydroxide, $Ni_xCu_{1-x}(OAc)_y(OH)_{2-y}\cdot nH_2O$ phase will undergo ion exchange with aqueous Ni^{2+} and Cu^{2+} ions.

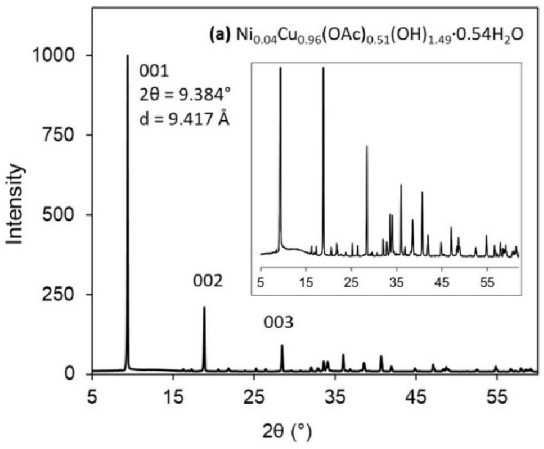
(a) $Ni_{0.04}Cu_{0.96}(OAc)_{0.51}(OH)_{1.49}\cdot 0.54H_2O$
001
2θ = 9.384°
d = 9.417 Å
002
003
Intensity
2θ (°)

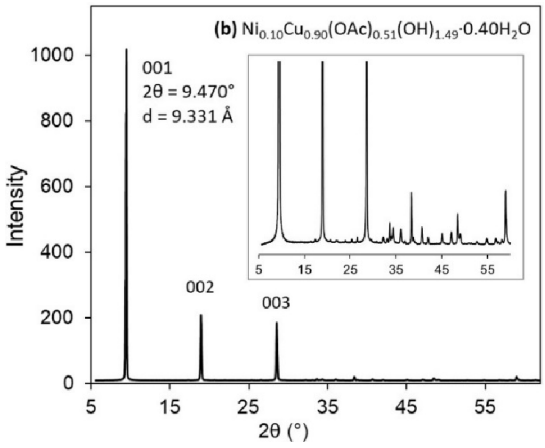
(b) $Ni_{0.10}Cu_{0.90}(OAc)_{0.51}(OH)_{1.49}\cdot 0.40H_2O$
001
2θ = 9.470°
d = 9.331 Å
002
003
Intensity
2θ (°)

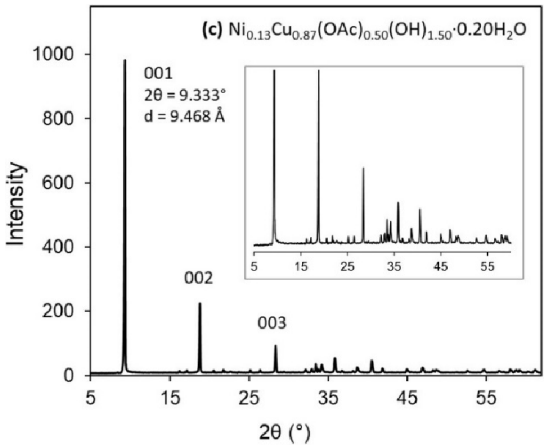
(c) $Ni_{0.13}Cu_{0.87}(OAc)_{0.50}(OH)_{1.50}\cdot 0.20H_2O$
001
2θ = 9.333°
d = 9.468 Å
002
003
Intensity
2θ (°)

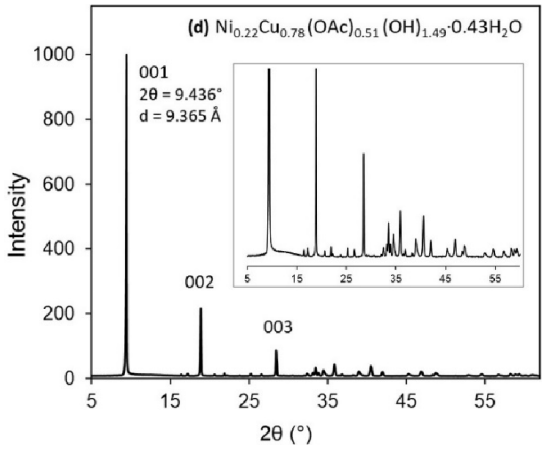
(d) $Ni_{0.22}Cu_{0.78}(OAc)_{0.51}(OH)_{1.49}\cdot 0.43H_2O$
001
2θ = 9.436°
d = 9.365 Å
002
003
Intensity
2θ (°)

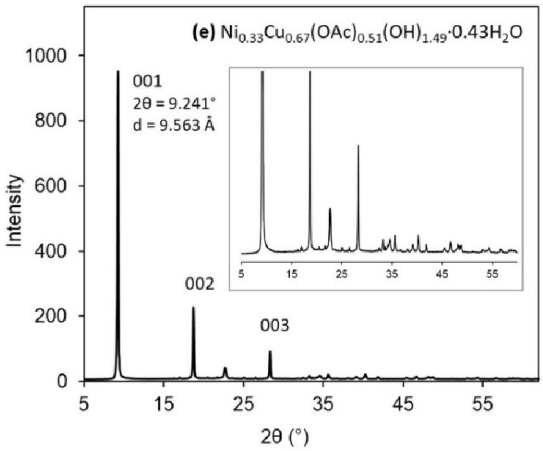
(e) $Ni_{0.33}Cu_{0.67}(OAc)_{0.51}(OH)_{1.49}\cdot 0.43H_2O$
001
2θ = 9.241°
d = 9.563 Å
002
003
Intensity
2θ (°)

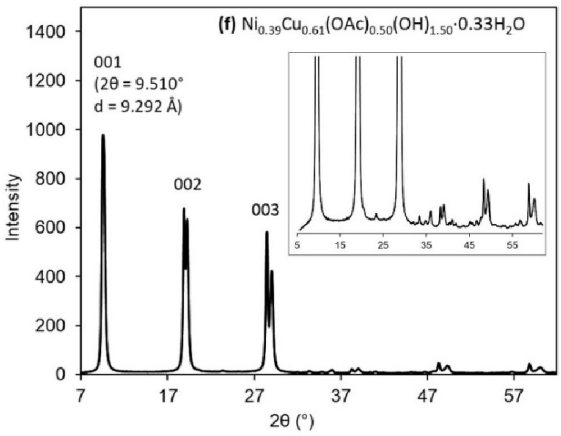
(f) $Ni_{0.39}Cu_{0.61}(OAc)_{0.50}(OH)_{1.50}\cdot 0.33H_2O$
001
(2θ = 9.510°
d = 9.292 Å)
002
003
Intensity
2θ (°)

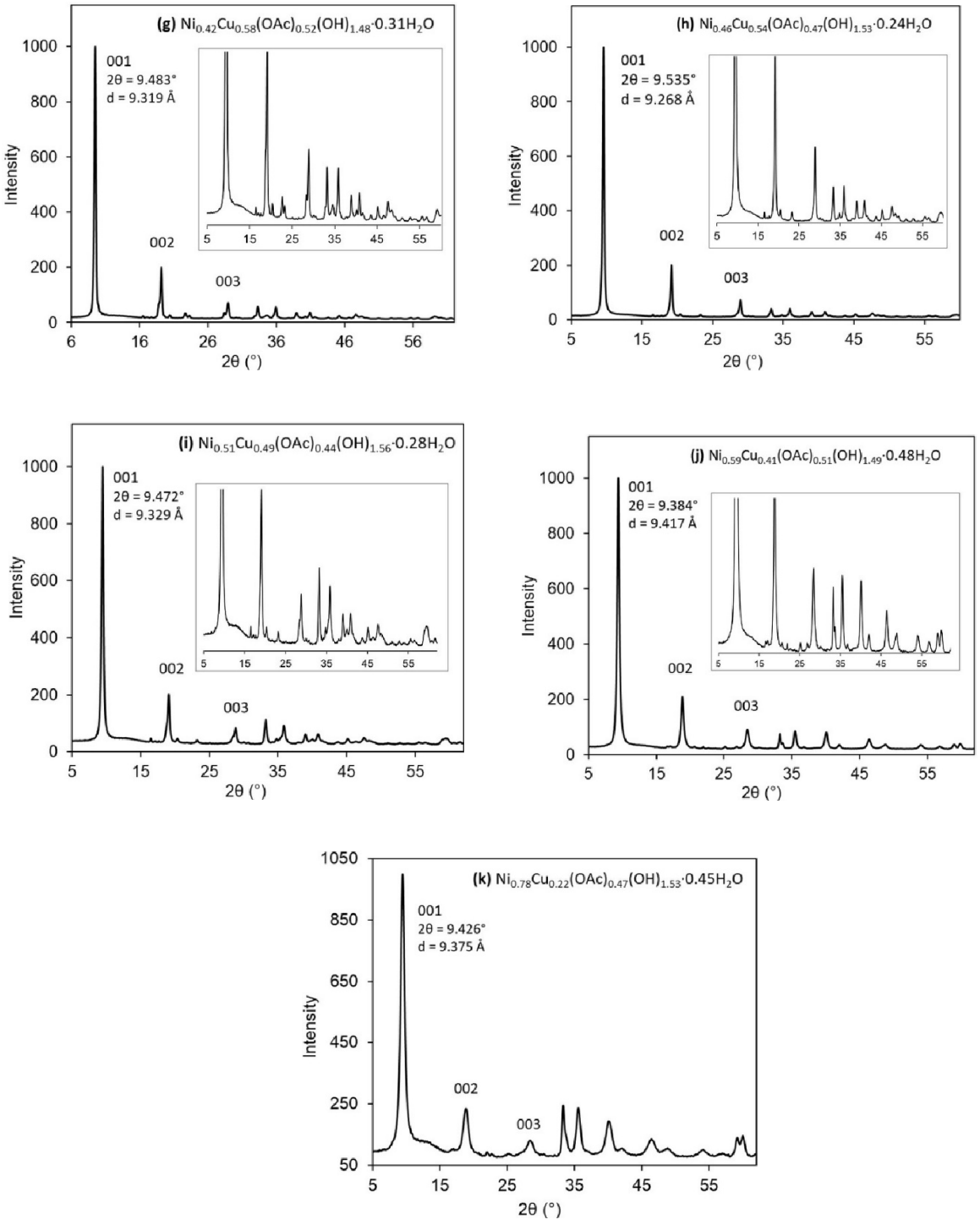

Figure 2: XRD patterns of nickel-copper acetate hydroxides – (a) $Ni_{0.04}Cu_{0.96}$ (b) $Ni_{0.10}Cu_{0.90}$ (c) $Ni_{0.13}Cu_{0.87}$ (d) $Ni_{0.22}Cu_{0.78}$ (e) $Ni_{0.33}Cu_{0.67}$ (f) $Ni_{0.39}Cu_{0.61}$ (g) $Ni_{0.42}Cu_{0.58}$ (h) $Ni_{0.46}Cu_{0.54}$ (i) $Ni_{0.51}Cu_{0.49}$ (j) $Ni_{0.59}Cu_{0.41}$ and (k) $Ni_{0.78}Cu_{0.22.}$ Insets are zoom-in XRD patterns to show peaks at higher angles.

One of the signature features of an XRD pattern of a layered structure is that it has a sharp reflection at the smaller angles (2θ is usually 5-15°) and weak reflections at higher angles.[10] X-ray powder diffraction patterns of all the nickel-copper acetate hydroxides as presented in Figure 2 (a) – (k) have this feature confirming that they are layered materials. Besides, the first peaks in the XRD patterns, the *001* planes, are stronger than the rest of the peaks, which also characterize the hydrolysis products as layered double hydroxides.[10-12] Acetate-intercalated nickel-copper layered double hydroxides adopt a monoclinic lattice structure, while acetate-intercalated pure nickel layered hydroxide adopts a hexagonal lattice phase.[3, 10] We define the first reflection as *001* like Hall *et al.* and L. Poul and his coworkers, which is equal to the c parameter of the lattice ($c = d_{001}$) and the interlayer distance between the layers of the layered structure.[10, 13] Literature also shows that the first sharp reflection can be termed as 003 planes, where the lattice parameter c is defined as $d_{003} = c/3$. By defining $c = d_{001}$, we determine the distances of the interlayers of the nickel-copper acetate hydroxides of our work using the 001 reflections and Bragg's law ($2d_{001} \sin\theta = n\lambda$) that are tabulated in Table 3. There is no particular trend in the interlayer distances with respect to nickel-copper content in the materials. The sharp 001 reflections in all the XRD patterns also suggest that the layered structures are preferentially grown along the c-axis of the lattice. The rest of the reflections of the XRD patterns can be assigned to their respective Miller Indices according to the calculated XRD pattern of copper acetate hydroxide, $Cu_2(OH)_2(OAc)\cdot H_2O$ crystal structure, i.e., an acetate-intercalated layered copper hydroxide structure built up by a monoclinic lattice.[14] The reflections' 2θ positions of all XRD patterns, their Miller Indices, and d-spacing are tabulated in Supporting Tables S3 (a) – (k) as in the order of Figure 2(a)-(k).

The XRD peaks of copper-rich products are symmetric and have no selective peak broadenings suggesting that the stacking of the layers in the layered structure is not turbostratic or disordered.[10,13] While the 001 peaks of the nickel-rich products are broader and a little bit asymmetric suggesting turbostratic stacking of the layers. Very copper-rich products such as

$Ni_{0.04}Cu_{0.96,}$ $Ni_{0.10}Cu_{0.90}$, $Ni_{0.13}Cu_{0.87}$, and $Ni_{0.22}Cu_{0.78}$ acetate hydroxides (Figure 2(a)-(d)) have very sharp peaks at both smaller and higher angles, indicating that they consist of large domains of nano-crystallites grains. While with an increasing nickel content in the products, the XRD peaks (Figure 2(f)-(k)) become broader, which may suggest the higher nickel content products have smaller crystallite sizes. Alternatively, the peak broadening with the increasing nickel content can be attributed to the increased lattice strain, suggesting that higher nickel content may cause more lattice strain.

Table 3: Interlayer distances of nickel-copper acetate hydroxides

Nickel-copper acetate hydroxides	2θ of 001 reflections (°)	Interlayer distances (Å)
$Ni_{0.04}Cu_{0.96}(OAc)_{0.51}(OH)_{1.49}\cdot 0.54H_2O$	9.384	9.417
$Ni_{0.10}Cu_{0.90}(OAc)_{0.51}(OH)_{1.49}\cdot 0.40H_2O$	9.470	9.331
$Ni_{0.13}Cu_{0.87}(OAc)_{0.50}(OH)_{1.50}\cdot 0.20H_2O$	9.333	9.468
$Ni_{0.22}Cu_{0.78}(OAc)_{0.51}(OH)_{1.49}\cdot 0.43H_2O$	9.436	9.365
$Ni_{0.33}Cu_{0.67}(OAc)_{0.51}(OH)_{1.49}\cdot 0.43H_2O$	9.241	9.563
$Ni_{0.39}Cu_{0.61}(OAc)_{0.50}(OH)_{1.50}\cdot 0.33H_2O$	9.510	9.292
$Ni_{0.42}Cu_{0.58}(OAc)_{0.52}(OH)_{1.48}\cdot 0.31H_2O$	9.483	9.319
$Ni_{0.46}Cu_{0.54}(OAc)_{0.47}(OH)_{1.53}\cdot 0.24H_2O$	9.535	9.268
$Ni_{0.51}Cu_{0.49}(OAc)_{0.44}(OH)_{1.56}\cdot 0.28H_2O$	9.472	9.329
$Ni_{0.59}Cu_{0.41}(OAc)_{0.51}(OH)_{1.49}\cdot 0.48H_2O$	9.384	9.417
$Ni_{0.78}Cu_{0.22}(OAc)_{0.47}(OH)_{1.53}\cdot 0.45H_2O$	9.426	9.375

Figure 3-5 presents the Attenuated Total Reflectance FTIR (ATR-FTIR) spectra of all the hydrolysis products (nickel-copper acetate hydroxides) that univocally confirm the presence of

acetate (CH_3COO^-) in them. All the FTIR spectra show intense peaks for acetate in the range of 1390 – 1410 cm^{-1} (symmetric stretching of -COO) and 1540 – 1560 cm^{-1} (asymmetric stretching of -COO). While the bands at 1368 – 1387 cm^{-1} arise due to the -CH_2- stretching of the acetate group.[15] Carbon content (Table 9) and thermogravimetric analysis further support that the products have acetate (discussed later). Table 4 tabulates the FTIR bands of acetate groups of all the products. The symmetric and asymmetric stretching modes of acetate vary with respect to nickel-copper contents in the products. The symmetric stretching modes of the nickel-rich products are within 1398-1400 cm^{-1}, which shifts to higher values to 1405-1411 cm^{-1} for copper-rich products (except $Ni_{0.46}Cu_{0.54}$ and $Ni_{0.42}Cu_{0.58}$, these two products have stretching modes at 1390 cm^{-1}). While the asymmetric stretching modes of the nickel-rich products shift to lower values with increasing copper contents in the products (the shift is from 1568 to 1537 cm^{-1}). This shifting of the symmetric and asymmetric stretching bands reveals that the stretching modes of acetate are directly correlated to the coordination environment with the metal (nickel and copper) ions in the layered double hydroxides. While the differences between the symmetric and asymmetric bands of COO- are smaller than an uncoordinated acetate group in all the products, confirming the acetate groups are pseudo bridged with intercalated water molecules through hydrogen bonding. In fact, there are three distinct bands for all products for hydrogen-bonded -OH stretching at the range of 3200-3400 cm^{-1}, indicating three different hydrogen bonding between the interlayer water molecules and the layers of $Ni_xCu_{1-x}(OH)_{6-y}(OAc)_y$ octahedra.[16] These three hydrogen-bonded -OH stretching can be attributed to (i) Cu-OH…H_2O, (ii) Ni-OH…H_2O, and (iii) CH_3COO…HO-H. This establishes the presence of interlayer water molecules and further confirms the existence of hydrogen-bonded pseudo bridged acetate groups. TGA experiments excellently agree with the FTIR results as the TGAs of all the products show loss of water followed by dehydroxylation of OH- groups and decomposition of acetate groups.

The Ni_xCu_{1-x}-OH vibration (deformation/bending) modes of the products are assigned by the sharp bands from 644 – 657 cm^{-1} and 723 – 773 cm^{-1}.[16] Interestingly, if we present the Ni_xCu_{1-x}-O-H deformation/bending vibrations positions at 723 – 773 cm^{-1} against the copper content of the products (Figure 6), it turns out there is almost a linear correlation between them. Increasing copper content exhibit higher deformation/bending vibrations. While the other deformation/ bending modes at 644 – 657 cm^{-1} increase with the increasing nickel content; however, there is no clear correlation between them. The Ni_xCu_{1-x}-OH stretching modes were confirmed by sharp bands within the range of 3610 to 3630 cm^{-1}.[17] The tiny peaks at 1654 – 1691 cm^{-1} may arise due to scissoring (bending) modes of the interlayer water molecules. These scissoring bands of the interlayer water molecules are clearly observable in the copper-rich products, while in the nickel-rich products, they are kind of buried under the asymmetric starching of -COO of the acetate groups.

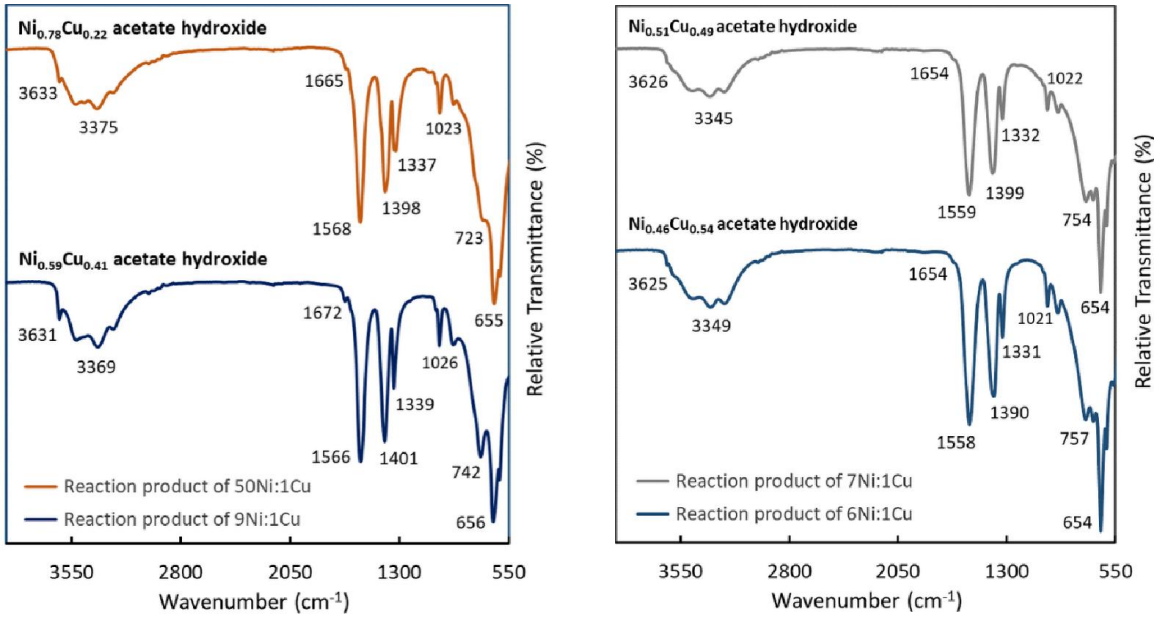

Figure 3: ATR-FTIR spectra of the products from hydrolysis of nickel-rich reactions; (left) 50:1 and 9:1, (right) 7:1 and 6:1 of nickel acetate to copper acetate.

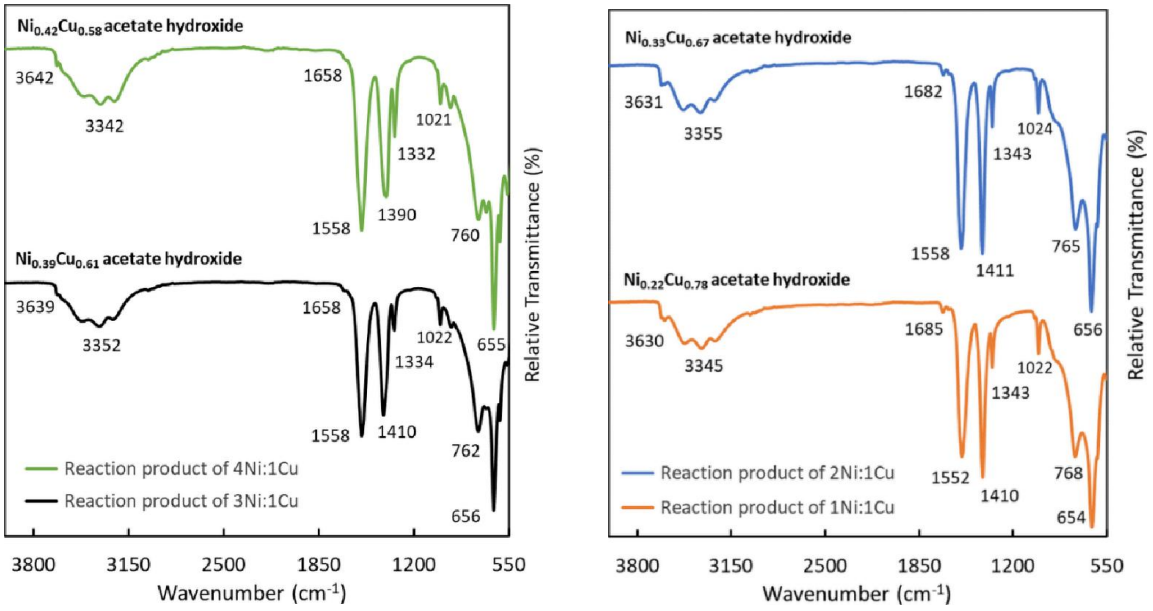

Figure 4: ATR-FTIR spectra of the hydrolysis products of (left) 4:1 and 3:1, (right) 2:1 and 1:1 of nickel acetate to copper acetate.

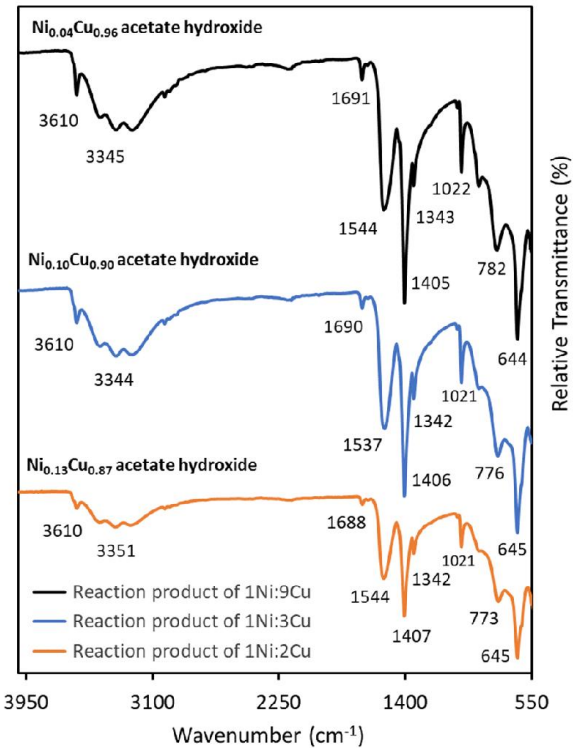

Figure 5: ATR-FTIR spectra of the products from hydrolysis of copper-rich reactions; 1:2, 1:3, and 1:9 of nickel acetate to copper acetate.

Table 4: Comparisons FTIR bands of -CH- stretching and symmetric and asymmetric stretching of -COO of the acetate group of nickel-copper acetate hydroxides

Nickel-copper acetate hydroxides	Acetate Bands		
	-CH- Stretching (cm^{-1})	-COO Symmetric Stretching (cm^{-1})	-COO Asymmetric Stretching (cm^{-1})
$Ni_{0.78}Cu_{0.22}$ acetate hydroxide	1337	1398	1568
$Ni_{0.59}Cu_{0.41}$ acetate hydroxide	1339	1401	1566
$Ni_{0.51}Cu_{0.49}$ acetate hydroxide	1332	1399	1559
$Ni_{0.46}Cu_{0.54}$ acetate hydroxide	1331	1390	1558
$Ni_{0.42}Cu_{0.58}$ acetate hydroxide	1332	1390	1558
$Ni_{0.39}Cu_{0.61}$ acetate hydroxide	1334	1410	1558
$Ni_{0.33}Cu_{0.67}$ acetate hydroxide	1343	1411	1558
$Ni_{0.22}Cu_{0.78}$ acetate hydroxide	1343	1410	1552
$Ni_{0.13}Cu_{0.87}$ acetate hydroxide	1342	1407	1544
$Ni_{0.10}Cu_{0.90}$ acetate hydroxide	1342	1406	1537
$Ni_{0.04}Cu_{0.96}$ acetate hydroxide	1343	1405	1544

Table 5: Comparisons of FTIR bands of Ni_xCu_{1-x}-OH deformation/bending, H-bonded -OH stretching (due to interlayer water molecules), Ni-OH stretching modes of nickel-copper acetate hydroxides

Nickel-copper acetate hydroxides	Ni_xCu_{1-x}-OH deformation/bending (cm^{-1})		H_2O scissoring (cm^{-1})	H-bonded -OH stretching (cm^{-1})	Ni-OH stretching (cm^{-1})
$Ni_{0.78}Cu_{0.22}$ acetate hydroxide	655	723	1665	3375	3633
$Ni_{0.59}Cu_{0.41}$ acetate hydroxide	656	742	1672	3369	3631
$Ni_{0.51}Cu_{0.49}$ acetate hydroxide	654	754	1654	3345	3626
$Ni_{0.46}Cu_{0.54}$ acetate hydroxide	654	757	1654	3349	3625
$Ni_{0.42}Cu_{0.58}$ acetate hydroxide	655	760	1658	3342	3642
$Ni_{0.39}Cu_{0.61}$ acetate hydroxide	656	762	1658	3352	3639
$Ni_{0.33}Cu_{0.67}$ acetate hydroxide	656	765	1682	3355	3631
$Ni_{0.22}Cu_{0.78}$ acetate hydroxide	654	768	1685	3345	3631
$Ni_{0.13}Cu_{0.87}$ acetate hydroxide	645	773	1688	3351	3610
$Ni_{0.10}Cu_{0.90}$ acetate hydroxide	645	776	1690	3344	3610
$Ni_{0.04}Cu_{0.96}$ acetate hydroxide	644	782	1691	3345	3610

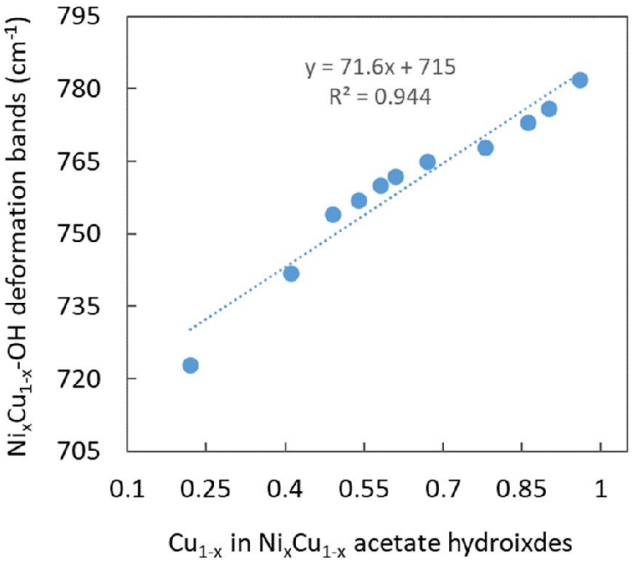

Figure 6: Ni_xCu_{1-x}-OH deformation (bending) vibrations bands (cm^{-1}) against Cu_{1-x} in the nickel-copper acetate hydroxides, $Ni_xCu_{1-x}(OAc)_y(OH)_{2-y}{\cdot}nH_2O$.

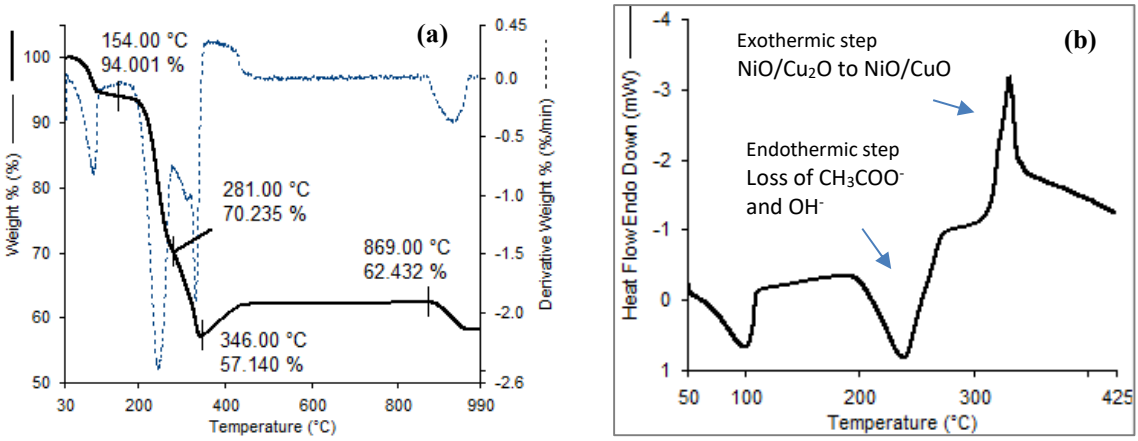

Figure 7: (a) Thermogravimetric analysis and (b) differential scanning calorimetry of $Ni_{0.22}Cu_{0.78}$ acetate hydroxide.

To enumerate the chemical formulas in conjunction with elemental analysis and understand the thermo-chemical events during heating of the nickel-copper acetate hydroxides, leading to their corresponding ceramic products (NiO/CuO), thermogravimetric and differential scanning calorimetric experiments were performed. Thermogravimetric analysis (TGA) traces of all the

nickel-copper acetate hydroxides are showcased in Figures 7-11. While Differential Scanning Calorimetry (DSC) plots of a few selected nickel-copper acetate hydroxides are presented in Figures 7(b) and 12.

Figure 7 presents a thermogravimetric analysis (TGA) and derivative TGA (dotted line) of $Ni_{0.22}Cu_{0.78}(OAc)_{0.51}(OH)_{1.49}\cdot 0.43H_2O$, the hydrolysis product of 1:1 nickel acetate and copper acetate. The first 6.00% mass loss up to 154 °C corresponds to dehydration of interlayer water molecules. The subsequent mass losses from 154 to 346 °C are due to the decomposition of acetate and hydroxyl groups.[10, 18] Both TGA and derivative TGA plots (dotted line) indicate that there are primarily two separate thermal decomposition events at 154 to 281 °C and 281 to 346 °C. The thermal events can be attributed to – (i) 154 to 281 °C: dehydroxylation of the hydroxyl groups and (ii) 281 to 346 °C: decomposition of the acetate groups. The mass increases after 346 °C to reach an elevated steady mass must be due to the oxidation of copper(I) oxide (Cu_2O) to copper (II) oxide (CuO). This confirms that during the decomposition of acetate that coordinated to copper (II) ions (Cu^{2+}) reduce Cu^{2+} to Cu^{+}, generating Cu_2O. To reduce Cu^{2+} to Cu^{+}, acetate ions become acetate radicals that, in turn, should be converted to ethane and CO_2. Similar phenomena of reducing Cu^{2+} to Cu_2O were also observed in the thermal decomposition of pure copper acetate hydroxide (discussed in Chapter III). In addition, the DSC of the $Ni_{0.22}Cu_{0.78}$ acetate hydroxide (Figure 7(b)) shows an exothermic step that starts at 310°C and ends at around 355°C, conforming an oxidation reaction of NiO/Cu_2O to NiO/CuO. This further supports that during thermal decomposition of Cu^{2+} species of the material reduce to Cu_2O before converting CuO. While the decomposition of acetate connected to nickel ions does not follow the chemistry of copper and acetate; instead, the acetate (OAc^{-}) decomposes as acetic anhydride (Ac_2O) to yield NiO. Heating above 870°C to around 965 °C, the mass of the ceramic product, $(NiO)_{0.22}/(CuO)_{0.78}$ is decreasing, suggesting the decomposition of $(CuO)_{0.78}$ to half equivalent of $(Cu_2O)_{0.78}$. In fact, the mass loss from 870 °C

(62.43%) to 970 °C (58.23%) supports the thermal conversion of $(NiO)_{0.22}/(CuO)_{0.78}$ to $(NiO)_{0.22}/0.5(Cu_2O)_{0.78}$.

TGA of $Ni_{0.22}Cu_{0.78}$ acetate hydroxide excellently agrees with its elemental analysis (Table 6) that establishes the formula of the product as $Ni_{0.22}Cu_{0.78}(OAc)_{0.51}(OH)_{1.49}\cdot 0.43H_2O$. Nickel and copper contents were determined using MP-AES analysis (Supporting Table S4(d)), whereas carbon content was determined using a carbon-nitrogen analyzer. In addition, the ceramic yield of TGA also closely agrees with the ceramic yield calculated from the formula of $Ni_{0.22}Cu_{0.78}$ acetate hydroxide (Table 7), which further instates the determined formula. Likewise, the TGA experiments and elemental analyses (Table 9 and Supporting Table S4) of all other nickel-copper acetate hydroxides excellently complement each other, establishing their formulas as presented in Table 1. The ceramic product of the $Ni_{0.22}Cu_{0.78}$ acetate hydroxide is nickel oxide-copper oxide, $Ni_{0.22}O\text{-}Cu_{0.78}O$, confirmed by XRD pattern analysis (discussed later, Figure 18). Therefore, the $Ni_{0.22}Cu_{0.78}$ acetate hydroxide is an excellent precursor for a mixed metal oxide of $Ni_{0.22}O\text{-}Cu_{0.78}O$. Notably, to prepare a solid solution of nickel-copper oxide, $Ni_xCu_{1-x}O$; a nickel-copper acetate hydroxides need to be highly nickel-rich as nickel oxide can accommodate up to 30 mole percent of copper oxide to make a solid solution.[19]

Table 6: Nickel, copper, and carbon contents of $Ni_{0.22}Cu_{0.78}(OAc)_{0.51}(OH)_{1.49}\cdot 0.43H_2O$

Metal content (%)		Carbon content (%)
Cu	37.6±0.77	9.81
Ni	9.73±0.19	

Table 7: Comparison of TGA ceramic yield with the calculated ceramic yield of $Ni_{0.22}Cu_{0.78}(OAc)_{0.51}(OH)_{1.49}\cdot 0.43H_2O$

Ceramic yield calculated from the formula	TGA ceramic yield
61.94%	62.43%

TGA experiments of other nickel-rich reaction products (Figure 8-10) and copper-rich reaction products (Figure 11) clearly show that all nickel-copper acetate hydroxides exhibit similar thermo-chemical events as $Ni_{0.22}Cu_{0.78}$ acetate hydroxide described above. The thermochemical reactions during heating of the nickel-copper acetate hydroxides can generally be depicted as follows in Scheme 4.

$$Ni_xCu_{1-x}(OAc)_y(OH)_{2-y}\cdot nH_2O\ (s) \longrightarrow Ni_xCu_{1-x}(OAc)_y(OH)_{2-y}\ (s) + nH_2O\ (g)$$

$$[Ni(OAc)(OH)_5]\ (s) \longrightarrow NiO\ (s) + [\,\tfrac{1}{2}\,(CH_3CO)_2O + 5/2\ H_2O]\ (g)$$

nickel(II) octahedra

$$Cu(OAc)(OH)_5 \xrightarrow{O_2} (CuO)_z/(Cu_2O)_{1-z}\ (s) + [\tfrac{1}{2}\,CH_3\text{-}CH_3 + \tfrac{1}{2}\,CO_2 + 5/2\ H_2O]\ (g)$$

copper(II) octahedra

$$(CuO)_z/(Cu_2O)_{1-z}\ (s) \xrightarrow{O_2} CuO(s)$$

Scheme 4: Possible reactions in the thermal decomposition of nickel-copper acetate hydroxides.

Dehydroxylation of OH^- and decomposition of OAc^-: Nickel copper acetate hydroxides are layered double hydroxides that are consisted of the layers of nickel(II) acetate hydroxide, $Ni(OAc)(OH)_5$ and copper (II) acetate hydroxide, $Cu(OAc)(OH)_5$ octahedra. As a result, the OH^- dehydroxylation and OAc^- decomposition steps observed in the second and third mass losses in TGA plots occur differently in both constituent octahedra (as explained earlier).

The overall thermal decomposition reactions of nickel-copper acetate hydroxides to corresponding nickel-copper oxides are as follows.

$$Ni_xCu_{1-x}(OAc)_y(OH)_{2-y}\cdot nH_2O\ (s) \longrightarrow (NiO)_x(CuO/Cu_2O)_{1-x}\ (s) \longrightarrow (NiO)_x(CuO)_{1-x}\ (s)$$

Scheme 5: Overall thermal conversion of nickel-copper acetate hydroxides to mixed oxides of nickel oxide-copper oxide.

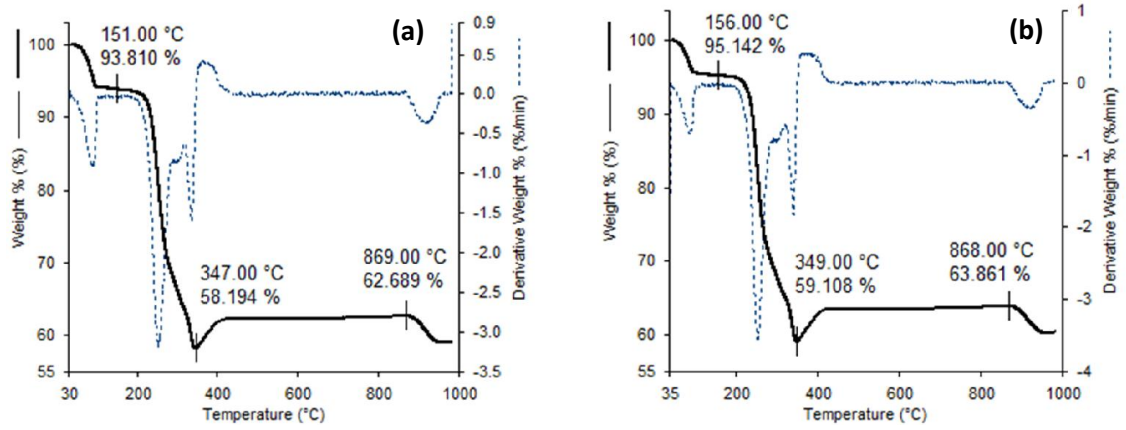

Figure 8: TGA plots of (a) $Ni_{0.33}Cu_{0.67}$ acetate hydroxide (product of 2Ni:1Cu reaction) and (b) $Ni_{0.39}Cu_{0.61}$ acetate hydroxide (product of 3Ni:1Cu reaction).

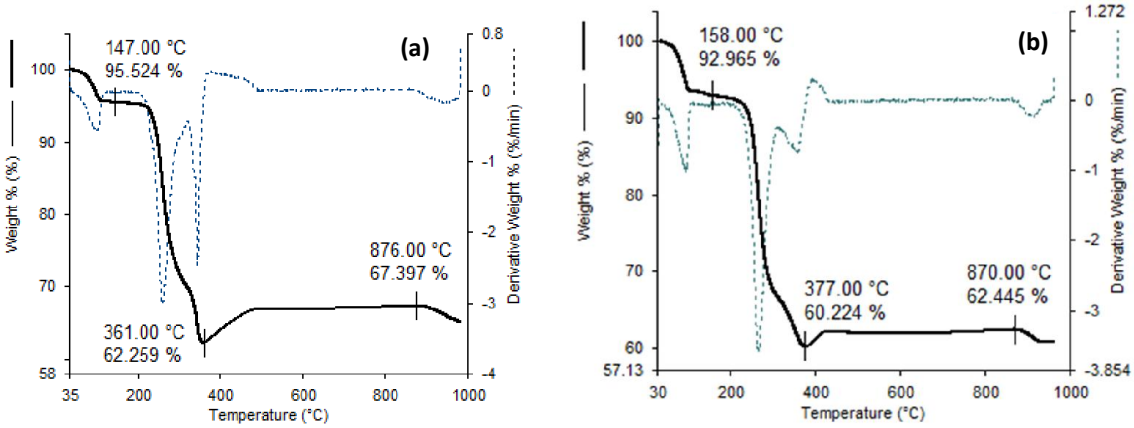

Figure 9: TGA plots of (a) $Ni_{0.42}Cu_{0.58}$ acetate hydroxide (product of 4Ni:1Cu reaction) and (b) $Ni_{0.46}Cu_{0.54}$ acetate hydroxide (product of 6Ni:1Cu reaction).

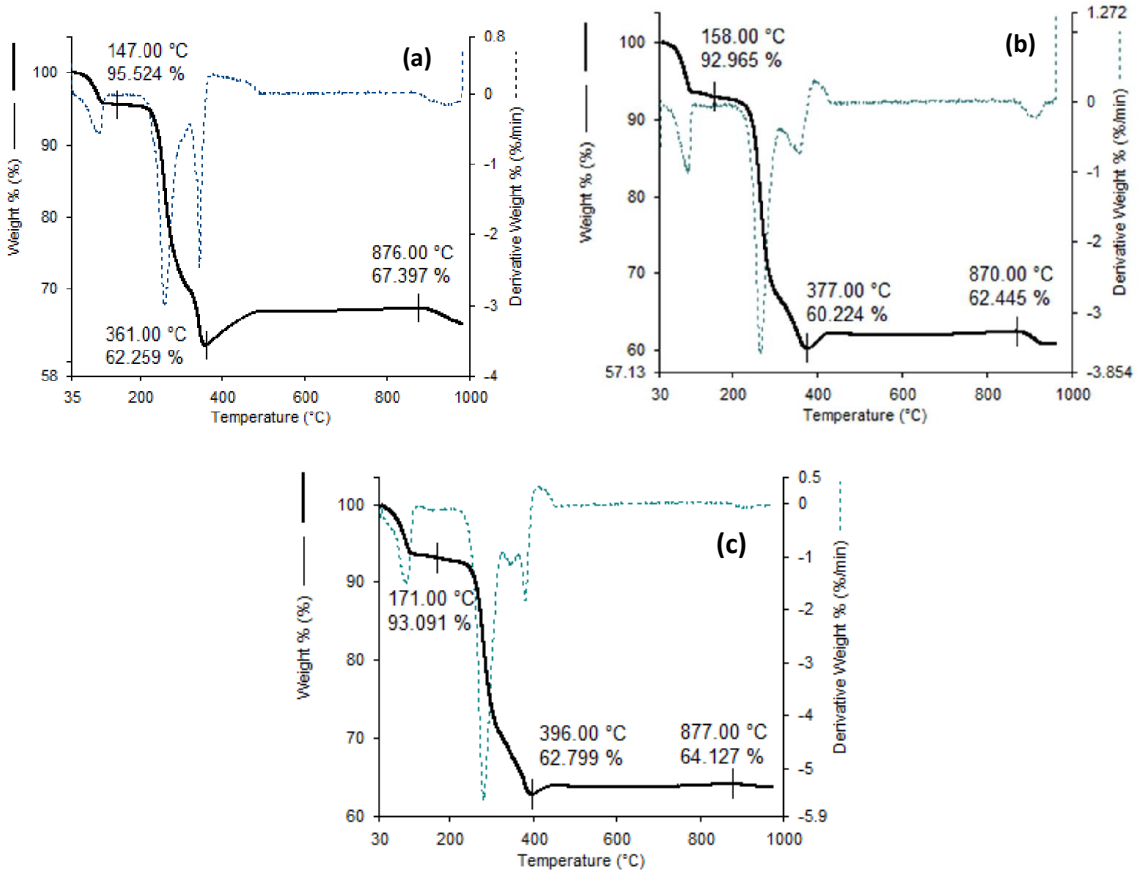

Figure 10: TGA plots of (a) $Ni_{0.51}Cu_{0.49}$ acetate hydroxide (product of 7Ni:1Cu reaction), (b) $Ni_{0.59}Cu_{0.39}$ acetate hydroxide (product of 9Ni:1Cu reaction), and (c) $Ni_{0.78}Cu_{0.22}$ acetate hydroxide (product of 50Ni:1Cu reaction).

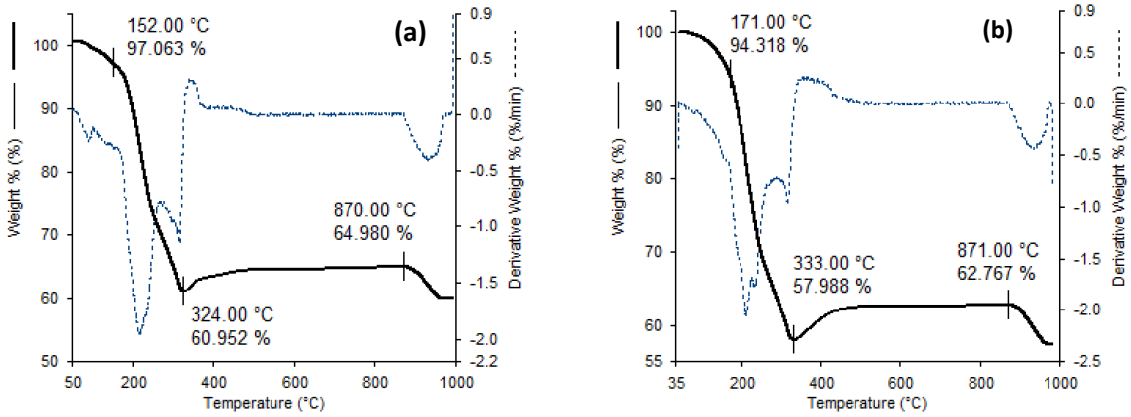

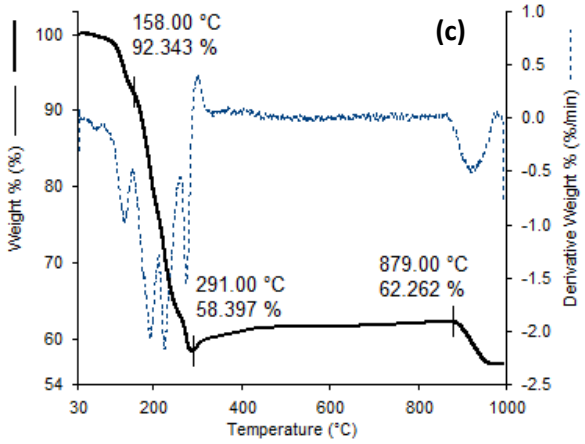

Figure 11: TGA plots of copper-rich reaction products. (a) $Ni_{0.13}Cu_{0.87}$ acetate hydroxide (product of 1Ni:2Cu reaction), (b) $Ni_{0.10}Cu_{0.90}$ acetate hydroxide (product of 1Ni:3Cu reaction), and (c) $Ni_{0.04}Cu_{0.96}$ acetate hydroxide (product of 1Ni:9Cu reaction).

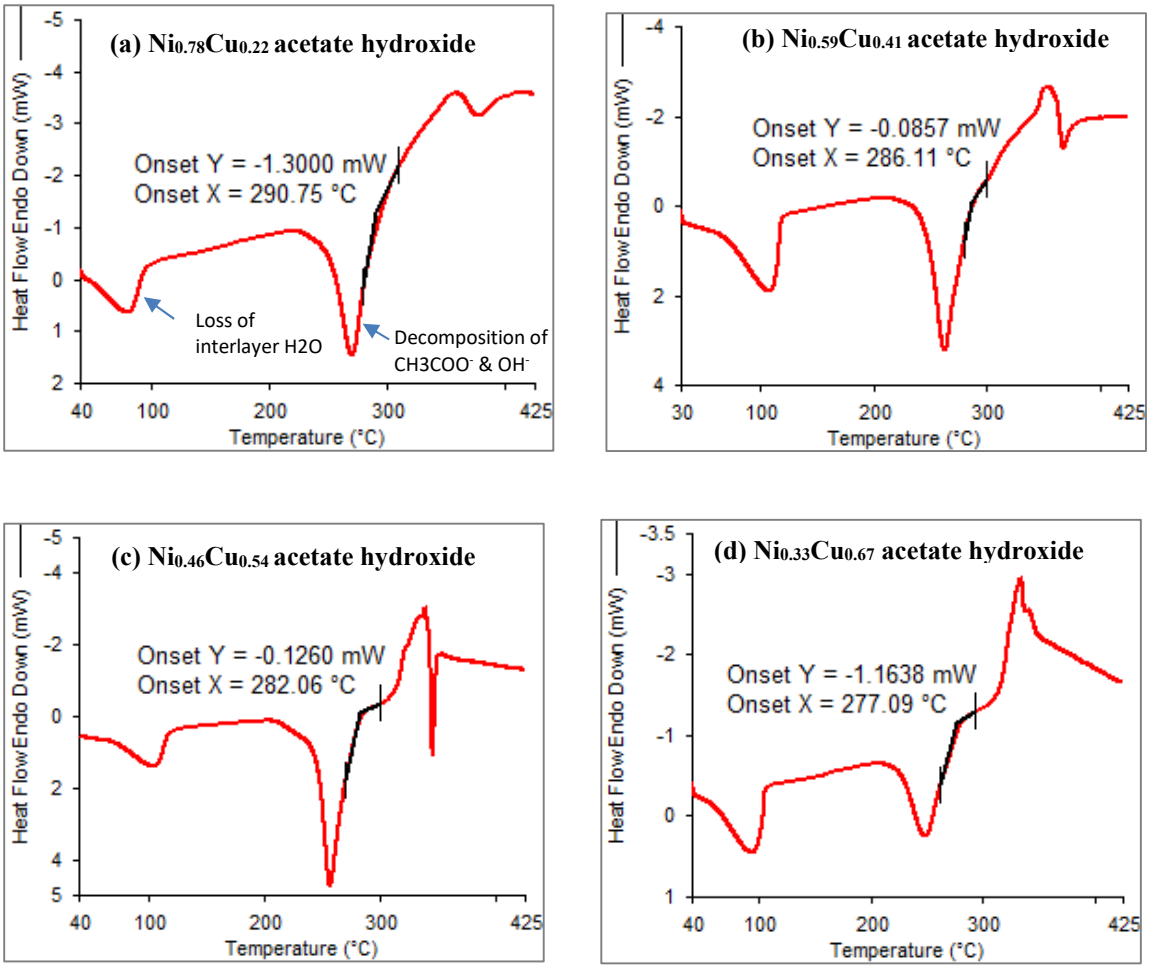

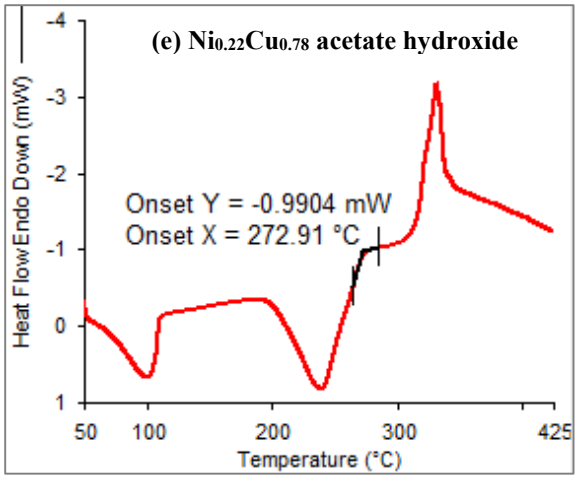

Figure 12: DSC plots of several nickel-copper acetate hydroxides – (a) $Ni_{0.78}Cu_{0.22}$, (b) $Ni_{0.59}Cu_{0.41}$, (c) $Ni_{0.46}Cu_{0.54}$, (d) $Ni_{0.33}Cu_{0.67}$, and (e)$Ni_{0.22}Cu_{0.78}$ acetate hydroxides.

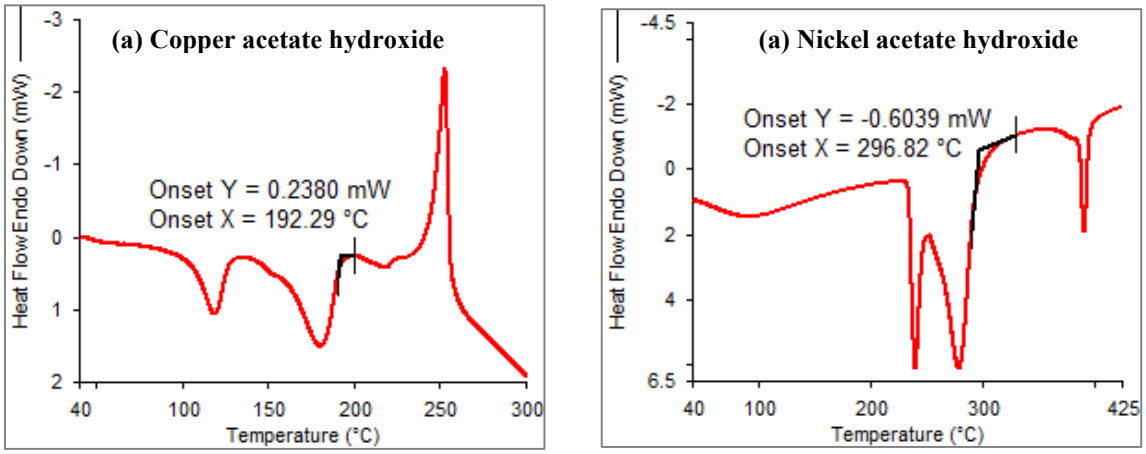

Figure 13: DSC plots of pure copper and nickel acetate hydroxides – (a) copper acetate hydroxide, $Cu(OAc)_{0.43}(OH)_{1.67}\cdot 0.41H_2O$ (b) nickel acetate hydroxide, $Ni(OAc)_{0.28}(OH)_{1.72}\cdot 0.25H_2O$.

DSC experiments excellently complement the mass losses of the TGA experiments. For example, as discussed earlier, the first mass losses in the TGA plots stand for the dehydration of interlayered water molecules, which must be an endothermic process. DSC experiments of selected nickel-copper acetate hydroxides (Figure 12) confirm that the water loss peaks are indeed endothermic (the first peaks). While the second thermal events (second peaks) in the DSC plots are

also endothermic, representing dehydroxylation of hydroxyl groups and decomposition of acetate groups to yield ceramic products. Therefore, the second endothermic peaks' temperatures can be termed as the average temperatures for the complete decomposition of acetate and hydroxyl groups. In addition, after the second endothermic step, there are exothermic peaks (after 300 °C) that correspond to oxidation. As (discussed earlier in the TGA discussion) $Ni_xCu_{1-x}(OAc)_y(OH)_{2-y}\cdot nH_2O$ during decomposition of acetate groups converts to $(NiO)_x(CuO/Cu_2O)_{1-x}$, which upon further heating, Cu_2O oxidize to CuO. Therefore, the oxidation steps on the DSC plot must be due to the conversion of Cu_2O to CuO that yield final ceramic products $(NiO)_x/(CuO)_{1-x}$.

Comparing the onset end temperatures of the DSC peaks that correspond decomposition of acetate and hydroxyl groups (the second endothermic peaks in the DSC plots) reveals that the decomposition event directly depends on nickel-copper contents (formulas) in products, as presented in Table 8 and Figure 14. Nickel-rich products require higher temperatures than the copper-rich products for the complete decomposition of acetate and hydroxyl groups. Increasing nickel content, *i.e.*, with decreasing copper content, the decomposition temperatures of acetate and hydroxyl groups get higher (Figure 14). It turns out that the decomposition temperatures are linearly increasing with the formula of nickel (Ni_x) in the products. This is because acetate or hydroxyl that are coordinated to nickel ($Ni(OAc)_x(OH)_{6-x}$ octahedra) requires more energy to break up than those that are connected to copper ($Cu(OAc)_x(OH)_{6-x}$ octahedra). The DSC of pure nickel acetate hydroxide and copper acetate hydroxide (Figure 13) establishes nickel acetate hydroxide ($Ni(OAc)_x(OH)_{6-x}$ octahedra) is more thermally stable than copper acetate hydroxide ($Cu(OAc)_x(OH)_{6-x}$ octahedra). This is consistent with our previous investigations (Chapter III and Chapter II) of pure copper acetate hydroxide, $Cu(OAc)_{0.41}(OH)_{1.59}\cdot 0.40H_2O$ that fully decomposed to Cu_2O/CuO at 283°C (Chapter III, Figure 12), while pure nickel acetate hydroxide, $Ni(OAc)_{0.28}(OH)_{1.72}\cdot 0.25H_2O$ decomposed to NiO at around 350°C (Chapter II, Figure 3).

Table 8: Comparison of decomposition temperatures of acetate groups and dehydroxylation of hydroxyls groups in nickel-copper acetate hydroxides using DSC experiments

Nickel-copper acetate hydroxides	Decomposition temperatures of acetate and hydroxyl groups from DSC peaks [a] (°C)
Ni acetate hydroxide	297
$Ni_{0.78}Cu_{0.22}$ acetate hydroxide	291
$Ni_{0.59}Cu_{0.41}$ acetate hydroxide	286
$Ni_{0.46}Cu_{0.54}$ acetate hydroxide	282
$Ni_{0.33}Cu_{0.67}$ acetate hydroxide	277
$Ni_{0.22}Cu_{0.78}$ acetate hydroxide	273
Cu acetate hydroxide	192

a. Decomposition temperatures were determined from the onset end temperatures of second endothermic peaks of the DSC plots corresponding to the complete decomposition of acetate and hydroxyl groups.

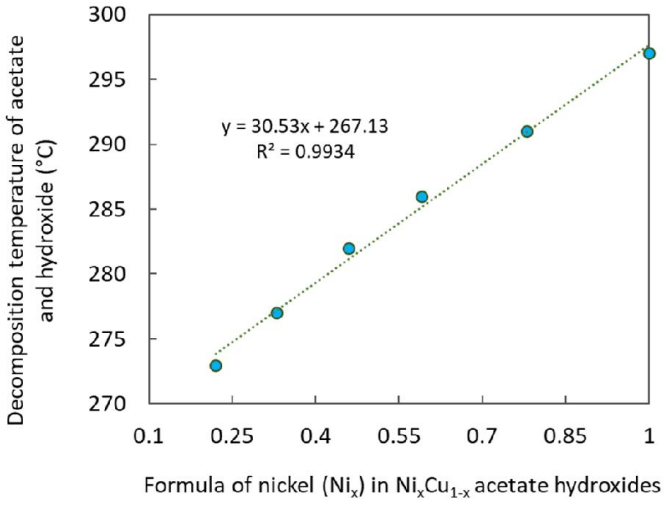

Figure 14: Decomposition temperatures of acetate and hydroxyl groups against the nickel formula (Ni_x) in Ni_xCu_{1-x} acetate hydroxides.

Table 9: Nickel, copper, and carbon contents of nickel-copper acetate hydroxides

Nickel-copper acetate hydroxides	Metal content (%)		Carbon content (%)
$Ni_{0.04}Cu_{0.96}$ acetate hydroxide	Cu	38.8	9.52
	Ni	1.46	
$Ni_{0.10}Cu_{0.90}$ acetate hydroxide	Cu	40.3	9.72
	Ni	4.3	
$Ni_{0.13}Cu_{0.87}$ acetate hydroxide	Cu	40.3	9.79
	Ni	5.56	
$Ni_{0.22}Cu_{0.78}$ acetate hydroxide	Cu	37.6	9.81
	Ni	9.73	
$Ni_{0.33}Cu_{0.67}$ acetate hydroxide	Cu	32.1	9.80
	Ni	14.8	
$Ni_{0.39}Cu_{0.61}$ acetate hydroxide	Cu	28.8	9.89
	Ni	16.7	
$Ni_{0.42}Cu_{0.58}$ acetate hydroxide	Cu	27.0	10.20
	Ni	17.0	
$Ni_{0.46}Cu_{0.54}$ acetate hydroxide	Cu	23.4	9.82
	Ni	18.5	
$Ni_{0.51}Cu_{0.49}$ acetate hydroxide	Cu	22.7	9.16
	Ni	21.6	
$Ni_{0.54}Cu_{0.46}$ acetate hydroxide	Cu	18.9	9.94
	Ni	24.9	
$Ni_{0.78}Cu_{0.22}$ acetate hydroxide	Cu	10.4	9.64
	Ni	34.6	

a. Supporting Table 4(a)-4(j) includes the Microwave Plasma Atomic Emission Spectroscopy (MP-AES) data for nickel and copper analysis.

The elemental analysis of nickel, copper, and carbon (Table 9) and TGAs together enumerate their formulas as tabulated in Table 1. The elemental analysis of all the products supports their TGA experiments. Because the carbon content calculated from the determined formula very closely agrees with experimental carbon analysis (Supporting Table 5). For all the products, the acetate content is not identical; however, it is around 0.5 for 1 equivalent of metals (copper & nickel), except for the 7Ni:1Cu product, where the acetate content is a little bit lower (0.44). The amount of acetate per equivalent of metals in our work is higher compared to a room temperature synthesis of bimetallic acetate hydroxides such as $Cu_{3.6}Zn_{1.6}(OH)_{7.6}(OAc)_{2.4}\cdot 5H_2O$ and $Zn_{3.2}Ni_{1.5}(OH)_{7.9}(CH_3CO_2)_{1.5}\cdot 1.7H_2O$ that were synthesized by the Meyn[20] method, reactions of ZnO with copper acetate and nickel acetate, respectively.[18] Interestingly, heating of ZnO and copper acetate at 65°C in the synthesis mentioned above generated increased acetate content (like our work, 0.5 per 1 equivalent of metals) in the products such as $Cu_{1.6}Zn_{0.4}(OH)_3(OAc)\cdot H_2O$.[21] This suggests that hydrolysis of metal acetates at lower temperatures (60-90°C) may favor generating more acetate intercalation in the bimetallic layered double hydroxides.

Unlike interconnected nanowalls of nickel acetate hydroxide grown by hydrolysis of only nickel acetate or hemisphere/trientsphere-type particles of CuO deposited using only copper acetate hydrolysis (discussed in Chapters II & III), the hydrolysis of mixtures of nickel-copper acetate grows different structures of nano-/micro walls. SEM of $Ni_{0.22}Cu_{0.78}$ acetate hydroxide (1Ni:1Cu hydrolysis product) and $Ni_{0.39}Cu_{0.61}$ acetate hydroxide (3Ni:1Cu hydrolysis product) reveals that the morphology of the grown particles is square-type plates. The SEM images were acquired using films of the materials deposited at the bottom of the reaction vessels; therefore, it can be said that $Ni_{0.22}Cu_{0.78}$ acetate hydroxide plates are grown as randomly oriented square-type particles as presented in Figure 15. While for $Ni_{0.3}Cu_{0.61}$ acetate hydroxide, smaller and thinner plates are aggregated on bigger and thicker plates, forming flower-like assemblies (Figure 16). The dimensions (length) of the square-type plates are mainly in the order of micrometers. The thickness

(height of the plates) is dominantly in the order of nanometers for $Ni_{0.22}Cu_{0.78}$ acetate hydroxide, whereas $Ni_{0.39}Cu_{0.61}$ acetate hydroxide has a considerable amount of micrometer thick walls. Overall, the preferential growth of the square plates is two-dimensional in both nickel-copper acetate hydroxide.

The particles' morphologies of nickel-copper hydroxide are very interesting since the reactions were performed without a templating agent or a surfactant. The initial nucleation makes seed particles that may grow as extremely ultra-thin square-plate morphology. The seed particles should be then played as a blueprint that facilitates the growth of bigger size square-type particles. Figure 16(f) clearly that zoom on a single plate to show the defect lines in the plates. The defect lines must happen during the growth of the particle. Hence, these defect lines evidently support that the square-plate particles are grown from smaller/thinner plates that should originate from much smaller/thinner seed particles in the reactions. The hydrolysis reaction involves a nucleation step followed by a growth step (Figure 17); these two steps determine the outcome of the shape of the particles in a hydrolysis reaction, i.e., to grow preferentially. It is unlikely that direct precipitation (a very fast reaction) would produce this type of two-dimensional morphology. The present investigation is the first work that shows that hydrolysis of mixtures of nickel and copper acetate (without a second reactant or reagent) preferentially creates square-type plate morphology of nickel-copper acetate hydroxides. Kozai *et al.*[3] work on nickel-copper acetate hydroxide and show a plate-type structure with no particular shape. Therefore, the present work invites the idea of exploring hydrolysis of other transition metal acetates' mixtures to find out what types of nano-/micro morphologies they would generate.

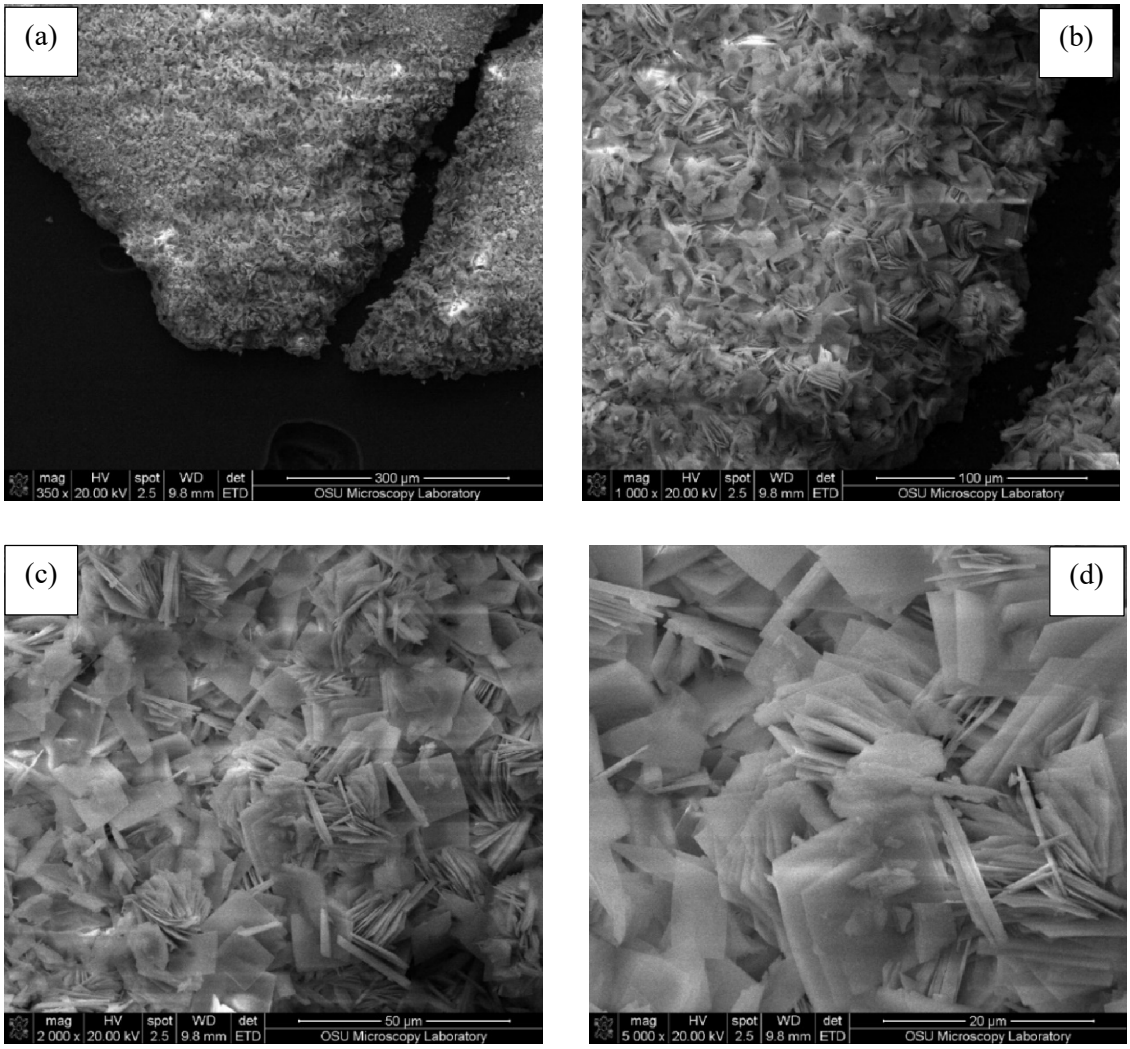

Figure 15: SEM images of $Ni_{0.22}Cu_{0.78}$ acetate hydroxide (hydrolysis product of 1:1 nickel acetate to copper acetate reaction).

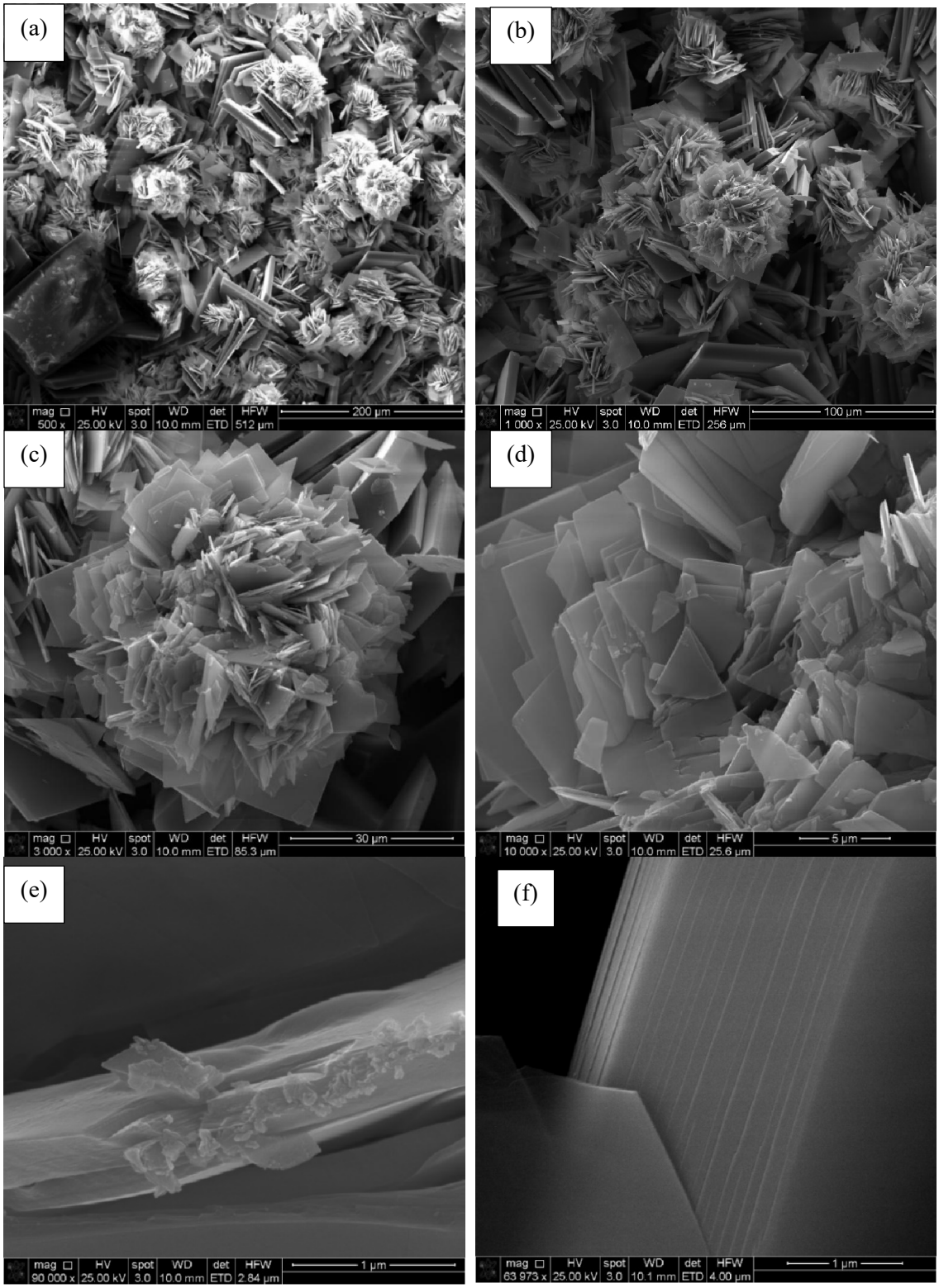

Figure 16: SEM images of $Ni_{0.39}Cu_{0.61}$ acetate hydroxide (hydrolysis product of 1:3 nickel acetate to copper acetate reaction).

Particle size analysis of a 1Ni(OAc)2:1Cu(OAc)2 hydrolysis reaction (Figure 17) shows that the reaction involves an initial incubation time to generate seed particles (initial nucleation), which follows by the speedy growth of the particles. When nucleation creates a critical size of particles, they play a role in the autocatalytic growth of the particles. That is why after nucleation, the growth of particles is very rapid. Notably, compared to hydrolysis of pure nickel or copper acetate, the particles' growth in the 1Ni:1Cu hydrolysis reaction is very fast, and the particles grow much bigger in size in a shorter time.

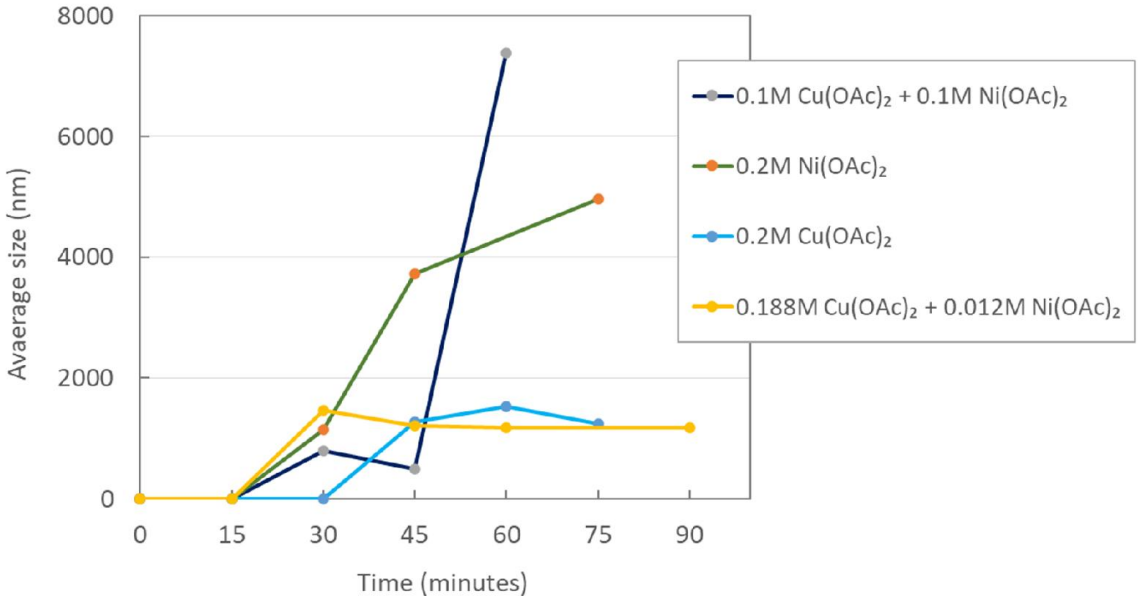

Figure 17: Particle size analysis during hydrolysis reactions of nickel acetate, copper acetate, 1:1 nickel acetate to copper acetate, and copper acetate with a catalytic amount of nickel acetate at 90 °C in water.

Pyrolysis of a few nickel-copper acetate hydroxides, namely $Ni_{0.10}Cu_{0.90}$, $Ni_{0.22}Cu_{0.78}$, $Ni_{0.33}Cu_{0.67}$, and $Ni_{0.39}Cu_{0.61}$ acetate hydroxide at 400 °C facilely produced two-phase oxide materials of corresponding nickel oxide-copper oxide. The XRD patterns of the pyrolyzed materials (Figures 18 and 19) are matched up with both copper(II) oxide, CuO (JCPDS card# 48-1548) [22] and nickel oxide, NiO (JCPDS card# 47-1049)[23] phases. This confirms the successful conversion of the nickel-

copper acetate hydroxides to their corresponding mixed oxides, $(NiO)_{0.10}(CuO)_{0.90}$, $(NiO)_{0.22}(CuO)_{0.78}$, $(NiO)_{0.33}(CuO)_{0.67}$, and $(NiO)_{0.39}(CuO)_{0.61}$. The peak indexing and their d-spacing are tabulated in supporting Tables S6(a) and S6(b). The *111* (NiO) and *200* (NiO) peaks at around 37.2° and 43.3° get broadened with an increasing nickel content in the nickel oxide-copper oxide materials. This suggests that the crystallite sizes of the nickel oxide phase also get smaller with the increasing nickel contents in the mixed oxide materials. Crystallite sizes are determined using the Scherrer equation (supporting Table S5) using the peaks at 37.2° of *111* (NiO), which presents the trend of the crystallite size with respect to the nickel content (Figure 20). Interestingly, the crystallite sizes along the *111* planes of the NiO phase are linearly co-related with the formula of nickel (Ni_x) in the nickel oxide-copper oxide materials. Mass changes (ceramic yields) in the pyrolysis of the nickel-copper acetate hydroxides to generate their corresponding mixed oxides are found to be consistent with calculated ceramic yields from the formulas of the nickel-coper acetate hydroxides (Table 10).

Table 10: Ceramic yields of the pyrolysis of a few selected nickel-copper acetate hydroxides for their corresponding nickel oxide-copper oxide materials at 400 °C

Nickel-copper acetate hydroxides	**Mass of nickel copper acetate hydroxides (g)**	**Mass of oxides after pyrolysis**	**Ceramic yield (%)**	**Calculated ceramic yield (%)**
$Ni_{0.10}Cu_{0.90}$ acetate hydroxide	0.2437	0.1507	61.84	62.89
$Ni_{0.22}Cu_{0.78}$ acetate hydroxide	0.4247	0.2652	62.44	62.48
$Ni_{0.33}Cu_{0.67}$ acetate hydroxide	0.2590	0.1619	62.51	62.28
$Ni_{0.39}Cu_{0.61}$ acetate hydroxide	0.2109	0.1337	63.39	63.30

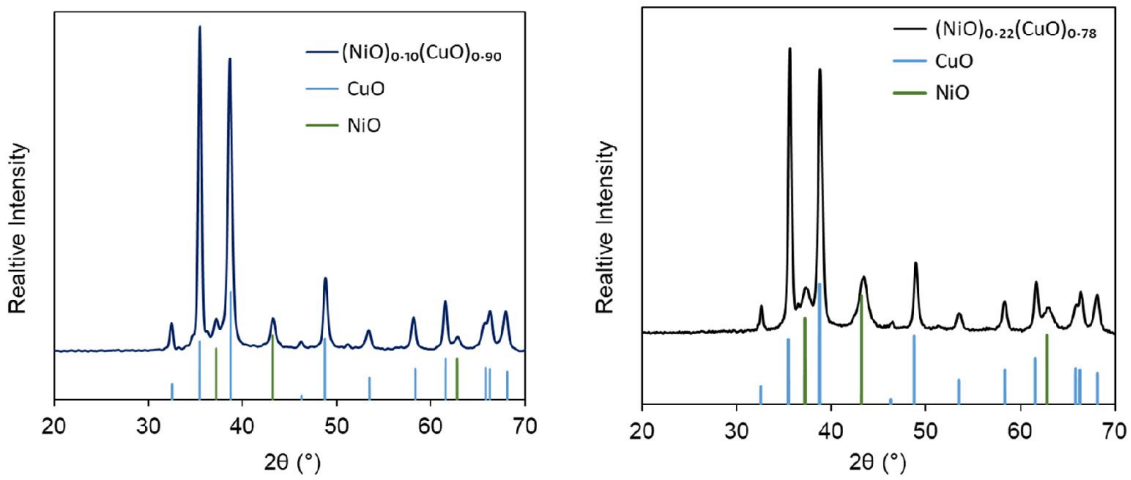

Figure 18: XRD patterns of $(NiO)_{0.10}(CuO)_{0.90}$ and $(NiO)_{0.22}(CuO)_{0.78}$, prepared from pyrolysis of corresponding nickel-copper acetate hydroxides.

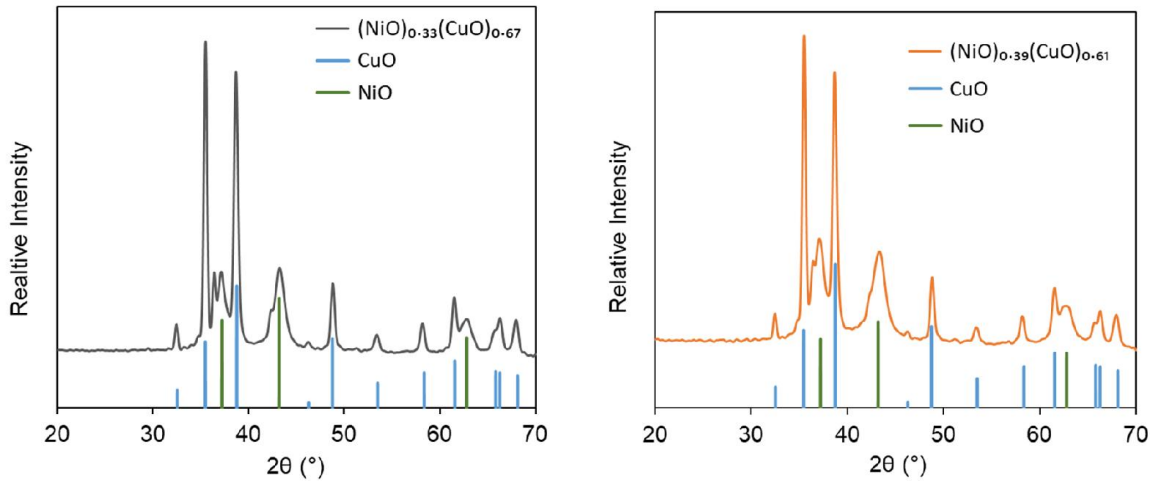

Figure 19: XRD patterns of $(NiO)_{0.33}(CuO)_{0.67}$ and $(NiO)_{0.39}(CuO)_{0.61}$, prepared from pyrolysis of corresponding nickel-copper acetate hydroxides.

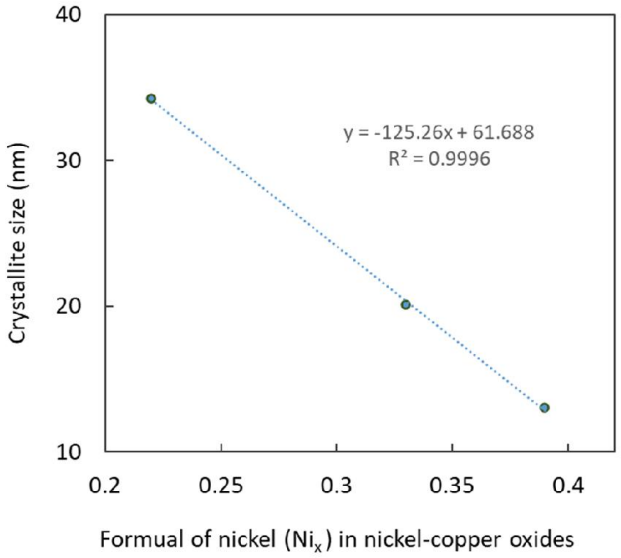

Figure 20: Crystallite size vs. formula of nickel (Ni_x) of nickel oxide-copper oxide, $(NiO)_x(CuO)_{1-x}$ materials prepared by pyrolysis of the corresponding nickel-copper acetate hydroxides.

Deposition of nickel-copper acetate hydroxides onto silica catalysts supports: Silica pellets were successfully functionalized by nickel-copper acetate hydroxides using the hydrolysis of nickel acetate and copper acetate mixtures. For example, $2Ni(OAc)_2$:$1Cu(OAc)_2$ hydrolysis reaction with 10.044g of silica pellets deposited $Ni_{0.55}Cu_{0.45}(OAc)_{0.30}(OH)_{1.70}\cdot nH_2O$ onto the pellets, confirmed by the elemental analysis (Table 11). The deposition transformed the white silica pellets into bluish-green silica pellets (Figure 21) and increased the mass of the pellets by 8.24%. As NiO can dissolve up to 30 mole percent of CuO as a solid solution,[19] the prepared nickel-copper acetate hydroxide deposited SiO_2 pellets can be converted to a nickel oxide-copper oxide (NiO-CuO) decorated SiO_2 pellets by pyrolysis. Notably, as a ratio 2Ni:1Cu generated $Ni_{0.55}Cu_{0.45}$ acetate hydroxide with silica pellet, the hydrolysis reaction can produce a $Ni_{0.70}Cu_{0.30}$ acetate hydroxide or even higher nickel content acetate hydroxides onto the pellets if higher ratios than 2:1 nickel acetate to copper acetate are used. Highly nickel-rich acetate hydroxides can be transformed into solid solutions of bimetallic nickel-copper oxides $Ni_xCu_{1-x}O$. Functionalizing or decorating catalyst supports with robust nano-/micro-structured mixed metal and bimetallic oxides is crucial in catalyst development as often

bimetallic oxides show better catalytic performance due to the synergy of two metals at the catalysts' surface. For example, mixed metal oxides such as NiO-CuO exhibited improved catalytic performances in useful organic transformations.[24-27] While in a bimetallic oxide, besides the bimetallic synergy, the d-band structure would adopt a new band structure that can offer optimum binding of reactants on its surface, rendering enhanced catalytic performance. Therefore, the developed hydrolysis process depositing NiO-CuO or a solid solution of bimetallic $Ni_xCu_{1-x}O$ onto silica catalysts supports is a significant advancement in preparing nano-/micro structured bimetallic oxide decorated catalysts supports. It is expected that the hydrolysis of other mixtures of other transition metal acetates will also generate corresponding layered bimetallic hydroxides to access their bimetallic oxides decorated silica pellets. As the process is inexpensive, straightforward, and scalable, it can be commercialized for the large-scale production of mixed metal or bimetallic oxide-coated silica support materials.

Figure 21: Nickel-copper acetate hydroxide, $Ni_{0.55}Cu_{0.45}(OAc)_{0.30}(OH)_{1.70}\cdot nH_2O$ deposited silica pellets

Table 11: Elemental contents of the bluish-green pellets prepared by hydrolysis of 2:1 $Ni(OAc)_2$ and $Cu(OAc)_2$ with silica pellets

Nickel (%)	Copper (%)	Carbon (%)
2.11	1.86	0.53

Note: As the deposition amount in the hydrolysis reaction was 8.24% (w/w), the elemental contents were normalized by 8.24% for determining the formula of the deposited nickel-copper acetate hydroxide.

■ **Conclusion:**

Hydrolysis of nickel acetate and copper acetate mixtures without an additional reagent or a reactant produced nickel-copper acetate hydroxides, which are acetate-intercalated nickel-copper layered double hydroxides (LDHs). A series of hydrolysis reactions with various nickel acetate and copper acetate ratios was investigated for the first time, showing an unusual dependency of nickel to copper in the products to the ratios of nickel and copper acetate as reactants. Reactions from 1Ni:1Cu to 6Ni:1Cu (nickel acetate to copper acetate) produced copper-rich nickel-copper LDHs. While reactions of 7Ni:1Cu generated $Ni_{0.51}Cu_{0.49}$-LDH and 9Ni:1Cu produced a nickel-rich nickel-copper LDH. The morphology of the particles of two selected nickel-copper LDHs, namely $Ni_{0.22}Cu_{0.78}$ and $Ni_{0.39}Cu_{0.61}$ acetate hydroxide, are square-type plates in the order of nano to micrometers in dimensions. Pyrolysis converted a few selected nickel-coper acetate hydroxides to the corresponding mixed metal oxides, $(NiO)_x(CuO)_{1-x}$. One of the nickel-copper LDHs such as $Ni_{0.33}Cu_{0.67}(OAc)_{0.51}(OH)_{1.49}\cdot 0.43H_2O$ is an excellent precursor for a mixed metal oxide of $(NiO)(CuO)_2$. Silica supports were also successfully functionalized with a bimetallic nickel-copper acetate hydroxide, $Ni_{0.55}Cu_{0.45}(OAc)_{0.30}(OH)_{1.70}\cdot nH_2O$ from a reaction of 2:1 nickel acetate to copper acetate reaction. These functionalized silica pellets can be converted to nickel oxide-copper

oxide decorated silica supports by pyrolysis. Interestingly, the hydrolysis of 2:1 nickel acetate copper acetate with silica pellets produces much higher nickel content in the layered hydroxide than without the silica. As a result, the hydrolysis process can be utilized to deposit much higher nickel-rich LDHs by using higher ratios than 2:1 nickel acetate to copper acetate, which can be exploited to prepare solid solutions of nickel-copper oxides ($Ni_xCu_{1-x}O$) decorated silica catalyst supports. It is expected that the hydrolysis process can also deposit bimetallic nickel-copper acetate hydroxides on other substrates and catalyst supports for direct use and for converting them into mixed metal oxides and possibly bimetallic oxides decorated substrates and supports. Therefore, the present investigation has opened a new avenue in hydrolysis mixtures of metal acetates to access nano-/micro-structured bimetallic LDHs and their corresponding nano-/micro-structured mixed metal or bimetallic oxides for various present-day necessary technologies.

- **Future Work:**

Change/control of particle shapes by adding a polymeric reagent or surfactant: In the future, the reactions will be investigated with an unreactive polymeric reagent or surfactant to look at whether the reactions can generate different morphologies of particles. Also, it would be critical to look at if the polymeric reagent, surfactant, or a templating agent can control the size of the particles to produce unform-particle sizes in the hydrolysis reactions. Because this would advance the hydrolysis mixtures of metal acetates process significantly to prepare a target morphology or size of nanoparticles of nickel-copper LDHs and possibly other bimetallic LDHs.

Synthesis of Nickle Cobaltite ($NiCo_2O_4$) or Copper Cobaltite ($CuCo_2O_4$): Nanostructured nickel-cobaltite or copper cobaltite are promising materials for electrode applications in batteries and supercapacitors, electro-/photo-catalysis, fuel cells, etc. The hydrolysis process has opened the door for synthesizing and depositing nano-/micro-structures of nickel-cobaltite or copper cobaltite via corresponding nickel-cobalt or copper-cobalt acetate hydroxides. To advance the hydrolysis

process of mixtures of metal acetates further, it would be important to look at the hydrolysis reactions of mixtures of nickel-cobalt acetate or copper-cobalt acetate to find out at what ratios of nickel to cobalt or copper to cobalt with or with silica catalyst supports would produce $NiCo_2(OAc)_x(OH)_{6-x}\cdot nH_2O$ or $CuCo_2(OAc)_x(OH)_{6-x}\cdot nH_2O$ and what nano-/micro-structure would these reactions generate.

■ **Supporting Information:**

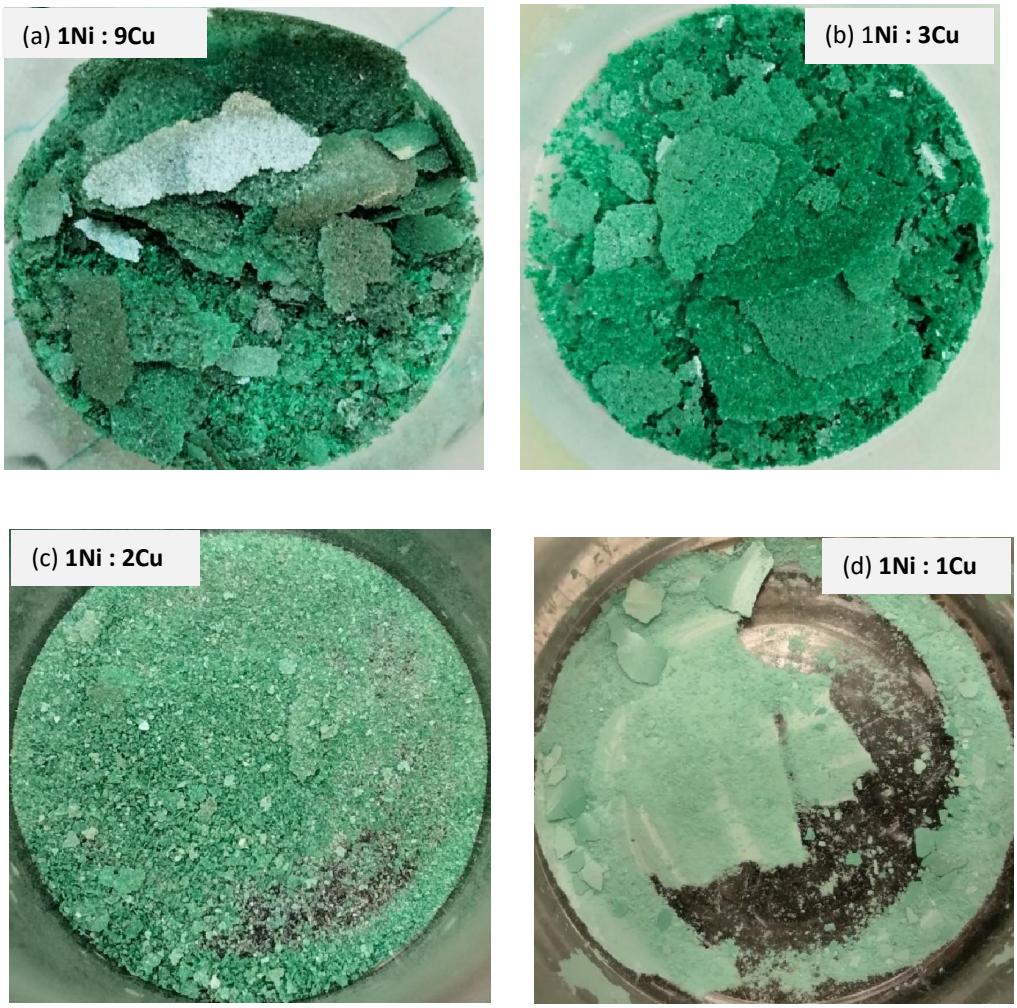


(e) **2Ni : 1Cu**


(f) **3Ni : 1Cu**

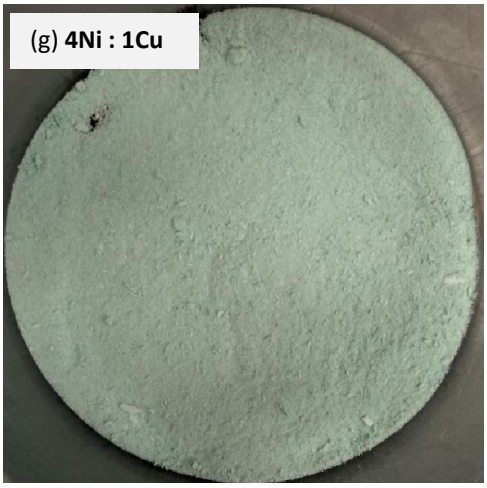
(g) **4Ni : 1Cu**

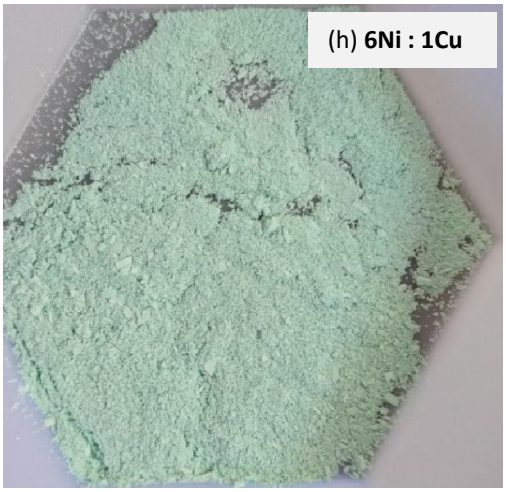
(h) **6Ni : 1Cu**


(i) **7Ni : 1Cu**


(j) **9Ni : 1Cu**

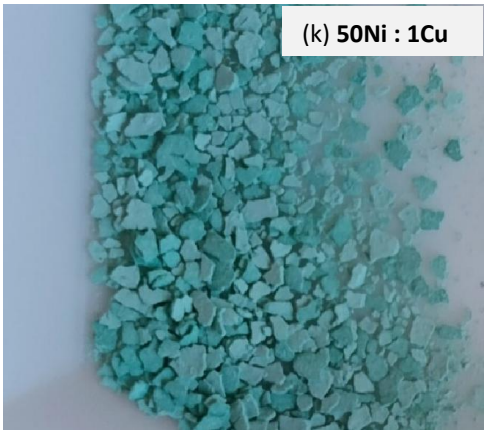

Figure S1: Camera pictures of the products of hydrolysis of nickel acetate and copper acetate mixtures at various ratios – (a) 1Ni : 9Cu, (b) 1Ni : 3Cu, (c) 1Ni : 2Cu, (d) 1Ni : 1Ni, (e) 2Ni : 1Cu, (f) 3Ni : 1Cu, (g) 4Ni : 1Cu, (h) 6Ni : 1Cu, (i) 7Ni : 1Cu, (j) 9Ni : 1Cu, and (k) 50Ni : 1Cu.

Table S1(a): Ion exchange experiment of pure nickel acetate hydroxide with copper ions (aqueous copper acetate) at room temperature

Analysis #	Stock Cu^{2+} Solution (ppm)	mass of stock solution (g)	Mass of nickel acetate hydroxide (g)	Final ppm of the stock solution	Amount of Cu^{2+} ion exchanged (mmol)
1	43.52	10.0209	0.0102	17.16	4.157
3		10.0183	0.0100	15.42	4.431
2		10.0231	0.0103	16.30	4.294

Table S1(b): Ion exchange constant of copper ions with pure nickel acetate hydroxide at room temperature

Analysis #	Amount of Cu^{2+} left in the solution (mmol)	Ion exchange or Equilibrium constant $K = Cu^{2+}_{(solid)}/Cu^{2+}_{(solution)}$	Average K
1	2.706	1.536	1.676
2	2.430	1.823	
3	2.571	1.670	

Table S2: MP-AES analysis of the precipitation product of 1:1 nickel acetate and copper acetate and 1 equivalent NaOH

Mass of solid (g)	Mass of digested solution (g)	Dilution of digested solution		MP-AES reading of the diluted solution (ppm)		Percent (%)	
		m_1 (g)	m_2 (g)	Ni	Cu	Ni	Cu
0.0141	8.1987	0.1951	18.8924	0.35	7.36	2.14	41.4

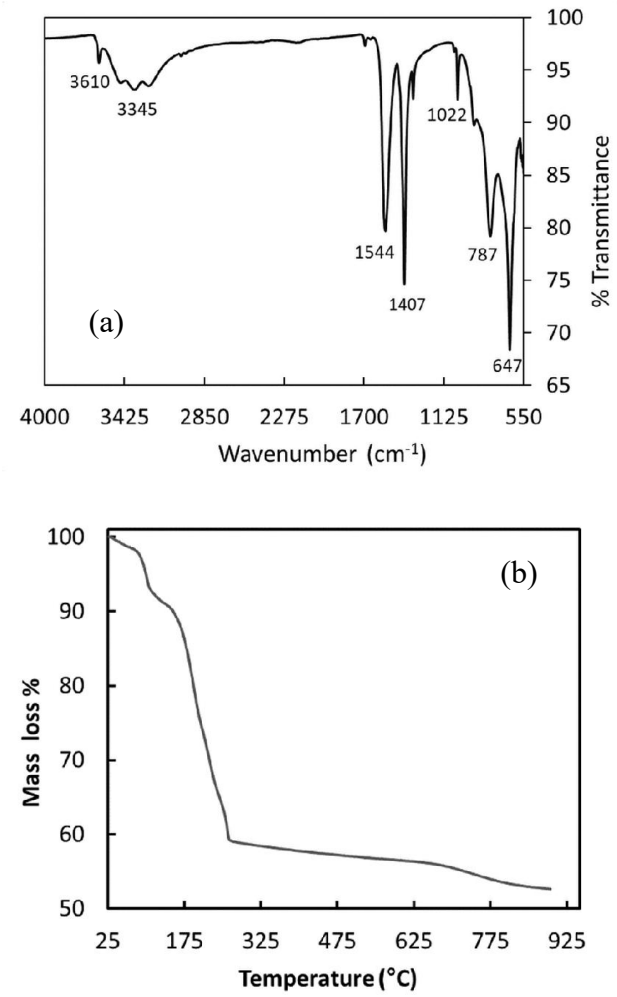

Figure S2: (a) ATR-FTIR spectrum and (b) TGA plot of precipitation product of 1:1 nickel acetate and copper acetate and 1eqivalent NaOH.

Table S3: The peak positions of the reflections, their Miller indices, and d-spacings of all the XRD patterns of nickel-copper acetate hydroxides

(a) $Ni_{0.04}Cu_{0.96}(OAc)_{0.51}(OH)_{1.49}\cdot 0.54H_2O$			(b) $Ni_{0.10}Cu_{0.90}(OAc)_{0.51}(OH)_{1.49}\cdot 0.40H_2O$		
h k l	**2θ (°)**	**d (nm)**	**h k l**	**2θ (°)**	**d (nm)**
0 0 1	9.384	9.417	0 0 1	9.47	9.331
1 0 0	16.235	5.455	0 1 1	17.39	5.095
0 1 1	17.260	5.133	0 0 2	18.92	4.687
0 0 2	18.841	4.706	1 0 1	20.81	4.265
1 0 1	20.573	4.314	1 1 1	25.35	3.511
1 0 2	21.811	4.071	1 1 3	26.56	3.353
1 1 0	22.685	3.916	0 0 3	28.55	3.124
1 1 1	25.240	3.526	2 0 1	32.22	2.776
1 1 3	26.405	3.373	1 0 3/ 0 1 3	33.64	2.662
0 0 3	28.433	3.136	1 2 1	34.33	2.610
2 0 0	32.023	2.793	1 1 -3	36.03	2.491
2 0 1	32.829	2.726	0 0 4	38.35	2.345
1 0 3/ 0 1 3	33.562	2.668	2 1 3	38.78	2.320
1 2 1	34.051	2.631	2 1 -2	40.69	2.216
2 0 3	35.971	2.495	1 2 5	42.01	2.149
1 2 3	36.819	2.439	1 2 -3	45.07	2.010
0 0 4	38.536	2.334	0 0 5	47.09	1.928
2 1 -2	40.653	2.217	1 3 -2	48.45	1.877
1 5 2/ 1 2 5	41.917	2.153	1 3 5	54.85	1.672
1 2 -3	44.809	2.021	0 0 6	56.77	1.620
0 0 5	47.067	1.929	3 2 0	58.08	1.587
1 3 -2	48.674	1.869	2 0 -5	58.96	1.565
1 0 5	52.466	1.743			
1 3 5	54.792	1.674			
0 0 6	56.628	1.624			
2 3 -3	57.892	1.592			
3 2 0	58.043	1.588			
3 0 2	58.500	1.576			
2 0 -5	59.099	1.562			

Table S3: continued

(c) $Ni_{0.13}Cu_{0.87}(OAc)_{0.50}(OH)_{1.50}\cdot 0.20H_2O$			(d) $Ni_{0.22}Cu_{0.78}(OAc)_{0.51}(OH)_{1.49}\cdot 0.43H_2O$		
h k l	**2θ (°)**	**d (nm)**	**h k l**	**2θ (°)**	**d (nm)**
0 0 1	9.333	9.468	0 0 1	9.436	9.365
1 0 0	16.229	5.457	1 0 0	16.396	5.402
0 1 1	17.176	5.158	0 1 1	17.229	5.143
0 0 2	18.792	4.718	0 0 2	18.893	4.693
1 0 1	20.552	4.318	1 0 1	20.631	4.302
1 0 2	21.777	4.078	1 0 2	21.895	4.056
1 1 1	25.184	3.533	1 1 1	25.26	3.523
1 1 3	26.409	3.372	1 1 3	26.597	3.349
0 0 3	28.385	3.142	0 0 3	28.475	3.132
2 0 0	32.152	2.782	2 0 0	32.387	2.762
2 0 1	32.965	2.715	2 0 1	33.146	2.700
1 0 3/ 0 1 3	33.469	2.675	1 0 3/ 0 1 3	33.505	2.672
2 0 2	33.799	2.650	2 0 2	33.843	2.646
1 2 1	34.210	2.619	1 2 1	34.499	2.598
2 0 3	35.857	2.502	2 0 3	35.862	2.502
1 2 3	36.742	2.444	1 2 3	36.850	2.437
0 0 4	38.688	2.325	0 0 4	38.983	2.309
2 1 -2	40.520	2.224	2 1 -2	40.538	2.223
1 5 2/ 1 2 5	41.858	2.156	1 5 2/ 1 2 5	41.990	2.150
1 2 -3	44.977	2.014	1 2 -3	45.293	2.001
0 0 5	46.942	1.934	0 0 5	46.906	1.935
1 2 7 /1 3 -2	48.672	1.869	1 2 7 /1 3 -2	48.773	1.866
1 0 5	52.614	1.738	1 3 5	54.635	1.678
1 3 5	54.734	1.676	0 0 6	56.742	1.621
0 0 6	56.587	1.625	3 2 0	58.246	1.583
3 2 0	58.007	1.589	3 0 2	58.896	1.567
3 0 2	58.799	1.569	2 0 -5	59.375	1.555
2 0 -5	59.191	1.560			

Table S3: continued

(e) $Ni_{0.33}Cu_{0.67}(OAc)_{0.51}(OH)_{1.49}\cdot 0.43H_2O$			(f) $Ni_{0.39}Cu_{0.61}(OAc)_{0.50}(OH)_{1.50}\cdot 0.33H_2O$		
h k l	**2θ (°)**	**d (nm)**	**h k l**	**2θ (°)**	**d (nm)**
0 0 1	9.241	9.563	0 0 1	9.510	9.292
1 0 0	16.270	5.443	0 0 2	18.900	4.691
0 1 1	17.001	5.211	1 1 0	23.380	3.802
0 0 2	18.699	4.741	0 0 3	28.460	3.134
1 0 1	20.48	4.333	1 0 3/ 0 1 3	33.390	2.681
1 0 2	21.726	4.087	1 2 3	36.010	2.492
1 1 1	25.019	3.556	0 0 4	38.280	2.349
1 1 3	26.481	3.363	2 1 -2	40.94	2.203
0 0 3	28.282	3.153	1 5 2/ 1 2 5	41.72	2.163
2 0 0	32.409	2.76	1 2 -3	45.18	2.005
2 0 1	33.243	2.693	0 0 5	47.78	1.902
1 0 3/ 0 1 3	33.634	2.662	1 2 7 / 1 3 -2	48.33	1.882
1 2 1	34.54	2.595	0 0 6	56.76	1.621
2 0 3	35.59	2.52	3 0 2	58.82	1.569
0 0 4	38.08	2.361			
0 0 4	39.12	2.301			
2 1 -2	40.232	2.24			
1 5 2/ 1 2 5	41.806	2.159			
1 2 3	45.44	1.994			
0 0 5	46.603	1.947			
1 3 -1	48.157	1.888			
1 3 -2	48.733	1.867			
1 3 5	54.271	1.689			
0 0 6	56.587	1.625			
3 0 2	58.676	1.572			

Table S3: continued

(g) $Ni_{0.42}Cu_{0.58}(OAc)_{0.52}(OH)_{1.48}\cdot 0.31H_2O$			(h) $Ni_{0.46}Cu_{0.54}(OAc)_{0.47}(OH)_{1.53}\cdot 0.24H_2O$		
h k l	**2θ (°)**	**d (nm)**	**h k l**	**2θ (°)**	**d (nm)**
0 0 1	9.483	9.319	0 0 1	9.535	9.268
1 0 0	16.479	5.375	1 0 0	16.537	5.356
0 0 2	19.132	4.635	0 1 1	17.749	4.993
1 0 1	20.396	4.351	0 0 2	19.164	4.628
1 1 0	22.654	3.922	1 0 1	20.423	4.345
0 0 3	28.902	3.087	1 1 1	23.278	3.818
2 0 0	32.018	2.793	0 0 3	28.922	3.085
2 0 1	33.261	2.691	1 0 3/ 0 1 3	33.302	2.688
1 2 1	34.577	2.592	1 2 1	34.801	2.576
2 0 3	35.888	2.5	2 0 3	35.945	2.496
2 1 3	38.921	2.312	0 0 4	39.03	2.306
2 1 -2	40.19	2.242	1 1 7/ 2 1 -2	40.918	2.204
0 0 4	40.876	2.206	2 1 5	43.753	2.067
2 1 5	43.701	2.070	1 2 -3	45.21	2.004
1 2 -3	45.147	2.007	0 0 5	47.623	1.908
0 0 5	47.602	1.909	1 2 7 / 1 3 -2	48.393	1.879
1 2 7 / 1 3 -2	48.414	1.879	3 1 2	55.655	1.65
3 1 2	55.619	1.651	2 0 -5	59.525	1.552
2 0 -5	59.114	1.562			

(i) $Ni_{0.51}Cu_{0.49}(OAc)_{0.44}(OH)_{1.56}\cdot 0.28H_2O$			(j) $Ni_{0.59}Cu_{0.41}(OAc)_{0.51}(OH)_{1.49}\cdot 0.48H_2O$		
h k l	**2θ (°)**	**d (nm)**	**h k l**	**2θ (°)**	**d (nm)**
0 0 1	9.535	9.268	0 0 1	9.384	9.417
1 0 0	16.537	5.356	1 0 0	16.651	5.32
0 1 1	17.749	4.993	0 1 1	17.067	5.191
0 0 2	19.164	4.628	0 0 2	18.836	4.707
1 0 1	20.423	4.345	1 0 1	20.646	4.298
1 1 1/1 1 2	23.278	3.818	1 0 2	21.915	4.052
0 0 3	28.922	3.085	1 1 1/ 1 1 2	25.161	3.536
1 0 3/ 0 1 3	33.302	2.688	1 1 3	26.868	3.316

1 2 1	34.801	2.576	0 0 3	28.428	3.137
2 0 3	35.945	2.496	1 0 3/ 0 1 3	33.24	2.693
0 0 4	39.03	2.306	2 0 2	33.63	2.663
1 1 7/ 2 1 -2	40.918	2.204	2 0 3	35.482	2.528
2 1 5	43.753	2.067	1 2 3	36.772	2.442
1 2 -3	45.21	2.004	0 0 4	40.081	2.248
0 0 5	47.623	1.908	1 5 2/ 1 2 5	42.016	2.149
1 2 7 / 1 3 -2	49.142	1.852	0 0 5	46.427	1.954
3 1 2	55.655	1.650	1 2 7 / 1 3 -2	48.82	1.864
0 0 6	56.79	1.620	1 2 4	54.001	1.697
2 0 -5	59.525	1.552	0 0 6	56.789	1.62
			3 0 2	58.932	1.566
			2 0 -5	59.827	1.545

(k) $Ni_{0.78}Cu_{0.22}(OAc)_{0.47}(OH)_{1.53}\cdot 0.45H_2O$

2θ (°)	**d (nm)**	**hkl**
9.426	9.375	0 0 1
18.836	4.707	0 0 2
21.957	4.045	1 0 1
22.644	3.924	1 1 0
25.5828	3.479	1 1 1
28.303	3.151	0 0 3
33.297	2.689	1 0 3/ 0 1 3
35.545	2.524	2 0 3
40.039	2.25	1 1 7/ 2 1 -2
42.078	2.146	1 5 2/ 1 2 5
46.385	1.956	0 0 5
48.82	1.864	1 2 7 / 1 3 -2
54.084	1.694	1 3 5
59.161	1.560	2 0 -5
59.993	1.541	0 0 6

Table S4(a): MP-AES analysis of $Ni_{0.04}Cu_{0.96}$ acetate hydroxides (1Ni:9Cu reaction product)

Analysis #	Mass of solid (g)	Mass of digested solution (g)	Dilution of digested solution		MP-AES reading of the diluted solution (ppm)		Average Percent (%)	
			m_1 (g)	m_2 (g)	Ni	Cu	Ni	Cu
	0.0108	19.5970	2.361	12.4133	1.52	40.81	1.46 ±0.012	38.8 ±1.02
1					1.55	42.14		
					1.53	39.11		

Table S4(b): MP-AES analysis of $Ni_{0.10}Cu_{0.90}$ acetate hydroxides (1Ni:3Cu reaction product)

Analysis #	Mass of solid (g)	Mass of digested solution (g)	Dilution of digested solution		MP-AES reading of the diluted solution (ppm)		Average Percent (%)	
			m_1 (g)	m_2 (g)	Ni	Cu	Ni	Cu
1	0.0113	9.6395	0.2848	11.9539	1.31	11.32	4.30 ±0.34	40.3 ±0.25
2	0.0119	8.5549	0.3041	11.3432	1.52	14.93		
3	0.0122	9.8222	0.4165	11.1978	1.91	18.65		

Table S4(c): MP-AES analysis of $Ni_{0.13}Cu_{0.87}$ acetate hydroxides (1Ni:2Cu reaction product)

Analysis #	Mass of solid (g)	Mass of digested solution (g)	Dilution of digested solution		MP-AES reading of the diluted solution (ppm)		Percent (%)	
			m_1 (g)	m_2 (g)	Ni	Cu	Ni	Cu
							5.56	40.3
1	0.0201	20.1380	0.2173	10.2244	1.18	8.55		

Table S4(d): MP-AES analysis of $Ni_{0.22}Cu_{0.78}$ acetate hydroxides (1Ni:1Cu reaction product)

Analysis #	Mass of solid (g)	Mass of digested solution (g)	Dilution of digested solution		MP-AES reading of the diluted solution (ppm)		Average Percent (%)	
			m_1 (g)	m_2 (g)	Ni	Cu	Ni	Cu
1	0.0116	12.8171	0.2094	10.9238	1.73	6.57	9.73 ±0.19	37.6 ±0.77
2	0.0184	19.3600	0.1921	10.3750	1.72	6.43		
3	0.0114	12.0120	0.2215	10.7240	1.85	7.52		

Table S4(e): MP-AES analysis of $Ni_{0.33}Cu_{0.67}$ acetate hydroxides (2Ni:1Cu reaction product)

Analysis #	Mass of solid (g)	Mass of digested solution (g)	Dilution of digested solution		MP-AES reading of the diluted solution (ppm)		Percent (%)	
			m_1 (g)	m_2 (g)	Ni	Cu	Ni	Cu
							14.8	32.1
1	0.0117	12.2738	0.2116	10.4414	6.34	2.92		

Table S4(f): MP-AES analysis of $Ni_{0.39}Cu_{0.61}$ acetate hydroxides (3Ni:1Cu reaction product)

Analysis #	Mass of solid (g)	Mass of digested solution (g)	Dilution of digested solution		MP-AES reading of the diluted solution (ppm)		Average Percent (%)	
			m_1 (g)	m_2 (g)	Ni	Cu	Ni	Cu
1	0.0105	8.7025	0.5189	11.9869	8.99	15.42	16.7 ±0.49	28.8 ±0.66
2	0.0106	9.0466	0.5128	9.2188	10.72	18.55		
3	0.0121	8.9332	0.2665	9.6693	6.08	10.57		

Table S4(g): MP-AES analysis of $Ni_{0.42}Cu_{0.58}$ acetate hydroxides (4Ni:1Cu reaction product)

Analysis #	Mass of solid (g)	Mass of digested solution (g)	Dilution of digested solution		MP-AES reading of the diluted solution (ppm)		Average Percent (%)	
			m_1 (g)	m_2 (g)	Ni	Cu	Ni	Cu
1	0.0122	8.1387	0.5076	10.3784	13.40	20.00	17.0 ±0.29	27.0 ±0.64
2	0.0111	0.3235	0.2728	8.4206	10.12	6.83		
3	0.0121	8.9229	0.4985	9.9061	12.25	18.71		

Table S4(h): MP-AES analysis of $Ni_{0.46}Cu_{0.54}$ acetate hydroxides (6Ni:1Cu reaction product)

Analysis #	Mass of solid (g)	Mass of digested solution (g)	Dilution of digested solution		MP-AES reading of the diluted solution (ppm)		Average Percent (%)	
			m_1 (g)	m_2 (g)	Ni	Cu	Ni	Cu
	0.0129	20.8795	3.1880	8.4082	44.78	56.93	18.5 ±0.98	23.4 ±1.13
1					41.64	51.11		
					39.18	56.55		

Table S4(i): MP-AES analysis $Ni_{0.51}Cu_{0.49}$ acetate hydroxides (7Ni:1Cu reaction product)

Analysis #	Mass of solid (g)	Mass of digested solution (g)	Dilution of digested solution		MP-AES reading of the diluted solution (ppm)		Average Percent (%)	
			m_1 (g)	m_2 (g)	Ni	Cu	Ni	Cu
	0.0136	20.6982	4.9121	11.4890	63.61	64.91	21.6 ±1.71	22.7 ±0.32
1					64.75	63.67		
					54.03	62.72		

Table S4(j): MP-AES analysis of $Ni_{0.59}Cu_{0.41}$acetate hydroxides (9Ni:1Cu reaction product)

Analysis #	Mass of solid (g)	Mass of digested solution (g)	Dilution of digested solution		MP-AES reading of the diluted solution (ppm)		Percent (%)	
			m_1 (g)	m_2 (g)	Ni	Cu	Ni	Cu
1	0.0240	20.4499	3.044	10.190	87.41	66.38	24.9	18.9

Table S4(k): MP-AES analysis of $Ni_{0.78}Cu_{0.22}$ acetate hydroxides (50Ni:1Cu reaction product)

Analysis #	Mass of solid (g)	Mass of digested solution (g)	Dilution of digested solution		MP-AES reading of the diluted solution (ppm)		Percent (%)	
			m_1 (g)	m_2 (g)	Ni	Cu	Ni	Cu
1	0.0143	20.8455	4.251	12.302	80.96	24.70	34.6	10.4

Table S5: Crystallite sizes of the nickel oxide phase in mixed oxides of $(NiO)_{0.22}(CuO)_{0.78}O$, $(NiO)_{0.33}(CuO)_{0.67}O$, and $(NiO)_{0.39}(CuO)_{0.61}$, determined using the XRD peaks at around 37.2° (*111*, NiO) and employing Scherrer equation

Nickel-copper oxides	Average Full Width Half Maximum (FWHM)	Average crystallite sizes (nm)
$Ni_{0.22}Cu_{0.78}O$	0.245	34.2
$Ni_{0.33}Cu_{0.67}O$	0.416	20.1
$Ni_{0.39}Cu_{0.61}O$	0.645	13.0

Table S6(a): Indexing of XRD peaks of $(NiO)_{0.10}(CuO)_{0.90}$ and $(NiO)_{0.22}(CuO)_{0.78}$ prepared by pyrolysis of the corresponding nickel-copper acetate hydroxides

Miller Indices	**$(NiO)_{0.10}(CuO)_{0.90}$**		**$(NiO)_{0.22}(CuO)_{0.78}$**	
hkl	**2θ (°)**	**d (nm)**	**2θ (°)**	**d (nm)**
1 1 0	32.449	2.757	32.595	2.745
0 0 2	35.482	2.528	35.607	2.519
1 1 1 (NiO)	37.219	2.414	37.282	2.41
2 0 0	38.655	2.327	38.78	2.32
2 0 0 (NiO)	43.254	2.09	43.441	2.081
1 1 -2	46.229	1.962	46.479	1.952
-2 0 2	48.809	1.864	48.929	1.86
2 0 2	53.408	1.714	53.512	1.711
0 2 0	58.188	1.584	58.36	1.58
-3 1 1	61.544	1.506	61.668	1.503
2 2 0 (NiO)	62.855	1.477	62.855	1.477
1 1 3	65.768	1.419	65.955	1.415
3 3 1	66.309	1.408	66.376	1.407

Table S6(b): Indexing of XRD peaks of $(NiO)_{0.33}(CuO)_{0.67}$ and $(NiO)_{0.39}(CuO)_{0.61}$ prepared by pyrolysis of the corresponding nickel-copper acetate hydroxides

Miller Indices	**$(NiO)_{0.33}(CuO)_{0.67}$**		**$(NiO)_{0.39}(CuO)_{0.61}$**	
hkl	**2θ (°)**	**d (nm)**	**2θ (°)**	**d (nm)**
1 1 0	32.455	2.756	32.475	2.755
0 0 2	35.477	2.528	35.503	2.526
New peak	36.392	2.467	36.45	2.463
1 1 1 (NiO)	37.136	2.419	37.074	2.423
2 0 0	38.666	2.327	38.676	2.326
2 0 0 (NiO)	43.233	2.091	43.316	2.087
1 1 -2	46.229	1.962	46.25	1.961
-2 0 2	48.794	1.865	48.825	1.864
2 0 2	53.408	1.714	53.408	1.714
0 2 0	58.194	1.584	58.194	1.584
-3 1 1	61.507	1.506	61.559	1.505
2 2 0 (NiO)	62.813	1.478	62.813	1.478
1 1 3	65.788	1.418	65.747	1.419
3 3 1	66.288	1.409	66.293	1.409

■ References:

(1) Yamanaka, S.; Sako, T.; Seki, K.; Hattori, M., Anion exchange reactions in layered basic copper salts. *Solid State Ionics* **1992,** 53-56, 527-533.

(2) He, J.; Xu, P.; Sun, J., Fe and B Codoped Nickel Zinc Layered Double Hydroxide for Boosting the Oxygen Evolution Reaction. *ACS Sustainable Chemistry & Engineering* **2020,** 8, (7), 2931-2938.

(3) Kozai, N.; Mitamura, H.; Fukuyama, H.; Esaka, F.; Komarneni, S., Synthesis and characterization of nickel–copper hydroxide acetate, $NiCu(OH)_{3.1}(OCOCH3)_{0.9}\cdot 0.9H_2O$. *Microporous and Mesoporous Materials* **2006,** 89, (1-3), 123-131.

(4) Meyn, M.; Beneke, K.; Lagaly, G., Anion-exchange reactions of hydroxy double salts. *Inorganic Chemistry* **1993,** 32, (7), 1209-1215.

(5) Kozai, N.; Ohnuki, T.; Komarneni, S., Selenium oxyanions: Highly selective uptake by a novel anion exchanger. *Journal of Materials Research* **2002,** 17, (12), 2993-2996.

(6) Yuasa, H. N. a. K., Preparation of Anion Exchangeable Layered Mixed Basic Salt $Ni_{1-x}Zn_{2x}(OH)_2(OCOCH_3)_2\cdot nH_2O$ Thin Film under Hydrothermal Condition. *Journal of Solid State Chemistry* **1998,** 141, 229-234.

(7) Komarneni, S.; Li, Q. H.; Roy, R., Microwave-hydrothermal processing of layered anion exchangers. *Journal of Materials Research* **1996,** 11, (8), 1866-1869.

(8) Guo, X. L.; Liu, X. Y.; Hao, X. D.; Zhu, S. J.; Dong, F.; Wen, Z. Q.; Zhang, Y. X., Nickel-Manganese Layered Double Hydroxide Nanosheets Supported on Nickel Foam for High-performance Supercapacitor Electrode Materials. *Electrochimica Acta* **2016,** 194, 179-186.

(9) Hawkes, S. J., All Positive Ions Give Acid Solutions in Water. *Journal of Chemical Education* **1996,** 73, (6), 516.

(10) Poul, L.; Jouini, N.; Fiévet, F., Layered Hydroxide Metal Acetates (Metal = Zinc, Cobalt, and Nickel): Elaboration via Hydrolysis in Polyol Medium and Comparative Study. *Chemistry of Materials* **2000,** 12, (10), 3123-3132.

(11) Wang, F.; Wang, T.; Sun, S.; Xu, Y.; Yu, R.; Li, H., One-step synthesis of Nickle Iron-layered double hydroxide/reduced graphene oxide/carbon nanofibres composite as electrode materials for asymmetric supercapacitor. *Sci Rep* **2018,** 8, (1), 8908.

(12) Xu, K.; Chen, G.; Shen, J., Facile synthesis of submicron-scale layered double hydroxides and their direct decarbonation. *RSC Advances* **2014,** 4, (17).

(13) Hall, D. S.; Lockwood, D. J.; Bock, C.; MacDougall, B. R., Nickel hydroxides and related materials: a review of their structures, synthesis and properties. *Proc Math Phys Eng Sci* **2015,** 471, (2174), 20140792.

(14) Švarcová, S.; Klementová, M.; Bezdička, P.; Łasocha, W.; Dušek, M.; Hradil, D., Synthesis and characterization of single crystals of the layered copper hydroxide acetate $Cu_2(OH)_3(CH_3COO)\cdot H_2O$. *Crystal Research and Technology* **2011,** 46, (10), 1051-1057.

(15) Bette, S.; Kremer, R. K.; Eggert, G.; Tang, C. C.; Dinnebier, R. E., On verdigris, part I: synthesis, crystal structure solution and characterisation of the 1-2-0 phase ($Cu_3(CH_3COO)_2(OH)_4$). *Dalton Trans* **2017,** 46, (43), 14847-14858.

(16) Secco, E. A.; Worth, G. G., Infrared spectra of unannealed and of annealed $Cu_4(OH)_6(NO_3)_2$. *Canadian Journal of Chemistry* **1987,** 65, (10), 2504-2508.

(17) Masciocchi, N.; Corradi, E.; Sironi, A.; Moretti, G.; Minelli, G.; Porta, P., Preparation, Characterization, andab initioX-Ray Powder Diffraction Study of $Cu_2(OH)_3(CH_3COO)\cdot H_2O$. *Journal of Solid State Chemistry* **1997,** 131, (2), 252-262.

(18) Kandare, E.; Hossenlopp, J. M., Thermal Degradation of Acetate-Intercalated Hydroxy Double and Layered Hydroxy Salts. *Inorganic Chemistry* **2006,** 45, (9), 3766-3773.

(19) Eric, H.; Timuçin, M., Equilibrium relations in the system nickel oxide-copper oxide. *Metallurgical Transactions B* **1979,** 10, (4), 561-563.

(20) Meyn, M.; Beneke, K.; Lagaly, G., Anion-exchange reactions of layered double hydroxides. *Inorganic Chemistry* **1990,** 29, (26), 5201-5207.

(21) RAJAMATHI, J. T. R. S. B. M., Synthesis and anion exchange reactions of a layered copper-zinc hydroxy double salt, $Cu_{1.6}Zn_{0.4}(OH)_3(OAc)\cdot H_2O$. *Journal of Chemical Sciences* **2005,** 117, (6), 629-633.

(22) Volanti, D. P.; Orlandi, M. O.; Andrés, J.; Longo, E., Efficient microwave-assisted hydrothermal synthesis of CuO sea urchin-like architectures via a mesoscale self-assembly. *CrystEngComm* **2010,** 12, (6), 1696-1699.

(23) Yan, H.; Zhang, D.; Xu, J.; Lu, Y.; Liu, Y.; Qiu, K.; Zhang, Y.; Luo, Y., Solution growth of NiO nanosheets supported on Ni foam as high-performance electrodes for supercapacitors. *Nanoscale Research Letters* **2014,** 9, (1), 424.

(24) Meloni, D.; Monaci, R.; Solinas, V.; Auroux, A.; Dumitriu, E., Characterisation of the active sites in mixed oxides derived from LDH precursors by physico-chemical and catalytic techniques. *Applied Catalysis A: General* **2008,** 350, (1), 86-95.

(25) Huang, J.-M.; Xu, L.-F.; Qian, C.; Chen, X.-Z., N-alkylation of ethylenediamine with alcohols catalyzed by CuO-NiO/γ-Al_2O_3. *Chemical Papers* **2012,** 66, (4).

(26) Chen, X.; Luo, H.; Qian, C.; He, C., Research on the N-alkylation of morpholine with alcohols catalyzed by CuO–NiO/γ–Al_2O_3. *Reaction Kinetics, Mechanisms and Catalysis* **2011,** 104, (1), 163-171.

(27) De Rogatis, L.; Montini, T.; Cognigni, A.; Olivi, L.; Fornasiero, P., Methane partial oxidation on NiCu-based catalysts. *Catalysis Today* **2009,** 145, (1-2), 176-185.

CHAPTER VA

Reaction of Zinc Acetate and Water: Deposition of Nanosphere-type $ZnO/Zn(OH)_2$

■ Introduction

To develop a simple deposition route and inquire further about the hydrolysis of later 3d transition metal acetates without a second reactant or organic solvent/reagent that deposits nanostructured metal oxides via their layered hydroxides (as presented in Chapters II and III), We were very much interested and motivated to investigate hydrolysis of zinc acetate to access nanostructured ZnO. Therefore, this chapter explores the hydrolysis of zinc acetate without an additional reagent/reactant to find out what material and nanostructure the hydrolysis process can generate.

Nanostructures of ZnO are valuable and attractive materials in various well-established and emerging technologies. For example, recently, it has been shown that nanostructured ZnO deposited onto fluorine-doped tin oxide substrates can efficiently electro-catalyze water to hydrogen peroxide.[1] ZnO nanoparticles have also been widely used as photocatalysts to degrade organic pollutants from water [2, 3] and as a catalyst for useful organic transformations.[4-6] While ZnO nanoparticles-loaded catalyst supports are promising materials for industrial catalytic applications such as biodiesel production.[7] Additionally, nano-/micro-structured ZnO films are up-and-coming materials in metal oxide semiconductor-based applications such as photovoltaics,[8, 9] field-effect

transistors,[10] biosensors,[11] transparent (semi-)conductive glasses,[12] electron-transport layers in perovskite solar cells,[13] piezoelectric device,[14] etc. As a result, since nanostructured ZnO can be used in a wide variety of applications mentioned above, in recent years, developing inexpensive, large-area accessible and scalable, lesser chemical involving, and straightforward deposition routes for nanostructured ZnO on substrates have drawn significant interest and widely investigated.

Herein this contribution, we report our investigation of hydrolysis of only zinc acetate acetates (without any additional reactant or organic solvent/reagent) that presents a new finding in the hydrothermal process to access nanostructured ZnO. It turned out that, unlike copper or nickel acetate, as discussed in the previous Chapters II and III, hydrolysis reaction of only zinc acetate at 95°C deposited white-colored films made up of nanosphere-type particles of zinc hydroxide/zinc oxide, $ZnO/Zn(OH)_2$. As the reaction involves only an aqueous solution of zinc acetate, water plays the role of a solvent as well as a reactant. Reactions of 0.25M zinc acetate aqueous solutions were investigated with clean glass substrates and gold-palladium coated glass substrates under the same reaction condition. It turned out that reactions deposited similar nanosphere-type morphology of $Zn(OH)_2/ZnO$ on both substrates. These deposited nanosphere-type $Zn(OH)_2/ZnO$ films were readily converted to zinc oxide, ZnO films by pyrolysis.

■ Experimental

Materials: Zinc acetate dehydrate, $Zn(OAc)_2 \cdot 2H_2O$ was purchased from Baker Analyzed Reagent and used without further purification, and deionized water was used as the solvent. Microscope glass slides were employed as substrates.

Cleaning glass substrates: The glass slides were first washed with soap water, followed by regular water, then deionized water and acetone. After final rinsing with deionized water followed by oven drying, they were used in the hydrothermal reactions.

Preparation of gold/palladium coated microscope glass slides: Gold/palladium coating on the microscope glass slides was performed using a sputter coater at Microscopy Laboratory of Oklahoma State University, Stillwater, OK 74078, USA. The sputter coater was operated at a high vacuum where argon gas was used as the agent gas, and a commercial gold/palladium rod was used as a target for the sputtering process. Each sputtering experiment was performed for 15 seconds to coat the microscope glass slides.

Deposition of $Zn(OH)_2$/ZnO films and their pyrolysis: A freshly prepared 40.02 g of 0.2499 M zinc acetate solution was taken in a 100 mL screw-cap pyrex media bottle for a typical hydrothermal reaction. A pre-cleaned microscope glass slide or a gold-palladium coated microscope glass slide was placed vertically inside the bottle. The solution was then heated in an oven at 95°C for 96 hours. After around 24 hours, a solid white film started appearing on the substrate, but the reaction was done for 96 hours to get a thicker film (Figure 1). The film was washed in deionized water thoroughly, followed by dried under air. The film of $Zn(OH)_2$/ZnO was pyrolyzed in an oven at 600 °C for 30 minutes. The heating rate to reach 600 °C was 10 °C per minute.

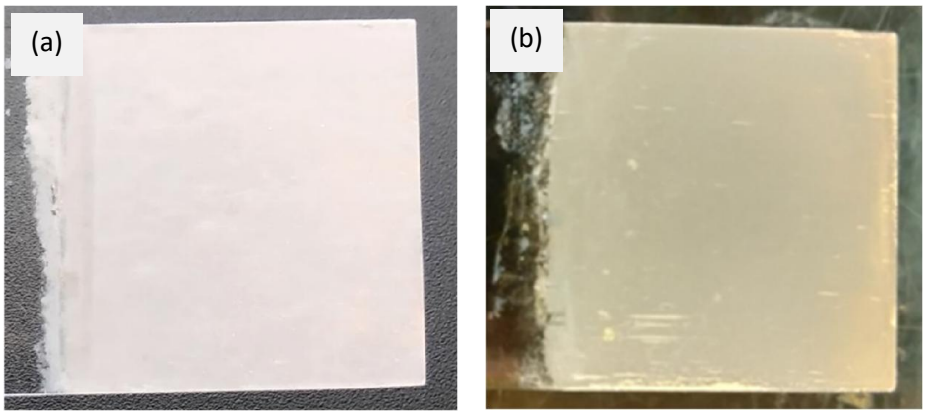

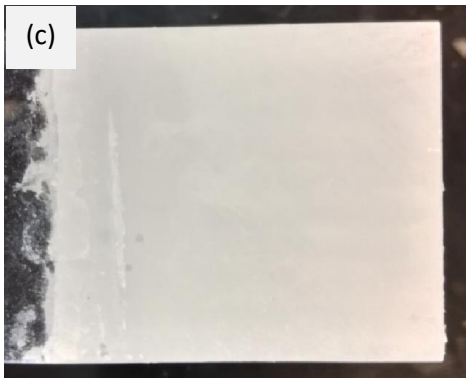

Figure 1: $ZnO/Zn(OH)_2$ films on (a) microscope glass slide and (b) gold-palladium microscope glass slide. (c) ZnO film on a microscope glass slide (after pyrolysis at 600 °C).

Characterization: XRD Bruker Discover D8, TGA Perkins Elmer TGA4000, FEI Quanta Scanning electron microscope, and Nicolet i50 ATR-FTIR instruments were used to characterize the films.

■ Results and Discussions

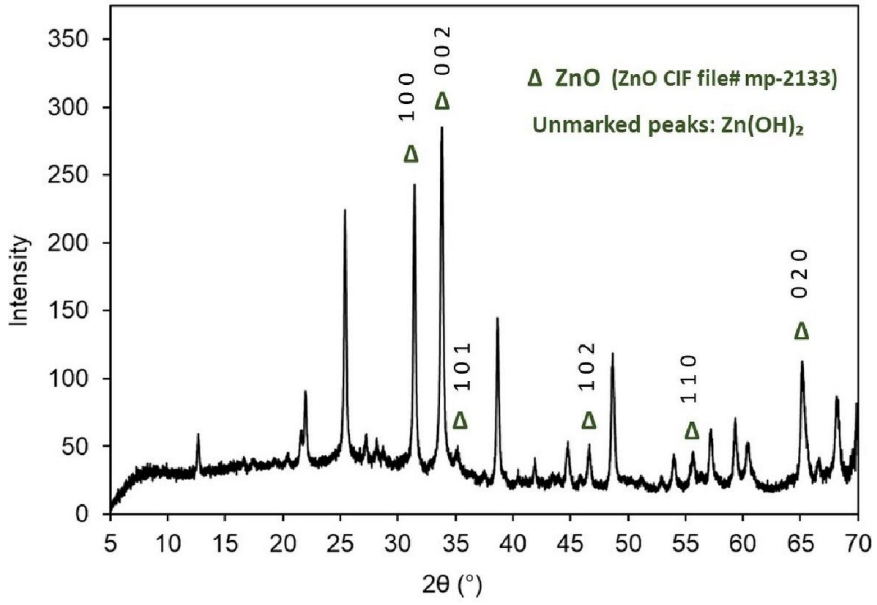

Figure 2: XRD of $ZnO/Zn(OH)_2$ film on a microscope glass slide prepared by hydrolysis of zinc acetate aqueous solution.

Table 1: Two thetas and d-spacings of the XRD peaks of a ZnO/$Zn(OH)_2$ film.

2θ (°)	**d-spacing (nm)**	**Phase**
12.65	6.992	$Zn(OH)_2$
16.60	5.336	$Zn(OH)_2$
17.51	5.061	$Zn(OH)_2$
20.43	4.343	$Zn(OH)_2$
21.61	4.109	$Zn(OH)_2$
21.95	4.046	$Zn(OH)_2$
25.41	3.502	$Zn(OH)_2$
27.27	3.268	$Zn(OH)_2$
28.16	3.166	$Zn(OH)_2$
28.72	3.106	$Zn(OH)_2$
31.44	2.843	ZnO (1 0 0)
33.82	2.648	ZnO (0 0 2)
35.20	2.547	ZnO (1 0 1)
37.51	2.396	$Zn(OH)_2$
38.67	2.326	$Zn(OH)_2$
41.90	2.154	$Zn(OH)_2$
44.78	2.022	$Zn(OH)_2$
45.87	1.977	$Zn(OH)_2$
46.64	1.946	ZnO (1 0 2)
48.69	1.869	$Zn(OH)_2$
51.13	1.785	$Zn(OH)_2$
52.90	1.729	$Zn(OH)_2$
53.98	1.697	$Zn(OH)_2$
55.66	1.65	ZnO (1 1 0)
57.22	1.609	$Zn(OH)_2$
59.33	1.556	$Zn(OH)_2$
60.39	1.532	$Zn(OH)_2$
65.16	1.43	ZnO (2 0 0)
66.62	1.403	$Zn(OH)_2$
68.13	1.375	$Zn(OH)_2$

XRD pattern of a typical ZnO/$Zn(OH)_2$ film deposited on a glass slide is presented in Figure 2, and the 2θ and d-spacing peaks are tabulated in Table 1. The peaks marked by Δ are matched with the ZnO phase (calculated XRD pattern using ZnO crystal structure of a conventional standard, ZnO CIF file# mp-2133[20]). The other peaks are not marked by Δ agrees with the peak positions of the $Zn(OH)_2$ phase (JCPDS 01-089-013[21] or COD ID# 9015545[22]). This establishes that film is a two-phase material of ZnO/$Zn(OH)_2$. The TGA experiment and FTIR analysis (discussed later) also confirm that deposited white material is ZnO/$Zn(OH)_2$, supporting the XRD result.

Interestingly, in our work, the peak at 35.20° for ZnO (*1 0 2*) is shifted from the reference value of 35.75°, and the peak at 65.16 for ZnO (*0 2 0*) is also sifted from 65.48°. This shifting of reflections may occur because the particles are grown as thin films where lattice strain or interplanar distances are likely to be different than the bulk material. Notably, the XRD reflection at 35.20° is much less intense than the often reported ZnO phase. Nevertheless, the *1 0 0*, *0 0 2*, and *2 0 0* reflections of ZnO are relatively sharp in the two-phase ZnO/$Zn(OH)_2$ material system, suggesting X-ray reflections from large crystallite domains of the ZnO phase. The size of the deposited sphere-type ZnO/$Zn(OH)_2$ particles determined using an SEM image is 880±160 nm (Table 4), agreeing with the sharp reflections of the XRD patterns. While the average crystallite size of the ZnO phase is 96±33 nm (determined using 100, 002, and 020 planes) shows that the ZnO phase was grown with crystallites big as around 100 nm. This also suggests initially deposited nucleated particles (nano-crystallites less than 100 nm) were developed into bigger crystallites with time since they were transformed to the ZnO phase during the growth process of the hydrolysis reaction.

The two-phase material establishes that the hydrolysis reaction initially nucleated zinc acetate hydroxide, $Zn(OAc)_x(OH)_{2-x}$ or $Zn(OH)_2$ (discussed later), which later converted to ZnO/ $Zn(OH)_2$ at the hydrothermal condition. The strong intensities for peaks at 31.44° (1 0 0) and

33.82° (0 0 2) are very common for various nanostructures of ZnO.[18] However, besides these two peaks in our study, the 65.16 ° (0 2 0) reflections are also kind of intense. These intense reflections of the 1 0 0, 0 0 2, and 0 2 0 planes indicate that the particles were grown three-dimensionally along the lattice axes. Indeed ZnO/$Zn(OH)_2$ particles were deposited three-dimensionally as nanosphere-type of particles on the substrates, as shown in SEM images (Figures 5 and 6), confirming that the XRD pattern is consistent with the morphology of the particles.

Notably, intensities of the peaks of $Zn(OH)_2$ are different than the reference $Zn(OH)_2$ as the material in the present investigation is nano-/micro-particles deposited as a thin film. The reflection at 12.65° should correspond to 001 planes $Zn(OH)_2$ phase, which is not observed in $Zn(OH)_2$ reference, JCPDS 01-089-013[21] due to the 2θ range of the XRD pattern was 20-70°. However, the calculated XRD pattern using a standard $Zn(OH)_2$ CIF file (CIF file # mp-625830[23]) shows possible theoretical reflections at the lower angles of 10-18°.

Table 2: Average crystallite size of the ZnO phase determined using Scherrer Equation[24]

2θ (°)	**FWHM**	**Crystallite size (nm)**	**Average crystallite size (nm)**
31.44	0.230	126	96±33
32.82	0.240	112	
65.16	0.280	50	

The thermogravimetric analysis (TGA) plot (Figure 3), in conjunction with the differential thermogravimetric plot (dotted line), exhibited a 2.23% mass loss for water up to 160 °C. These water molecules are connected through H-bonding with the hydroxide groups of $Zn(OH)_2$ and/or oxide of ZnO, as confirmed by the FTIR plot (Figure 4). After 160 °C, the mass loss must be due to dehydroxylation of hydroxide groups as water in the $Zn(OH)_2$ phase to reach ceramic product ZnO at 600 °C. There is still a slight mass loss after 600 to 775 °C suggesting the loss of a tiny

amount of spare hydroxyl groups that are not dehydroxylated within 600 °C. These spare hydroxyl groups may not be in the vicinity of each other. As a result, these hydroxyl groups need to migrate across the material to come close to each other to be dehydroxylated as water; since to dehydroxylate as one water molecule, two hydroxyl groups are required. The migration of these spare hydroxyls should occur at relatively high temperatures. In addition, the TGA experiment is a temperature scan plot; therefore, leftover hydroxyl groups are dehydroxylated after 600 °C. Nevertheless, the ceramic yield in the TGA plot is 92.81% at 775 °C, determining the total mass lass from the starting material is 7.19%. This 7.19% of mass loss confirms that the deposited white material in the hydrolysis reaction is not $Zn(OH)_2$ or zinc acetate hydroxide, $Zn(OAc)_x(OH)_{2-x}\cdot nH_2O$. The 2.23% water loss and 4.96% (7.19 - 2.23%) dehydroxylation of the $Zn(OH)_2$ phase enumerate the formula of the deposited film material as $(ZnO)_{0.14}\cdot(Zn(OH)_2)_{0.86}\cdot 0.12H_2O$.

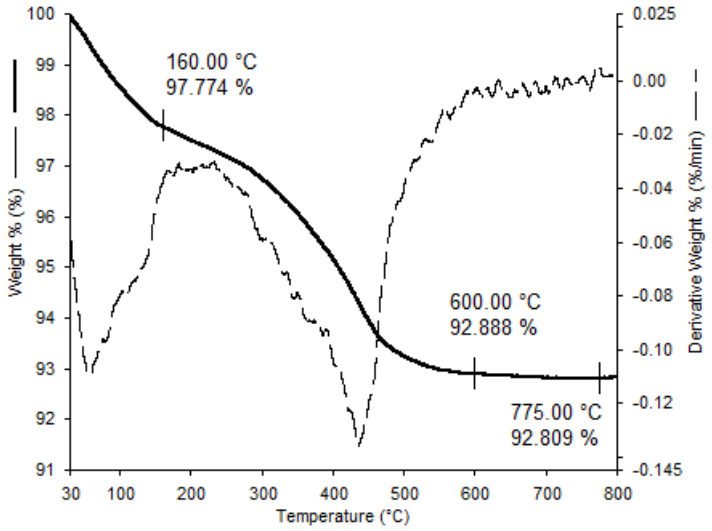

Figure 3: TGA plot of deposited $ZnO/Zn(OH)_2$ thin film material. From the TGA, the formula of the material was determined as $(ZnO)_{0.14}\cdot(Zn(OH)_2)_{0.86}\cdot 0.12H_2O$.

$$(ZnO)_{0.14}\cdot(Zn(OH)_2)_{0.86}\cdot 0.12H_2O\ (s) \xrightarrow{30\text{-}160\ ^oC} (ZnO)_{0.14}\cdot(Zn(OH)_2)_{0.86}\ (s) + 0.12H_2O\ (g)$$

$$(ZnO)_{0.14}\cdot(Zn(OH)_2)_{0.86}\ (s) \xrightarrow{160\text{ -}775\ ^oC} ZnO\ (s) + 0.43H_2O\ (g)$$

Scheme 1: Thermal events in the TGA experiment of ZnO/$Zn(OH)_2$ thin film material.

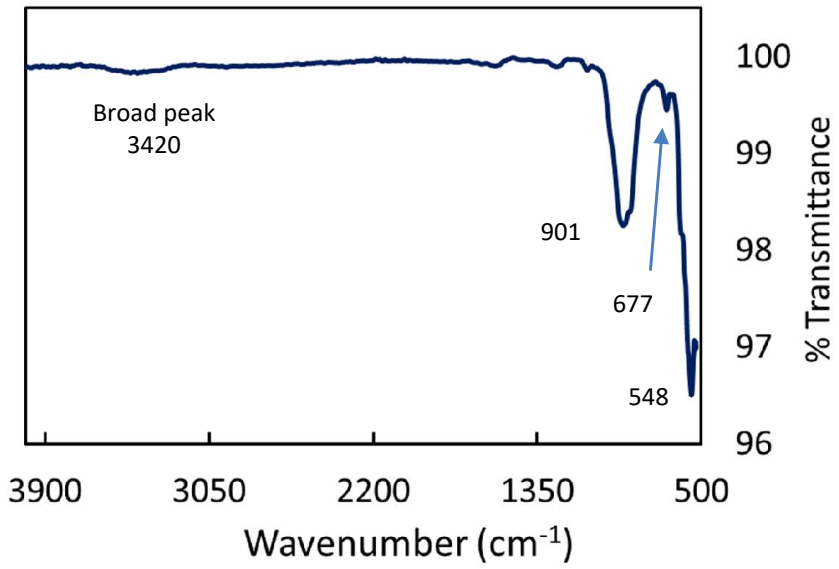

Figure 4: Attenuated total reflectance-FTIR spectrum of a deposited film of ZnO/ $Zn(OH)_2$.

Table 3: FTIR peak assignments of the ZnO/$Zn(OH)_2$ film.

Peaks (cm^{-1})	Assignment
548	Zn-O stretching
677	Week Zn-OH bending
901	Strong Zn-OH bending (out plane defamation)
1086	Zn-OH bending
3420	Hydrogen bonded -OH stretching

The film's ATR-FTIR experiment (Figure 4) is consistent with the TGA and XRD results that further establish that deposited white film is ZnO/$Zn(OH)_2$. The sharp band at 548 cm^{-1} indicates Zn-O symmetric stretching modes of $Zn(OH)_2$.[25] Also, Zn-O stretching vibration for ZnO has been reported at 570 cm^{-1} or for films at 580 cm^{-1}.[26, 27] Therefore, the Zn-O band of our study may be buried under the intense band at 548 cm^{-1} as it ranges over 525 – 636 cm^{-1}. While the bands at 677, 901, and 1086 cm^{-1} arises due to Zn-OH bending vibrations (also known as -OH librations).[25, 28] These bands also can be termed as out plane bending or deformation.[29] The broad peak at 3420 confirms the presence of H-bonded water molecules. These H-bonded water are connected through hydrogen-bonding with hydroxyl groups of the $Zn(OH)_2$ phase and/or oxide of the ZnO phase.

The hydrolysis of only zinc acetate (without any second reactant or organics) generated nanosphere-type particles as films onto glass substrates as presented in the SEM pictures (Figures 5 and 6). The significant aspects of the hydrolysis reaction are (i) it deposited almost uniformly distributed nanosphere-type particles across the substrates, and (ii) it deposited robust films of particles on the substrates meaning the particles adhered to substrates very strongly (as it required scratching to peel them off from the substrates). Pyrolysis of these nanosphere-type particles as films at 600°C directly converted them to ZnO films, as shown in the TGA experiment. Figure 1(c) presents such a ZnO film showing heating at that high temperature did not peel off or break the film material. In fact, after pyrolysis, the films of the nanoparticles got significantly more robust than the starting films (verily likely ZnO nanoparticles became cemented with the substrates), which makes them excellent candidates for various thin-film applications such as electro-/photo-catalysis, chemical/gas sensors, photoelectrodes, etc. In particular, for electro-/photo-catalytic applications, nanostructures as films needed to be robust as they would interact with chemicals and solvents and would be under voltage (electrocatalysis). In addition, in terms of electrocatalytic application (after depositing on conductive surfaces/substrates), strong bonding (robustness) of the

nanostructures onto the substrates (electrodes) is essential for better charge (electron) transfer performance in electrocatalytic processes. Also, it would be interesting to look at how the nanosphere-type morphology of ZnO performs in semiconductive-based electrolytic applications compared to other very common morphology such as hexagonal rods. Whereas photocatalysis would also be a surface phenomenon as light would absorb by the nanostructures at the surface (to be working as photocatalysts) rather than the nanostructures buried under the aggregated nanostructures deposited onto supports or substrates. Therefore, uniformly distributed nanosphere-type ZnO (after pyrolysis of the deposited $ZnO/Zn(OH)_2$ film*) would also be an excellent nanostructure for photocatalysis.

* (Note): Most likely, the pyrolysis will retain the morphology of the nanospheres-type particles. Pyrolysis of nanostructured metal hydroxides or layered double hydroxides often generates similar nanostructured metal oxides. For example, Chapter II shows that web-like interconnected nanowalls of nickel acetate hydroxide after pyrolysis produced nano-NiO with identical morphology.

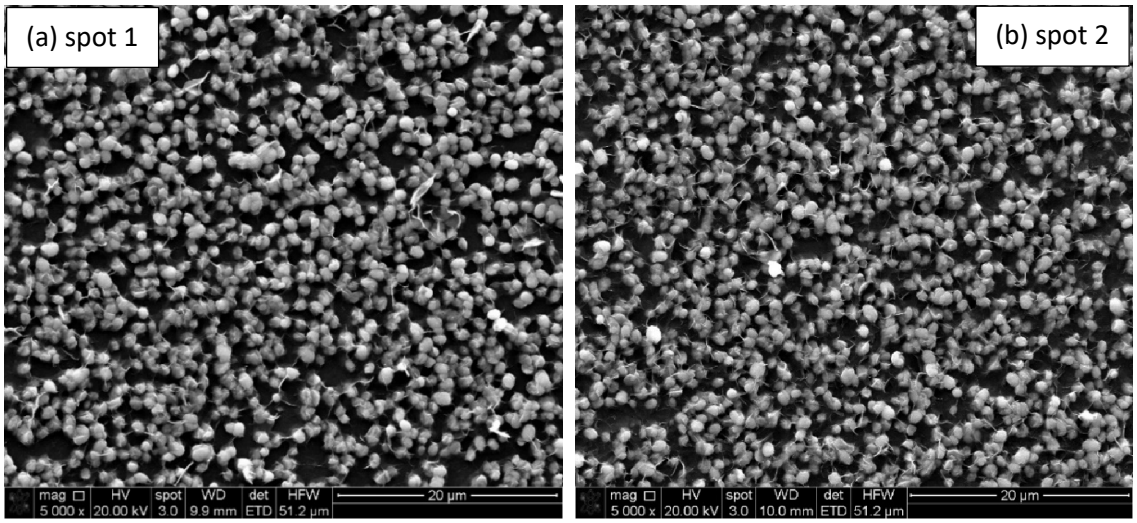

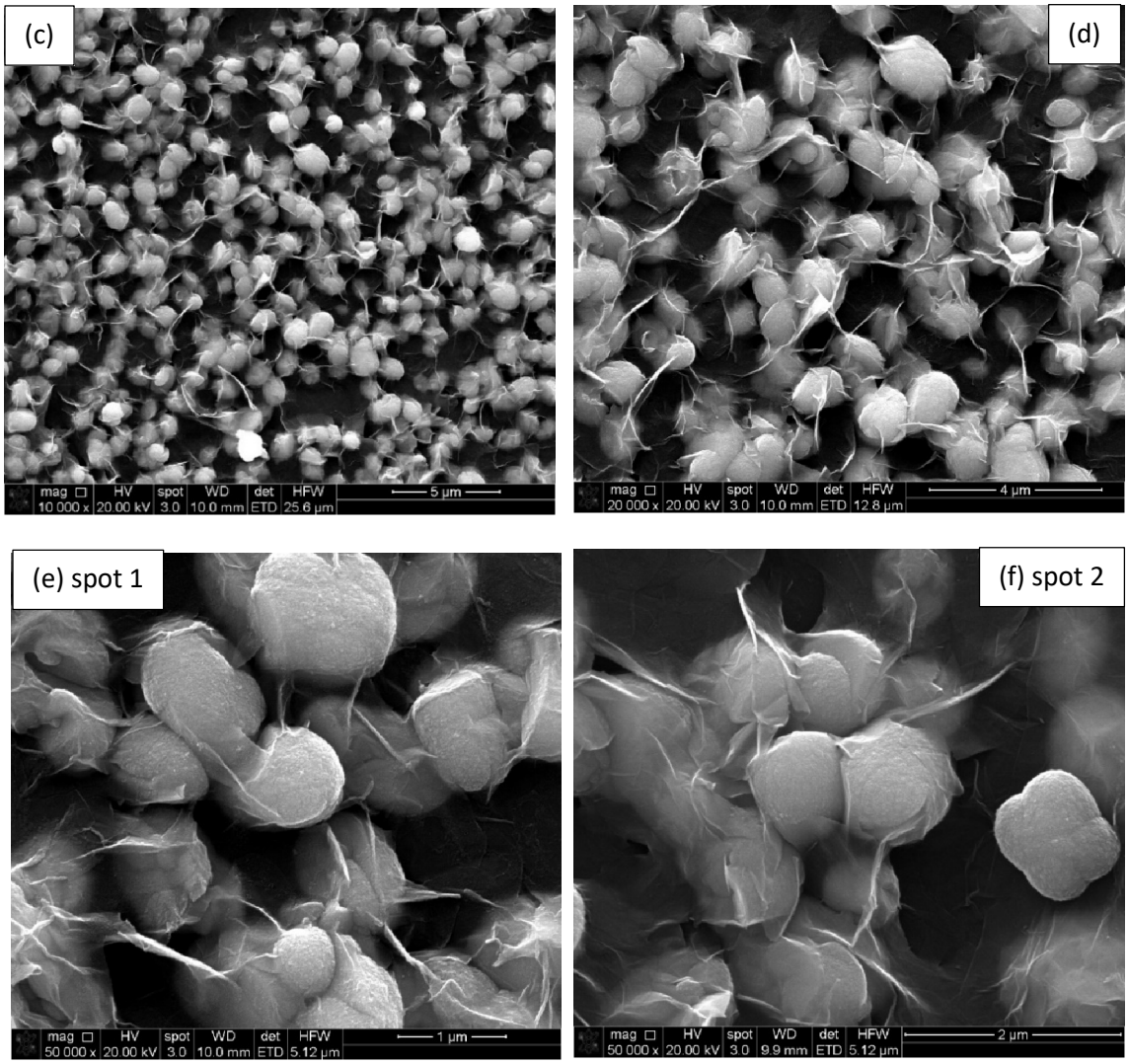

Figure 5: Scanning electron microscope images of $ZnO/Zn(OH)_2$ film on a glass substrate at different magnifications and spots.

The hydrolysis reaction also deposited similar morphology of $ZnO/Zn(OH)_2$ as films on the gold-palladium coated substrates, as evidenced by the SEM images (Figure 6). However, the average size of the nanosphere-type is grown bigger on these substrates than on the uncoated glass substrates. The ultra-thin coating of the gold-palladium surface plays a role as heterogeneous nucleation sites that may facilitate bigger particles in the hydrolysis reaction compared with bare glass substrates. Additionally, isles of sharp nanorod formation and aggregation of combined nanosphere-nanorod particles were observed. It is expected that lowering the concentration of zinc

acetate or hydrolysis reaction time for deposition on gold-palladium coated substrates would decrease the size of sphere-type particles and most likely stop the formation of aggregation, as mentioned above.

Average sizes (approximate diameters) of the nanosphere-type particles on the glass and gold-palladium coated glass were determined using Image J software and scales of their respective SEM images. Figure 7 showcases their size distribution plots. The average size of nanosphere-type articles on the glass substrates is 880±160 nm, determined using randomly chosen 25 particles where 16% of the particles are above 1000 nm. While the particles on gold-palladium glass substrates were grown bigger as the average size was determined as 1210 ± 250 nm (25 randomly selected particles), where 80% of the particles are above 1000 nm. Since the hydrolysis reactions were investigated for 96 hours that deposit the average sizes of particles mentioned above, it would be interesting to look at reactions within 12 hours. Because it would deposit $Zn(OH)_2$ nucleated substrates that can be pyrolyzed in ex-situ to prepare ZnO seeded substrates. As ZnO seeded substrates have been used to grow nano-structured ZnO such as nanorods,[30] the hydrolysis process can be employed readily for seeding substrates for accessing nano-structured ZnO as films. Additionally, lower time, such as 48 hours of hydrolysis reactions, would generate ultra-thin layers or films of nano ZnO (via pyrolysis) that can be used in metal oxide semiconductor-based ultra-thin-film technologies. While looking at the literature to find other reactions that deposit nanosphere-type morphology of ZnO, it turned out that direct solution deposition of nanorod of ZnO is very commonly reported. However, direct solution deposition reactions for the nanosphere-type morphology of ZnO have been seldom reported. For example, a polyoxometalate-assisted electrochemical deposition was reported to deposit nanospheres of ZnO onto graphite substrates at 2V and room temperature in an aqueous solution – where a Zn foil was used as cathood as the source of zinc.[31]

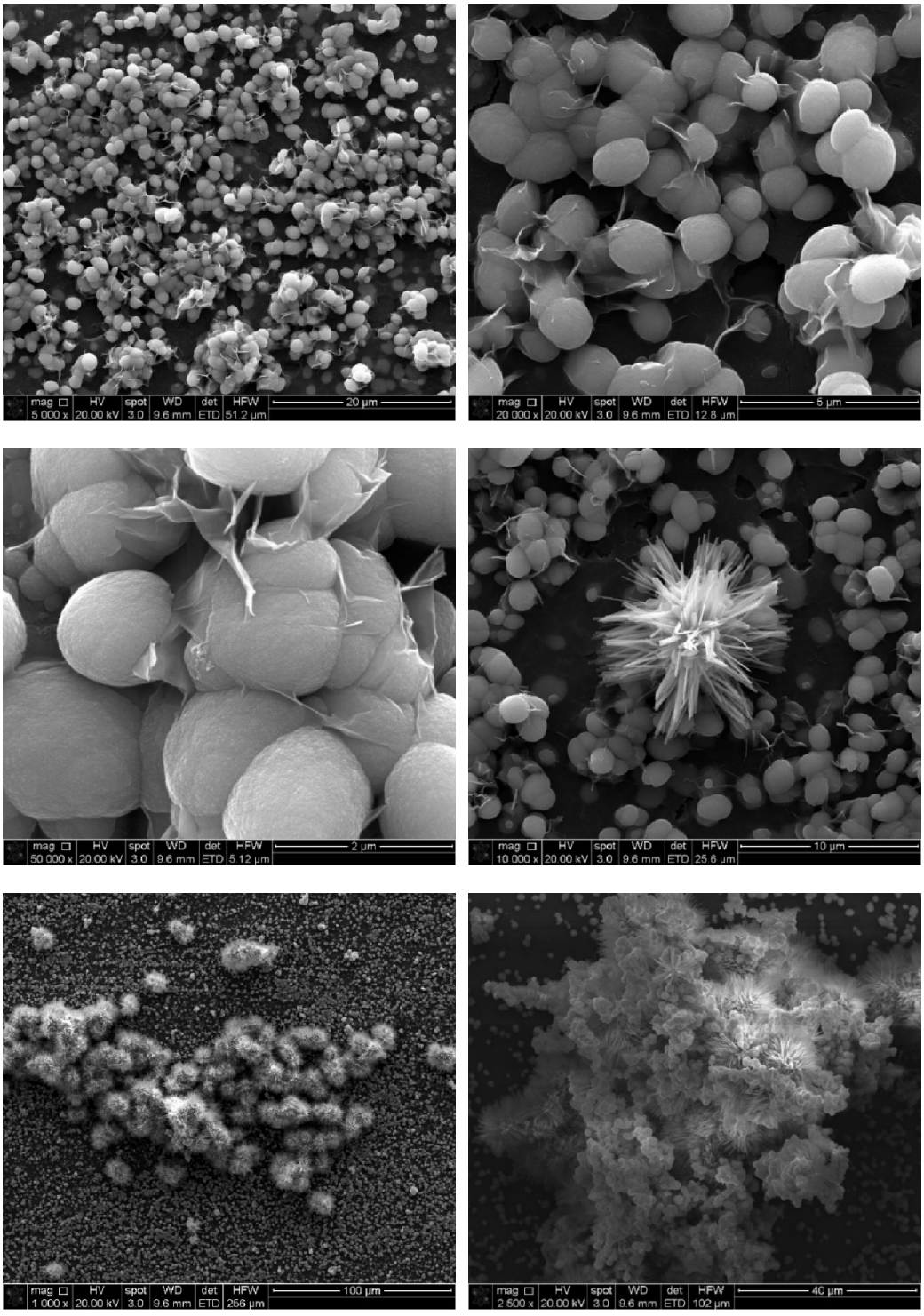

Figure 6: SEM images of $ZnO/Zn(OH)_2$ film on a gold-pallidum coated glass substrate.

Table 4: Average sizes of $ZnO/Zn(OH)_2$ particles deposited on the substrates

Substates	Average Approximate diameter (nm)
Glass	880 ± 160
Gold-palladium coated glass	1210 ± 250

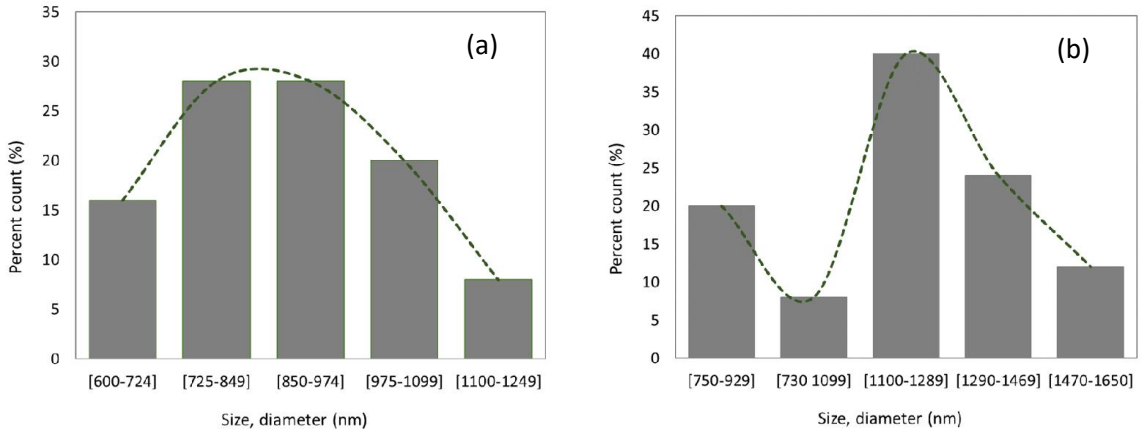

Figure 7: Size (approximate diameter) distribution plots of the deposited nanosphere-type $ZnO/Zn(OH)_2$ particles on (a) glass substrate and (b) gold-palladium coated glass substrate.

XRD, TGA, and FTIR results of the white-colored film material univocally establish that the film material is $ZnO/Zn(OH)_2$. The important question is what happens in the hydrolysis of zinc acetate (without an additional reactant) that deposits $ZnO/Zn(OH)_2$. The possible reactions are presented in Scheme 2 to address the question. The critical step of the hydrolysis process is that at the reaction temperature of 95 °C, the equilibrium between acetate and water produces more in situ OH^- that starts the nucleation. In the nucleation step, two possible phase formations can occur – zinc hydroxide, $Zn(OH)_2$ or zinc acetate hydroxide, $Zn(OAc)_x(OH)_{2-x}$ phase that deposit at the substrate. In the case of the $Zn(OH)_2$ phase, it slowly decomposes to ZnO in the hydrothermal condition by dehydroxylation. If the reaction nucleates a $Zn(OAc)_x(OH)_{2-x}$ phase that during the growth stage converts to $Zn(OH)_2$ followed by slowly to $ZnO/Zn(OH)_2$ as the final material.

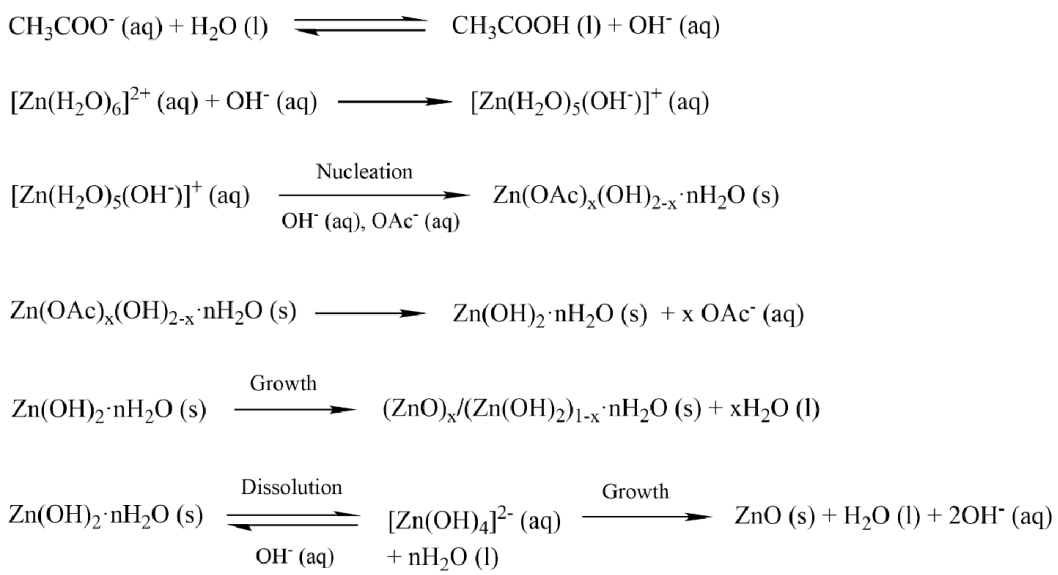

Scheme 2: Possible reactions in the hydrolysis of zinc acetate in water.

An investigation by Liang *et al.* showed with XRD experiments that the hydrolysis of zinc acetate ammonia complex at pH 7 and 50 °C initially generated a layered material of zinc acetate hydroxide, $Zn(OAc)_x(OH)_{2-x}\cdot nH_2O$ (basic zinc acetate salt that is also known layered zinc hydroxide). The zinc acetate hydroxide later in the reaction transformed into ZnO with a morphology of cylindrical nanorods.[28] Additionally, as shown in previous chapters, nickel or copper acetate hydrolysis can generate nickel or copper acetate hydroxide, where the starting nickel or copper acetate solution is slightly acidic. As zinc acetate solution (without additional reactant or reagent) is slightly acidic, it is therefore very likely that in our hydrolysis investigation of zinc acetate initially formed a $Zn(OAc)_x(OH)_{2-x}\cdot nH_2O$ phase that later turned into $Zn(OH)_2$ and then slowly into $ZnO/Zn(OH)_2$. Notably, unlike the nickel or copper acetate reaction, there was no visible particle growth in the first 24 hours of the zinc acetate hydrolysis reaction. This implies that the nucleation stage in zinc acetate hydrolysis is much slower than that of nickel or copper acetate. Nevertheless, the deposition and growth particles in the hydrolysis of zinc acetate should follow the similar steps of nucleation followed by rapid growth explained in previous chapters on hydrolysis of nickel and copper acetate.

The second important inquiry is why the reaction deposits nanosphere-type of morphology. One possible answer to the question is related to nucleation and the following growth of nucleated particles. Since the start of the nucleation and follow-up growth of nucleated particles depend on the in-situ formed OH^- ions, it can be hypothesized that the amount (moles or concentration) of OH^- generated during the reaction will very likely control or influence the morphology of the particles. The hypothesis can be paved up with evidence reported in the literature. For example, Masuda and coworkers established that hydrolysis of zinc acetate and ammonia at various ratios at 50 °C generates different morphologies. They showed that a ratio of $[Zn^{2+}]/[NH_3] = 2$ produced long cylindrical nanorods ZnO with an aspect ratio of 5, which at $[Zn^{2+}]/[NH_3] = 3$ grown shorter nanorods with an aspect ratio of 1.5. While at $[Zn^{2+}]/[NH_3] = 3.25$, the hydrolysis generated ellipses rather than cylindrical nanorods.[18] In other words, the higher amount of ammonia (i.e., OH^-) in the hydrolysis reaction favors nanorods generation. Another study also confirmed that higher a concentration of OH^- in hydrolysis reaction of Zn^{2+} favors the formation of nanorods, whereas lower OH^- concentration facilitates sphere-type particles, as nicely explained and schematized by Gupta and coworkers as in the following schematic diagram.[32]

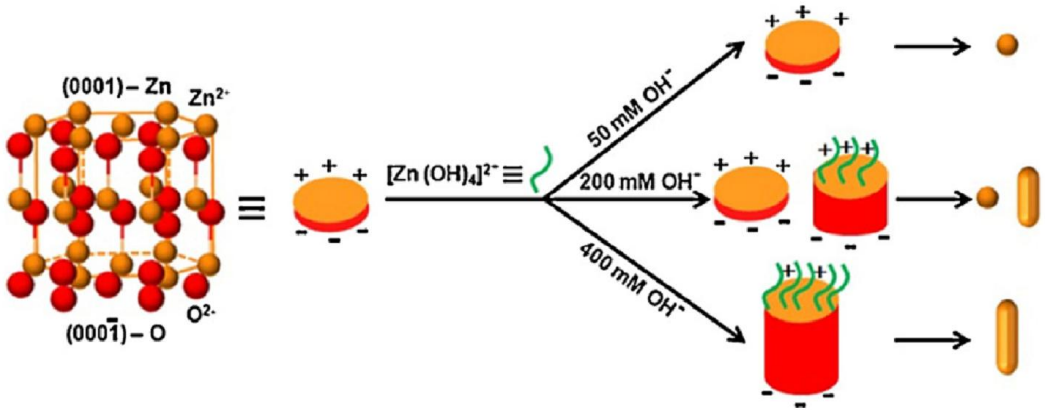

Figure 8: Schematic presentation showing the effect of OH^- ion concentrations in growing ZnO morphology. [The figure is taken from Reference 32]

According to the above diagram, the lattice facets in a wurtzite ZnO structure can be considered polarized since the (0 0 0 1) face has Zn^{2+} ions as terminated, whereas the (0 0 0 -1) face has O^{2-} ions. As the above study explained, at a higher OH^- ions concentration, there will be higher intermediate species $[Zn(OH)4]^{2-}$ that almost will block the (0 0 0 1) face of ZnO nuclei due to strong electrostatic attraction. This will render the growth along the (0 0 0 -1) face and result in an anisotropic growth along the facets to generate rod-type structures. Lower concertation of OH^- will have a lower number of intermediate species, $[Zn(OH)4]^{2-}$ resulting in uniform growth of all lattice faces as no lattice faces will be blocked by enough intermediates. In other words, lower OH^- concentration will not have the critical number of intermediate species to favor an anisotropic growth of nuclei. As a result, this will prefer a uniform growth of the lattice facets forming sphere-type particles. While an intermediate OH^- concentration can have both unfirm and anisotropic growth, generating both sphere and rod-type particles. The above diagram and explanation delineating the influence of OH^- ions neatly explain the morphology of the particles in the present study of only zinc acetate hydrolysis. Because in hydrolysis, only zinc acetate (without any second reactant) produces a small amount of OH^- ions from the reaction between acetate ions (pKb = 9.25) and water. Hence, the OH^- concentration in only zinc acetate solution must be smaller than ammonia (pKb = 4.74) added reaction systems as ammonia has lower pKb than acetate (i.e., ammonia is more basic than acetate). Therefore, hydrolysis of only zinc acetate creates a sphere-type of morphology due to the generation of a lower concentration of in situ OH^- ions during the reactions than the critical concentration for forming hexagonal nanoplates or nanorods. Similarly, other organics that can produce in situ OH^- ions better or similar concertation like ammonia may result in hexagonal nanorods or plates.

■ Conclusion:

This investigation established a straightforward hydrolysis reaction of only zinc acetate that deposited nano/micro-size $ZnO/Zn(OH)_2$ on substrates as films. On glass and gold-palladium

coated glass substrates, the hydrolysis reaction deposited sphere-type particles of $ZnO/Zn(OH)_2$. The average size of the particles deposited on the glass substrates is the order of nanometers (880 nm ±160 nm), while for the gold-palladium coated glass, they were in the order of micrometers (1210±250 nm). On glass substrates, the particles were almost uniformly distributed across the substrates. While for gold-palladium coated glass, although some aggregations of the particles were found, it is very likely that the hydrolysis reaction would produce a uniform distribution of particles if a lower concentration of zinc acetate or reaction time is used. The nano-/micro-sphere-type $ZnO/Zn(OH)_2$ particles decorated films generated by the hydrolysis reactions were robust (firmly adhered/coated) films, which is a desirable and valuable property of nano-/micro-structured ZnO films for their myriad applications. Therefore, the developed hydrolysis reaction is a promising way to prepare nano-/micro-structured ZnO as films on substrates.

- **Future work:**

To achieve monodisperse deposition of $ZnO/Zn(OH)_2$ particles, the hydrolysis reaction can be investigated in the presence of a surfactant. Because the surfactant would create micelles Zn^{2+} in the solution. The Zn—micelles may facilitate the monodisperse growth of particles. Also, the hydrolysis reaction with Zn or ZnO seeded substrates would be very interesting to investigate since these seeded substrates may generate hexagonal nanorod morphology of $ZnO/Zn(OH)_2$.

Additionally, the nucleation in the hydrolysis of zinc carboxylates (acetate, propionate, or butanoate) starts with the formation/addition of OH^- ions and the subsequent growth of the particles (the morphology) depends on OH^- ions concentration. Thus, an intriguing concept is that if we design a reaction set-up where the addition of ammonia would happen slowly but continuously to a zinc carboxylate, the hydrolysis reaction may generate new morphologies that would be time-dependent (addition rate of ammonia) nanostructures.

■ **Reference:**

(1) Kelly, S. R.; Shi, X.; Back, S.; Vallez, L.; Park, S. Y.; Siahrostami, S.; Zheng, X.; Nørskov, J. K., ZnO As an Active and Selective Catalyst for Electrochemical Water Oxidation to Hydrogen Peroxide. *ACS Catalysis* **2019,** 9, (5), 4593-4599.

(2) Ong, C. B.; Ng, L. Y.; Mohammad, A. W., A review of ZnO nanoparticles as solar photocatalysts: Synthesis, mechanisms and applications. *Renewable and Sustainable Energy Reviews* **2018,** 81, 536-551.

(3) Chen, X.; Wu, Z.; Liu, D.; Gao, Z., Preparation of ZnO Photocatalyst for the Efficient and Rapid Photocatalytic Degradation of Azo Dyes. *Nanoscale Res Lett* **2017,** 12, (1), 143.

(4) Kumar, B. V.; Naik, H. S. B.; Girija, D.; Kumar, B. V., ZnO nanoparticle as catalyst for efficient green one-pot synthesis of coumarins through Knoevenagel condensation. *Journal of Chemical Sciences* **2011,** 123, (5), 615-621.

(5) Sarvari, M. H.; Sharghi, H., Reactions on a Solid Surface. A Simple, Economical and Efficient Friedel−Crafts Acylation Reaction over Zinc Oxide (ZnO) as a New Catalyst. *The Journal of Organic Chemistry* **2004,** 69, (20), 6953-6956.

(6) Kim, Y. J.; Varma, R. S., Microwave-assisted preparation of cyclic ureas from diamines in the presence of ZnO. *Tetrahedron Letters* **2004,** 45, (39), 7205-7208.

(7) Wang, A.; Quan, W.; Zhang, H.; Li, H.; Yang, S., Heterogeneous ZnO-containing catalysts for efficient biodiesel production. *RSC Advances* **2021,** 11, (33), 20465-20478.

(8) Wibowo, A.; Marsudi, M. A.; Amal, M. I.; Ananda, M. B.; Stephanie, R.; Ardy, H.; Diguna, L. J., ZnO nanostructured materials for emerging solar cell applications. *RSC Advances* **2020,** 10, (70), 42838-42859.

(9) Huang, J.; Yin, Z.; Zheng, Q., Applications of ZnO in organic and hybrid solar cells. *Energy & Environmental Science* **2011,** 4, (10).

(10) Hoffmann, R. C.; Sanctis, S.; Schneider, J. J., Molecular Precursors for ZnO Nanoparticles: Field-Assisted Synthesis, Electrophoretic Deposition, and Field-Effect Transistor Device Performance. *Inorg Chem* **2017,** 56, (13), 7550-7557.

(11) Ahmad, M.; Zhu, J., ZnO based advanced functional nanostructures: synthesis, properties and applications. *J. Mater. Chem.* **2011,** 21, (3), 599-614.

(12) Özgür, Ü.; Hofstetter, D.; Morkoç, H., ZnO Devices and Applications: A Review of Current Status and Future Prospects. *Proceedings of the IEEE* **2010,** 98, (7), 1255-1268.

(13) Liu, C.; Wu, W.; Zhang, D.; Li, Z.; Ren, G.; Han, W.; Guo, W., Effective stability enhancement in ZnO-based perovskite solar cells by MACl modification. *Journal of Materials Chemistry A* **2021,** 9, (20), 12161-12168.

(14) Garcia-Farrera, B.; Velasquez-Garcia, L. F., Ultrathin Ceramic Piezoelectric Films via Room-Temperature Electrospray Deposition of ZnO Nanoparticles for Printed GHz Devices. *ACS Appl Mater Interfaces* **2019,** 11, (32), 29167-29176.

(15) McPeak, K. M.; Le, T. P.; Britton, N. G.; Nickolov, Z. S.; Elabd, Y. A.; Baxter, J. B., Chemical bath deposition of ZnO nanowires at near-neutral pH conditions without hexamethylenetetramine (HMTA): understanding the role of HMTA in ZnO nanowire growth. *Langmuir* **2011,** 27, (7), 3672-7.

(16) Laila, I. K. R.; Mufti, N.; Maryam, S.; Fuad, A.; Taufiq, A.; Sunaryono, Synthesis and Characterization of ZnO Nanorods by Hydrothermal Methods and Its Application on Perovskite Solar Cells. *Journal of Physics: Conference Series* **2018,** 1093, 012012.

(17) Reed, T. Novel Materials Chemistry for Structural, Photovoltaic, and Environmental Applications. Ph.D. Dissertaion, Advisor: A. Apblett, Oklahoma State University, 2018.

(18) Masuda, Y.; Kinoshita, N.; Koumoto, K., Morphology control of ZnO crystalline particles in aqueous solution. *Electrochimica Acta* **2007,** 53, (1), 171-174.

(19) Zhang, Y.; Chung, J.; Lee, J.; Myoung, J.; Lim, S., Synthesis of ZnO nanospheres with uniform nanopores by a hydrothermal process. *Journal of Physics and Chemistry of Solids* **2011,** 72, (12), 1548-1553.

(20) Materials Data on ZnO by Materials Project. DOI: https://doi.org/10.17188/1196748

(21) Podlogar, M.; Rečnik, A.; Yilmazoglu, G.; Özer, I. Ö.; Mazaj, M.; Suvaci, E.; Bernik, S., The role of hydrothermal pathways in the evolution of the morphology of ZnO crystals. *Ceramics International* **2016,** 42, (14), 15358-15366.

(22) CrystallographyOpenDatabase, http://www.crystallography.net/cod/9015545.html. In.

(23) Materials Data on $Zn(HO)_2$ by Materials Project.

(24) Holder, C. F.; Schaak, R. E., Tutorial on Powder X-ray Diffraction for Characterizing Nanoscale Materials. *ACS Nano* **2019,** 13, (7), 7359-7365.

(25) Gordeeva, A.; Hsu, Y. J.; Jenei, I. Z.; Brant Carvalho, P. H. B.; Simak, S. I.; Andersson, O.; Haussermann, U., Layered Zinc Hydroxide Dihydrate, Zn5(OH)10.2H2O, from Hydrothermal Conversion of epsilon-Zn(OH)2 at Gigapascal Pressures and its Transformation to Nanocrystalline ZnO. *ACS Omega* **2020,** 5, (28), 17617-17627.

(26) Winiarski, J.; Tylus, W.; Winiarska, K.; Szczygieł, I.; Szczygieł, B., XPS and FT-IR Characterization of Selected Synthetic Corrosion Products of Zinc Expected in Neutral Environment Containing Chloride Ions. *Journal of Spectroscopy* **2018,** 2018, 2079278.

(27) Elilarassi, R.; Chandrasekaran, G. In *Preparation and optical characterization of ZnO thin film for optoelectronic applications*, 2009 International Conference on Emerging Trends in Electronic and Photonic Devices & Systems, 22-24 Dec. 2009, 2009; 2009; pp 497-499.

(28) Liang, M.-K.; Limo, M. J.; Sola-Rabada, A.; Roe, M. J.; Perry, C. C., New Insights into the Mechanism of ZnO Formation from Aqueous Solutions of Zinc Acetate and Zinc Nitrate. *Chemistry of Materials* **2014,** 26, (14), 4119-4129.

(29) Srivastava, O. K.; Secco, E. A., Studies on metal hydroxy compounds. II. Infrared spectra of zinc derivatives ϵ-Zn(OH)2, β-ZnOHCl, ZnOHF, Zn5(OH)8Cl2, and Zn5(OH)8Cl2·H2O. *Canadian Journal of Chemistry* **1967,** 45, (6), 585-588.

(30) Vasudevan, A.; Jung, S.; Ji, T., Synthesis and Characterization of Hydrolysis Grown Zinc Oxide Nanorods. *ISRN Nanotechnology* **2011,** 2011, 1-7.

(31) Li, Q.; Wang, C.; Ju, M.; Chen, W.; Wang, E., Polyoxometalate-assisted electrochemical deposition of hollow ZnO nanospheres and their photocatalytic properties. *Microporous and Mesoporous Materials* **2011,** 138, (1-3), 132-139.

(32) Gupta, J.; Barick, K. C.; Bahadur, D., Defect mediated photocatalytic activity in shape-controlled ZnO nanostructures. *Journal of Alloys and Compounds* **2011,** 509, (23), 6725-6730.

CHAPTER VB

Deposition of Web-like Nanostructured Cobalt Hydroxide for Cobalt Oxyhydroxide and Cobalt Oxide

■ Introduction

Nanostructures of cobalt hydroxides are precursors for corresponding nanostructured cobalt oxides that have been proven as excellent materials for electrodes in supercapacitors,[1] catalysts for the electro-/photo-catalytic splitting of water for H_2 generation,[2, 3] and CO_2 electroreduction to CO or formate.[4, 5] Recently, it has been shown that cobalt oxide (Co_3O_4) decorated onto the outer surface of mesoporous silica particles can photo-reduce CO_2 to CO with 83% selectivity with an excellent conversion rate in a photosensitizer/aqueous-organic solvent system.[6] Cobalt hydroxide can also be easily transformed into cobalt oxyhydroxide (CoOOH), which has better conductivity than cobalt oxides or hydroxides, making the CoOOH an attractive material for electrode applications for lithium-ion batteries.[7] While cobalt hydroxide, $Co(OH)_2$ can directly be employed as electrodes for batteries and supercapacitors.[8, 9] Nano-$Co(OH)_2$ is investigated as a promising bifunctional catalyst for oxygen evolution and oxygen reduction reactions that occur in rechargeable metal-air batteries.[10] Also, it was found that 20 mole percent doping of cobalt hydroxide in nickel hydroxide significantly improves the performance of nickel hydroxide electrodes.[11] Due to being valuable and promising materials for essential and emerging

technologies mentioned above, deposition and synthesis of nanostructures or nanoparticles of cobalt hydroxides and oxides have drawn significant attention.

Deposition of nanostructured cobalt hydroxide by heating cobalt salt solutions is a popular solution-processed (hydrothermal or solvothermal) method. The hydrothermal or solvothermal process often involves additional reactants such as bases or organics for assisting nucleation and growth of cobalt hydroxide and morphology-directing reagents for tuning or attaining nano-structures cobalt hydroxide. For example, it was found that the urea-assisted hydrothermal process of cobalt nitrate generated nanoplates of β-$Co(OH)_2$ at 100 °C, while the reaction produced two types of morphologies – nanoplates and nano-octahedra at 150 °C.[12] While hydrazine hydrate assisted hydrothermal reaction of cobalt nitrate in the presence of Na_3PO_4 morphology directing agent produced β-$Co(OH)_2$ nano-columns consisting of nano-discs.[13] Nano-cone type β-$Co(OH)_2$ were reported to deposit on nickel foam by a hydrothermal process of cobalt nitrate and NH_4F and NH_3 solution at 120 °C in an autoclave.[14] Precipitation of $CoCl_2$ and hexamethylenetetramine with NaOH produced nano-hexagonal plates of β-$Co(OH)_2$. While the same precipitation reaction in the presence of NaCl generated nano-hexagonal plates α-$Co(OH)_2$.[15] Electrodeposition process using an aqueous solution of cobalt nitrate and hexamethylenetetramine is also reported to yield flower-like β-$Co(OH)_2$ nanowalls.[16] These are the few documented routes out of many studies in the literature for accessing nanostructured cobalt hydroxide. Nevertheless, often reported hydrothermal process in the literature involves additional reactants or regents.

In continuation of investigating the discovered hydrothermal (hydrolysis) reactions of later 3d transition metal acetate without any additional reactants or reagent deposit nanostructured metal layered hydroxides or hydroxides and oxides (as presented in Chapters II-VA); this chapter investigates hydrolysis of only cobalt acetate aqueous solution. Therefore, herein the chapter presents a simple hydrothermal (hydrolysis) process of pure cobalt acetate aqueous for deposition of nanostructured cobalt hydroxide as films. The hydrothermal reaction of aqueous cobalt acetate

solution in a closed system deposited nanostructured β-$Co(OH)_2$. Since the reaction involved only cobalt acetate aqueous solution, water played a dual role as a solvent and a reactant. The water molecules react with the acetate ions producing in situ OH^- ions that nucleate $Cu(OH)_2$. The $Co(OH)_2$ nanostructure was deposited as a dual nanomorphology – interconnected nanowalls alongside sphere-type nanoparticles inside the network of the nanowalls. The $Co(OH)_2$ nanostructures were deposited as high-quality, robust films since the nanostructured films were found to be firmly coated to the glass substrates. The $Co(OH)_2$ nanostructured films can readily be converted to cobalt oxyhydroxide (CoOOH) or cobalt oxide (Co_3O_4) films by pyrolysis, depending on the pyrolysis temperature.

■ Experimental

Materials: Cobalt acetate tetrahydrate, $Cu(OAc)_2 \cdot 4H_2O$ from Fisher Scientific was used without further purification. Deionized water was used as a solvent.

Cleaning Substrates: The microscope glass slides were used as substrates for deposition. The substrates were washed adequately with DI water followed by acetone. Finally, they were dried in an oven after rising again with DI water.

Hydrolysis of cobalt acetate for depositing $Co(OH)_2$ films: For a typical deposition reaction, 3.11 g (12.5 mmol) cobalt acetate tetrahydrate was dissolved in 50.1 g of water. A pre-cleaned microscope glass substrate was immersed almost vertically in the solution. The solution with the substrate was heated at 95 °C for 24 hours. A red-rose-colored film was deposited on the substrate (Figure 1). The wet film was air-dried followed by washed thoroughly by dipping it in deionized water until the conductivity of the washed solution was zero. After washing, the film was dried under the air again. Similarly, the material grown in the solution was washed, dried, and collected for a TGA experiment. Pyrolysis at 500 °C converted the $Co(OH)_2$ film to a CoOOH

hydroxide film according to the TGA experiment). After pyrolysis, the red-rose color film was turned into a black film (Figure 1, right).

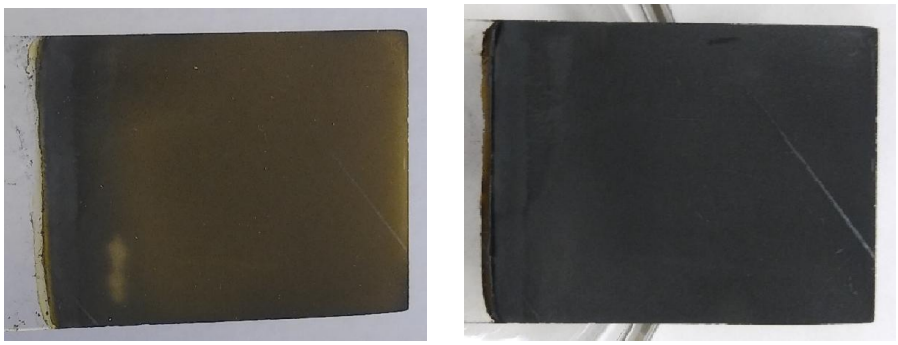

Figure 1: $Co(OH)_2$ film deposited by hydrolysis of cobalt acetate aqueous solution without additional reagents or reactants (left). CoOOH film prepared by pyrolysis of $Co(OH)_2$ film (right).

Hydrolysis of cobalt acetate with silica gel: 1.254 g (5.035 mmol) of cobalt acetate tetrahydrate was dissolved in 50.21 g of DI water. 5.0216 g of high surface area silica gel (Sigma Aldrich) was introduced to the solution and was placed in an oven at 90 °C. Within a few hours, the silica gel became bluish-pink-colored. After 24 hours, the reaction was stopped, which yielded pink-colored silica gel (Figure 2a). The pink-colored silica gel was separated from the reaction solution and washed thoroughly until the conductivity of the washed solution became zero. The pink-silica pellets were dried in an oven at 90 °C. The mass of the dried pink silica gel was 5.193 g.

Hydrolysis of cobalt acetate with silica pellets: A reaction of 0.200 M 50.1 g cobalt acetate solution (2.495 g cobalt acetate dissolved in 50.104 g water) and 5.021 g silica pellets (Alfa Aesar) were heated in closed pyrex bottle at 90 °C. After 24 hours, the silica pellets were isolated, washed thoroughly with DI water, and dried overnight in an oven at 90 °C. The reaction converted the white silica pellets into pink-colored silica pellets, as presented in Figure 2b. The mass of the dried pink silica pellets was 5.292 g.

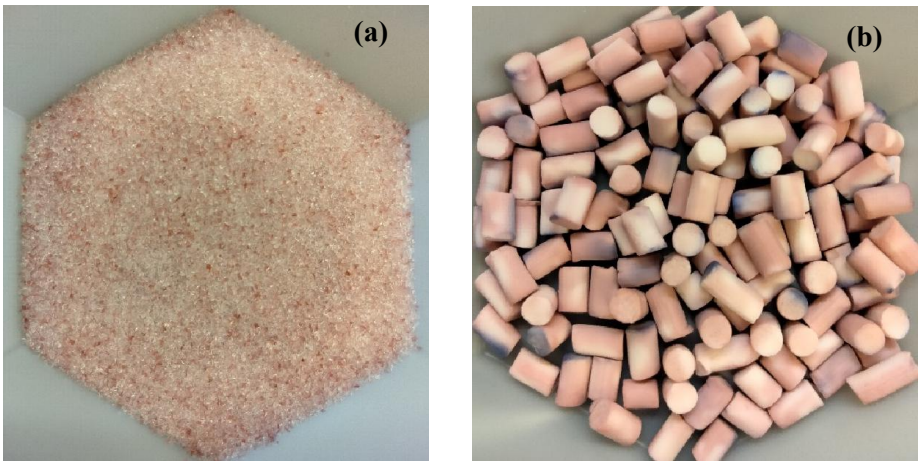

Figure 2: (a) Pink silica gel and (b) pink-silica pellets prepared by the hydrolysis of cobalt acetate and silica gel and silica pellets, respectively.

Characterization: The Scanning Electron Microscope (SEM) images were acquired using an FEI Quanta 600 field emission gun ESEM instrument at the Microscopy Lab of Oklahoma State University, Stillwater, Oklahoma. A Nicolet iS50 attenuated total reflectance-FTIR instrument was used to collect the FTIR spectrum. Thermogravimetric analysis (TGA) was performed using a TA Q50 thermogravimetric analyzer. An Agilent MPAES 4200 instrument analyzed cobalt in an acid digested solution of cobalt hydroxide deposited pink-silica gel.

■ Results and Discussion

SEM images (Figure 3) of a typical β-$Co(OH)_2$ film revealed that the deposited material has a dual morphology of web-like interconnected nanowalls accompanying sphere-type nanoparticles between the interconnected nanowalls. The two morphologies indicate two separate growth stages involved during the hydrolysis process. The different growths of morphology can be attributed to the pH change of the reaction solution (Table 1). The initial pH of the reaction solution is 7.3, which turns 6.0 after the hydrolysis reaction of 24 hours. Therefore, it is very likely the initial nucleation (deposition) followed by the growth of one type of particle occurs at a slightly basic pH (since the initial pH is 7.3). While as the reaction progress and the pH change to a slightly acidic

pH (since the final pH was 6.0), the growth process starts generating the second type of morphology. Two nanostructured morphologies were also observed in other reported hydrothermal or electrodeposition processes. For example, (i) nanoplates and nano-octahedra of Co_3O_4 via $Co(OH)_2$ and (ii) flower-like nanowalls and circular-nanoplates of $Co(OH)_2$ were observed in urea-assisted hydrothermal and hexamethylenetetramine-assisted electrodeposition processes, respectively, when the processes underwent longer time.[12, 16] Compared to nickel acetate hydrolysis, which deposited only one type of morphology of interconnected nanowalls forming a web-like structure (as shown in Chapter II), the initial pH of 6.8 changed to 6.1. Notably, the pH change for the nickel acetate hydrolysis was from an acidic to acidic pH. While for cobalt acetate hydrolysis that deposits cobalt hydroxide, the pH changed from slightly basic (7.3) to an acidic pH of 6.0, generating two nano-morphologies. Therefore, it can be hypothesized like nickel, interconnected nanowalls may start to form when the pH of the cobalt acetate solution is turned into an acidic pH from its starting pH during the hydrolysis process. This implies that the initial deposition occurs at a slightly basic pH that generates sphere-type nanoparticles, as shown in the SEM images (Figures 3c and 3d). Further, after looking at the SEM image at higher magnification (Figure 3d), it can be observed that ultrathin sheets that are yet to grow as nanowalls are produced on the top of deposited sphere-type nanoparticles in a few spots. This indicates that the growth of the nanowalls occurs after the deposition of sphere-type nanoparticles.

Table 1: pH change in the hydrolysis of 0.249 M cobalt acetate aqueous solution at 95 °C.

Initial pH	Final pH
7.3	6.0

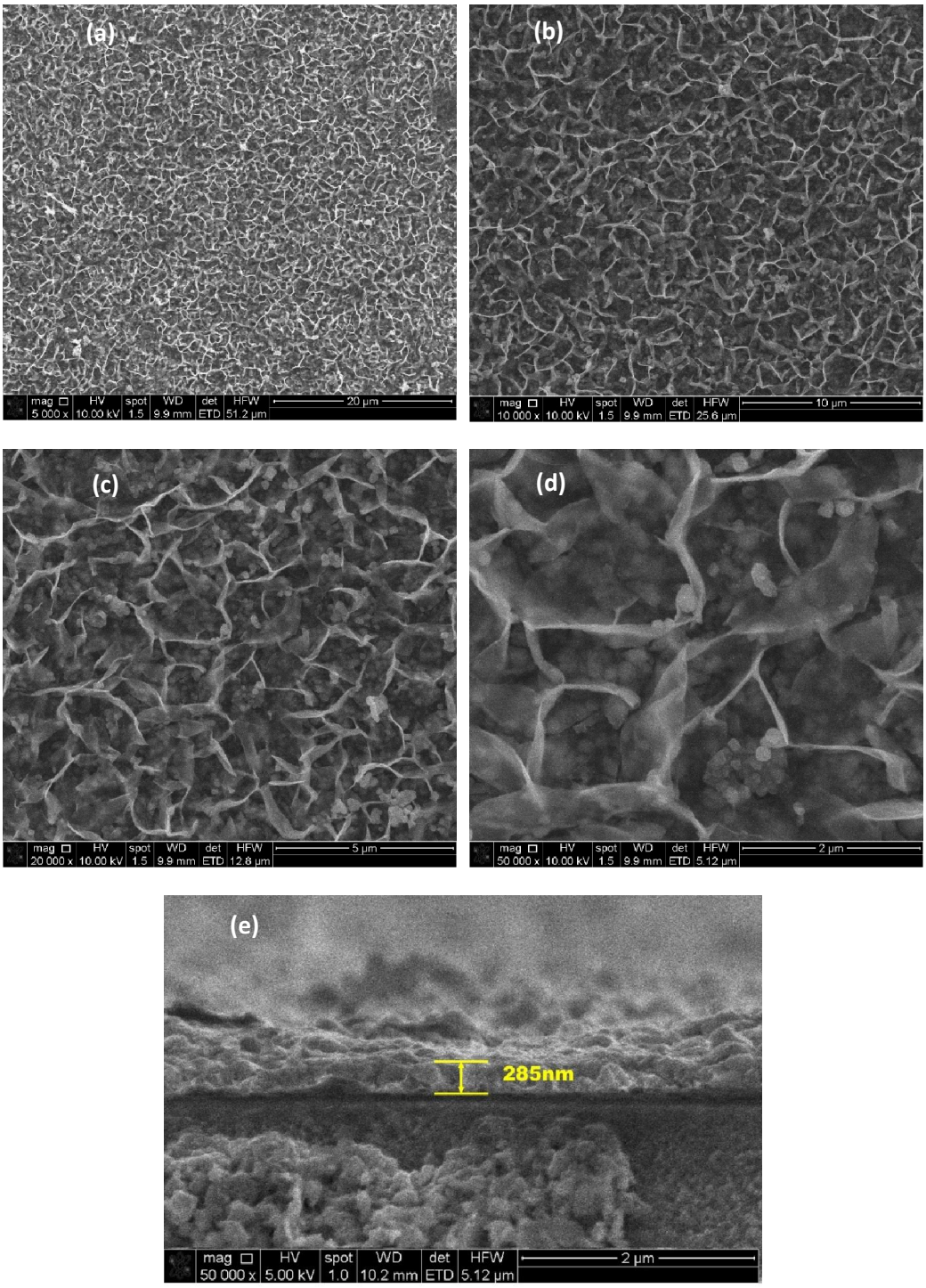

Figure 3: Scanning Electron Microscopy (SEM) images of a typical $Co(OH)_2$ nanostructured film at different spots and magnifications (a-d). The bottom picture (e) is the side view of the $Co(OH)_2$ nanostructured film, showing the thickness of the film as 285 nm.

The solution's initial pH (7.3) changes to an acid pH (6.0) can be explained in the following possible reactions in the hydrolysis process as presented in Scheme 1. Acetate ions react with water that forms in situ OH^- ions. The OH^- consumed in reacting with the $[Co(H_2O)]^{2+}$ followed by $[Co(OH)(H_2O)5]^+$ species that generate $Co(OH)_2$ nanostructures. As the OH^- ions are consumed to produce $Co(OH)_2$ in the hydrolysis process, the equilibrium between the acetate and hydroxide sifts to the right, forming more acidic. This results in the lowering of pH in the hydrolysis process. While the pungent smell of acetic acid at the end of the reaction was observed, further confirming acetic acid production. To support the lowing of pH that occurs due to the formation of acetic acid, the pH of an arbitrary 1.0 mM or 1.0 μM acetic acid aqueous solution was calculated using the acid dissociation constant of acetic acid (Ka =1.754×10^{-5} at 25 °C[17]). The calculated pH of a 1.0 mM pure acetic acid aqueous solution is 3.87, while for 1.0 μM aqueous acetic acid solution is 5.37, indicating that the pH lowering in the hydrothermal reaction occurs due to the formation of acetic acid from acetate ions and water.

$$CH_3COO^-_{(aq)} + H_2O_{(l)} \rightleftharpoons CH_3COOH_{(l)} + OH^-_{(aq)}$$

$$Co[(H_2O)_6]^{2+}_{(aq)} + OH^-_{(aq)} \rightleftharpoons [Co(OH)(H_2O)_5]^+_{(aq)} + H_2O_{(aq)}$$

$$[Co(OH)(H_2O)_5]^+_{(aq)} + OH^-_{(aq)} \longrightarrow Co(OH)_2 \cdot xH_2O_{(s)}$$

$$CH_3COOH_{(l)} \rightleftharpoons CH_3COO^-_{(aq)} + H^+_{(aq)}$$

Scheme 1: Possible reactions in the hydrolysis of only cobalt acetate aqueous solution (without any additional reactant or reagent) for nanostructured $Co(OH)_2$ film.

The average thickness of the interconnected nanowalls is 40 ± 10 nm, and the average size (approximate diameter) of the sphere-type nanoparticles is 145 ± 30 nm. The thickness and approximate diameter of the particles were determined using ImageJ software and the SEM picture in Figure 3d. In the side view of the deposited nanostructured $Co(OH)_2$ film, as presented in the

SEM image in Figure 3(e), the thickness of (height of the interconnected nanowalls) is 285 nm. The deposited nanostructured $Co(OH)_2$ was found to be as robust films since they did not peel off easily. A scratch was needed to scrape off the deposited material from the substrate. After pyrolysis, like the films of ZnO prepared in Chapter VB, the films became more firmly coated on the substrate. The robustness of a deposited nanostructure is critical to be employed in electro-/photo-catalysts and sensors applications. Since the interactions with the reaction solution or analytes, they will not peel them off from the substrates in operando conditions. Additionally, the dual nano-morphology would facilitate excellent sites for adsorption/interaction of reactants or analytes. Because the interconnected nanowalls will behave like a porous structure that can adsorb analytes or reactants to undergo detection or reactions. While the nanoparticles in between them will also be additional sites of adsorption and reaction to take place. Therefore, the prepared dual-nanostructures of $Co(OH)_2$ and corresponding cobalt oxide and oxyhydroxide in the present study would be promising materials for electro-/photo-catalysis and sensor applications.

Table 2: Average thickness of the web-like nanowalls and average size of the nano-sphere type of particles of $Co(OH)_2$ nanostructures from the SEM image (Figure 3d).

Average thickness of the nanowalls (nm)	Average size of the nanosphere-type particles (nm)
40±10	145±30

TGA experiment exhibits an overall mass loss of 13.15%, and the FTIR plot does not show bands for acetate that confirm that the deposited cobalt hydroxide nanostructures do not contain any acetate intercalation. In TGA, the first mass loss up to 150 °C dehydration of a tiny amount of lattice water and slow dehydroxylation of hydroxide groups of $Co(OH)_2$. While the second dehydroxylation of $Co(OH)_2$ to a cobalt oxyhydroxide-type species occur from 150 – 255 °C.

During this step, simultaneous oxidation of $Co(OH)_2$ to CoOOH by air oxygen also occurs.[18, 19] Therforeore, the mass loss of 150-225 °C can be attributed to dehydroxylation and oxidation of $Co(OH)_2$ to a cobalt oxyhydroxide-type species, $(Co^{x+})(O)_y(OH)_{x-2y}$ (where x is the average oxidation state of cobalt). By further dehydroxylation, this cobalt oxyhydroxide-type species was converted entirely to CoOOH at around 485 °C, which at 600 °C transformed into cobalt oxide Co_3O_4. The percent masses at 485 at 600 °C are 87.93 and 86.85%, which closely correspond to the molar mass of CoOOH and one-third of the molas mass of Co_3O_4, respectively, establishing that starting material is $Co(OH)_2$. While FTIR exhibited strong bands at 580 and 666 cm^{-1} confirmed the presence of Co-O and Co-OH bending vibrations. Weak broadband at near 3250 cm^{-1} suggests the presence of hydrogen-bonded OH stretching. Therefore, TGA and FTIR spectroscopy show that the hydrolysis of only cobalt acetate did not deposit acetate-intercalated layered hydroxide like nickel or copper acetate.

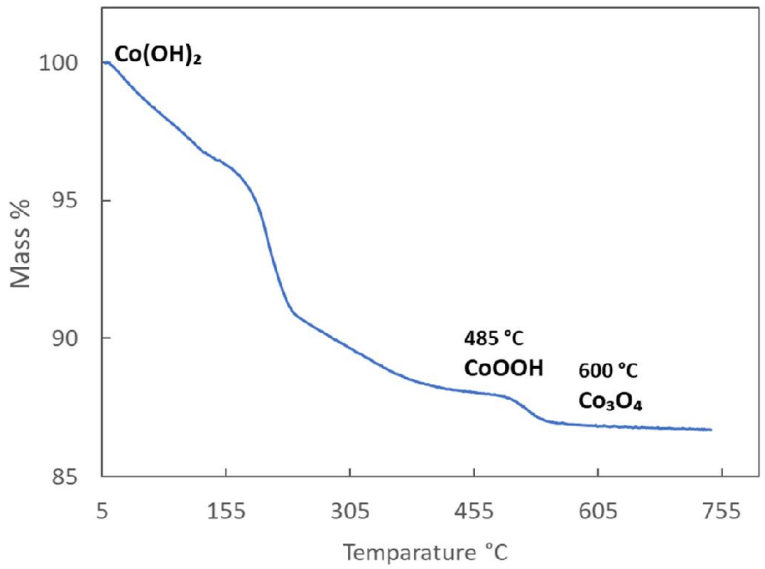

Figure 4: TGA plot of cobalt(II) hydroxide, $Co(OH)_2$, the product of cobalt acetate hydrolysis.

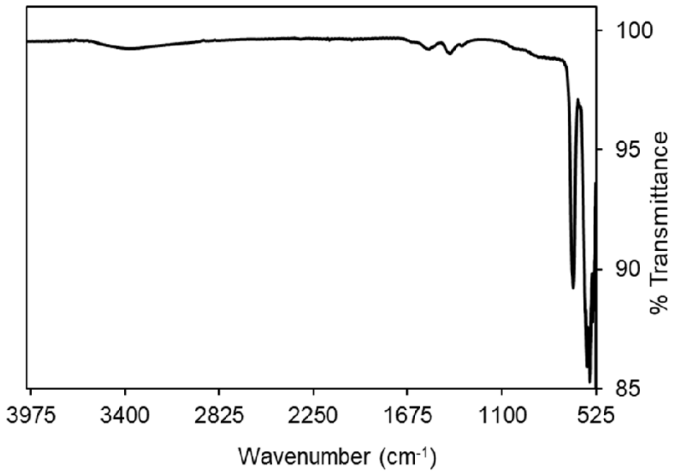

Figure 5: ATR-FTIR spectrum of nanostructured $Co(OH)_2$ film.

Hydrolysis (hydrothermal) reactions of cobalt acetate aqueous solutions with porous silica gel and silica pellets produced cobalt hydroxide deposited pink-colored silica gel and pellets (Figure 2). The deposited cobalt hydroxide onto these materials was robust as concentrated acid digestion with heating for several days turned the pink-silica gel into colorless silica gel. Besides the pink color, microwave plasma atomic emission peak at 340.507 nm for cobalt (Figure 6) of the digested solution of pink-silica gel confirmed that cobalt hydroxide was deposited on the silica gel. The MPAES confirmed that the percent deposition (w/w%) as $Co(OH)_2$ onto the silica gel was 3.24%. The percent deposition of cobalt hydroxide onto porous silica gel and pellets is tabulated in Table 2. Pyrolysis at 600 °C readily converted these pink silica gel and pellets to reddish-brown silica gel and blackish-brown pellets (Figure 7). The color change confirmed that $Co(OH)_2$ supported silica gel and pellets were converted to Co_3O_4 supported corresponding materials. The Co_3O_4 supported silica gel has very dark and light-colored particles suggesting the deposition was not homogeneous, which might occur due to secondary deposition on the silica gel. Shorter-time hydrolysis of cobalt acetate with silica gel, such as 6 or 8 hours rather than 24 hours, may facilitate avoiding secondary deposition. Therefore, the shorter-time hydrolysis reaction will likely result in

uniform color due to the homogenous deposition of cobalt hydroxide onto porous silica gel and pellets.

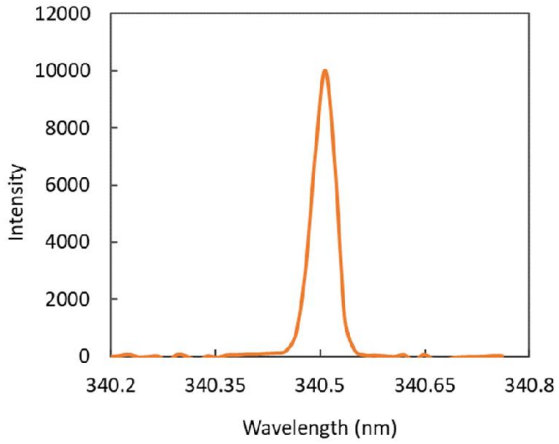

Figure 6: Cobalt emission peak at 340.507 nm of a digested solution of pink silica gel. The emission spectrum is acquired in a microwave plasma atomic emission spectrophotometer.

Figure 7: Cobalt oxide, Co_3O_4 decorated silica-gel (left), and silica-pellets (right) prepared by pyrolysis of $Co(OH)_2$ deposited silica-gel and silica-pellets at 600 °C.

Table 3: Percent deposition of $Co(OH)_2$ on silica gel and pellets by hydrolysis of cobalt acetate aqueous solutions with silica gel and pellets at 90 °C for 24 hours.

Deposition of $Co(OH)_2$ on porous silica gel by hydrolysis of 0.10 M $Co(OAc)_2$ (w/w %)	Deposition of $Co(OH)_2$ on silica pellets by hydrolysis of 0.20 M $Co(OAc)_2$ (w/w %)
3.24	5.39

■ Conclusion

Straightforward hydrolysis of only cobalt acetate (without additional reactants or reagents) deposited nanostructured $Co(OH)_2$ as thin films. A 0.249 M cobalt acetate aqueous solution deposited a nanostructured thin film with a thickness of 285 nm. The deposited nanostructured thin films consisted of a dual nanomorphology – sphere-type nanoparticles and web-like interconnected nanowalls. The average size of the sphere-type nanoparticles was found as 145±30 nm, while the average thickness of the interconnected nanowalls was determined as 40±10 nm. TGA investigation of the nanostructured $Co(OH)_2$ thin film material showed that pyrolysis can transform them into CoOOH and Co_3O_4. Additionally, it was found that the hydrolysis of only cobalt acetate deposited cobalt hydroxide on porous silica gel and silica pellets catalyst supports. These materials were also effortlessly converted to Co_3O_4 decorated corresponding materials by pyrolysis. Therefore, the hydrolysis of only cobalt acetate developed in the current work has established a new, straightforward, and inexpensive route for deposition of nanostructured-cobalt hydroxide for nanostructured-cobalt oxyhydroxide or oxides onto substrates, porous materials and catalyst supports.

■ Future work:

Hydrolysis of 1M $Co(OAc)_2$ and nanostructure directing reagents: To deposit much thicker nanostructured films of $Co(OH)_2$, hydrolysis of 1M $Co(OAc)_2$ should be investigated. Also,

it would be interesting to look at if that high concentration can maintain the identical nano morphologies. Additionally, the hydrolysis of cobalt acetate should be investigated in an acetate buffer soliton to examine if it can produce one type of nanomorphology. Also, nanostructure directing reagents with cobalt acetate aqueous solution will be interesting to explore to find out what nanomorphology they can generate.

Deposition on the conductive substrates: Hydrolysis of only cobalt acetate with glassy carbon films/electrodes can be exploited to deposit nonstructured cobalt oxides via cobalt hydroxide. This would avoid additional ex-situ steps for preparing cobalt oxide decorated glassy carbon film/electrodes for electrocatalytic, photo-electrocatalytic, and sensor technologies.

Hydrolysis of cobalt acetate with macroporous materials: Hydrolysis of only cobalt acetate with commercial macroporous polymer, glass, and ceramic beads will be promising to explore. Since the hydrolysis reaction will likely functionalize these materials with cobalt-based nanomaterials.

■ References:

(1) Aboelazm, E. A. A.; Ali, G. A. M.; Algarni, H.; Yin, H.; Zhong, Y. L.; Chong, K. F., Magnetic Electrodeposition of the Hierarchical Cobalt Oxide Nanostructure from Spent Lithium-Ion Batteries: Its Application as a Supercapacitor Electrode. *The Journal of Physical Chemistry C* **2018,** 122, (23), 12200-12206.

(2) Gupta, S.; Yadav, A.; Bhartiya, S.; Singh, M. K.; Miotello, A.; Sarkar, A.; Patel, N., Co oxide nanostructures for electrocatalytic water-oxidation: effects of dimensionality and related properties. *Nanoscale* **2018,** 10, (18), 8806-8819.

(3) Moridon, S. N. F.; Salehmin, M. I.; Mohamed, M. A.; Arifin, K.; Minggu, L. J.; Kassim, M. B., Cobalt oxide as photocatalyst for water splitting: Temperature-dependent phase structures. *International Journal of Hydrogen Energy* **2019,** 44, (47), 25495-25504.

(4) Aljabour, A.; Coskun, H.; Apaydin, D. H.; Ozel, F.; Hassel, A. W.; Stadler, P.; Sariciftci, N. S.; Kus, M., Nanofibrous cobalt oxide for electrocatalysis of CO2 reduction to carbon monoxide and formate in an acetonitrile-water electrolyte solution. *Applied Catalysis B: Environmental* **2018,** 229, 163-170.

(5) Gao, S.; Jiao, X.; Sun, Z.; Zhang, W.; Sun, Y.; Wang, C.; Hu, Q.; Zu, X.; Yang, F.; Yang, S.; Liang, L.; Wu, J.; Xie, Y., Ultrathin Co3O4 Layers Realizing Optimized CO2 Electroreduction to Formate. *Angew Chem Int Ed Engl* **2016,** 55, (2), 698-702.

(6) Fu, Z. C.; Moore, J. T.; Liang, F.; Fu, W. F., Highly efficient photocatalytic reduction of CO2 to CO using cobalt oxide-coated spherical mesoporous silica particles as catalysts. *Chem Commun (Camb)* **2019,** 55, (77), 11523-11526.

(7) Fu, Y.; Li, L.; Ye, S.; Yang, P.; Liao, P.; Ren, X.; He, C.; Zhang, Q.; Liu, J., Construction of cobalt oxyhydroxide nanosheets with rich oxygen vacancies as high-performance lithium-ion battery anodes. *Journal of Materials Chemistry A* **2021,** 9, (1), 453-462.

(8) Gao, X.-P.; Yao, S.-M.; Yan, T.-Y.; Zhou, Z., Alkaline rechargeable Ni/Co batteries: Cobalt hydroxides as negative electrode materials. *Energy & Environmental Science* **2009,** 2, (5).

(9) Deng, T.; Zhang, W.; Arcelus, O.; Kim, J. G.; Carrasco, J.; Yoo, S. J.; Zheng, W.; Wang, J.; Tian, H.; Zhang, H.; Cui, X.; Rojo, T., Atomic-level energy storage mechanism of cobalt hydroxide electrode for pseudocapacitors. *Nat Commun* **2017,** 8, 15194.

(10) Zhan, Y.; Du, G.; Yang, S.; Xu, C.; Lu, M.; Liu, Z.; Lee, J. Y., Development of Cobalt Hydroxide as a Bifunctional Catalyst for Oxygen Electrocatalysis in Alkaline Solution. *ACS Appl Mater Interfaces* **2015,** 7, (23), 12930-6.

(11) NASA; *Cobalt improves nickel hydroxide electrodes for batteries*; https://ntrs.nasa.gov/citations/19690000228, 1969.

(12) Samal, R.; Dash, B.; Sarangi, C. K.; Sanjay, K.; Subbaiah, T.; Senanayake, G.; Minakshi, M., Influence of Synthesis Temperature on the Growth and Surface Morphology of Co(3)O(4) Nanocubes for Supercapacitor Applications. *Nanomaterials (Basel)* **2017,** 7, (11).

(13) Shao, Y.; Sun, J.; Gao, L., Hydrothermal Synthesis of Hierarchical Nanocolumns of Cobalt Hydroxide and Cobalt Oxide. *The Journal of Physical Chemistry C* **2009,** 113, (16), 6566-6572.

(14) Cao, F.; Pan, G. X.; Tang, P. S.; Chen, H. F., Hydrothermal-synthesized Co(OH)2 nanocone arrays for supercapacitor application. *Journal of Power Sources* **2012,** 216, 395-399.

(15) Liu, Z.; Ma, R.; Osada, M.; Takada, K.; Sasaki, T., Selective and Controlled Synthesis of α- and β-Cobalt Hydroxides in Highly Developed Hexagonal Platelets. *Journal of the American Chemical Society* **2005,** 127, (40), 13869-13874.

(16) Nagaraju, G.; Ko, Y. H.; Yu, J. S., Self-assembled hierarchical β-cobalt hydroxide nanostructures on conductive textiles by one-step electrochemical deposition. *CrystEngComm* **2014,** 16, (48), 11027-11034.

(17) Harned, H. S.; Ehlers, R. W., The Dissociation Constant of Acetic Acid from 0 to 60° Centigrade1. *Journal of the American Chemical Society* **1933,** 55, (2), 652-656.

(18) Figlarz, M.; Guenot, J.; Tournemolle, J. N., Oxidation of cobalt (II) hydroxide to oxide hydroxide: solids evolution during reaction. *Journal of Materials Science* **1974,** 9, (5), 772-776.

(19) Ebrahimzade, H.; Khayati, G. R.; Schaffie, M., Preparation and kinetic modeling of β-Co(OH)2 nanoplates thermal decomposition obtained from spent Li-ion batteries. *Advanced Powder Technology* **2017,** 28, (10), 2779-2786.

CHAPTER VI

Green Process for Preparation of Nickel Hydroxide Films and Membranes

Note: This chapter was published in the Journal of Materials Engineering and Performance.

DOI: https://doi.org/10.1007/s11665-020-05100-5

■ Introduction

In continuation of the previous works (Chapters II-V) on developing straightforward and inexpensive solution methods for deposition of later 3d transition metal acetate hydroxides and hydroxides, the present work was motivated to develop a novel green process for preparing nickel hydroxide films and membranes using commercial nickel hydroxide powder. The current work exploits the solubility of nickel hydroxide in excess aqueous ammonia that forms hexamine nickel(II) hydroxide complex, $Ni(NH_3)_6(OH)_2$. In an open chemical bath system, $Ni(NH_3)_6(OH)_2$ can deposit the nickel hydroxide as films on substrates and grow membranes upon release of ammonia. The deposition or growth process using $Ni(NH_3)_6(OH)_2$ does not leave any waste chemical behind, making the process a green process.[1]

Nickel hydroxides are best known for their use as electrode materials in batteries as popular nickel-cadmium (Ni-Cd) and nickel metal-hydride (NiMH) batteries' electrodes have been made

by nickel hydroxides.[2] They are also an electrode material for some rare battery types, such as nickel-hydrogen batteries used for the space program.[3] While nickel-iron and nickel-zinc rechargeable batteries offer low environmental impact, nickel hydroxides are a popular choice as positive electrodes for these batteries.[4-6] Additionally, as nickel hydroxide and aluminum substituted α-nickel hydroxide exhibit high lithium storage capacities, they are promising materials for electrodes in lithium-ion batteries.[7, 8] However, due to the beneficial electro-/photo-chemical properties of nickel hydroxides, they have significant technological applications beyond their use in batteries.[9] Nickel hydroxides are useful co-catalysts for photocatalytic hydrogen production from water,[10] excellent electrocatalysts for the oxygen evolution reaction, [11, 12] and safer hydrogen generation from alkaline water,[13] and electrocatalysis of small molecules in fuel cells, energy storage, organic synthesis, and wastewater treatment.[14] Nickel hydroxides can be used as sensors for many analytes such as vitamins, hydrogen peroxide, and glucose due to their excellent electrochemical behavior.[15-18] Upon oxidation, they can change the color that has been exploited for making electrochromic devices.[19-21] Nanometric nickel hydroxides have pseudo capacitance property that makes them valuable materials for supercapacitors applications.[22, 23] Also, nickel hydroxides produced by electrochemical oxidation or by corrosion of nickel metal and nickel-containing alloys play an important role as substituents of the surface layers.[24]

The useful properties of nickel hydroxides originate in their layered structures, as presented in Figure 1, which showcases the two known polymorphs of nickel hydroxides that are α-$Ni(OH)_2$ and β-$Ni(OH)_2$. The β-$Ni(OH)_2$ is the most stable form[25] that occurs naturally as the mineral theophrastite and isostructural with brucite, $Mg(OH)_2$. Closely arranged $Ni(OH)_2$ layers constitute the β-$Ni(OH)_2$ structure,[26] where the pendent protons of the hydroxide groups of two adjacent layers are in with the van der Walls radius (Figure 1, top-left). $Ni(OH)_6$ octahedra compose the layers by sharing their in-plane edges in the a and c directions of the lattice to form sheets. When a fragment of a layer is presented by a ball and stick representation (Figure 1 bottom), it shows the octahedral

nickel centers are connected to hydroxides and how hydroxides are connected to three nickel ions forming a cube-like structure with a missing nickel vertex, which is a common structural motif in the main group hydroxides.

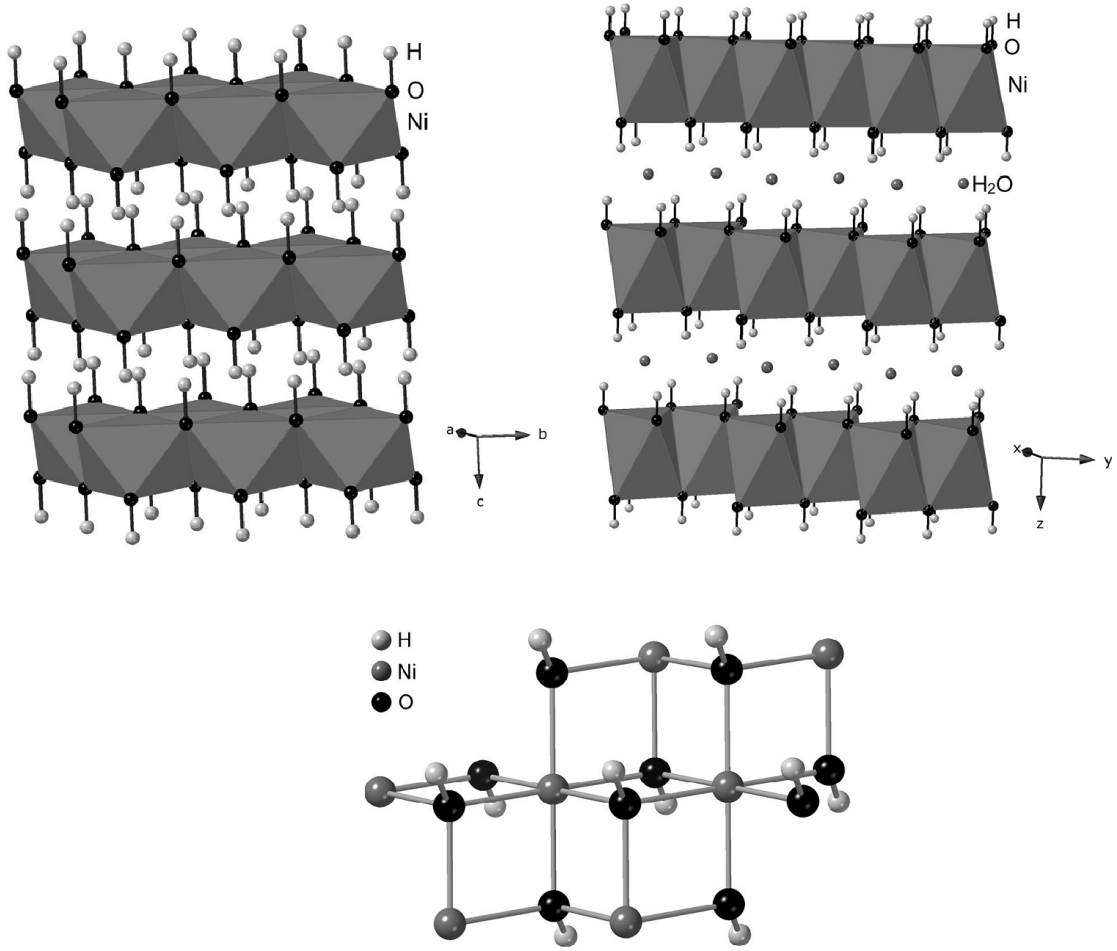

Figure 1: Structures of nickel hydroxide. Top-left: β-$Ni(OH)_2$ drawn with data from Reference.[24] Top-right: the idealized structure of α-$Ni(OH)_2$ drawn with data from Reference.[25] Hydrogen atoms were added to the hydroxyl groups in calculated positions. Bottom: ball and stick representation of the arrangement of nickel and hydroxide ions in the layers of both structures.

While α-$Ni(OH)_2$ is a hydrated β-$Ni(OH)_2$ ($Ni(OH)_2 \cdot xH_2O$; $0.41 \leq x \leq 0.7$); therefore, it is not truly β-$Ni(OH)_2$.[24, 25, 27] Like the β-$Ni(OH)_2$ they are constituted by the same layers of $Ni(OH)_6$ octahedra. However, the layers are intercalated with water molecules, as shown in Figure 1 (Top,

Right).[27] The presented is structure is an idealized of α-$Ni(OH)_2$, as the water molecule can rotate and translate along the ab plane. The disorder in the interlayered water molecules causes unaligned orientation (stacking faults) of the layers relative to each other, resulting in a turbostratic structure. The transformation of α-$Ni(OH)_2$ to β-$Ni(OH)_2$ is a spontaneous process in aqueous media or chemical aging since β-$Ni(OH)_2$ is the more stable form. At higher temperatures, this process occurs faster, while in concentrated alkaline media is much more rapid than in pure water.[25] Usually, a turbostratic β-$Ni(OH)_2$ forms during the transformation from the α- $Ni(OH)_2$. However, further chemical aging slowly removes the turbostratic features (stacking faults) and produces a more crystalline material.

The electrochemical behavior of a nickel hydroxide profoundly depends on its structure: β-$Ni(OH)_2$ and α-$Ni(OH)_2$ reversibly generate β-NiOOH and γ-NiOOH, respectively, by oxidation.[27] However, prolonged charging converts α-$Ni(OH)_2$ to γ-NiOOH by causing irreversible damage due to the accompanying mechanical deformation,[28] while β-$Ni(OH)_2$ reversibly cycles to β-NiOOH without any mechanical alteration. As a result, β-$Ni(OH)_2$ is frequently the preferred electrode material in alkaline batteries due to its better stability than the α-$Ni(OH)_2$ in alkaline environments. To stabilize the structure of α-$Ni(OH)_2$ in alkaline media for electrode applications, much effort has been devoted to developing processes that would slightly alter the chemical composition of α-$Ni(OH)_2$.

Based on the structural similarities between Ni-Al layered double hydroxides and α-$Ni(OH)_2$, the aluminum-substituted α-nickel hydroxide phase is an established choice for accessing a stable α-$Ni(OH)_2$ material.[6, 29, 30] Aluminum substituted α-$Ni(OH)_2$ was synthesized by addition of NaOH and sodium carbonate to a solution containing the mixtures of nickel and aluminum nitrates with a ratio of Ni/Al = 4:1.[30] Notably, upon aging in a 1M KOH solution for a month, the structure was retained it starting structure. In aluminum-substituted α-nickel hydroxide, the Al^{3+} ions

substitute Ni^{2+} ions that require the addition of intercalated anions to maintain the charge neutrality within the structure and thereby preserve the extended space between the metal hydroxide layers.

According to a review article published by Hall and co-workers, there are hundreds of reported methods for synthesizing nickel hydroxide materials such as – chemical precipitation, impregnation–precipitation, electrochemical precipitation, the sol–gel process, hydrothermal or solvothermal procedures, electrochemically formation of surface layers on nickel metal and nickel-based alloys, electrodialysis, solid-state synthesis, microwave-assisted synthesis, and sonochemistry.[25] Herein, the current work presents a development of a novel and straightforward process that directly converted commercial nickel hydroxide powder to β-$Ni(OH)_2$ film coatings and aluminum substituted α-$Ni(OH)_2$ membranes. The process simply exploited the solubility of $Ni(OH)_2$ in aqueous ammonia that has been used to recover $Ni(OH)_2$ from used nickel-metal hydride batteries.[31] $Ni(OH)_2$ solution in aqueous ammonia deposited β-$Ni(OH)_2$ films on substrates while $Ni(OH)_2$ and sodium aluminate solution in aqueous ammonia generated free-standing aluminum substituted α-$Ni(OH)_2$ membranes.

■ Experimental

Materials: Nickel hydroxide $Ni(OH)_2$ and nickel acetate tetrahydrate $Ni(CH_3\text{-}COO)_2.4H_2O$ were collected from Strem Chemicals and Sigma Aldrich. Fine aluminum powder from Valmet, sodium hydroxide from Fisher Scientific, and ACS reagent grade concentrated ammonium hydroxide NH_4OH (28% NH_3 aqueous solution) from Scientific Products were used. All chemicals were used without further purification.

Characterization: X-ray powder diffraction patterns were collected using a Bruker AXS D8 Advance diffractometer. Copper Kα (1.5418 A˚) radiation was used for acquiring the XRD patterns. A Quantachrome Nova 1200 instrument was employed to determine surface area by nitrogen adsorption and the BET six-point method with P/Po<0.30. Before surface area analysis,

samples were prepared by degassing under a vacuum at 100 °C. An FEI Quanta 600 field-emission gun Environmental Scanning Electron Microscope was used for acquiring scanning electron micrographs. The nickel, aluminum, and sodium contents of aluminum substituted α-$Ni(OH)_2$ were determined by microwave plasma atomic emission spectroscopy (MP-AES) after dissolution in dilute nitric acid. An Agilent 4200 MPAES instrument was used for the metal analysis. While thermogravimetric analysis (TGA) studies were performed on a Seiko EXSTAR 6000 TG/DTA 6200 instrument under a 100 ml/min nitrogen flow. A temperature programmable muffle furnace was used for bulk pyrolysis at various temperatures. Bulk pyrolysis was performed in ambient air at a temperature ramp of 1°C/min and a hold time of 14 hours.

Deposition of β-$Ni(OH)_2$ films on glass substrates: 2 g of $Ni(OH)_2$ powder was added to 40 ml of concentrated ammonium hydroxide and stirred for 1.5 hours at room temperature in a sealed flask that produced a blue solution. The excess $Ni(OH)_2$ was separated by filtration using a 20-μm nylon membrane filter. The separated $Ni(OH)_2$ was dried in a vacuum overnight and then weighed to determine the amount of dissolved $Ni(OH)_2$. The blue solution was evaporated slowly under a fume hood in a 50-ml flask. Upon slow release of NH_3 from the solution, a thin film of $Ni(OH)_2$ was deposited on flask walls. The precipitate deposited on flask walls and bottom were collected, placed under a vacuum overnight, and weighed. IR (cm^{-1}) (KBr) 3638 (s, sh), 1483 (m), 1355 (m), 833 (w), 582 (m).

In another procedure, a microscope glass slide was immersed vertically in 40 ml of nickel hydroxide solution, which resulted in β-$Ni(OH)_2$ film deposition on the slide (Figure 2). The glass substrate coated with $Ni(OH)_2$ was used to acquire SEM images.

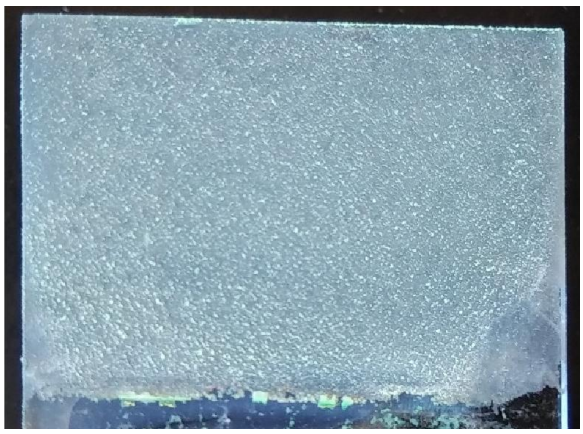

Figure 2: β-$Ni(OH)_2$ film grown on a microscope glass substrate from saturated nickel hydroxide-aqueous ammonia solution.

Preparation of aluminum substituted α-$Ni(OH)_2$ membranes: To prepare a 0.33M sodium aluminate, $NaAl(OH)_4$ solution, 1.78 g (0.066 moles) of aluminum powder was slowly added to a 200 g of DI water that contained excess sodium hydroxide (6.03g, 0.15 moles). Due to the nature of the highly exothermic reaction with rapid hydrogen gas evolution, the process was carried out under an ice water bath with continuous stirring. To determine the amount of sodium aluminate that is necessary for the stabilization of α-$N(OH)_2$, increasing volumes of 0.33 M $NaAl(OH)_4$ were added to 40 ml of saturated $Ni(OH)_2$-NH_3 solutions. Evaporation of the ammonia produced a solid α-$Ni(OH)_2$ phase characterized by x-ray diffraction and infrared spectroscopy. It turned out that the 6 ml of 0.33 M $NaAl(OH)_4$ solution was required for complete stabilization of the α-$Ni(OH)_2$ phase. IR (cm^{-1}) (KBr) 3457 (s, br), 1360 (s), 854 (br). A membrane of aluminum substituted α-$Ni(OH)_2$ grown using a typical solution of saturated $Ni(OH)_2$-NH_3 and sodium aluminate is shown in Figure 3.

Figure 3: Aluminum substituted α-nickel hydroxide membrane grown from saturated hexamine nickel(II) hydroxide and sodium aluminate solution.

■ Results and Discussion

The current investigation developed a novel solution growth method for nickel hydroxide films and membranes using nickel hydroxide powder that takes advantage of the strong complexation of nickel by ammonia ($K_f\,[Ni(NH_3)_6]^{2+} = 5.5x10^8$)[32]. This strong complexation results dissolution of nickel hydroxide in a concentrated aqueous ammonia that overcomes the insolubility of $Ni(OH)_2$ in water ($Ksp = 2.0 \times 10^{-15}$)[33] as presented in scheme 1.

$$Ni(OH)_{2(s)} \rightleftharpoons Ni^{2+}_{(aq)} + 2\,OH^-_{(aq)}$$

$$Ni^{2+}_{(aq)} + 6\,NH_{3(aq)} \rightleftharpoons [Ni(NH_3)_6]^{2+}_{(aq)}$$

$$Ni(OH)_{2(s)} + 6\,NH_{3(aq)} \rightleftharpoons [Ni(NH_3)_6]^{2+}_{(aq)} + 2\,OH^-_{(aq)}$$

Scheme 1: Dissolution of nickel hydroxide in ammoniacal solution

Dissolution of the $Ni(OH)_2$ in concentrated ammonia solution produced a blue solution of hexamine nickel (II) hydroxide, $Ni(NH_3)_6(OH)_2$. Figure 4 presents a UV-Visible spectrum of the blue solution. Five different solutions of saturated $Ni(OH)_2$ were prepared to determine the

solubility in concentrated ammonia. After filtration, the weighed amounts of each solution were evaporated to complete dryness. The amounts of undissolved $Ni(OH)_2$ were also weighed after drying. The calculated concentration of nickel hydroxide in the initial solutions was 0.139±0.006 M which closely agrees with the value calculated by Miyake and coworkers.[31] Notably, Miyake and coworkers also determined the maximum solubility $Ni(OH)_2$ in ammoniacal solution was 0.9 M and occurred at a pH of around 10. However, at pH above 10, the solubility decreases with increasing pH. Because the additional hydroxide ions shift the equilibrium toward solid $Ni(OH)_2$ following Le Chatelier's principle. The pH of saturated $Ni(OH)_2$ solution in 28% aqueous ammonia was measured as 13.7. While the concentration of dissolved $Ni(OH)_2$ in the saturated $Ni(OH)_2$ solution in 28% aqueous ammonia was significantly less than the maximum possible value at lower pH, it facilitated stopping immediate precipitation of $Ni(OH)_2$ due to unavoidable losses of ammonia when the solution was manipulated. As a result, a setup for solution growth experiments was possible for deposition of $Ni(OH)_2$ to occur after the bath remained undisturbed for some time.

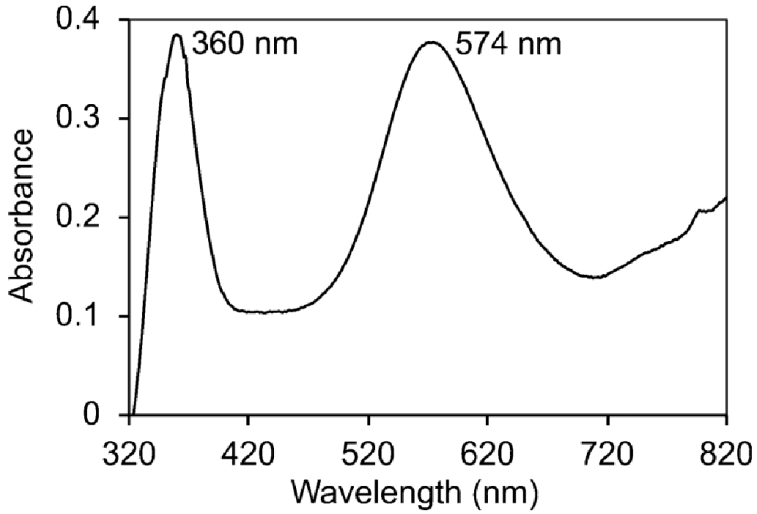

Figure 4: UV-visible spectrum of hexamine nickel (II), $[Ni(NH_3)_6]^{2+}$ complex prepared by dissolution of $Ni(OH)_2$ in concentrated aqueous ammonia solution.

The deposition of $Ni(OH)_2$ films occurs as ammonia escapes from the chemical bath. Under a critical concentration of ammonia, the hexamine nickel (II) ion, $[Ni(NH_3)_6]^{2+}$ will start to lose ammonia and replace by water molecules. At some point, the interaction of either $[Ni(NH_3)_6]^{2+}$ or an intermediate complex, $[Ni(NH_3)_{6-x}(H_2O)_x]^{2+}$ with hydroxide, OH^- ions form a hydroxide complex, $[Ni(NH_3)_5(OH)]^+$ or $[Ni(NH_3)_{5-x}(H_2O)_x(OH)]^+$. This hydroxide complex formation very likely occurs due to the deprotonation of a coordinated aqua ligand. While the addition of the second hydroxide ion or deportation of the second aqua ligand of the previous complex would generate a $Ni(OH)_2$ complex that would be deposited onto substrates or precipitated out. The second reaction may occur on the surface of the substrate to deposit $Ni(OH)_2$ or the putative $Ni(OH)_2$ complex after diffusion deposit on the growing film. The preferred growth of $Ni(OH)_2$ on the beaker's walls or on the glass slides immersed in the bath indicated that either the second reaction on the surface that deposits $Ni(OH)_2$ or the deposition of putative $Ni(OH)_2$ complex occurs. Additionally, the growth of extremely-thin films that were optically transparent happened at the air-water interface, but these only contain a tiny amount of material.

$Ni(OH)_2$ deposition rate was determined using 30 ml of saturated $Ni(OH)_2$-NH_3 solution in eight identical beakers. At varying time, the deposition was stopped by discarding the remaining solutions of the beakers, and the deposited solid with the beakers were vacuum dried. The weights of the beakers with solid determined the amounts of nickel hydroxide deposited at various times. The solution became colorless after 120 hours, which indicated that all the Ni^{2+} initially dissolved had deposited. A plot of mass of $Ni(OH)_2$ against time is presented in Figure 5, which shows a complex pattern. The initial deposition was linear at a rate of 0.224g/hour on the first day. During the second day, the deposition was slowed down with a rate of 0.0025g/hour, and then the rate was increased to 0.0137g/hour before stopping after 5 days when all dissolved Ni^{2+} was depleted. The deposition process generated a homogenous pale mint-green-colored film on the sides of the

beaker. Notably, the elemental analysis of the deposited $Ni(OH)_2$ found only 0.17% by weight of nitrogen, confirming that it does not contain significant amounts of ammonia or ammonium ions.

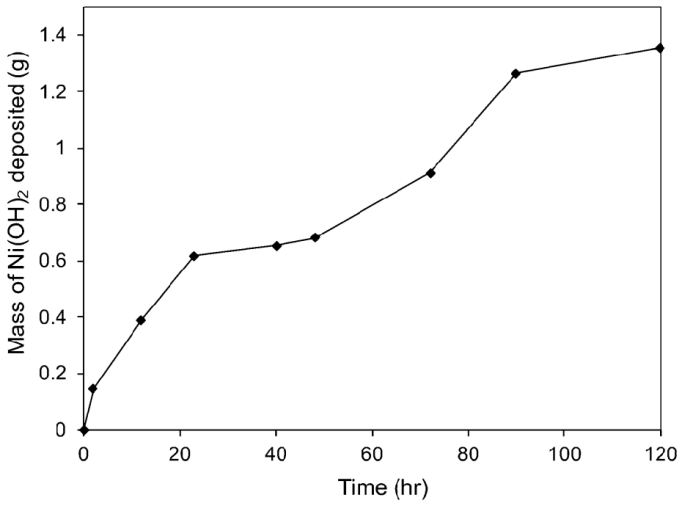

Figure 5: Deposition of $Ni(OH)_2$ with time as ammonia escapes from the saturated $Ni(OH)_2$-NH_3 solution.

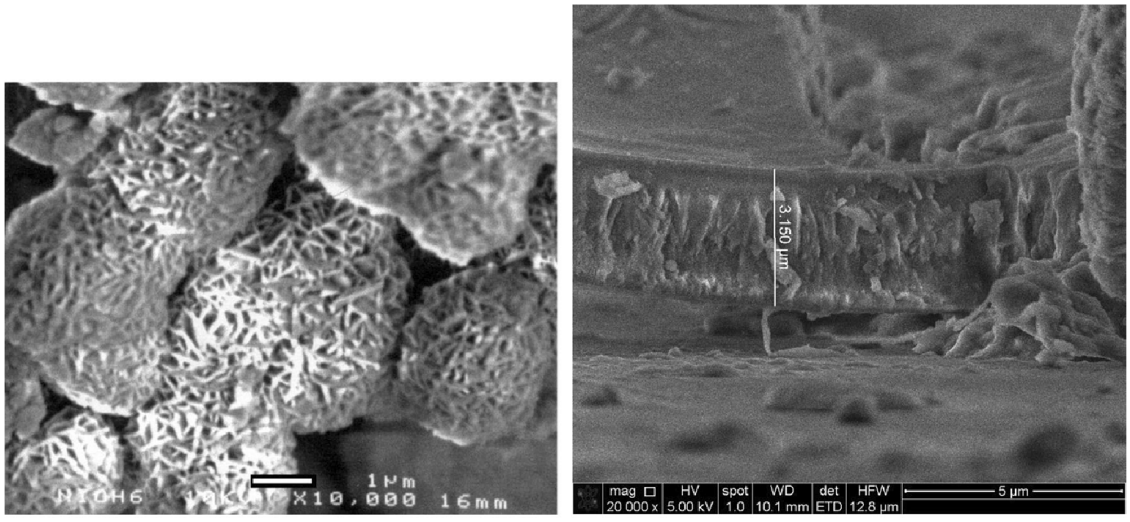

(a) **(b)**

Figure 6: Scanning electron microscopy images of β-$Ni(OH)_2$ films.

Scanning Electron Microscopy (SEM) images illustrated a quite unusual morphology of nickel hydroxide prepared from the ammonia solution, as shown in Figure 6a. Extremely small,

interconnected needles of $Ni(OH)_2$ form large sphere-type particles with a diameter of 3.8 μm. Although the microstructure looks very porous and a small particle size of $Ni(OH)_2$ was observed when viewed from the top, the surface area is not high as it was determined as 20.6 m^2/g. The side view of a cracked film in the scanning electron microscope revealed that the film is dense (Figure 6b). Additionally, the SEM image also showed the thickness of the film is about 3 μm.

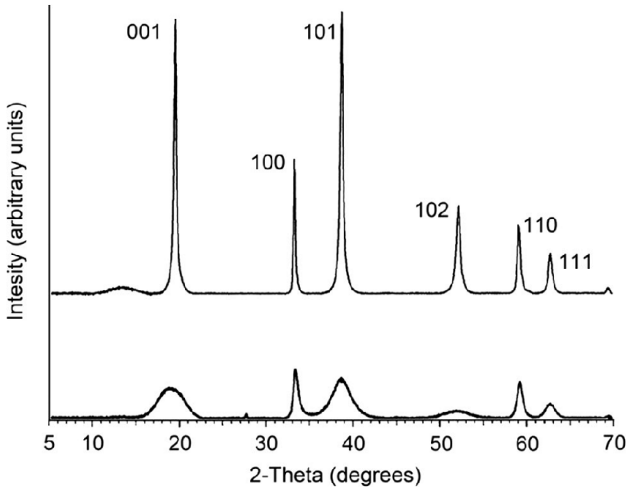

Figure 7: XRD patterns for β-$Ni(OH)_2$ from the solution growth method (top) and from a precipitation method of $Ni(NO_3)_2$ solution with a base (bottom). The top XRD pattern shows the hkl values for β-$Ni(OH)_2$ (JCPDS# 14-0117).

The X-ray diffraction pattern of nickel hydroxide grown from a typical saturated $Ni(OH)_2$-NH_3 solution is showcased in Figure 7 (top). While Figure 7 (bottom) presents an XRD pattern of a turbostratic nickel hydroxide prepared by precipitation of nickel nitrate by ammonia.[34] The patterns match with a β-$Ni(OH)_2$ phase in the JCPDS database (JCPDS# 14-0117). The chemical bath-grown hydroxide shows a considerably higher intensity of *001*, *101,* and *102* reflections, indicating the better ordering of layers in the c-axis of crystallographic directions. This confirms a high degree of ordered $Ni(OH)_2$ layers to each other. Besides the increased registration of layers, the reflection for *001* is shifted toward a higher angle (smaller d-spacing) which confirmed a

decreased interlayer-spacing from 4.72 to 4.59 A˚. The d-spacings of *101* and *102* planes are also slightly shifted due to the change in *001* planes' d-spacing. However, these shifts are observed to a lesser extent. The XRD patterns confirm that the slow growth of β-$Ni(OH)_2$ by evaporation of ammonia from $Ni(OH)_2$-aqueous ammonia solution results in a highly ordered layered compound, whereas rapid precipitation produces a turbostratic β-$Ni(OH)_2$. The turbostratic β-$Ni(OH)_2$ showed much broader *001* and *101* reflections (Figure 7, bottom).

The successful deposition of β-$Ni(OH)_2$ using the solution growth process further motivated the present work to investigate whether the process can be advanced to generate a stable α-$Ni(OH)_2$ material. It is well established that aluminum substitution can influence the formation of a stable phase of α-$Ni(OH)_2$;[29, 30] therefore, the current investigation decided to introduce aluminum ions into the solution growth bath. An aqueous sodium aluminate solution was added to the $Ni(OH)_2$-aqueous ammonia chemical bath solution for doping $Ni(OH)_2$ with aluminum. The current work successfully determined the approximated ratio of Ni^{2+}/Al^{3+} by adding an increasing amount of 0.33 M sodium aluminate solution to 40 ml of saturated $Ni(OH)_2$-NH_3 solution. Upon ammonia release from most of the water, the solid product was isolated, washed, and dried. Figure 8 presents the XRD patterns of the solution-grown products that show that 1 ml of 0.33M sodium aluminate $NaAl(OH)_4$ solution was sufficient to generate a small fraction of α-$Ni(OH)_2$ phase along with the predominant β-$Ni(OH)_2$ phase. The XRD patterns also show that the increasing volume of $NaAl(OH)_4$ solution progressively facilitated the α-$Ni(OH)_2$ formation. When 6 ml of $NaAl(OH)_4$ was added, a crystalline phase of α-$Ni(OH)_2$ (JCPDS# 38-0175) was produced, corresponding to 0.36 Al^{3+} ions for per Ni^{2+} ion in the crystalline solid. Compared to the work published by Kamath *et al.*, nickel-aluminum layered double hydroxides, $Ni_{1-x}Al_x(OH)_2(CO_3)_{0.5x}$ with the α-$Ni(OH)_2$ structure are stable in strongly basic conditions when x is greater than 0.2 that corresponds to 0.25 Al^{3+} ions for per Ni^{2+} ions.[30]

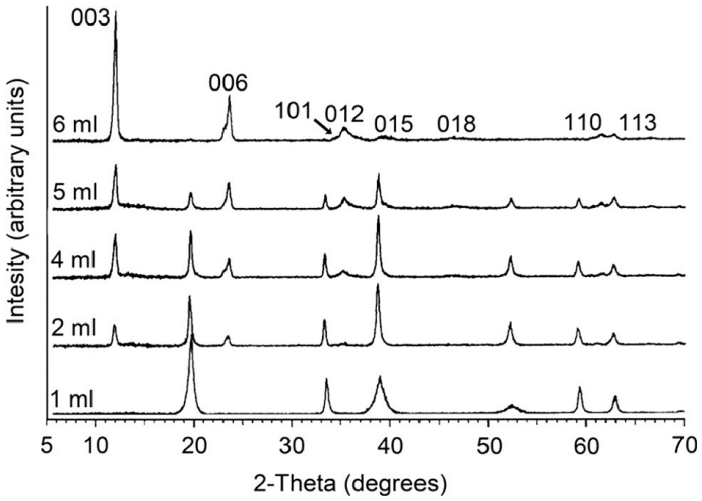

Figure 8: XRD patterns for the solids from 40 mL $Ni(OH)_2$-NH_3 solution with various amounts of added 0.33 M $NaAl(OH)_4$ solution. The top XRD pattern shows the hkl values of α-$Ni(OH)_2$ (JCPDS# 38-0175). The hkl values for the XRD pattern of β-$Ni(OH)_2$ (JCPDS# 14-0117) are shown in Figure 7.

The presence of aluminum has a profound effect on the morphology of grown α-$Ni(OH)_2$, as shown in the SEM images in Figure 9. Although the aluminum-containing solutions were not amenable to depositing thin films of α-$Ni(OH)_2$ on substrates, but the solutions formed free-standing membranes at the solution-air interface. This free-standing membrane formation was the primary growth method; however, a small amount of precipitation at the bottom of the solution was also observed. The difference from the aluminum-free deposition is that Al^{3+} substitutes Ni^{2+} during the growth of α-$Ni(OH)_2$ in the aluminum-containing solution. This substitution produces positively charged particles that repel each other; therefore, they resist aggregation into a film onto a surface. However, ammonia evaporation from the solution facilitates the particles to be carried out to the solution-air interface, where they aggregate into a membrane of an average thickness of 0.10 mm. The release of ammonia from Ni^{2+} ions on the surface possibly links the particles through the formation of hydroxide bridging. When an original membrane produces a free-standing ultra-thin skin at the interface of solution-air, it grows to a thicker membrane due to the continuous

follow-up deposition on its bottom. The overall process generates an opaque green membrane standing freely at the solution-air interface, as presented in a camera picture in Figure 2. SEM images show that the upper surface of the films is smooth (Figure 9a). While the bottom surface is rough due to the aggregation of particles, Figure 9b shows the edge of a cracked membrane where it is evidently clear that the membrane is made up of tightly aggregated small particles. The membranes are found to be somewhat brittle; therefore, they must be manipulated with a careful hand to separate them from the deposition bath.

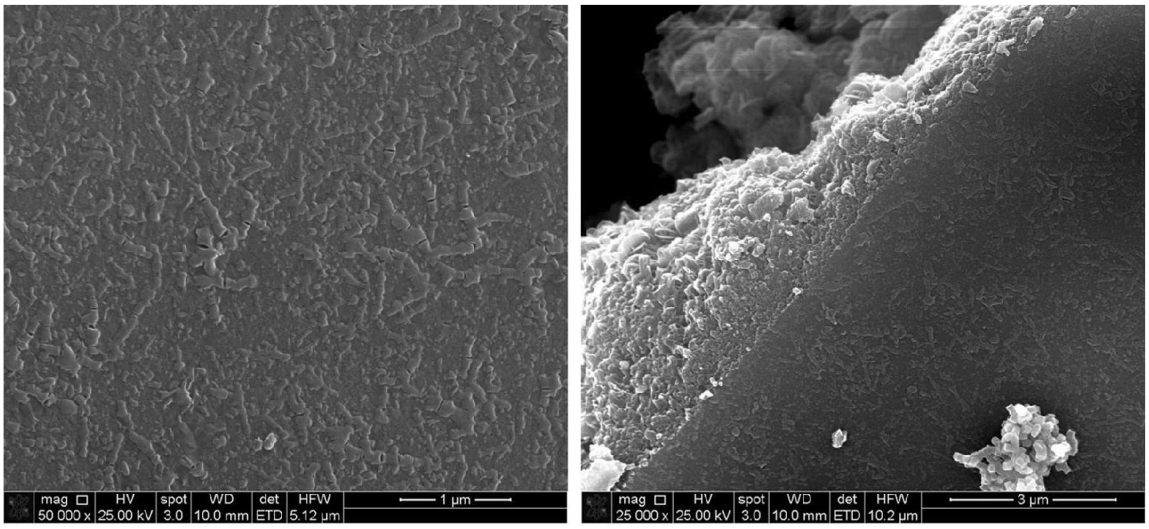

Figure 9: Scanning electron micrographs of aluminum substituted α-$Ni(OH)_2$ membrane – (a) top surface and (b) view along a crack.

Figure 10 shows the thermogravimetric traces of β-$Ni(OH)_2$ (dashed lined) and aluminum substituted α-$Ni(OH)_2$ (solid line). For the β-$Ni(OH)_2$, the dehydration step of incorporated water occurs up to 160 °C, followed by a broad mass loss starting at 170 °C ending at 525 °C representing the hydroxylation of the hydroxide groups of $Ni(OH)_2$ to nickel oxide, NiO. The TGA analysis excellently agrees with the literature reported study for β-$Ni(OH)_2$.[30] Notably, the mass at low temperature is believed to be the loss of water molecules loosely bound to the Ni^{2+} ions.[35] The 70.58% ceramic yield determines the formula of the β-nickel hydroxide as $Ni(OH)_2 \bullet 0.73H_2O$. A

more dramatic loss of water content was observed in the aluminum substituted α-$Ni(OH)_2$ as in the dehydration step, water content loss is higher than the β-$Ni(OH)_2$, confirming more water intercalation in the layered structure. The 60.68% ceramic yield enumerates the formula of the aluminum substituted α-$Ni(OH)_2$ as $Ni_{0.74}Al_{0.26}(OH)_{2.26} \bullet 1.5H_2O$. In the current investigation, the intercalated water of α- and β- $Ni(OH)_2$ is higher than the reported nickel hydroxides in literature produced by other synthetic routes. One possible reason is that the elevated surface areas of α- and β- $Ni(OH)_2$ prepared in the current study are 20.6 and 28.3 m^2/g, respectively. The higher surface areas may lead to the adsorption of more water molecules on the surface of the nickel hydroxides.

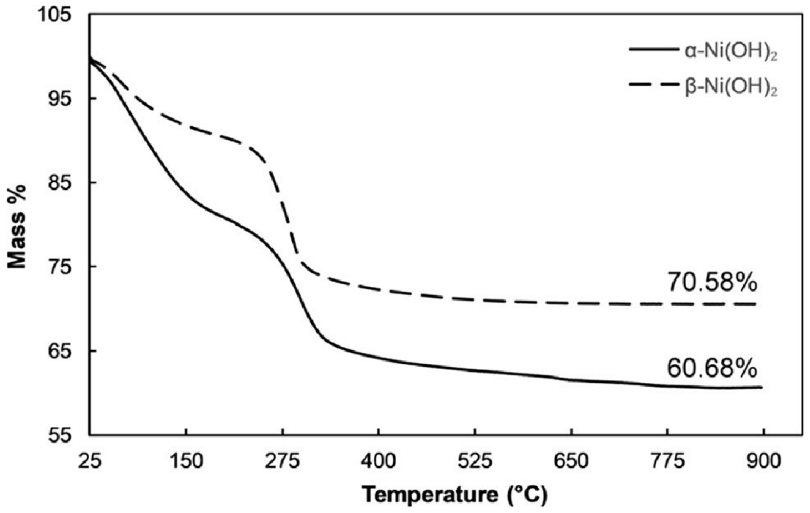

Figure 10: Thermogravimetric traces of the α- and β-nickel hydroxide products.

■ Conclusion

Dissolution of nickel hydroxide in concentrated aqueous ammonia generates a blue solution of nickel(II)hexamine hydroxide, $Ni(NH_3)_6(OH)_2$. The solution makes an excellent chemical bath. Because when the ammonia is allowed to escape slowly, the chemical bath deposits films of β-$Ni(OH)_2$ on the container walls or onto the suspended substrates. It also generates ultra-thin and optically transparent membranes at the surface of the bath solution. While the addition of a sufficient amount of sodium aluminate solution in the hexamine nickel(II) hydroxide chemical

bath solution generated aluminum substituted stable α-$Ni(OH)_2$ membranes grown at the water-air interface. The thick membranes formed at the solution's surface facilitated the isolation of free-standing membranes of aluminum substituted α-$Ni(OH)_2$. Hence, the developed chemical bath process shows promising growth characteristics and flexibility in nickel hydroxides deposition and growth as films and membranes, which will allow the use of the process in numerous applications of nickel hydroxides in present-day technologies.

Additionally, the approach for accessing nickel hydroxide films and membranes advances green engineering, which is the design of processes and products to lower pollution and promote sustainability while mitigating the risk to human health and the environment without losing economic viability or efficiency. The developed novel method for preparing nickel hydroxides films and membranes is a green process as it avoids the production of waste of salts like the conventional methodologies. The process can potentially recycle $Ni(OH)_2$ from the endo-of-life products that contain nickel hydroxides. Also, it would be possible to make the process further "green" if it can be utilized in industrial applications for ammonia recovery.

■ References:

(1) ACS 12 Principles of Green Chemistry. https://www.acs.org/content/acs/en/greenchemistry/principles/12-principles-of-green-chemistry.html

(2) J. McBreen, Nickel Hydroxides,Handbook of Battery Materials, 2nd ed., J.O. Besenhard and C. Daniel, Ed., Verlag GmbH, Wiley-VCH, 2011, p 149–168.

(3) Smithrick, J. J.; O'Donnell, P. M., Nickel-hydrogen batteries - An overview. *Journal of Propulsion and Power* **1996,** 12, (5), 873-878.

(4) Chakkaravarthy, C.; Periasamy, P.; Jegannathan, S.; Vasu, K. I., The nickel/iron battery. *Journal of Power Sources* **1991,** 35, (1), 21-35.

(5) Shukla, A. K.; Ravikumar, M. K.; Balasubramanian, T. S., Nickel/iron batteries. *Journal of Power Sources* **1994,** 51, (1), 29-36.

(6) Kimmel, S. W.; Hopkins, B. J.; Chervin, C. N.; Skeele, N. L.; Ko, J. S.; DeBlock, R. H.; Long, J. W.; Parker, J. F.; Hudak, B. M.; Stroud, R. M.; Rolison, D. R.; Rhodes, C. P., Capacity and phase stability of metal-substituted α-Ni(OH)2 nanosheets in aqueous Ni–Zn batteries. *Materials Advances* **2021,** 2, (9), 3060-3074.

(7) Li, Y.; Xu, W.; Zheng, Y.; Yao, J.; Xiao, J., Hierarchical flower-like nickel hydroxide with superior lithium storage performance. *Journal of Materials Science: Materials in Electronics* **2017,** 28, (22), 17156-17160.

(8) Li, Y.; Pan, G.; Xu, W.; Yao, J.; Zhang, L., Effect of Al substitution on the microstructure and lithium storage performance of nickel hydroxide. *Journal of Power Sources* **2016,** 307, 114-121.

(9) M.E.G. Lyons, A. C., P. O'Brien, I. Godwin, and R.L. Doyle, Redox, pH sensing and Electrolytic Water Splitting Properties of Electrochemically Generated Nickel Hydroxide Thin Films in Aqueous Alkaline Solution. *Int. J. Electrochem. Sci* **2012,** 7(11), p 768–811.

(10) Xie, L.; Hao, J.-G.; Chen, H.-Q.; Li, Z.-X.; Ge, S.-Y.; Mi, Y.; Yang, K.; Lu, K.-Q., Recent advances of nickel hydroxide-based cocatalysts in heterogeneous photocatalysis. *Catalysis Communications* **2022,** 162.

(11) Luan, C.; Liu, G.; Liu, Y.; Yu, L.; Wang, Y.; Xiao, Y.; Qiao, H.; Dai, X.; Zhang, X., Structure Effects of 2D Materials on alpha-Nickel Hydroxide for Oxygen Evolution Reaction. *ACS Nano* **2018,** 12, (4), 3875-3885.

(12) Gao, M.; Sheng, W.; Zhuang, Z.; Fang, Q.; Gu, S.; Jiang, J.; Yan, Y., Efficient water oxidation using nanostructured alpha-nickel-hydroxide as an electrocatalyst. *J Am Chem Soc* **2014,** 136, (19), 7077-84.

(13) Chen, L.; Dong, X.; Wang, Y.; Xia, Y., Separating hydrogen and oxygen evolution in alkaline water electrolysis using nickel hydroxide. *Nat Commun* **2016,** 7, 11741.

(14) Miao, Y.; Ouyang, L.; Zhou, S.; Xu, L.; Yang, Z.; Xiao, M.; Ouyang, R., Electrocatalysis and electroanalysis of nickel, its oxides, hydroxides and oxyhydroxides toward small molecules. *Biosens Bioelectron* **2014,** 53, 428-39.

(15) Yang, H.; Gao, G.; Teng, F.; Liu, W.; Chen, S.; Ge, Z., Nickel Hydroxide Nanoflowers for a Nonenzymatic Electrochemical Glucose Sensor. *Journal of The Electrochemical Society* **2014,** 161, (10), B216-B219.

(16) Xia, K.; Yang, C.; Chen, Y.; Tian, L.; Su, Y.; Wang, J.; Li, L., In situ fabrication of Ni(OH)2 flakes on Ni foam through electrochemical corrosion as high sensitive and stable binder-free electrode for glucose sensing. *Sensors and Actuators B: Chemical* **2017,** 240, 979-987.

(17) Canevari, T. C.; Cincotto, F. H.; Landers, R.; Machado, S. A. S., Synthesis and characterization of α-nickel (II) hydroxide particles on organic-inorganic matrix and its application in a sensitive electrochemical sensor for vitamin D determination. *Electrochimica Acta* **2014,** 147, 688-695.

(18) Fang, B.; Gu, A.; Wang, G.; Li, B.; Zhang, C.; Fang, Y.; Zhang, X., Synthesis hexagonal ß-Ni(OH)2 nanosheets for use in electrochemistry sensors. *Microchimica Acta* **2009,** 167, (1-2), 47-52.

(19) Kotok, V.; Kovalenko, V., The electrochemical cathodic template synthesis of nickel hydroxide thin films for electrochromic devices: role of temperature. *Eastern-European Journal of Enterprise Technologies* **2017,** 2, (11 (86)), 28-34.

(20) Inamdar, A. I.; Sonavane, A. C.; Pawar, S. M.; Kim, Y.; Kim, J. H.; Patil, P. S.; Jung, W.; Im, H.; Kim, D.-Y.; Kim, H., Electrochromic and electrochemical properties of amorphous porous nickel hydroxide thin films. *Applied Surface Science* **2011,** 257, (22), 9606-9611.

(21) Guo, L.; Ren, Y.; Liu, J.; Chiam, S. Y.; Chim, W. K., Nanostructuring of nickel hydroxide via a template solution approach for efficient electrochemical devices. *Small* **2014,** 10, (13), 2611-7.

(22) Liu, Y.; Wang, R.; Yan, X., Synergistic Effect between Ultra-Small Nickel Hydroxide Nanoparticles and Reduced Graphene Oxide sheets for the Application in High-Performance Asymmetric Supercapacitor. *Sci Rep* **2015,** 5, 11095.

(23) Tang, Y.; Liu, Y.; Yu, S.; Zhao, Y.; Mu, S.; Gao, F., Hydrothermal synthesis of a flower-like nano-nickel hydroxide for high performance supercapacitors. *Electrochimica Acta* **2014,** 123, 158-166.

(24) Oliva, P.; Leonardi, J.; Laurent, J. F.; Delmas, C.; Braconnier, J. J.; Figlarz, M.; Fievet, F.; Guibert, A. d., Review of the structure and the electrochemistry of nickel hydroxides and oxy-hydroxides. *Journal of Power Sources* **1982,** 8, (2), 229-255.

(25) Hall, D. S.; Lockwood, D. J.; Bock, C.; MacDougall, B. R., Nickel hydroxides and related materials: a review of their structures, synthesis and properties. *Proc Math Phys Eng Sci* **2015,** 471, (2174), 20140792.

(26) Ramesh, T. N.; Kamath, P. V.; Shivakumara, C., Classification of stacking faults and their stepwise elimination during the disorder --> order transformation of nickel hydroxide. *Acta Crystallogr B* **2006,** 62, (Pt 4), 530-6.

(27) Bode, H.; Dehmelt, K.; Witte, J., Zur kenntnis der nickelhydroxidelektrode—I.Über das nickel (II)-hydroxidhydrat. *Electrochimica Acta* **1966,** 11, (8), 1079-1087.

(28) Delmas, C.; Faure, C.; Gautier, L.; Guerlou-Demourgues, L.; Rougier, A.; Dell, R. M.; Huggins, R. A.; Parsons, R.; Steele, B. C. H.; Vincent, A. C., The nickel hydroxide electrode from the solid-state chemistry point of view. *Philosophical Transactions of the Royal Society of London. Series A: Mathematical, Physical and Engineering Sciences* **1996,** 354, (1712), 1545-1554.

(29) Hu, W.-K.; Gao, X.-P.; Noréus, D.; Burchardt, T.; Nakstad, N. K., Evaluation of nano-crystal sized α-nickel hydroxide as an electrode material for alkaline rechargeable cells. *Journal of Power Sources* **2006,** 160, (1), 704-710.

(30) Kamath, P. V.; Dixit, M.; Indira, L.; Shukla, A. K.; Kumar, V. G.; Munichandraiah, N., Stabilized α-$Ni(OH)_2$ as Electrode Material for Alkaline Secondary Cells. *Journal of The Electrochemical Society* **1994,** 141, (11), 2956-2959.

(31) Miyake, M.; Maeda, M., Dissolution of nickel hydroxide in ammoniacal aqueous solutions. *Metallurgical and Materials Transactions B* **2006,** 37, (2), 181-188.

(32) Dean, J. A., Cumulative Formation Constants for Metal Complexed with Inorganic Ligand, Lange's Handbook of Chemistry, 14th ed., McGraw Hill, New York, p 8.7. In 1992.

(33) Dean, J. A., Solubility Products, Lange's Handbook of Chemistry, 14th ed. McGraw-Hill, New York, p 8.84. In 1992.

(34) Flevet, F.; Flglarz, M., Preparation and study by electron microscopy of the development of texture with temperature of a porous exhydroxide nickel oxide. *Journal of Catalysis* **1975,** 39, (3), 350-356.

(35) Kober, F. P., Analysis of the Charge-Discharge Characteristics of Nickel-Oxide Electrodes by Infrared Spectroscopy. *Journal of The Electrochemical Society* **1965,** 112, (11), 1064.

CHAPTER VII

Reactions of Metal Acetates and Propylene Oxide in Water: Synthesis of Acetate-Intercalated Layered Hydroxides or Hydroxides of Later 3d Transition Metals

■ Introduction

In the hydrolysis of a metal acetate aqueous solution, hexaaqua metal ions, $[M(H_2O)_6]^{2+}$ reacts with in situ formed OH^-, which generates the following hydroxide aqua complex.

$$[M(H_2O)_6]^{2+}(aq) + OH^-(aq) \rightleftharpoons [M(H_2O)_5(OH^-)]^+(aq) + H_2O(l)$$

The $[M(H_2O)_5(OH)]^+$ complex is the key species that end up generating either metal acetate hydroxide, $M(OAc)_x(OH)_{2-x}$ or metal hydroxide, $M(OH)_2$, depending on the metal ions in hydrolysis or hydrothermal reactions. Chapters II, III, VA, and VB show that the hydrolysis of later 3d transition metal (Co, Ni, Cu, and Zn) acetates deposited nano-/micro-structured corresponding metal acetate hydroxides or hydroxides as films upon heating without any second chemicals or reagent. Therefore, the amount of deposition by hydrolysis of metal acetates is dependent and limited in the formation of in situ OH^- ions. However, in order to synthesize metal acetate hydroxides or hydroxides in very high yields as powders by the hydrolysis of metal acetates, the above equilibrium must be needed to shift to the right to produce more $[M(H_2O)_5(OH)]^+$. This can be achieved by the addition of a species (reagent) that would remove hydrogen ions (protons) from the water molecules of $[M(H_2O)_6]^{2+}$ species. The idea of removing a proton from the $[M(H_2O)_6]^{2+}$

species prompted the present investigation to add a proton (H^+) scavenger in the hydrolysis reactions of later 3d transition metal acetates to produce their acetate-intercalated layered hydroxides (metal acetate hydroxides) in very high yields. Another goal of adding a proton scavenger was to find out if the hydrolysis reactions with a proton scavenger can generate acetate-intercalation in metal hydroxides. Therefore, the present work explored the addition of propylene oxide as a proton scavenger in the hydrolysis reactions of later 3d transition metal (zinc, copper, cobalt, and nickel) acetates in water. In the presence of propylene oxide, the present work expected that the hydrolysis reactions of transition metal acetates would involve the following possible reactions to produce acetate-intercalated layered metal hydroxides.

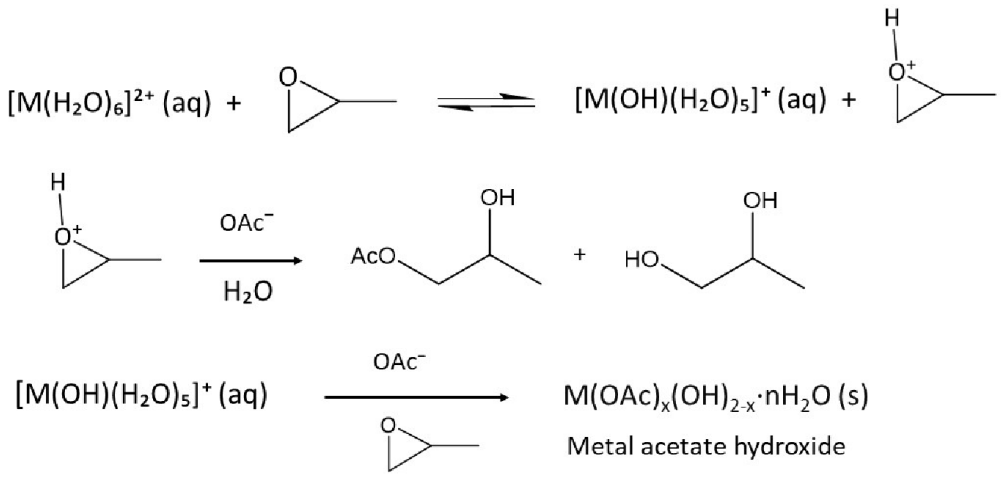

Scheme 1: Possible reactions involved in propylene oxide-assisted hydrolysis of a transition metal acetate in water. Where M is a divalent transition metal.

Acetate-intercalated layered metal hydroxides (LMHs) of later 3d transition metals such as copper or zinc are very interesting materials due to their layered structure where the acetate groups are intercalated in between layers of $Cu(OH)_6$ octahedra or $Zn(OH)_6$ octahedra/$Zn(OH)_4$ tetrahedra.[1, 2] The intercalated-acetate groups of zinc or copper layered hydroxide, their bimetallic layered double hydroxides (LDHs), and other LDHs of later 3d transition metals can undergo anion exchange with other anions such chloride, chlorate, sulfate, phosphate, arenite, arsenate,

antimonate, selenite, selenate, and benzoate.[3-7] Due to the excellent anion exchangeability of the intercalated acetate groups of zinc or copper acetate hydroxide and other LMHs and LDHs of later 3d transition metals, they are promising materials for uptake of anionic pollutants. Their very inexpensive synthesis with straightforward scaling up, medium to high surface areas, and their environmental beingness (extremely low to no release of metals ions) make them an attractive material in real-world pollutants uptake applications. Additionally, although acetate-intercalated zinc or copper layered hydroxides (zinc or copper acetate hydroxide) have never been investigated for removing radioactive ions such as $TcO4^-$ in nuclear wastewater, they would likely be an attractive alternative for cleaning nuclear waste streams due to their acetate (anion) exchangeability. Zinc or copper acetate hydroxide also can be employed for direct air capture of pollutants and gases indoors, such as in chemistry research laboratories and industries. While zinc acetate hydroxide is proven to be a valuable catalyst for the esterification of fatty acids.[8]

Acetate-intercalated layered metal hydroxides (LMHs) of later 3d transition metals are excellent precursors for corresponding metal oxides. Because pyrolysis of these metal acetate hydroxides decomposes the acetate groups and dehydroxylate the hydroxide groups that leave metal oxides. Often these metal acetate hydroxides produce nano metal oxides – such as zinc acetate hydroxide, $Zn_5(OH)_8(OAc)_2 \cdot nH_2O$ thermally transformed into nanocrystalline zinc oxide, ZnO.[9] Copper acetate hydroxide with a morphology of flower-like structure assembled by nanoplates upon pyrolysis generated identical porous morphology of copper(II) oxide CuO.[10] While nanostructured metal acetate hydroxides deposited on substrates can also yield metal oxides having similar nano-morphology to the starting metal acetate hydroxides. For example, Chapter II shows that web-like nanowalls of nickel acetate hydroxide, $Ni(OAc)_{0.28}(OH)_{1.72} \cdot 0.25H_2O$ upon pyrolysis produced identical web-like nanostructured nickel oxide, NiO. Later 3d transition metal oxides as nanoparticles and deposited nano-/micro-structures have numerous important technological applications, as mentioned in the previous chapters' introductions (Chapters II-V).

Due to being impressive anion exchange materials for pollutant removal and valuable precursors for zinc or copper oxide nanoparticles and nano-/micro-structures, the synthesis of acetate-intercalated zinc or copper layered hydroxide (zinc or copper acetate hydroxide) has drawn significant interest. Widely used method for synthesis of acetate-intercalated zinc hydroxide, $Zn(OAc)_x(OH)_{2-x}\cdot nH_2O$ or copper acetate hydroxide, $Cu(OAc)_x(OH)_{2-x}\cdot nH_2O$ involves two process – (i) precipitation of zinc or copper acetate by NaOH,[4, 9, 11] and (ii) reaction of ZnO with zinc acetate aqueous solution at room temperature;[12, 13] this route may also work for copper oxide and copper acetate. This route was developed and extensively investigated by Meyn and coworkers using metal oxides and aqueous solutions of corresponding nitrates.[14] While Poul and coworkers developed polyol-mediated hydrolysis of zinc, nickel, or cobalt acetate that can produce corresponding acetate hydroxides at room temperature to 60 °C.[15] Švarcová *et al.* made a single crystal of copper acetate hydroxide, $Cu_2(OAc)(OH)_3\cdot H_2O$ by refluxing 0.1M copper acetate aqueous solution at 60 °C.[1] However, the process has a low yield; therefore, it may not be good enough for large-scale synthesis of copper acetate hydroxide. Nevertheless, the routes mentioned above are the existing routes reported in the literature for accessing zinc and copper acetate hydroxides.

While bimetallic hydroxide of later 3d transition metals such as Nickel-cobalt hydroxide, $NiCo_2(OH)_4$ is a useful precursor for accessing nickel-cobalt oxyhydroxide, $NiCo_2O_x(OH)_{4-x}$ and nickel cobaltite, $NiCo_2O_4$. These oxyhydroxide and cobaltite, due to their superior electrochemical activity and conductivity, are up-and-coming materials for electrocatalysis and electrodes for batteries, supercapacitors, and methanol-based fuel cells.[16-18] Additionally, Nickel cobaltite has a low bandgap and can be employed as a photocatalyst for degrading organic pollutants.[19] While bimetallic nickel-cobalt hydroxide can be directly used for electrodes for supercapacitors[20] and as catalysts for hydrogen evolution reaction (HER) from alcohols[21] and electrooxidation of urea[22]. Bimetallic nickel-cobalt hydroxide can be prepared by precipitation of mixtures of nickel and cobalt salts by a base such as NaOH. As the pKa of nickel(II) ions (9.85) and cobalt(II) ions (9.84) in

water are almost the same,[23] it is expected that the precipitation will generate a stoichiometric bimetallic hydroxide. Precipitation is, in fact, found to produce nickel-cobalt hydroxides.[20] A Hydrothermal method such as mixtures of nickel and cobalt nitrate and hexamethylenetetramine solutions were reported to generate nickel-cobalt hydroxides that have a morphology of flower-like interconnected nanowalls.[24] Electrodeposition of nickel-cobalt hydroxides was also reported, involving nickel and cobalt nitrate solution under electrochemical conditions.[25]

Herein the current investigation presents new hydrolysis routes for synthesizing acetate-intercalated copper and zinc layered hydroxides with very high yields. The reaction routes involved propylene oxide and corresponding metal acetate aqueous solutions at near room temperature. The copper acetate aqueous solution with propylene oxide at 40 °C produced crystalline copper acetate hydroxide, $Cu(OAc)_{0.43}(OH)_{1.67}{\cdot}0.41H_2O$ with a 100% yield. While zinc acetate and propylene oxide in water produced zinc acetate hydroxide, $Zn(OAc)_{0.33}(OH)_{1.67}{\cdot}\ 0.50H_2O$ with a yield of 93.6%. Literature investigation reveals that the synthesis of copper acetate hydroxide has never been reported by such a reaction. Although zinc chloride and propylene oxide reaction in the presence of a polymer was reported to generate microporous $Zn(OH)_2$,[26] zinc acetate and propylene oxide reaction to produce zinc acetate hydroxide is investigated in this work for the first time. Reactions of cobalt acetate and nickel acetate aqueous solutions with propylene oxide were also tested at 60 °C. It turned out that these reactions could not generate acetate-intercalated cobalt and nickel layered hydroxides (α-type nickel or cobalt hydroxide), as evident by their XRD patterns. These reactions produce β-type cobalt and nickel hydroxides.

Additionally, a hydrolysis reaction of 2:1 nickel acetate and cobalt acetate aqueous solution with propylene oxide was investigated to determine if the hydrolysis process generates a stochiometric nickel-cobalt hydroxide, $NiCo_2(OH)_6$. It turned out the hydrolysis reaction produced a stochiometric nickel-cobalt hydroxide with the formula of $NiCo_2(OAc)_{0.15}(OH)_{5.85}{\cdot}0.4H_2O$.

■ Experimental

Chemicals: Zinc acetate dihydrate, $Zn(OAc)_2 \cdot 2H_2O$ (98%), and Copper acetate monohydrate, $Cu(OAc)_2 \cdot H_2O$ (98%) were purchased from BAKER ANALYZED™ Reagent (where OAc stands for acetate, CH_3COO^-). While hydrated nickel acetate $Ni(OAc)_2 \cdot 4.4H_2O$ (98%) and cobalt acetate tetrahydrate, $Co(OAc)_2 \cdot 4H_2O$ (98%) were collected from Alfa Assar and Fisher Scientific, respectively. Propylene oxide was purchased from Fisher Scientific. All the metal acetates were used without further purification. Deionized water (~18 $M\Omega cm^{-1}$) was used as a solvent for all the reactions and for washing the collected products.

Reaction of copper acetate aqueous solution with propylene oxide at 60°C: 10.0 mmol (2.00 g) of copper acetate monohydrate was dissolved in 39.95 g of water in a 100 ml screw cap pyrex jar. After adding 100. mmol (5.81 g) propylene oxide to the above solution, it was closed with a screw cap and placed in an oven at 60°C. The reaction produced a bluish-green crystalline product (Figure 1). The reaction stopped at 24 hours, and the isolated product was washed several times with deionized water until the conductivity of the washing water read zero. The product was dried at 60°C. The reaction jar was also coated with the product as a robust film. The coating product was washed, dried, and scraped out. The total mass of the collected product was 1.105 g. Elemental analysis (carbon content 8.40%) and TGA experiment (copper content 52.07%) established the formula of the product as $Cu(OAc)_{0.44}(OH)_{1.56} \cdot 0.40H_2O$. The yield of the reaction was 89.8%.

Reaction of copper acetate aqueous solution with propylene oxide at 40°C: Another reaction of 10.01 mmol (1.998 g) copper acetate with 199.7 (11.60 g) mmol of propylene oxide in 40.0 g water was performed at 40 °C. The reaction produced the same bluish-green crystalline product (Figure 2) as the reaction product at 60 °C. However, the product's particles of this reaction look finer than the reaction at 60 °C. The collected product amount was 1.230 g. Elemental analysis

(carbon content 8.36%) and TGA experiment (copper content 50.20%) enumerated the formula of the product as $Cu(OAc)_{0.44}(OH)_{1.56}\cdot 0.50H_2O$. This confirmed the yield of the reaction as 100%.

Figure 1: Copper acetate hydroxide, $Cu(OAc)_{0.44}(OH)_{1.56}\cdot 0.40H_2O$ synthesized at 60 °C.

Figure 2: Bluish-green crystalline copper acetate hydroxide, $Cu(OAc)_{0.44}(OH)_{1.56}\cdot 0.50H_2O$ synthesized at 40°C. (a) The crystalline product in water during washing, exhibiting diffraction of visible light, and (b) isolated product.

Synthesis of zinc acetate hydroxide, $Zn(OAc)_{0.33}(OH)_{1.67}\cdot 0.50H_2O$ by hydrolysis reaction of aqueous $Zn(OAc)_2$ and propylene oxide at 40 °C: After dissolving 49.125 mmol (10.986 g) zinc acetate dihydrate in 200.1 g of deionized water, 1000 mmol (58.1 g) propylene oxide was added. Immediate light cloudiness was observed (due to the change of polarity of the solution, zinc acetate crystallized, making the solution cloudy). The reaction solution was filtered to get a clear solution, and the mass of the collected reaction solution was 238.0 g (which contained 43.5 mmol of zinc acetate). The reaction solution was heated at 40°C in a closed 500 mL pyrex bottle for 96 hours. The reaction produced a white material that slowly became almost a cake inside the container (Figure 3) at 96 hours. The cake was broken and washed on a glass frit filter using deionized water until the conductivity of the wash water became close to zero. The collected white product was vacuum dried, and the mass of the product was 5.0 g. Elemental analysis (carbon content 6.40%) and FTIR spectrum (Figure 13) confirmed the presence of acetate. While TGA enumerated the formula of the product as $Zn(OAc)_{0.33}(OH)_{1.67}\cdot 0.50H_2O$. The product's formula determined the yield of the reaction as 93.6%.

Figure 3: Hydrolysis reaction of zinc acetate and propylene oxide in water at 40°C (left) and its dried product zinc acetate hydroxide, $Zn(OAc)_{0.33}(OH)_{1.67}\cdot 0.50H_2O$ (right)

Reaction of aqueous $Co(OAc)_2$ with propylene oxide for β-$Co(OH)_2$: After dissolving 10.0 mmol (2.49 g) cobalt acetate dihydrate in 40 g deionized water in 100 mL pyrex bottle, 100. mmol (5.81 g) propylene oxide was added to it. The reaction solution was heated at 80°C for 24 hours. After a few hours of the reaction, a bluish-purple solid was formed that in 24 hours turned into a pink-colored solid. After washing and drying, the mass of the pink-colored product was 0.682 g. The XRD pattern (Figure 15c) confirmed that the final product is a β-$Co(OH)_2$ with a formula of $Co(OAc)_{0.07}(OH)_{1.93}\cdot 0.057H_2O$. The formula was determined by elemental analysis (carbon content 1.74%), TGA, and FTIR spectrum (Figures 15a & 15b). The yield of the reaction was 73.4%.

Reaction of aqueous $Ni(OAc)_2$ and propylene oxide for β-$Ni(OH)_2$: 10.0 mmol (2.56 g) of hydrated nickel acetate ($Ni(OAc)_2\cdot 4.4H_2O$) was dissolved in 39.99 g of deionized water. 200.1 mmol (11.62 g) of propylene oxide was added to the above solution. The reaction solution was then placed in an oven at 60°C for 24 hours. Green colored powder product was formed, accompanying a thin coating on the walls of the reaction container. The product was filtered off and washed thoroughly. After vacuum drying, the product weighed 0.909g. The XRD pattern, TGA (nickel content 62.3%), and elemental analysis (carbon content 0.95%) as presented in Figure 16a-c confirmed that the product was turbostratic β-$Ni(OH)_2$ with a formula of $Ni(OAc)_{0.05}(OH)_{1.95}\cdot 0.06H_2O$. The yield of the reaction was 95.3%.

Reaction of aqueous 2:1 cobalt acetate and nickel acetate with propylene oxide: 3.35 mmol (0.858 g) of nickel acetate ($Ni(OAc)_2\cdot 4.4H_2O$) and 6.69 mmol (1.666 g) of cobalt acetate ($Co(OAc)_2\cdot 4H_2O$) were dissolved in 40.38 g of deionized water. 199.9 mmol (11.61 g) of propylene oxide was added to the above solution. The reaction solution was then placed in an oven at 60°C for 48 hours. A greenish-pink-colored powder product was formed. The product was centrifuged and washed thoroughly. After vacuum drying, the product weighed 0.970g. FTIR spectrum, TGA (Figure 19), and elemental analysis (carbon, nickel, and cobalt contents were 1.08,

18.4, and 37.9%, respectively) confirmed that the product was nickel-cobalt hydroxide with a formula of $NiCo_2(OAc)_{0.05}(OH)_{1.95}\cdot 0.4H_2O$. The yield of the reaction was 99.1%.

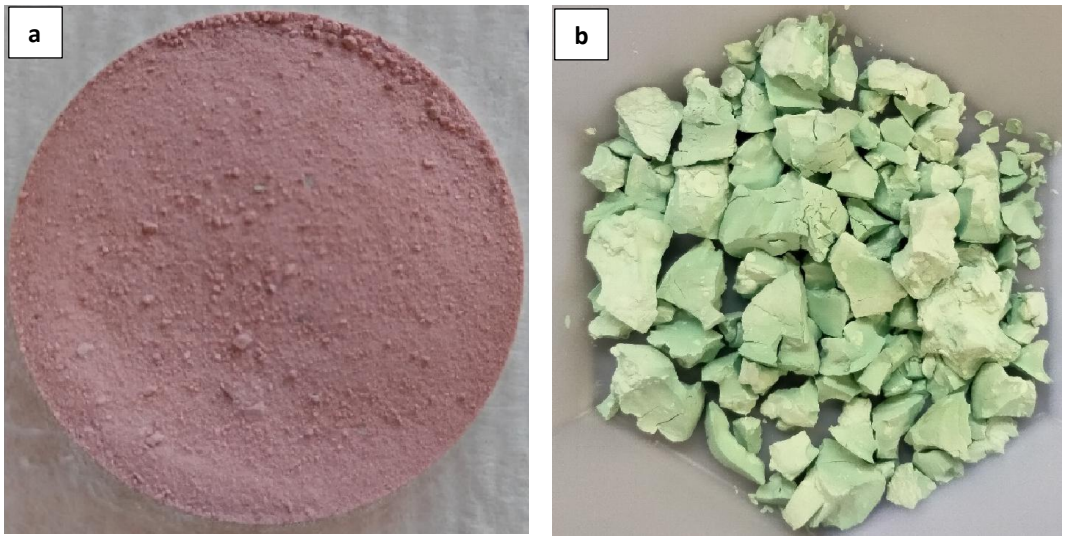

Figure 4: (a) β-$Co(OH)_2$ and (b) β-$Ni(OH)_2$ synthesized by hydrolysis of aqueous cobalt acetate and aqueous nickel acetate, respectively, in the presence of propylene oxide.

Figure 5: Nickel-cobalt hydroxide, $NiCo_2(OAc)_{0.05}(OH)_{1.95}\cdot 0.4H_2O$ prepared from hydrolysis of aqueous 2:1 cobalt acetate and nickel acetate with propylene oxide.

Characterization:

XRD: The XRD patterns were acquired using a Discover D8 instrument at the Microscopy lab, Oklahoma State University, Stillwater, Oklahoma. The setting was 40 kV and 40mA current at the 2θ range of 5 to 70° with an interval of 0.01°.

For matching the XRD pattern of the prepared copper acetate hydroxide, a calculated XRD pattern was used using the known crystal structure of Cu2 OAc)(OH)3·H2O. An open software, VESTA (Visualization for Electronic and Structural Analysis), was used to generate the calculated pattern where the sharpest peak was chosen as 001 planes. Average crystallite sizes were determined using the Scherrer equation (citation) and the 001, 002, and 003 reflections.

TGA and ATR-FTIR: Thermogravimetric Analysis (TGA) experiments employed a PerkinElmer TGA 4000 instrument. All TGA experiments were performed under air. A Nicolet i50 Attenuated Total Reflectance (ATR)-FTIR instrument collected the FTIR spectra.

Elemental Analysis: Metal contents analysis was performed using an Agilent 4200 microwave plasma atomic emission spectrophotometer. Typically, samples were digested in contorted HCl followed by diluted to conduct the metal content analysis experiments. While the carbon contents were determined using a LECO CHN 628 analyzer.

■ Results and Discussion:

Copper acetate hydroxide, $Cu(OAc)_{0.44}(OH)_{1.56}\cdot nH_2O$:

XRD pattern of copper acetate hydroxide prepared at 60°C (Figure 6) establishes that the material is a layered double hydroxide (LDH). Since the XRD pattern exhibits strong peaks at smaller angles and weaker peaks at higher angles, which is the signature feature of a layered hydroxide material.[4, 5, 15] The three strongest reflections at two thetas of 9.42°, 18.93°, and 28.58° can be indexed as *001*, *002,* and *003* planes, respectively.[4] Rest of the peaks' positions and their d-

spacing with indexing are tabulated in the supporting information (Table S1). It is well known that copper acetate hydroxide adopts a monoclinic lattice structure, unlike zinc or nickel acetate hydroxide, which adopts a hexagonal lattice structure.[1, 15] Therefore, all the peaks were indexed to a monoclinic lattice structure that constitutes the layered copper acetate hydroxide. The indexing was done according to the calculated XRD patterns of the $Cu_2(OH)_3(CH_3COO)\cdot H_2O$ crystal structure published by S. Švarcová et al.[1] Notably, the position of the peaks in LDHs can be shifted a little bit depending on the number of intercalated anions and water molecules. After assigning the first reflection (the strongest peak) as the 001 planes, the two theta (2θ) of the 002 reflection is found to be multiples of 2 of the 001 reflection's two theta, and similarly, the 003 planes piston is multiple of 3 of the 001 planes. As a result, the peaks at 38.449 and 48.664° should be indexed as 004 and 005 planes, respectively, corresponding multiples to the 001 planes. This indexing at higher angles for 00l planes agrees with the calculated XRD pattern of the $Cu_2(OH)_3(CH_3COO)\cdot H_2O$ structure (where the first strongest reflection was assigned as 001). However, Kozai et al. indexed the 004 and 005 planes at higher angles where they did not precisely the multiples of 4 and 5, respectively.[4] Nevertheless, the XRD peaks are sharp, indicating the polycrystalline nature of the prepared copper acetate hydroxide. The XRD reflection of the copper acetate hydroxide synthesized at 40 °C (Figure 7 and Supporting Table S1) has the same pattern as copper acetate hydroxide prepared at 60 °C. However, there their average crystallite sizes are different (Table 1). The copper acetate hydroxide synthesized at 40 °C has a lower average crystallite size (56.8±1.6 nm) than that of 60°C (72.7±2.7 nm). At higher temperature, the growth of crystallites in the hydrolysis reactions should be faster; therefore, the hydrolysis product at 60°C produce bigger crystallites. While interestingly, interlayer distances (d-spacing of 001 planes) of copper acetate hydroxides synthesized at 40 and 60 °C are not identical. For 40°C's copper acetate hydroxide, the interlayer spacing is 9.360 Å which is a little bit (0.026 Å) smaller than the 60°C's copper acetate hydroxide as its interlayer distance is 9.386 Å.

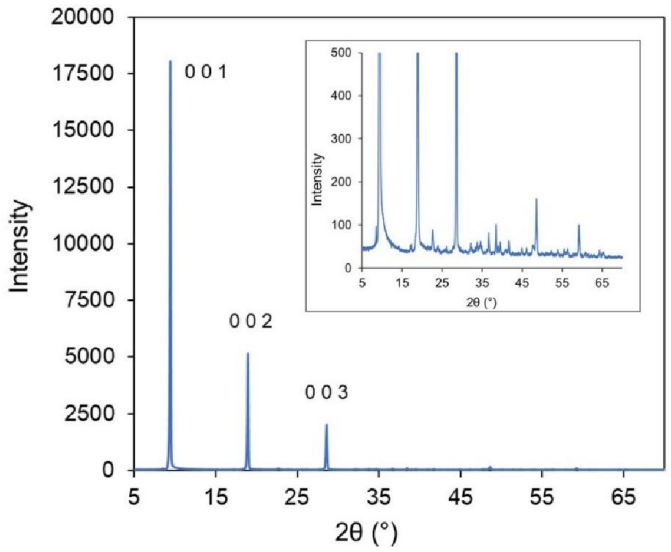

Figure 6: XRD pattern of copper acetate hydroxide, $Cu(OAc)_{0.44}(OH)_{1.56}\cdot 0.40H_2O$ synthesized at 60°C with 1:10 copper acetate and propylene oxide. Inset is the zoom-in pattern showing other reflections at higher angles.

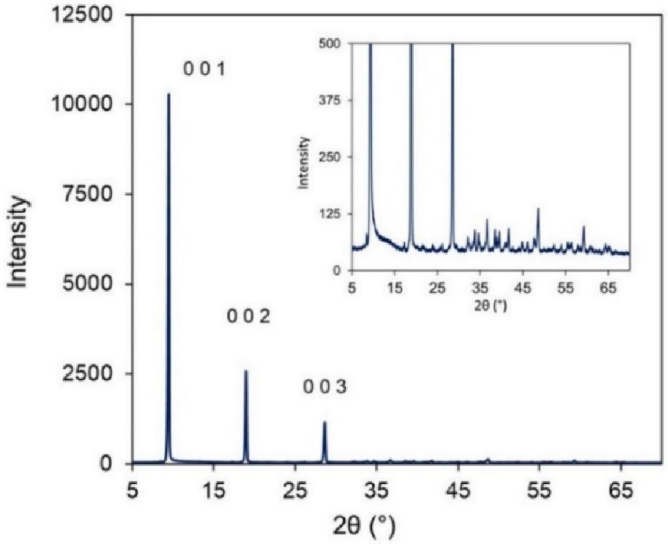

Figure 7: XRD pattern of copper acetate hydroxide, $Cu(OAc)_{0.44}(OH)_{1.56}\cdot 0.50H_2O$ synthesized at 40°C with 1:20 copper acetate and propylene oxide. Inset is the zoom-in pattern showing other reflections at higher angles.

Table 1: Comparison of average crystallite sizes of copper acetate hydroxide synthesized at different temperatures. Crystallite sizes were determined using the Scherer equation.[27]

Temperatures for synthesis of copper acetate hydroxide	Average crystallite size (nm)
60 °C	72.7 ± 2.7
40 °C	56.8 ± 1.6

Table 2: Interlayer distances of copper acetate hydroxide synthesized at 60 and 40 °C

Temperatures for synthesis of copper acetate hydroxide	Copper acetate hydroxide	Interlayer distance (Å)
60 °C	$Cu(OAc)_{0.44}(OH)_{1.56}\cdot 0.40H_2O$	9.386
40 °C	$Cu(OAc)_{0.44}(OH)_{1.56}\cdot 0.50H_2O$	9.360

Thermogravimetric analysis (Figures 8 and 9)**,** elemental analysis for carbon contents (Table 3), and FTIR spectrum (Figure 10) excellently complement each other that establish the formula of the copper acetate hydroxides prepared at 40 and 60°C as $Cu(OAc)_{0.44}(OH)_{1.56}\cdot 0.50H_2O$ and $Cu(OAc)_{0.44}(OH)_{1.56}\cdot 0.40H_2O$, respectively. Also, the copper contents estimated from TGA ceramic yields agree with calculated copper contents (Table 4), further confirming the determined formulas. While the strong acetate bands in FTIR (Figure 10, further discussed later) prove the presence of intercalated acetate groups in the layered structure of the copper acetate hydroxide.

In TGAs (Figures 8 and 9), the first mass losses at 133 and 143°C for both copper acetate hydroxides were chosen in conjunction with the differential thermal analysis (DTA) plots (dotted lines). The percent mass losses of water were 6.03 and 7.16%, confirming that copper acetate hydroxides have different amounts of intercalated water. It can be hypothesized that slow growth during hydrolysis, i.e., a lower temperature reaction favors more intercalation of water molecules

in $Cu(OAc)_x(OH)_{6-x}$ octahedra layers that build up the layered lattice structure of copper acetate hydroxide. While the follow-up mass losses, 133 to 267°C (Figure 8) and 143 to 287°C (Figure 9), were due to dehydroxylation of hydroxide and decomposition of acetate. The DTA plots (blue dotted lines), after the water loss, explicitly show that there are few thermochemical steps in the TGA experiments. These thermal events can be described with the following proposed steps.

Possible thermal events in TGA of copper acetate hydroxide:

(i) After the loss of interlayer water molecules, dehydroxylation of hydroxide groups from 133 to 203°C (Figure 8) and from 43 to 207 °C (Figure 9) occurs. Dehydroxylation of hydroxide as water leaves an oxide (O^{2-}); therefore; this step may convert the anhydrous copper acetate hydroxide, $Cu(OAc)_{0.44}(OH)_{1.56}$ to a $CuO_x(OAc)_{0.44}(OH)_{2-2x}$ species, where x is the number of oxides after the first dehydroxylation step.

(ii) Decomposition of acetate groups and dehydroxylation of the remaining hydroxide groups occur after 203 up to 267°C (Figure 8) and from 207 to 288 °C (Figure 9). Acetate reduces copper(II) to copper(I) as evidently an oxidation step that is a mass increase happens after 267°C (Figure 8) and 288°C (Figure 9). To reduce copper, acetate groups should form acetate radicals. Two acetate radicals are immediately dimerized and decompose as CO_2 and ethane. Additionally, simultaneous partial oxidation of Cu^+ to Cu^{2+} due to air oxygen may also occur at this step. As a result, the overall thermochemical events at this step convert $CuO_x(OAc)_{0.44}(OH)_{2-2x}$ to copper(II) oxide/copper(I) oxide, $(CuO)_x/(Cu_2O)_{1-x}$.

(iii) In the presence of oxygen, oxidation of the remaining Cu^+ to Cu^{2+} starts after 267 °C (Figure 8) or 288 °C (Figure 9). As a result, in the TGAs, the mass increase occurs until all copper(I) oxide, Cu_2O, is transformed into copper (II) oxide, CuO.

$$Cu(OAc)_{0.44}(OH)_{1.56}\cdot nH_2O \longrightarrow Cu(OAc)_{0.44}(OH)_{1.56} + nH_2O\ (g)$$

$$Cu(OAc)_{0.44}(OH)_{1.56} \longrightarrow CuO_x(OAc)_{0.44}(OH)_{2-2x} + xH_2O\ (g)$$

$$CuO_x(OAc)_{0.44}(OH)_{2-x} \xrightarrow{O_2} (CuO)_x(Cu_2O)_{1-x} + 0.44CO_2\ (g) + 0.22C_2H_6\ (g) + \tfrac{1}{2}(2-x)H_2O\ (g)$$

$$(CuO)_x(Cu_2O)_{1-x} \xrightarrow{O_2} CuO$$

Scheme 2: Possible thermochemical events of copper acetate hydroxide in a TGA experiment.

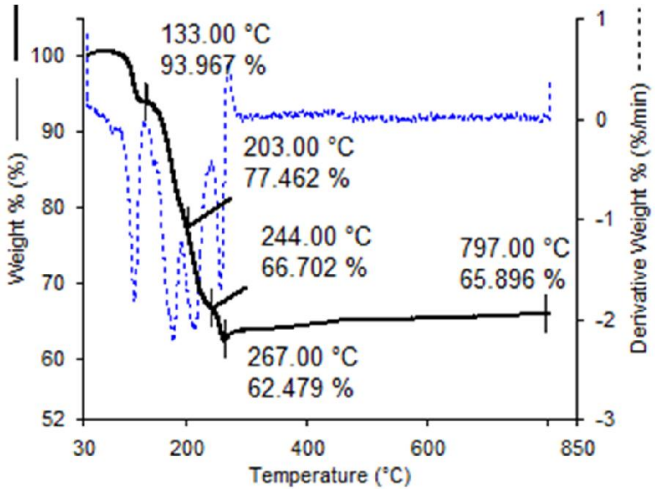

Figure 8: TGA of copper acetate hydroxide, $Cu(OAc)_{0.44}(OH)_{1.56}\cdot 0.40H_2O$ synthesized at 60°C.

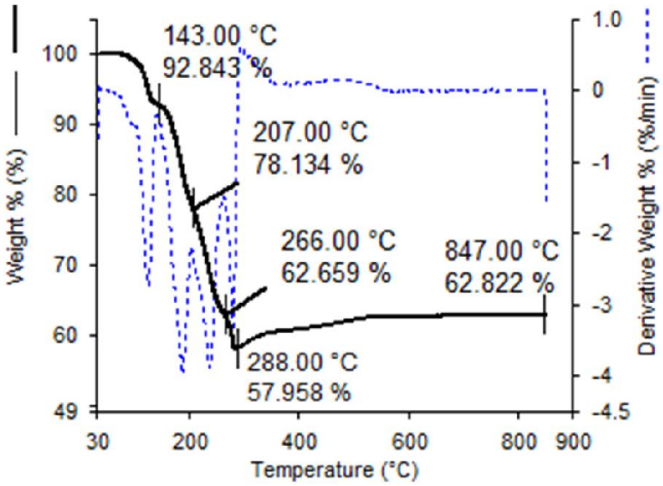

Figure 9: TGA of copper acetate hydroxide, $Cu(OAc)_{0.44}(OH)_{1.56}\cdot 0.50H_2O$ synthesized at 40°C.

Table 3: Carbon contents of copper acetate hydroxide prepared at 60 and 40 °C

Carbon content (%) of copper acetate hydroxide prepared at 60°C	Carbon content (%) of copper acetate hydroxide prepared at 40°C
8.40	8.36

Table 4: Copper contents of copper acetate hydroxide prepared at 60 and 40 °C

Copper acetate hydroxides	Copper content (%)
Copper acetate hydroxide prepared at 60°C	51.5 (calculated) 52.6 (TGA)
Copper acetate hydroxide prepared at 40°C	50.8 (calculated) 50.2 (TGA)

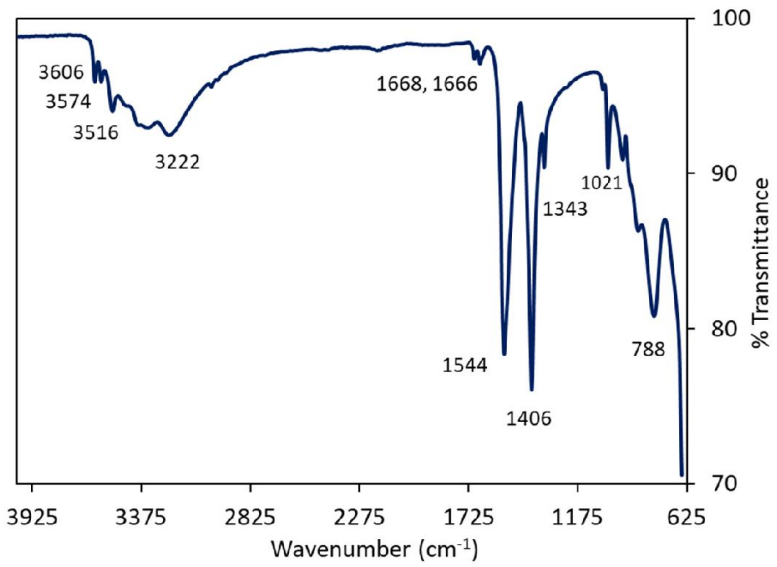

Figure 10: ATR-FTIR spectrum of copper acetate hydroxide, $Cu(OAc)_{0.44}(OH)_{1.56}\cdot 0.40H_2O$.

Table 5: FTIR peak assignments of copper acetate hydroxide

Bands (cm^{-1})	Assignments
788	Cu-OH deformation/bending
1021	$-CH_2-$ bending (rocking) of the acetate groups
1343	$-CH_2-$ bending (scissoring) of the methyl of acetate groups
1406	symmetric stretching of -COO-
1544	asymmetric stretching of -COO-
1666, 1668	Scissoring/bending modes of H_2O
3222	Hydrogen-bonded -OH stretching due to hydrogen-bonding between interlayer water molecules and Cu-OH groups
3516	Weakly hydrogen-bonded Cu-OH stretching
3606 and 3575	Cu-OH stretching modes (not hydrogen-bonded)

ATR-FTIR spectrum (Figure 10) is consistent with other reported layered copper acetate hydroxides such as $Cu_2(OH)_3(OAc)\cdot H_2O$ prepared by hydrolysis of 0.2M copper acetate.[11] The strong bands for acetate's symmetric and asymmetric stretching at 1406 and 1544 cm^{-1}, respectively, confirm the presence of acetate groups in the copper acetate hydroxide. The difference between the symmetric and asymmetric bands is 138 cm^{-1}. The difference is smaller than 200 cm^{-1}, suggesting the acetate is bridged with the nonboring hydroxyl group of $Cu(OAc)_{2-x}(OH)_x$ octahedra[11] and/or with the interlayer water molecule through hydrogen bonding. The sharp peaks at 3606 and 3575 cm^{-1} are attributed to Cu-OH stretching modes that are not hydrogen-bonded with the interlayer water molecules.[11] The two peaks for Cu-OH stretching modes indicate two types of hydroxyl groups present in the layered structure. While the band at 3516 cm^{-1} may indicate the

presence of weakly hydrogen-bonded Cu-OH stretching. The peak at 788 cm^{-1} arises due to Cu-OH deformation mode.[28] The broad peak at 3222 cm^{-1} confirms the presence of interlayer water molecules hydrogen-bonded to Cu-OH groups since the broad peak is attributed to a strongly hydrogen-bonded OH stretching. While the bands at 1666 and 1668cm^{-1} indicate the scissoring (bending) modes of the water molecules that further confirm the presence of water molecules in the layered structure.

Zinc acetate hydroxide, $Zn(OAc)_{0.33}(OH)_{1.67}\cdot 0.50H_2O$

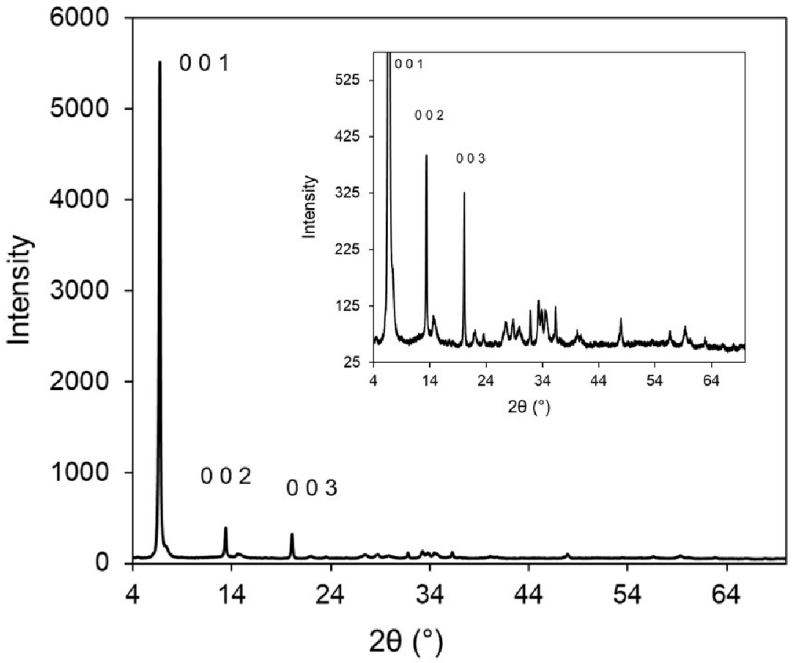

Figure 11: XRD of zinc acetate hydroxide, $Zn(OAc)_{0.33}(OH)_{1.67}\cdot 0.50H_2O$ synthesized by aqueous $Zn(OAc)_2$ and propylene oxide

XRD pattern of zinc acetate hydroxide (Figure 11) exhibits an intense 001 peak at 6.663° and lesser intense reflections compare to 001 planes at the higher angles. This establishes the synthesized zinc acetate hydroxide is a layered material. The next two intense peaks can be indexed as 002 and 003 planes; [29] their positions are multiples of 2 and 3, respectively, of the two theta (2θ) of 001 planes. The position of the rest of peaks (2θ) and their d-spacings are in Supporting Table

T2. Unlike copper acetate hydroxide, zinc acetate hydroxide adopts a hexagonal lattice structure.[15] In the layered structure, Zn^{2+} is octahedrally coordinated with hydroxides (OH^-) ions, where it is expected that up to 25% of the octahedral sites are vacant. These vacant sites are neighbored by tetrahedrally coordinated Zn^{2+} located directly above and below the vacancies.[30, 31] Each tetrahedrally coordinated Zn^{2+} is coordinated with three hydroxide ions and one acetate group. These afore-mentioned Zn^{2+} polyhedral are expected to constitute a modified brucite-like layered structure.[30-32] The structure of zinc acetate hydroxide should be analogous to the zinc hydroxy nitrate structure, as showcased in Figure 12. However, in the case of zinc acetate hydroxide, the acetate ions will be coordinated with the tetrahedral zinc ions and will be hydrogen-bonded to interlayer water molecules or neighboring OH groups.

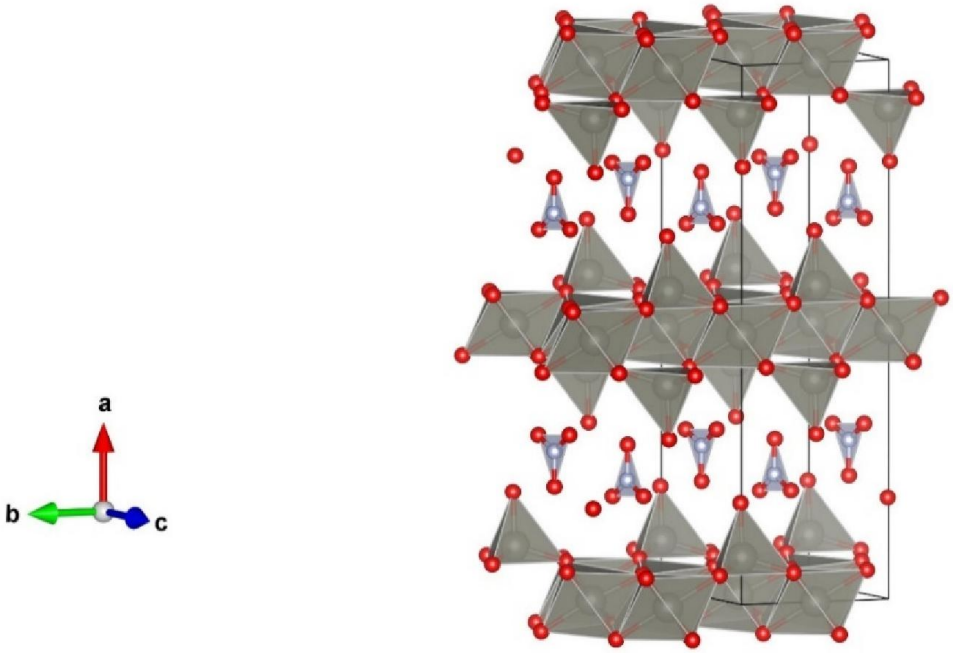

Figure 12: Crystal structure of zinc hydroxy nitrate, $Zn_5(OH)_8(NO_3)_2{\cdot}2H_2O$ where hydrogen atoms are not included.[2] The CIF file (#210–6442) was collected from the crystallographic open database (COD) and redrawn using VESTA software.

Interlayers distance (d_{001}) of the zinc acetate hydroxide, $Zn(OAc)_{0.33}(OH)_{1.67}\cdot 0.50H_2O$ in this work is 13.25 Å. Other reported zinc acetate hydroxides such as $Zn_5(OH)_8(OAc)_2\cdot 4H_2O$ (d_{001} is13.4 Å)[33] and $Zn(OH)_{1.58}(OAc)_{0.42}\cdot 0.31H_2O$ (d_{001} is 14.68Å)[15] have larger interlayer distances of compared to this work. Comparing the acetate contents against per mole of zinc and d-spacings of the mentioned zinc acetate hydroxides shows that higher acetate contents result in a higher distance between the interlayers. The average crystallite size (Scherrer equation[27]) of zinc acetate hydroxide in this work was determined using 001 planes as 37 nm.

While XRD establishes that the prepared zinc acetate hydroxide is a layered material, its FTIR spectrum (further detailed below) exhibiting intense acetate bands and elemental analysis for carbon content (6.48%) clearly prove the presence of acetate intercalation in the layered material. The TGA experiment (discussed later) excellently complements the FTIR spectrum and carbon content analysis result and enumerates the formula of the zinc acetate hydroxide as $Zn(OAc)_{0.33}(OH)_{1.67}\cdot 0.50H_2O$.

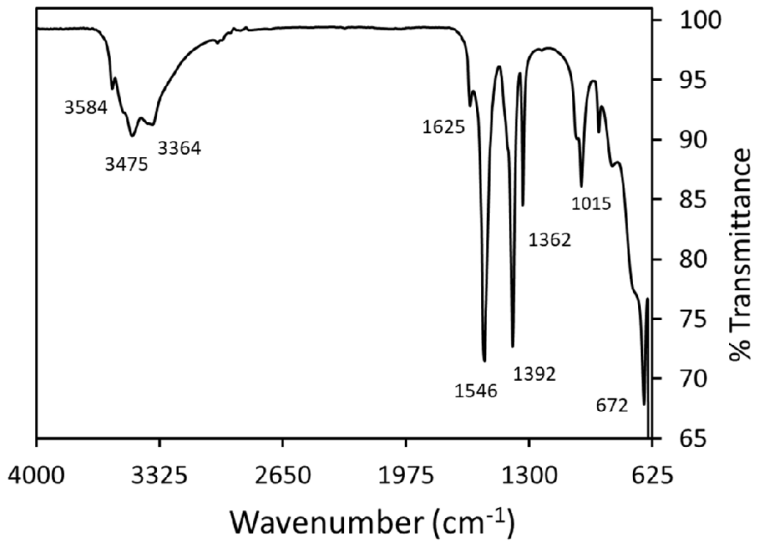

Figure 13: ATR-FTIR of zinc acetate hydroxide, $Zn(OAc)_{0.33}(OH)_{1.67}\cdot 0.50H_2O$

Table 6: FTIR peak assignments of $Zn(OAc)_{0.33}(OH)_{1.67}\cdot 0.50H_2O$.

Bands (cm^{-1})	Assignments
672	Zn-OH deformation/bending
1015	$-CH_2-$ bending (rocking) of the acetate groups
1362	$-CH_2-$ bending (scissoring) of the acetate groups
1392	symmetric stretching of -COO-
1546	asymmetric stretching of -COO-
3364, 3475	H-bonding of interlayer water molecules with OH^- and OAc^-
3584	Cu-OH stretching modes

ATR-FTIR spectrum of zinc acetate hydroxide (Figure 13) shows intense peaks at 1392 and 1546 cm^{-1} due to symmetric and asymmetric stretching of -COO- of acetate groups.[15] The band at 1362 and 1015 cm^{-1} are attributed to the acetate group's $-CH_2-$ scissoring (bending) and $-CH_2-$ rocking vibration modes, respectively. While the strong peak at 672 cm^{-1} indicates Zn-OH bending vibration and the sharp peak at 3584 cm^{-1} stands for Zn-OH stretching vibration. The two distinct peaks, 3364 and 3475 cm^{-1}, stand for hydrogen-bonded OH stretching vibration, indicating two types of hydrogen bonding present in the layered zinc acetate hydroxide structure.[28] Therefore, if one of the bands (3364 or 3475 cm-1) stands for OH stretching due to hydrogen bonding between Zn-OH groups with the interlayer water molecules (Zn-OH…OH-H). Then the other band should indicate OH stretching for hydrogen bonding between acetate and the interlayer molecules (CH3COO-…HO-H) or neighboring OH groups of $Zn(OH)_6$ octahedra (CH3COO-…HO-Zn). However, upon dehydrating the material at 100 °C (according to the TGA plot), the two peaks (3364 and 3475 cm^{-1}) transformed into one broad peak, confirming that acetate groups were hydrogen bonded with the intercalated water molecules in the hydrated zinc acetate hydroxide.

Nevertheless, the hydrogen bonding makes the acetate groups pseudo bridged acetate groups; hence have a smaller difference (smaller than 200 cm-1) between their symmetric and asymmetric stretching modes, 154 cm^{-1}.[11]

Table 7: Zinc and carbon contents of zinc acetate hydroxide, $Zn(OAc)_{0.33}(OH)_{1.67}\cdot 0.50H_2O$.

Zinc content (%)[a]	Carbon content (%)
53.22	6.48

a. Determined using TGA ceramic yield

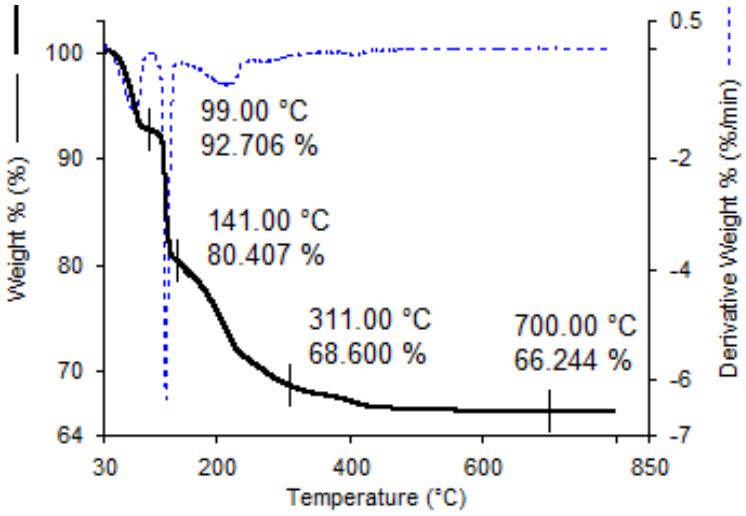

Figure 14: TGA of zinc acetate hydroxide, $Zn(OAc)_{0.33}(OH)_{1.67}\cdot 0.50H_2O$.

In the TGA plot (Figure 14), the mass loss of 7.29% up to 99 °C is the loss of interlayer molecules. Therefore, besides the FTIR spectrum, the TGA experiment further confirms the presence of interlayer water molecules in the layered structure of the zinc acetate hydroxide. Intercalated water is a ubiquitous feature for layered hydroxide and layered double hydroxide materials.[15, 29, 31, 34] The subsequent mass loss from 99 to 141 °C is dehydroxylation of hydroxide groups as water. TGA coupled with mass spectrophotometer experiment of $Zn_5(OH)_8(OAc)_2\cdot 4H_2O$

investigated by Beswick et al. showed that the second stage mass loss (follow-up step of dehydration of interlayer water) only released water vapor, confirming only dehydroxylation of hydroxide groups occurs during this step.[33] Notably, the second mass loss for hydroxide in this study is 12.44%, which shows all the hydroxide groups are not decomposed in this step. This 12.44 % mass loss at 144 °C suggests the material at this point is $ZnO_{0.79}(OAc)_{0.33}(OH)_{0.09}$. In fact, the molar mass of $ZnO_{0.79}(OAc)_{0.33}(OH)_{0.09}$ is 80.90%, almost agreeing with the percent mass at 144 °C in the TGA plot. Decomposition of acetate occurs from 141 °C (80.41%) to 311 °C (68.60%), which corresponds to a mass loss of 11.81% as acetic anhydride. Because two equivalent acetate ions decompose to one equivalent acetic anhydride, leaving one equivalent of oxide ions (O^{2-}) that yield ZnO. Additionally, the 11.81% mass loss excellently agrees with the decomposition of acetate to acetic anhydride and oxide ions. Decomposition of acetate as acetic anhydride in $Zn_5(OH)_8(OAc)_2 \cdot 4H_2O$ was established using the TGA-mass spectrophotometry experiment by Beswick *et al.* that further supports the thermal decomposition step of acetate of $Zn(OAc)_{0.33}(OH)_{1.67} \cdot 0.5H_2O$ in our study.[33] The rest of the mass loss after 311 to 700 °C represents the dehydroxylation of leftover OH groups to reach a ceramic product of ZnO. These OH groups are not close to each other to be decomposed as water. Therefore, they need a higher temperature to dehydrate as water since they need to migrate to be close to each other to decompose as water. All the thermal events in the TGA of $Zn(OAc)_{0.33}(OH)_{1.67} \cdot 0.5H_2O$ are summarized in Scheme 3.

$$Zn(OAc)_{0.33}(OH)_{1.67} \cdot 0.50H_2O \xrightarrow{99\ ^\circ C} Zn(OAc)_{0.33}(OH)_{1.67} + 0.50H_2O$$

$$Zn(OAc)_{0.33}(OH)_{1.67} \xrightarrow{99-141\ ^\circ C} ZnO_{0.79}(OAc)_{0.33}(OH)_{0.09} + 0.79H_2O$$

$$ZnO_{0.79}(OAc)_{0.33}(OH)_{0.09} \xrightarrow{141-311\ ^\circ C} ZnO_{0.955}(OH)_{0.09} + 0.165\ (CH_3CO)_2O$$

$$ZnO_{0.955}(OH)_{0.09} \xrightarrow{311-700\ ^\circ C} ZnO + 0.045H_2O$$

Scheme 3: Thermal events in TGA of zinc acetate hydroxide, $Zn(OAc)_{0.33}(OH)_{1.67} \cdot 0.50H_2O$

β-cobalt or nickel hydroxide via hydrolysis of cobalt or nickel acetate with propylene oxide in water.

Interestingly, hydrolysis of cobalt or nickel acetate with propylene oxide, unlike copper and zinc acetate, generated β-cobalt hydroxide, $Co(OH)_2$, and β-nickel hydroxide $Ni(OH)_2$. These hydroxides have a small amount of acetate intercalation inside the layers of $Co(OH)_6$ or $Ni(OH)_6$ octahedra, as evidenced by the FTIR spectra (Figure 15b and 16b) and carbon contents (Table 8). FTIR spectra showed symmetric and asymmetric bands for acetate groups in 1400 – 1600 cm^{-1} for both materials. While elemental analysis for carbon contents further established that the hydroxide materials have small fractions of acetate. Based on the TGA ceramic yields and carbon contents, the formula of these cobalt and nickel hydroxides are $Co(OAc)_{0.07}(OH)_{1.93}\cdot 0.057H_2O$ and $Ni(OAc)_{0.05}(OH)_{1.95}\cdot 0.059H_2O$

Notably, XRDs of these hydroxide materials (figure 15c and 16c) evidently confirmed that they are not layered double hydroxides or α-type hydroxides as the XRD patterns as they do not exhibit intense reflections in the smaller angles (5 – 12°). Additionally, cobalt hydroxide, $Co(OAc)_{0.07}(OH)_{1.93}\cdot 0.057H_2O$ matched with a β-$Co(OH)_2$ phase, and nickel hydroxide, $Ni(OAc)_{0.05}(OH)_{1.95}\cdot 0.059H_2O$ matched with a β-$Ni(OH)_2$ phase.[35, 36] This suggests that to be acetate-intercalated layered hydroxides or α-type hydroxides, there is a critical value of acetate contents against per moles of metal in a metal hydroxide. For example, Chapter II shows that approximately 0.25 of acetate for one equivalent of nickel generated nickel acetate hydroxide, $Ni(OAc)_{0.28}(OH)_{1.72}\cdot 0.25H_2O$ that is a layered nickel hydroxide as confirmed by XRD. In fact, upon literature investigation, the nickel acetate hydroxide, $Ni(OAc)_{0.28}(OH)_{1.72}\cdot 0.25H_2O$ is a layered double hydroxide with one of the lowest acetate contents ever reported so far. Therefore, it can be theorized that to be an acetate-intercalated layered hydroxide, the minimum value of acetate should be 0.25 for one equivalent of metal in hydroxide materials.

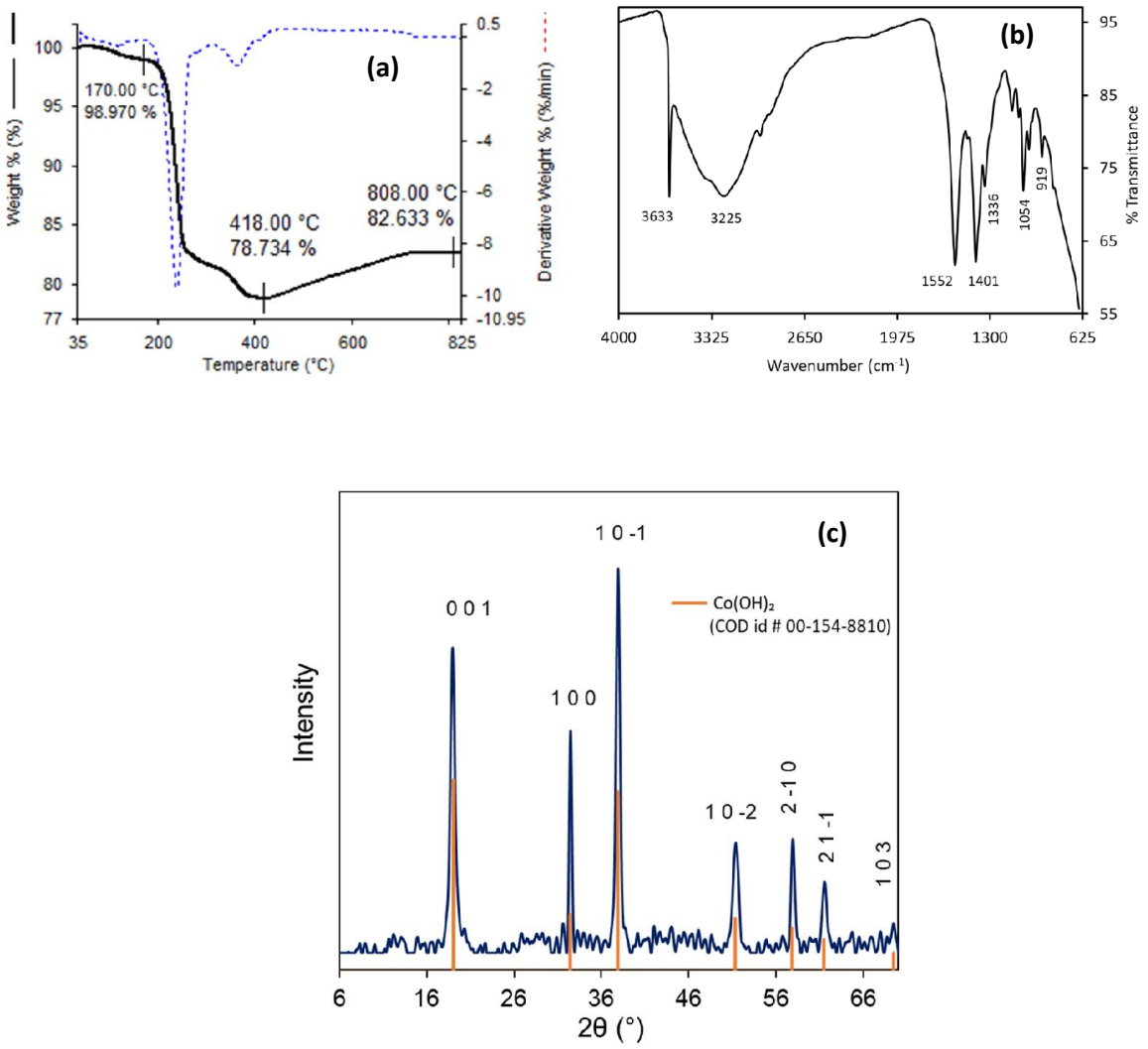

Figure 15: (a) TGA trace, (b) ATR-FTIR spectrum, and (c) XRD pattern of cobalt hydroxide, $Co(OAc)_{0.07}(OH)_{1.93}\cdot 0.057H_2O$ synthesized by hydrolysis of aqueous cobalt acetate and propylene oxide (Orange lines are calculated XRD pattern of cobalt hydroxide as a reference; Crystallographic Open Database, COD id # 00-154-8810 for cobalt hydroxide[35]).

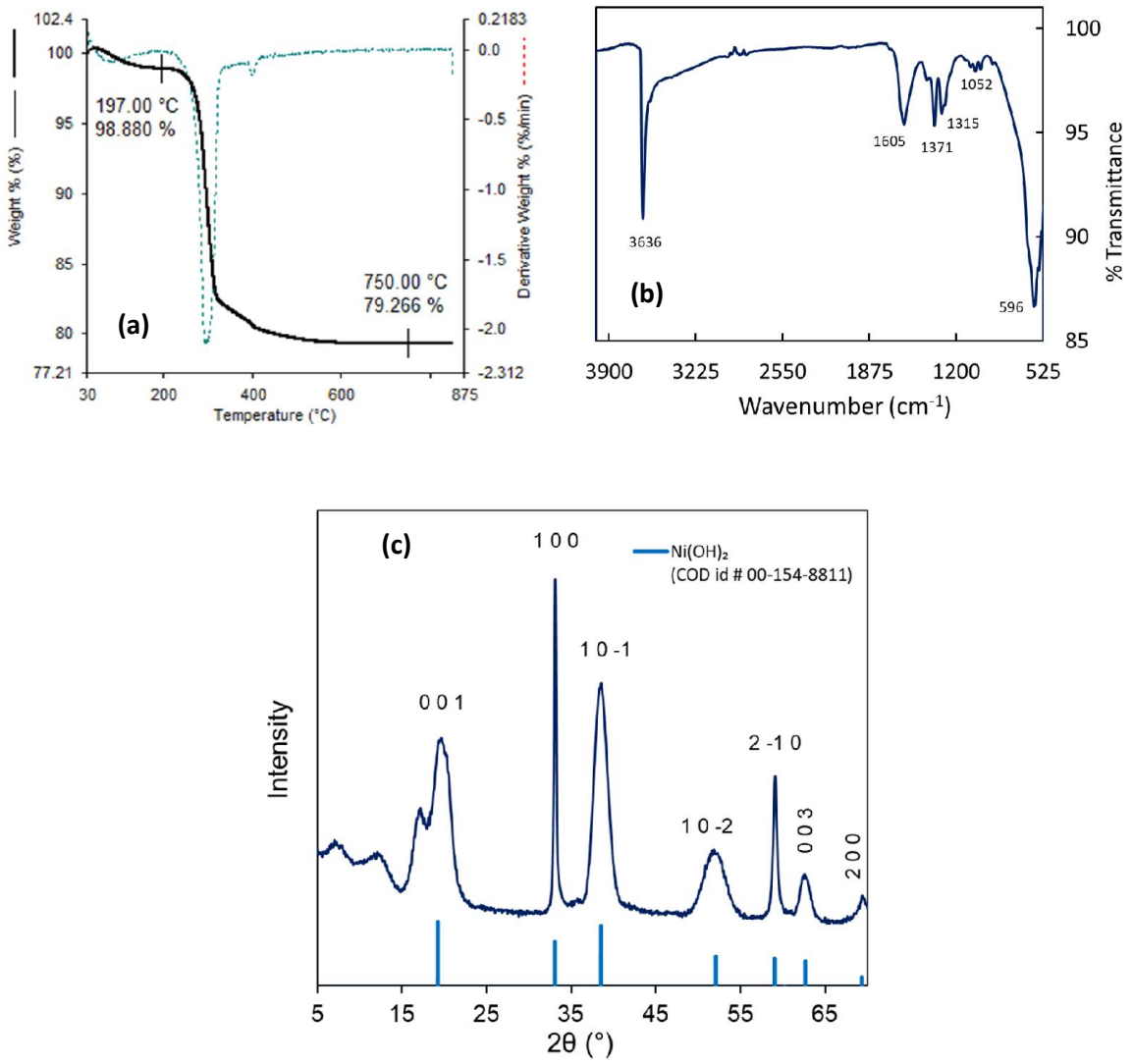

Figure 16: (a) TGA plot, (b) ATR-FTIR spectrum, and (c) XRD pattern of nickel hydroxide, $Ni(OAc)_{0.05}(OH)_{1.95}\cdot 0.059H_2O$ synthesized by hydrolysis aqueous nickel acetate and propylene oxide (Blue lines are calculated XRD pattern of nickel hydroxide as a reference; Crystallographic Open Database, COD id # 00-154-8811 for nickel hydroxide[36]).

Table 8: Elemental analysis of β-cobalt hydroxide and β-nickel hydroxide prepared by hydrolysis of aqueous cobalt acetate and aqueous nickel acetate with propylene oxide.

Hydroxides	Carbon (%)	Cobalt (%)[a]	Nickel (%)[b]
Cobalt hydroxide	1.74	61.92	-
Nickel hydroxide	0.95	-	62.29

a. Determined from TGA ceramic yield at 808 °C (Figure 15a)

b. Determined from TGA ceramic yield at 750 °C (Figure 15b)

Table 9: Comparison of pKa of metals and the acetate contents (moles of acetate/moles of metals) of products in the hydrolysis of metal acetates and propylene oxide.

Metal ions	pKa of aquo-divalent metal ions, $[M(H_2O)_6]^{2+}$ (Ref. [23])	Moles of acetate in the hydrolyzed products for one mole of a metal
Cu^{2+}	7.9	0.44
Zn^{2+}	8.96	0.33
Co^{2+}	9.84	0.07
Ni^{2+}	9.85	0.05

The important question is why hydrolysis of copper and zinc acetate (under the reaction conditions of this work) form acetate-intercalated products while cobalt or nickel acetate does not. One possible answer to the question is that lower pKa of metal ions may favor the formation of acetate intercalation. In fact, a comparison of pKa vs. acetate contents for one mole of metals (Figure 17 and Table 9) of all the synthesized products shows that a lower pKa metal ion contains higher acetate content in the products than that of a higher pKa metal ion. Lower pKa of metal ions are more acidic, and acetate ions are weakly basic (the conjugate base of acetic acid). Therefore, in

the hydrolysis process, during the nucleation of $[M(H_2O)_5(OH)]^+$ complex to acetate-intercalated nucleated particles, $M(OAc)_x(OH)_{2-x}\cdot nH_2O$ (where M is Cu, Zn, Ni, and Co), lower pKa metal ions likely to favor more acetate intercalation into the intercalated particles and the follow-up growth to the acetate-intercalated products.

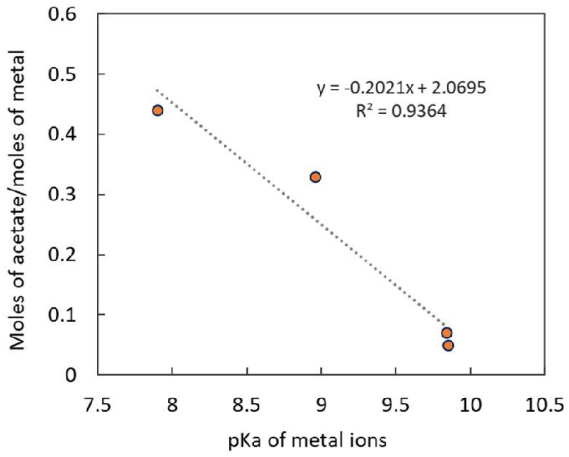

Figure 17: pKa of metals vs. acetate contents (moles of acetate/moles of metals) of products in the hydrolysis of metal acetates and propylene oxide.

Nickel-cobalt hydroxide by hydrolysis reaction of aqueous 2:1 $Co(OAc)_2$ and $Ni(OAc)_2$ with propylene oxide:

Hydrolysis of 2:1 cobalt to nickel acetate with propylene oxide in water produced a little bit of acetate-intercalated nickel-cobalt hydroxide, $NiCo_2(OAc)_{0.15}(OH)_{5.85}\cdot 0.4H_2O$. The formula of the product was confirmed by the elemental analysis, FTIR spectroscopy, and TGA, as presented in Table 10 and Figure 19. Microwave plasma atomic emission spectroscopy (MPAES) of digested solution of the nick-cobalt hydroxide established the presence of both nickel and cobalt (Figure 18) and determined the nickel and cobalt contents as 18.4 and 37.9%, respectively. While carbons content (1.08%) established the presence of acetate in the material. Additionally, FTIR Spectrum showed a medium-intense peak for acetate stretching bands at 1379 and 1565 cm^{-1}, further confirming the presence of acetate. A very intense band at 3627 cm^{-1} establishes the Ni-OH and

Co-OH stretching modes. Hydrogen bonded -OH stretching modes due to intercalated water or acetate may be buried under the intense band at 3627 cm^{-1} as it spreads over a long range. The strong peak at 541 cm^{-1} indicates NiCo-OH bending vibration.

A small amount of acetate intercalation was expected, like cobalt or nickel acetate hydrolysis. The amount of acetate in the nickel-cobalt hydroxide is 0.05 for one mole of metals, which rules out that the material is not an α-type hydroxide or layered hydroxide (similar to nickel or cobalt hydroxide discussed earlier). Nevertheless, pyrolysis will decompose the acetate to generate nickel-cobalt oxyhydroxide or nickel cobaltite depending on the pyrolysis temperatures, as evidenced by the TGA experiment (Figure 19b). In TGA, the mass loss from 170 to 303 °C is dehydration of intercalated water and partial dehydroxylation of hydroxide to generate $NiCo_2O_x(OAc)_{0.15}(OH)_{5.85-2x}$. After 303 °C, acetate starts decomposing as acetic anhydride accompanying further dehydroxylation that produces nickel-cobalt oxyhydroxide, $NiCo_2O_x(OH)_{6-2x}$ at around 690 °C. By considering the percent mass at 690 °C, the material at this stage can be enumerated as $NiCo_2O_{3.4}(OH)_{1.2}$. This nickel-cobalt oxyhydroxide converts nickel cobaltite, $NiCo_2O_4$, as the final ceramic product at 865 °C.

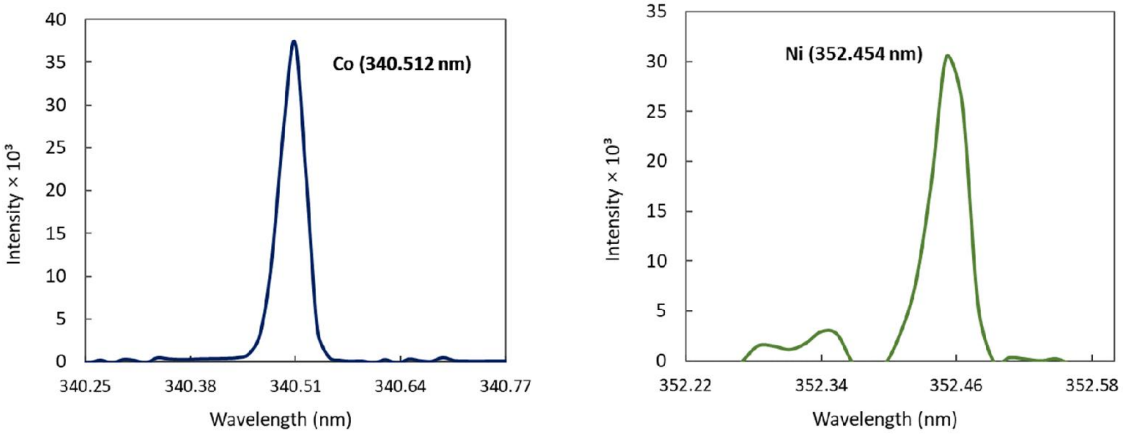

Figure 18: Cobalt and nickel emission peaks in an MP-AES instrument, acquired using a digested solution of bimetallic nickel-cobalt hydroxide.

Table 10: Elemental analysis of nickel-cobalt hydroxide, $NiCo_2(OAc)_{0.15}(OH)_{5.95}\cdot 0.4H_2O$

Cobalt (%)	Nickel (%)	Carbon (%)
37.9	18.4	1.08

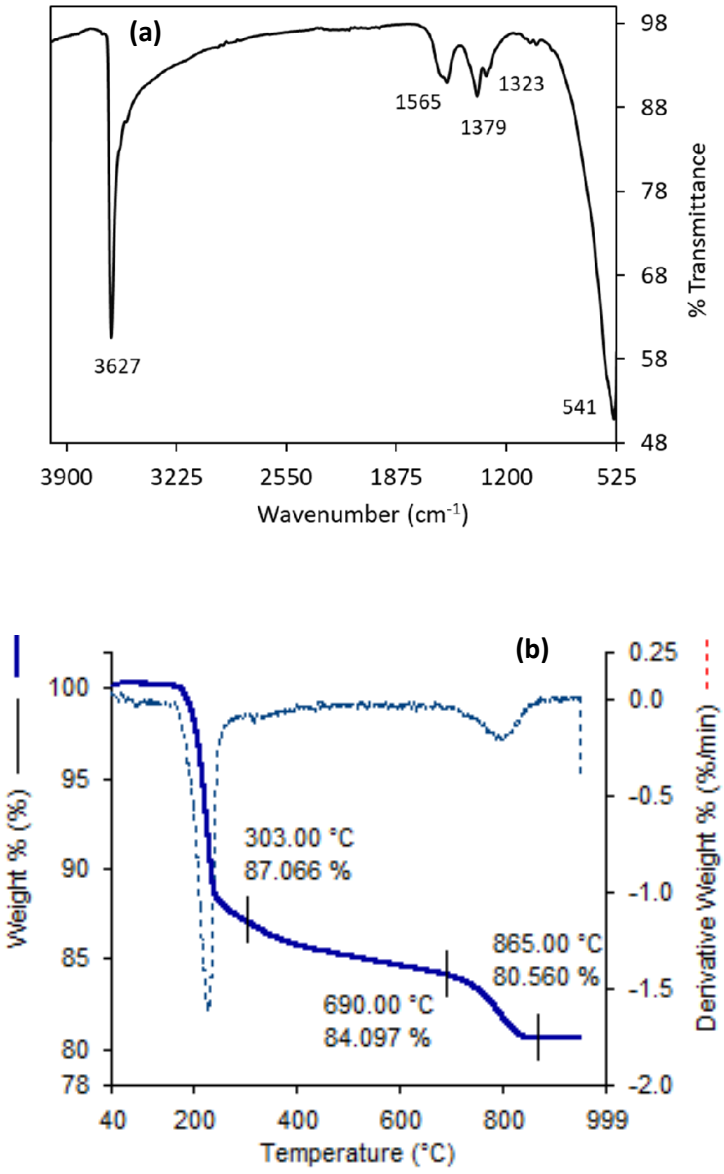

Figure 19: (a) FTIR spectrum and (b) thermogravimetric analysis of nickel-cobalt hydroxide, $NiCo_2(OAc)_{0.15}(OH)_{5.85}\cdot 0.40H_2O$.

The significant feature of the nickel-cobalt oxyhydroxide, $NiCo_2O_x(OH)_{6-2x}$, is that it shows a wide temperature window (approximately 400 °C to 690 °C, as evident from TGA) for its thermal stability. This makes it an excellent candidate as a catalyst for high-temperature catalytic reactions such as the Fischer–Tropsch process for hydrocarbon synthesis.[37, 38] While nickel-cobalt oxyhydroxide can be an attractive material for catalytic reduction of CO_2 to ethanol due to bimetallic synergy of nickel and cobalt.[39] Additionally, nickel-cobalt oxyhydroxide can potentially be used as an electrocatalyst for valuable organic transformations,[40, 41] and as electrodes for supercapacitors.[16] Whereas nickel cobaltite, $NiCo_2O_4$ is an up-and-coming material as electrodes for supercapacitors, hybrid supercapacitors, and lithium-ion batteries.[17, 42, 43] Nickel cobaltite can electro-oxidize methanol efficiently with a better lifetime than NiO or Co_3O_4; hence, it is a promising material for the direct methanol fuel cell.[17]

The nickel-cobalt hydroxide, $NiCo_2(OAc)_{0.15}(OH)_{5.85}\cdot 0.4H_2O$, is the precursor for both nickel-cobalt oxyhydroxide and nickel cobaltite, as shown by the TGA experiment. Therefore, the propylene oxide-assisted hydrolysis process developed in this work for a high yield synthesis of nickel-cobalt hydroxide has advanced a new route for synthesizing a precursor for nickel cobaltite and nickel-cobalt oxyhydroxide that are technologically important materials as discussed above.

■ Conclusion:

This investigation established a new route to synthesize acetate-intercalated layered hydroxides of zinc and copper. Hydrolysis of zinc acetate in the presence of propylene oxide in water at 40°C produced zinc acetate hydroxide, $Zn(OAc)_{0.33}(OH)_{1.67}.0.50H_2O$, while copper acetate generated copper acetate hydroxide, $Cu(OAc)_{0.44}(OH)_{1.56}.0.40H_2O$. The reaction yield was 100% for copper acetate hydroxide and ~ 94% for zinc acetate hydroxide. While cobalt and nickel acetate in propylene oxide and water produced their β-type hydroxides. It was hypothesized that the pKa of the metal ions may determine the amount of acetate intercalation in a corresponding hydroxide under the hydrolysis condition of this work. Additionally, the developed route successfully

produced stochiometric bimetallic hydroxides such as nickel-cobalt hydroxide as a 2:1 $Co(OAc)_2$ and $Ni(OAc)_2$ generated nickel-cobalt hydroxide, $NiCo_2(OAc)_{0.15}(OH)_{5.85}\cdot 0.4H_2O$ with a yield of 99%. This nickel-cobalt hydroxide is an excellent precursor for nickel-cobalt oxyhydroxide, $NiCo_2O_x(OH)_{6-2x}$, and nickel cobaltite, $NiCo_2O_4$.

■ **Future Work:**

Based on the developed hydrolysis reactions in the present work, the following reactions will be very promising to explore:

(i) Reactions of zinc or copper acetate hydroxides with metal oxyanions such as molybdate MO_4^{2-} may produce their ternary metal oxides – zinc molybdate, $ZnMO_4$ and copper molybdate, $CuMO_4$. If these reactions work, it will add new facile routes to prepare these ternary metal oxides that are attractive materials for various valuable technologies such as corrosion inhibitor pigments,[44] catalysis,[45] and thermochromic and smart materials applications[46].

(ii) Like the hydrolysis of 2:1 nickel-cobalt acetate, the reaction of 2:1 $Mn(OAc)_2$ and $Zn(OAc)_2$ in propylene oxide and water may generate zinc-manganese hydroxide, $ZnMn_2(OAc)_x(OH)_{6-x}\cdot nH_2O$. By pyrolysis, the zinc-manganese hydroxide will convert to spinel zinc manganese oxide, $ZnMn_2O_4$. This $ZnMn_2O_4$ is an essential material as an electrode for zinc ion batteries.[47] Additionally, $ZnMn_2O_4$ can also be used as an electrode in lithium-ion batteries.

(iii) Hydrolysis reaction of zinc iodide with propylene oxide will be valuable to investigate to produce iodide-intercalated zinc layered hydroxide, $ZnI_x(OH)_{2-x}\cdot nH_2O$. Since iodide is a bulky anion, based on hard-soft acid-base theory, the $ZnI_x(OH)_{2-x}\cdot nH_2O$ layered material will be a promising sorbent for effectively removing big-size heavy metal ions, especially Pd^{2+} and Hg^{2+}, by adsorption from heavy metal polluted water.

■ Supporting Information:

Table S1: The peak positions (2θ), their Miller Indices, and d-spacings of the XRD patterns of copper acetate hydroxide synthesized at 60 °C and 40 °C

	$Cu(OAc)_{0.43}(OH)_{1.67}\cdot 0.41H_2O$ (Synthesized at 60°C)		$Cu(OAc)_{0.44}(OH)_{1.66}\cdot 0.50H_2O$ (Synthesized at 40°C)	
h k l	**2θ (°)**	**d (nm)**	**2θ (°)**	**d (nm)**
0 0 1	9.441	9.36	9.441	9.360
1 0 0	17.286	5.126	17.286	5.126
0 0 2	18.961	4.677	18.961	4.677
1 1 0	21.884	4.058	21.884	4.058
0 1 2	23.923	3.717	23.923	3.717
1 1 3	26.171	3.402	26.171	3.402
0 0 3	28.615	3.117	28.615	3.117
2 0 0	32.132	2.783	32.132	2.783
2 0 2	33.776	2.652	33.776	2.652
2 0 -3	34.639	2.587	34.639	2.587
1 2 3/ 1 2 -3	36.668	2.449	36.668	2.449
0 0 4	38.499	2.336	38.499	2.336
2 1 3	38.947	2.311	38.947	2.311
2 0 -5	39.519	2.278	39.519	2.278
1 2 5	41.724	2.163	41.724	2.163
2 0 -3	42.713	2.115	42.713	2.115
1 2 3	44.929	2.016	44.929	2.016
2 2 -3	46.156	1.965	46.156	1.965
1 3 -1	47.696	1.905	47.696	1.905
0 0 5	48.664	1.87	48.664	1.870
2 0 4	52.305	1.748	52.305	1.748
3 1 3	54.074	1.695	54.074	1.695
3 1 4	55.437	1.656	55.437	1.656
3 1 -5	56.415	1.63	56.415	1.630
0 0 6	59.276	1.558	59.276	1.558

Table S2: The peak positions (2θ) and their d-spacings of the XRD pattern of zinc acetate hydroxide, $Zn(OAc)_{0.33}(OH)_{1.67}\cdot 0.50H_2O$ synthesized at 40°C

2θ (°)	**d (nm)**
6.663	13.254
13.337	6.633
14.612	6.057
20.058	4.423
21.957	4.045
23.497	3.783
27.471	3.244
28.704	3.108
29.817	2.994
31.789	2.813
33.25	2.692
33.807	2.649
34.504	2.597
36.278	2.474
40.143	2.244
40.746	2.213
47.92	1.897
56.602	1.625
59.312	1.557
62.844	1.478
65.965	1.415
67.942	1.379

■ **References:**

(1) Švarcová, S.; Klementová, M.; Bezdička, P.; Łasocha, W.; Dušek, M.; Hradil, D., Synthesis and characterization of single crystals of the layered copper hydroxide acetate $Cu_2(OH)_3(CH_3COO)\cdot H_2O$. *Crystal Research and Technology* **2011,** 46, (10), 1051-1057.

(2) Moezzi, A.; Lee, P.-S.; McDonagh, A. M.; Cortie, M. B., On the thermal decomposition of zinc hydroxide nitrate, $Zn_5(OH)_8(NO_3)_2\cdot 2H_2O$. *Journal of Solid State Chemistry* **2020,** 286.

(3) Almasri, D. A.; Essehli, R.; Tong, Y.; Lawler, J., Layered zinc hydroxide as an adsorbent for phosphate removal and recovery from wastewater. *RSC Advances* **2021,** 11, (48), 30172-30182.

(4) Kozai, N.; Mitamura, H.; Fukuyama, H.; Esaka, F.; Komarneni, S., Synthesis and characterization of copper hydroxide acetate with a layered discoid crystal. *Journal of Materials Research* **2005,** 20, (11), 2997-3003.

(5) Kozai, N.; Mitamura, H.; Fukuyama, H.; Esaka, F.; Komarneni, S., Synthesis and characterization of nickel–copper hydroxide acetate, $NiCu(OH)_{3.1}(OCOCH3)_{0.9}\cdot 0.9H_2O$. *Microporous and Mesoporous Materials* **2006,** 89, (1-3), 123-131.

(6) Rajamathi, J. T.; Britto, S.; Rajamathi, M., Synthesis and anion exchange reactions of a layered copper-zinc hydroxy double salt, $Cu_{1.6}Zn_{0.4}(OH)_3(OAc)\cdot H_2O$. *Journal of Chemical Sciences* **2005,** 117, (6), 629-633.

(7) Yamanaka, S.; Sako, T.; Hattori, M., Anion-Exchange in Basic Copper Acetate. *Chemistry Letters* **1989,** 18, (10), 1869-1872.

(8) Reinoso, D. M.; Fernandez, M. B.; Damiani, D. E.; Tonetto, G. M., Study of zinc hydroxy acetate as catalyst in the esterification reaction of fatty acids. *International Journal of Low-Carbon Technologies* **2012,** 7, (4), 348-356.

(9) Moezzi, A.; McDonagh, A.; Dowd, A.; Cortie, M., Zinc hydroxyacetate and its transformation to nanocrystalline zinc oxide. *Inorg Chem* **2013,** 52, (1), 95-102.

(10) Ganga, B. G.; Santhosh, P. N., Facile synthesis of porous copper oxide nanostructure using copper hydroxide acetate precursor. *Materials Letters* **2015,** 138, 113-115.

(11) Masciocchi, N.; Corradi, E.; Sironi, A.; Moretti, G.; Minelli, G.; Porta, P., Preparation, Characterization, andab initioX-Ray Powder Diffraction Study of $Cu_2(OH)_3(CH_3COO)\cdot H_2O$. *Journal of Solid State Chemistry* **1997,** 131, (2), 252-262.

(12) Morioka, H.; Tagaya, H.; Karasu, M.; Kadokawa, J.-i.; Chiba, K., Effects of Zinc on the New Preparation Method of Hydroxy Double Salts. *Inorganic Chemistry* **1999,** 38, (19), 4211-4216.

(13) Kandare, E.; Hossenlopp, J. M., Thermal Degradation of Acetate-Intercalated Hydroxy Double and Layered Hydroxy Salts. *Inorganic Chemistry* **2006,** 45, (9), 3766-3773.

(14) Meyn, M.; Beneke, K.; Lagaly, G., Anion-exchange reactions of hydroxy double salts. *Inorganic Chemistry* **1993,** 32, (7), 1209-1215.

(15) Poul, L.; Jouini, N.; Fiévet, F., Layered Hydroxide Metal Acetates (Metal = Zinc, Cobalt, and Nickel): Elaboration via Hydrolysis in Polyol Medium and Comparative Study. *Chemistry of Materials* **2000,** 12, (10), 3123-3132.

(16) Gao, M.; Li, Y.; Yang, J.; Liu, Y.; Liu, Y.; Zhang, X.; Wu, S.; Cai, K., Nickel-cobalt (oxy)hydroxide battery-type supercapacitor electrode with high mass loading. *Chemical Engineering Journal* **2022,** 429.

(17) Liu, S.; Hu, L.; Xu, X.; Al-Ghamdi, A. A.; Fang, X., Nickel Cobaltite Nanostructures for Photoelectric and Catalytic Applications. *Small* **2015,** 11, (34), 4267-83.

(18) Pralong, V.; Delahaye-Vidal, A.; Chabre, Y.; Beaudoin, B.; Tarascon, J. M., The Outcome of Cobalt in the Nickel–Cobalt Oxyhydroxide Electrodes of Alkaline Batteries. *Journal of Solid State Chemistry* **2001,** 162, (2), 270-281.

(19) Shafique, M.; Iqbal, T.; Khan, M. A.; Naeem, M.; Ahmed, I.; Ahmad, P.; Mahmood, H., Structural, Optical, Electrical, and Photocatalytic Properties of Nickel Cobaltite ($NiCo_2O_4$) Nanocomposite Fabricated by a Facile Microplasma Electrochemical Process. *Journal of Electronic Materials* **2020,** 50, (2), 629-639.

(20) Vidhya, M. S.; Ravi, G.; Yuvakkumar, R.; Velauthapillai, D.; Thambidurai, M.; Dang, C.; Saravanakumar, B., Nickel–cobalt hydroxide: a positive electrode for supercapacitor applications. *RSC Advances* **2020,** 10, (33), 19410-19418.

(21) Baranton, S.; Coutanceau, C., Nickel cobalt hydroxide nanoflakes as catalysts for the hydrogen evolution reaction. *Applied Catalysis B: Environmental* **2013,** 136-137, 1-8.

(22) Yan, W.; Wang, D.; Botte, G. G., Nickel and cobalt bimetallic hydroxide catalysts for urea electro-oxidation. *Electrochimica Acta* **2012,** 61, 25-30.

(23) Souaya, E. R.; Hanna, W. G.; Ismail, E. H.; Milad, N. E., Studies On Some Acid Divalent-Metal Nitrilotriacetate Complexes. *Molecules* **2000,** 5, (10).

(24) Zhang, J.; Liu, F.; Cheng, J. P.; Zhang, X. B., Binary Nickel-Cobalt Oxides Electrode Materials for High-Performance Supercapacitors: Influence of its Composition and Porous Nature. *ACS Appl Mater Interfaces* **2015,** 7, (32), 17630-40.

(25) Bai, Y.; Wang, W.; Wang, R.; Sun, J.; Gao, L., Controllable synthesis of 3D binary nickel–cobalt hydroxide/graphene/nickel foam as a binder-free electrode for high-performance supercapacitors. *Journal of Materials Chemistry A* **2015,** 3, (23), 12530-12538.

(26) Liu, F.; Feng, D.; Yang, H.; Guo, X., Preparation of macroporous transition metal hydroxide monoliths via a sol-gel process accompanied by phase separation. *Sci Rep* **2020,** 10, (1), 4331.

(27) Holder, C. F.; Schaak, R. E., Tutorial on Powder X-ray Diffraction for Characterizing Nanoscale Materials. *ACS Nano* **2019,** 13, (7), 7359-7365.

(28) Secco, E. A.; Worth, G. G., Infrared spectra of unannealed and of annealed $Cu_4(OH)_6(NO3)_2$. *Canadian Journal of Chemistry* **1987,** 65, (10), 2504-2508.

(29) Hosono, E.; Fujihara, S.; Kimura, T.; Imai, H., Growth of layered basic zinc acetate in methanolic solutions and its pyrolytic transformation into porous zinc oxide films. *J Colloid Interface Sci* **2004,** 272, (2), 391-8.

(30) Kandare, E.; Hossenlopp, J. M., Hydroxy Double Salt Anion Exchange Kinetics: Effects of Precursor Structure and Anion Size. *The Journal of Physical Chemistry B* **2005,** 109, (17), 8469-8475.

(31) Lee, J. W.; Choi, W. C.; Kim, J.-D., Size-controlled layered zinc hydroxide intercalated with dodecyl sulfate: effect of alcohol type on dodecyl sulfate template. *CrystEngComm* **2010,** 12, (10).

(32) Rojas, R.; Barriga, C.; Angeles Ulibarri, M.; Malet, P.; Rives, V., Layered Ni(ii)-Zn(ii) hydroxyacetates. Anion exchange and thermal decomposition of the hydroxysalts obtained. *Journal of Materials Chemistry* **2002,** 12, (4), 1071-1078.

(33) Biswick, T.; Jones, W.; Pacuła, A.; Serwicka, E.; Podobinski, J., Evidence for the formation of anhydrous zinc acetate and acetic anhydride during the thermal degradation of zinc hydroxy acetate, $Zn_5(OH)_8(CH_3CO2)_2 \cdot 4H_2O$ to ZnO. *Solid State Sciences* **2009,** 11, (2), 330-335.

(34) Schlur, L.; Carton, A.; Pourroy, G., A new zinc hydroxy acetate hydrogen carbonate lamellar phase for growing large and clean ZnO nanorod arrays. *Chem Commun (Camb)* **2015,** 51, (16), 3367-70.

(35) Crystallography Open Database, http://www.crystallography.net/cod/1548810.html In.

(36) Crystallography Open Database, http://www.crystallography.net/cod/1548811.html In.

(37) Li, X.; Almkhelfe, H.; Bedford, N. M.; Back, T. C.; Hohn, K. L.; Amama, P. B., Characterization and catalytic behavior of Fischer–Tropsch catalysts derived from different cobalt precursors. *Catalysis Today* **2019,** 338, 40-51.

(38) Casci, J. L.; Lok, C. M.; Shannon, M. D., Fischer–Tropsch catalysis: The basis for an emerging industry with origins in the early 20th Century. *Catalysis Today* **2009,** 145, (1-2), 38-44.

(39) Wang, L.; He, S.; Wang, L.; Lei, Y.; Meng, X.; Xiao, F.-S., Cobalt–Nickel Catalysts for Selective Hydrogenation of Carbon Dioxide into Ethanol. *ACS Catalysis* **2019,** 9, (12), 11335-11340.

(40) Taitt, B. J.; Nam, D.-H.; Choi, K.-S., A Comparative Study of Nickel, Cobalt, and Iron Oxyhydroxide Anodes for the Electrochemical Oxidation of 5-Hydroxymethylfurfural to 2,5-Furandicarboxylic Acid. *ACS Catalysis* **2018,** 9, (1), 660-670.

(41) Zhou, H.; Li, Z.; Xu, S. M.; Lu, L.; Xu, M.; Ji, K.; Ge, R.; Yan, Y.; Ma, L.; Kong, X.; Zheng, L.; Duan, H., Selectively Upgrading Lignin Derivatives to Carboxylates through Electrochemical Oxidative C(OH)-C Bond Cleavage by a Mn-Doped Cobalt Oxyhydroxide Catalyst. *Angew Chem Int Ed Engl* **2021,** 60, (16), 8976-8982.

(42) Mahadik, S. M.; Chodankar, N. R.; Han, Y. K.; Dubal, D. P.; Patil, S., Nickel Cobaltite: A Positive Electrode Material for Hybrid Supercapacitors. *ChemSusChem* **2021,** 14, (24), 5384-5398.

(43) Chen, Y.; Qu, B.; Hu, L.; Xu, Z.; Li, Q.; Wang, T., High-performance supercapacitor and lithium-ion battery based on 3D hierarchical NH4F-induced nickel cobaltate nanosheet-nanowire cluster arrays as self-supported electrodes. *Nanoscale* **2013,** 5, (20), 9812-20.

(44) Sheng, X.-X.; Zhou, L.-Z.; Guo, X.-J.; Bai, X.; Liu, X.-R.; Liu, J.-K.; Luo, C.-X., Composition design and anticorrosion performance optimization of zinc molybdate pigments. *Materials Today Communications* **2021,** 28.

(45) Soltys, E. V.; Urazov, K. K.; Kharlamova, T. S.; Vodyankina, O. V., Redox and Catalytic Properties of Copper Molybdates with Various Composition. *Kinetics and Catalysis* **2018,** 59, (1), 58-69.

(46) Joseph, N.; Varghese, J.; Teirikangas, M.; Jantunen, H., A Temperature-Responsive Copper Molybdate Polymorph Mixture near to Water Boiling Point by a Simple Cryogenic Quenching Route. *ACS Appl Mater Interfaces* **2020,** 12, (1), 1046-1053.

(47) Cai, K.; Luo, S. H.; Feng, J.; Wang, J.; Zhan, Y.; Wang, Q.; Zhang, Y.; Liu, X., Recent Advances on Spinel Zinc Manganate Cathode Materials for Zinc-Ion Batteries. *Chem Rec* **2022,** 22, (1), e202100169.

CHAPTER VIII

Uptake of Phosphate and Arsenate from Water Using Acetate-Intercalated Layered Zinc Hydroxide

■ Introduction

A facile hydrolysis route for a high yield synthesis of acetate-intercalated layered zinc hydroxide was developed for the first time by hydrolysis of zinc acetate with propylene oxide, as presented in the previous chapter. Acetate-intercalated layered zinc hydroxide (zinc acetate hydroxide) is a promising material for removing pollutants such as phosphate (PO_4^{3-}) ad arsenate (AsO_4^{3-}) due to its excellent anion exchangeability. Therefore, this chapter aimed to investigate the interaction of phosphate and arsenate with zinc acetate hydroxide for uptake (removal) of these species from water. The investigation discovered that a high ppm of phosphate solution initially involved an acetate (anion) exchange stage followed by a slow reaction stage that released hydroxide ions from the zinc acetate hydroxide. While arsenate underwent only adsorption with possibly accompanying a minimal acetate exchange.

Phosphate is a crucial nutrient for plants, vegetation, crops, and any plant species; therefore, it is an essential ingredient for making fertilizers. However, as phosphate is the nutrient for plants and plant species, excess phosphate in water causes algal bloom (eutrophication) and aquatic plants in surface water. This algal bloom and aquatic plants can threaten biodiversity in surface water and even in coastal marine water as the algal bloom causes low dissolved oxygen

when they die. Algal bloom also stops the sunlight from going under-water, which damages the under-water plants essential for the aquatic environment. The area of surface water bodies where aquatic life cannot survive is also known as "Dead Zones."[1] In the US, the largest Dead Zones is about 6,500 square miles in the Gulf of Mexico, which occurs every summer due to the nutrient (total phosphorous and nitrogen) pollution from the Mississippi River Basin.[1] While some types of algae, such as cyanobacteria (blue-green algae), release harmful chemicals (toxins) for human and aquatic species and cause harmful algal blooms.[1] According to the 2014 Integrated Water Quality Assessment Report by the Oklahoma Department of Environmental Quality, 204 miles of water streams in Oklahoma were impaired with phosphorus (P) and nitrogen (N), and 29351 acres of lakes were impaired with total P (phosphorus).[2] Phosphate pollution is, in fact, a global issue that is difficult to deal with as phosphate species can run off to surface water bodies from many point and non-point sources.

While arsenic pollution in water is another critical water pollution problem. Because arsenic exposure to humans results in serious health issues – for example, arsenic exposure by drinking water, juice, or food has proven to cause chronic skin problems such as skin lesions and may cause skin cancer.[3, 4] According to the Minnesota Department of Health, prolonged exposure to low levels of arsenic in humans through drinking water may cause diabetes and increase the risk of cancer bladder, lungs, liver, and other organs.[5] While EPA has concluded that inorganic arsenic is carcinogenic to humans.[6] Additionally, arsenic species can be bioaccumulated in aquatic and marine species that ends up in human through diet.[7] Unfortunately, beside natural sources, there are many anthropogenic sources that cause arsenic pollution in surface water systems.[8]

Due to the severe effect of phosphate (algal bloom) and arsenic pollution, it is one of the critical demands of our current era to remediate phosphate and arsenate species from natural water and manmade wastewater sources. Removal of phosphate or arsenate by uptake using suitable materials (sorbents) is one of the effective and inexpensive processes that has been widely used and

explored across industries and academia. Developing effective materials/sorbents that offer high uptake capacities and are inexpensively synthesizable is essential in making the phosphate or arsenate uptake/removal process practical. Further, the material must be environmentally benign that pose no secondary pollution. In this regard, layered hydroxides and layered double hydroxides are attractive materials, and they have drawn significant attention as sorbents for uptake of phosphate and arsenate due to the inexpensive synthesis routes, anion exchange property, and adsorption sites in between the interlayer space.

The literature investigation shows that anion intercalated layered metal hydroxides (LMHs) or layered double hydroxides (LDHs) undergo anion exchange with phosphate or arsenate. For example, chloride-, nitrate-, and carbonate-intercalated zinc-aluminum LDHs ($Zn_{1.25}$Al-Cl, $Zn_{1.25}$ Al-NO_3, and $Zn_{1.25}$Al-CO_3) exhibited uptake of phosphate due to their anion exchangeability. It was found that $Zn_{1.25}$ Al-NO_3 was a better sorbent for uptake of phosphate as nitrate ions were facilely exchanged with phosphate compared to chloride and carbonate.[9] A zinc-aluminum sulfate LDH, proven to uptake arsenate from water with a Langmuir uptake capacity of 47.4 mg/g. The uptake mechanism was considered the arsenate exchange with the sulfate of the external surface and edges of the Zn-Al-SO_4 LDH along with some topotactic exchange by substituting arsenate ions with the sulfate in the interlayer region.[10] Nickle-copper acetate hydroxide was shown excellent uptake of phosphate, arsenate, arsenite, selenate, and selenite from water by acetate exchange, where the uptake was determined by distribution coefficient (K_d, defined by the ratio of the amount of anion uptake per gram of solid to the amount of anion per mL of solution).[11] Acetate or nitrate intercalated layer hydroxides of transition metals have excellent anion exchange capability, [12, 13] hence can be used to uptake phosphate and arsenate from water. For example, acetate-intercalated layered zinc hydroxide (zinc acetate hydroxide) prepared by precipitation was studied for uptake of phosphate that showed an uptake capacity of 134.4 mg/g of uptake in 120 minutes.[14] The article explained that phosphate uptake occurred initially due to adsorption followed

by anion exchange supported by intraparticle diffusion investigation. However, the article did not investigate any uptake after 120 minutes and hence did not report uptake after that. These are a few of the articles out of many reports in the literature that show that the LDHs and layered metal hydroxides (LMHs) have excellent anion exchange properties to uptake phosphate or arsenate. Although literature often talks about adsorption/uptake of phosphate by anion exchange with LDHs or LMHs; however, prolonged treatment of a high concentration phosphate solution can start reacting with an LMH after the initial adsorption or anion exchange step. Notably, to follow the reaction stage after initial adsorption or anion exchange, prolonged interaction of phosphate with a layered metal hydroxide is required as the reaction is slow. But literature often investigates the interaction of phosphate with LMHs or LDHs for a short time.[9, 10, 14, 15] The reaction stage of phosphate with an LMH material can lead to superior phosphate removal (uptake) capacity from water. Similarly, arsenate was also reported to involve adsorption or anion exchange with LDHs or LMHs; but the arsenate species during adsorption may release OH^- ions from a layered metal hydroxide due to coordination arsenate species into the layered structure.

To investigate the uptake capacity of phosphate from water using zinc acetate hydroxide, $Zn(OAc)_{0.33}(OH)_{1.67}\cdot 0.50H_2O$ that was synthesized by polyene oxide assisted hydrolysis method in Chapter VII, we prompted to treat the zinc acetate hydroxide (ZAH) with high concertation phosphate solution. A prolonged interaction was investigated to find an equilibrium for the uptake process for that high concentration of phosphate solution. It was discovered that the phosphate ions did not reach equilibrium even after 7 days, confirming a reaction of phosphate and ZAH occurred after the initial anion exchange step. Therefore, herein the chapter presents a new finding that the prolonged treatment of a high concentration phosphate solution with zinc acetate hydroxide involved an initial anion exchange followed by a slow reaction stage (accompanying a release of OH^- ions) that generated a zinc phosphate hydroxide type material. The dual-process – anion exchange and follow-up reaction – resulted in a very high uptake of phosphate, 259 mg/g at 7 days

(that is yet to reach completion), from water at room temperature. While at 45 °C, the phosphate uptake was 356 mg/g at 7 days, indicating the formation of $Zn(PO_4)_{0.43}(OH)_{0.71}\cdot xH_2O$, a zinc phosphate hydroxide type material.

While the exploration of prolonged interaction of a high ppm of arsenate solution with the zinc acetate hydroxide (ZAH) showed a different result. Unlike phosphate, arsenate species did not involve the acetate (anion) exchange and the follow-up reaction with the ZAH. Instead, arsenate uptake was limited to surface adsorption. The adsorption was accompanied by a slow release of OH^- ions from ZAH, possibly due to arsenate incorporation in the layered structure to maintain the overall charge neutrality. The arsenate adsorption reached an equilibrium in 4 days to an uptake capacity of around 60 mg/g. The arsenate uptake process was found to follow the Langmuir isotherm, while in the case of phosphate uptake, only the initial acetate exchange process followed the Langmuir isotherm.

■ Experimental:

Materials: Zinc acetate dehydrate, $Zn(CH_3COO)_2\cdot 2H_2O$ (Baker Analyzed Reagent) was used to synthesize acetate-intercalated layered zinc hydroxide (zinc acetate hydroxide). Dibasic potassium phosphate, K_2HPO_4 (Fisher Scientific) was used for phosphate uptake experiments, while dibasic sodium arsenate heptahydrate, $Na_2AsO_4\cdot 7H_2O$ (GFS Chemicals) was used for the arsenate uptake investigation.

Synthesis of zinc acetate hydroxides, $Zn(OAc)_{0.33}(OH)_{1.67}\cdot 0.5H_2O$: Zinc acetate hydroxide synthesized in the previous chapter (Chapter VII) was used in investigating the current work. Briefly, hydrolysis of 43.5 mmol of zinc acetate in water with excess propylene oxide at 40 °C produced 5.0 g zinc acetate hydroxide, $Zn(OAc)_{0.33}(OH)_{1.67}\cdot 0.5H_2O$ with a yield of ~ 94%. Chapter VII presents the synthesis and complete characterization of the synthesized zinc acetate hydroxide.

BET Surface Area: BET surface area of the synthesized zinc acetate hydroxide was determined by employing a Qutachrome NOVA 1200 instrument. Samples for three separate experiments were vacuum dried overnight before performing the experiments.

Uptake Experiments and Analysis:

Analysis of phosphate using colorimeter: Phosphate analysis was performed using a HACH colorimeter (model# DR3900). Commercial phosphate powder pillows (PhosVer® 3 Phosphate Reagent; PERMACHEM Reagents) were used as the colorimetric reagent. One pillow was added to 10.0 g of a solution for typical phosphate analysis.

Phosphate uptake experiments: Approximately 25 mg of zinc acetate hydroxide was introduced to 40 g of a phosphate solution for all batch experiments. 50 mL centrifuged tubes were used for the batch experiments; the tubes with solutions and zinc acetate hydroxide were placed on a rotor for continuous rotation during the batch experiments. A 550. ppm of phosphate stock solution was used for the time vs. uptake experiment. After desired time intervals, the solutions were separated from the solid zinc by centrifugation for analysis. While 27.5, 55.7, 113, 229 and 539 ppm phosphate solutions were used to investigate Langmuir isotherm. Isotherm experiment was performed for 48 hours.

Effect of temperatures in removing phosphate from water by zinc acetate hydroxide: To investigate the impact of temperatures in removing phosphate, the batch experiments were performed at 25, 35, and 45 °C employing a hybridization oven with a rotor. Similar to the other batch experiments, 40 g of 539 ppm phosphate solutions and approximately 25 mg zinc acetate hydroxide were used in 50 ml centrifuged tubes. The experiment was performed for 48 hours.

Additionally, another batch experiment of 0.0273 g of zinc acetate hydroxide with 539 ppm phosphate for 7 days and for 15 days was performed at 45 °C to enumerate the uptake after prolonged treatment and equivalent zinc phosphate hydroxide materials. After 7 days of treatment,

the concentration of the phosphate solution was 298 ppm, while after 15 days, it was 233 ppm determining the uptake as 356 and 452 mg/g, respectively.

Analysis of arsenic using Microwave Plasma Atomic Emission Spectroscopy (MP-AES): Arsenic analysis was performed without hydride generation since the arsenate solutions used in the uptake experiments have high concentrations of 5 – 250 ppm. Following is the experimental set-up that was sued for analyzing arsenic in an Agilent 4200 microwave plasma atomic emission spectrophotometer

Experimental conditions in MPAES 4200 for analyzing arsenic:

Arsenic (As) emission peak: 193.695 nm

Uptake time: 20s

Read time: 30s

In between rinse time: 15 s (fast pumping, 80 rpm); rinse solution (2-5% HCl)

Pre-rinse with analyte solution: 15 s (fast pumping 80 rpm)

Calibration function: Rational function provided in the Agilent MP-AES 4200 software was used for calibration.

Arsenate uptake experiments: Like the phosphate uptake experiments, approximately 25 mg of zinc acetate hydroxide was introduced to 40 g of an arsenate solution for all batch experiments. The same setup was used to continuously rotate the solutions using 50 mL centrifuge tubes during the batch experiments. 220. ppm of arsenate solution was used for the time vs. uptake experiment. While investigating Langmuir isotherm, 11, 24, 58, 109, and 220. ppm arsenate solutions were used. Isotherm experiments were performed for 96 hours.

■ Results and Discussion:

The chemical formula synthesized zinc acetate hydroxide, $Zn(OAc)_{0.33}(OH)_{1.67}\cdot 0.50H_2O$**,** was confirmed by elemental, thermogravimetric, and ATR-FTIR spectroscopic analysis. While the XRD pattern established that the zinc acetate hydroxide is an acetate-intercalated layered hydroxide. Chapter VII includes all the characterization in detail.

The surface area of the synthesized zinc acetate hydroxide was determined by employing the BET adsorption experiment using N_2 gas adsorbate. Three BET adsorption experiments were performed, and their results are in Table 1. The average surface area was found as 41 ± 6 m^2/g. Compared to other reported synthesis routes, such as precipitation of zinc acetate by NaOH at room temperature, which is a typical process documented in the literature, the hydrolysis process that we developed here produced zinc acetate hydroxide with a moderate surface area. Synthesis of zinc acetate hydroxide by titrimetric precipitation at room temperature was reported to have a surface area of 25 m^2/g.[16] However, precipitation of zinc acetate with NaOH at 45 °C produced zinc acetate hydroxide with a surface area of 71m^2/g.[14]

Table 1: Surface area of zinc acetate hydroxide, $Zn(OAc)_{0.33}(OH)_{1.67}\cdot 0.50H_2O$ determined using BET experiment.

Experiment #	Surface area m^2/g	Average surface area m^2/g
1	49	
2	33	41 ± 6
3	39	

Investigation of phosphate interaction with zinc acetate hydroxide:

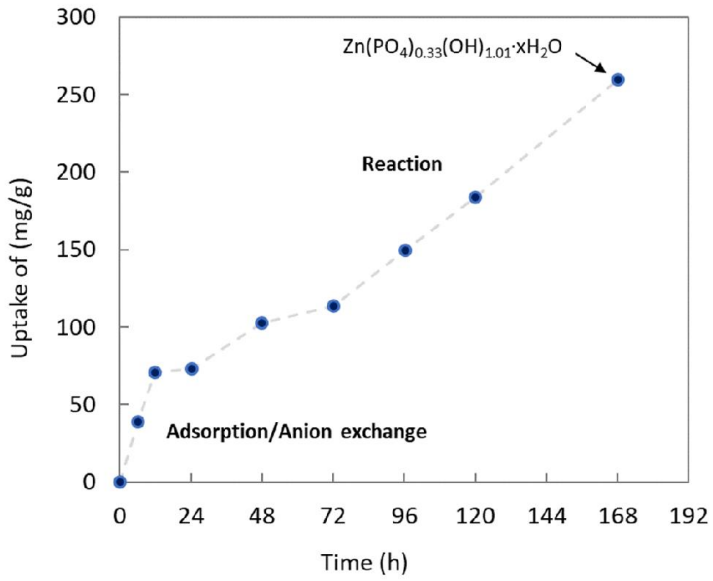

Figure 1: Uptake vs. time plot of the interaction of 550. ppm phosphate with zinc acetate hydroxide at room temperature.

Investigation of the interaction of phosphate with zinc acetate hydroxide, $Zn(OAc)_{0.33}(OH)_{1.67}\cdot 0.50H_2O$ against time generates an interesting plot as presented in Figure 1. The figure shows that phosphate uptake reaches a plateau at 24 hours, followed by an increasing phosphate uptake with time. This suggests that during the initial 24 hours, the phosphate ions involved in the acetate (anion) exchange process that reaches a plateau due to the initial adsorption equilibrium (Scheme 1). At 24 hours, the phosphate uptake is 72.8 mg/g, which can be calculated to a $Zn(PO_4)_{0.09}(OAc)_{0.24}(OH)_{1.49}\cdot xH_2O$ solid phase, showing that about one-fourth of acetate ions of zinc acetate hydroxide is replaced by the adsorbed phosphate ions. After 24 hours, the follow-up increase in phosphate uptake indicates a slow reaction of hydrogen phosphate with the zinc acetate hydroxide, which involves a surface acid-base reaction accompanying the exchange of the rest of the acetate groups and release of OH^- ions. Notably, speciation of phosphate species[17] and the pH of the solution (Figure 2) confirm that the species in the solution are hydrogen phosphate (HPO_4^{2-})

during the interaction with zinc acetate hydroxide. Therefore, the HPO_4^{2-} species adsorb first on the solid that turns into surface-adsorbed phosphate ($–PO_4^{2-}$). The absorbed phosphate species in the inter-layers of zinc acetate hydroxide neighboring to acetate groups may replace the intercalated-acetate ions as follows.

$$Zn(OAc)_{0.33}(OH)_{1.67\,(s)} + HPO_4^{2-}{}_{(aq)} \rightleftharpoons Zn(OAc)_{0.33}(OH)_{1.67}\ldots.(HPO_4^{2-})_{x\,(ads)}$$

$$Zn(OAc)_{0.33}(OH)_{1.67}\ldots.(HPO_4^{2-})_{x\,(ads)} \longrightarrow Zn(OAc)_{0.33}(OH)_{1.67-x}–(PO_4^{2-})_x + xH_2O$$

$$Zn(OAc)_{0.33}(OH)_{1.67-x}–(PO_4^{2-})_x \longrightarrow Zn(PO_4)_x(OAc)_{0.33-x}(OH)_{1.67-x} + x\ OAc^-$$

$$Zn(OAc)_{0.33-x}(OH)_{1.67}–(PO_4^{2-})_x \longrightarrow Zn(PO_4)_x(OAc)_{0.33-x}(OH)_{1.67-2x} + x\ OH^-$$

Scheme 1: Possible interaction steps of phosphate species with zinc acetate hydroxide led to acetate exchange (where "ads" stands for adsorption). The follow-up incorporation of the phosphate spices in the zinc acetate hydroxide causes a release of OH^- ions.

To picture the acetate exchange process, zinc acetate hydroxide's structure must be considered. The zinc acetate hydroxide layered structure is a modified brucite-like layered structure constituted by $Zn(OAc)(OH)_3$ tetrahedra/$Zn(OH)_6$ octahedra, where the intercalated-acetate ions are coordinated with $Zn(OAc)(OH)_3$ tetrahedra (Figure 2).[18-20] Hence, one surface-adsorbed phosphate group ($–PO_4^{2-}$) during incorporation into the interlayers of the layered structure possibly can replace one neighboring intercalated-acetate group. Thus, this should cause a release of one OH^- from the zinc acetate hydroxide to maintain the charge neutrality of the material and coordinate adsorbed phosphate with $Zn(OH)_x$ polyhedra. Therefore, as zinc acetate hydroxide contains 0.33 acetate for one mole of zinc, to replace all the acetate (CH_3COO^-) groups, 0.33 surface-adsorbed phosphate ($–PO_4^{2-}$) would be needed. At 72 hours, the uptake was 113 mg/g, which corresponds to $Zn(PO_4)_{0.15}(OAc)_{0.18}(OH)_{1.40}\cdot xH_2O$, showing almost half the acetate groups are replaced by phosphate. While at 96 hours, the uptake was 150 mg/g, which is equivalent to $Zn(PO_4)_{0.19}(OAc)_{0.14}$

$(OH)_{1.29}\cdot xH_2O$, confirming more acetate is replaced. The phosphate uptake vs. time plot shows that the material will uptake more phosphate and replace all the acetate groups in the zinc acetate hydroxide. The completion of the acetate exchange process (reaction) will produce a zinc phosphate hydroxide, $Zn_x(PO_4)_y(OH)_{2x-3y}$ type material.

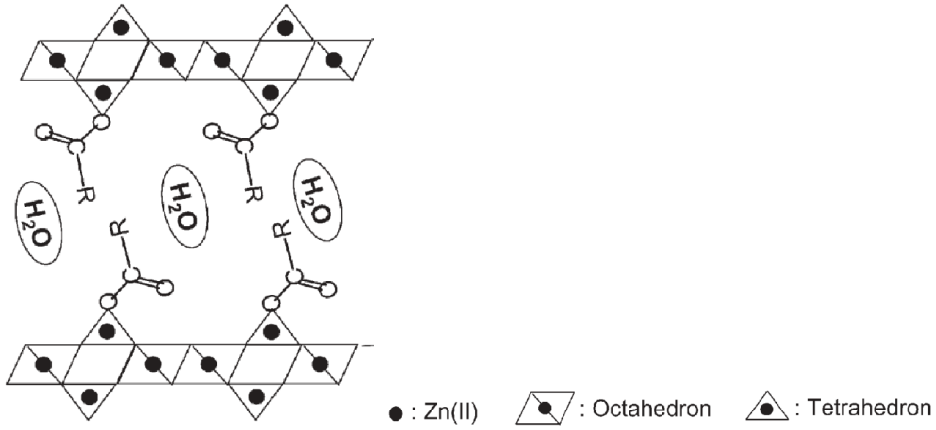

Figure 2: Schematic presentation of zinc acetate hydroxide (where $RCOO^-$ is acetate, CH_3COO^-) The figure is directly adopted from the published work by Miao *et al*.[18]

The first plateau in the phosphate uptake vs. time plot (Figure 1) was disrupted after 24 hours, confirming the adsorption equilibrium (which led to initial acetate exchange stage) was no longer maintained after 24. Therefore, the time afterward of 24 hours can be delineated as the start of the second stage of the phosphate interaction, where the reaction between hydrogen phosphate and zinc acetate hydroxide begins to occur. The reaction stage should release OAc^- and OH^- ions due to incorporating phosphate in the zinc acetate hydroxide to form a zinc phosphate hydroxide material. The pH vs. time plot (Figure 3) supports the initial acetate exchange stage and follow-up reaction stages, as the plot shows very little pH change from 0-24 hours while an increase of pH occurs after 24 hours (discussed later). The phosphate uptake after 24 hours slowly and almost linearly increases, confirming a reaction stage continuing between zinc acetate hydroxide and HPO_4^{2-} species in the solution. At 7 days, the reaction did not reach completion, showing that the

martial can still react with more phosphate. Based on the uptake quantity (259 mg/g), the composition at 7 days can be enumerated as $Zn(PO_4)_{0.33}(OH)_{1.01}\cdot xH_2O$. The FTIR spectrum of the material (discussed later, Figure 5b) confirmed that the material is indeed a hydrated zinc phosphate hydroxide. The phase of the material is close to a known zinc phosphate hydroxide mineral, $Zn_2(PO_4)(OH)$, which is also known as Tarbuttite.[21] The FTIR spectrum of $Zn(PO4)_{0.33}(OH)_{1.01}\cdot xH_2O$ also nearly agrees with the FTR spectrum of Tarbuttite, suggesting that the reaction stage of phosphate with zinc acetate hydroxide heading toward the formation of $Zn_2(PO_4)(OH)$ material.

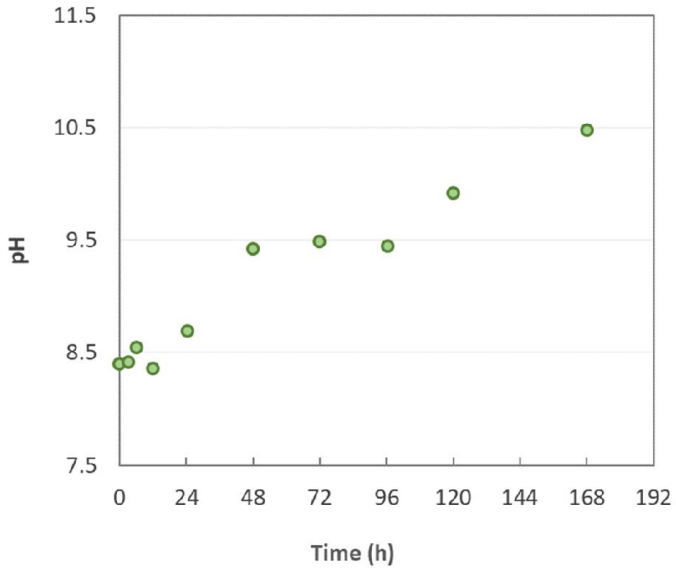

Figure 3: pH during the interaction of 550. ppm phosphate with zinc acetate hydroxide at room temperature.

The pH against time plot (Figure 3) excellently corroborates the phosphate uptake vs. time plot. There was little pH change during the initial 24 hours, indicating no reaction occurred during the time. This also supports the existence of initial acetate exchange equilibrium. As hydrogen phosphate starts reacting with zinc acetate hydroxide sometime between 24-48 hours, pH increases, confirming the release of OH^- ions. The release of OH^- ions is expected to occur to coordinate adsorbed phosphate species with the zinc polyhedra in the layered hydroxide structure and maintain

the charge neutrality of the material, as elaborated earlier. Additionally, during the continuation of the reaction stage (after 24 hours to 7 days), as more surface -PO_4^{2-} species will be in the layered material, more release of OH^- ions is expected. As a result, the pH of the solution should increase after 24 hours. This was also observed in the pH against the time plot. The increasing pH in the pH vs. time plot clearly has established that phosphate's interaction with zinc acetate hydroxide involved a reaction phenomenon besides an initial acetate exchange stage.

Notably, the uptake amount vs. time during the reaction stage was a slow process, and so were the corresponding pH changes. The slow uptake (reaction) can be attributed to a slow structural transformation of the layered structure. The process of phosphate coordination in a layered structure will replace acetate (OAc^-) and hydroxide (OH^-) groups. The acetate replacement is expected to be easier and faster without any change in the layered structure. But substituting OH^- groups in the layered hydroxide will induce a structural change; therefore, it will be a slow process.

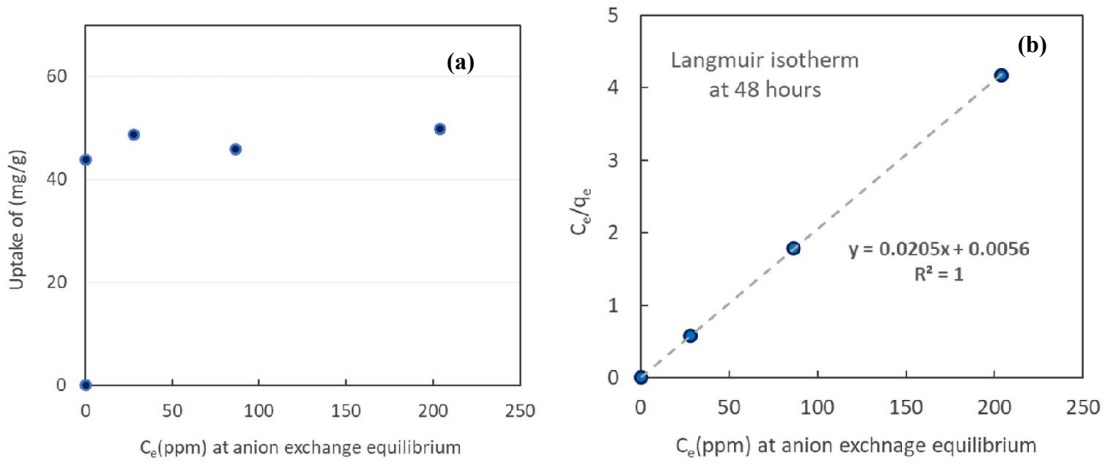

Figure 4: Investigation of Langmuir isotherm of phosphate interaction with zinc acetate hydroxide during the initial anion exchange stage. (a) Uptake vs. concentration (at 48 hours), and (b) Langmuir linear-isotherm plot

Interaction of various concentrations of phosphate solutions (27.5, 55.7 113, and 229 ppm) with zinc acetate hydroxide for 48 hours was investigated. Uptake vs. concentrations at 48 hours

and its corresponding Langmuir linear-isotherm plot is presented in Figure 4a and 4b, respectively. The Langmuir plot was found to be perfectly linear (linear regression, R^2 is 1.000), which suggests that the interaction of zinc acetate hydroxide with the phosphate solutions is at equilibria at 48 hours. Additionally, as the interaction of the phosphate solutions follows the Langmuir isotherm within 48 hours suggests that the initial anion (acetate) exchange occurred via adsorption, meaning the initial anion exchange process will reach a steady value when the initial adsorption reaches an equilibrium. The calculated formulas of the related material at 48 hours using the uptake values are tabulated in Table 2. Calculated formulas show that materials at 48 hours have both acetate and phosphate intercalation, suggesting that initially adsorbed phosphate exchanged a fraction of the acetate groups. While the slope of the linear Langmuir plot is 0.0205, which calculates the uptake capacity as 48.8 mg/g. This uptake capacity is due to the initial acetate exchange step.

Table 2: Uptake at initial anion exchange stage (48 hours) for the interaction of 27.5, 55.7 113, and 229 ppm phosphate solutions with zinc acetate hydroxide and calculated formulas of the corresponding materials at 48 hours.

Concentration at 48 hours (ppm)	Uptake of phosphate (mg/g)	Corresponding materials at 48 hours (calculated)
0.20	43.9	$Zn(PO_4)_{0.055}(OAc)_{0.275}(OH)_{1.56}\cdot xH_2O$
28.0	48.7	$Zn(PO_4)_{0.062}(OAc)_{0.268}(OH)_{1.55}\cdot xH_2O$
86.3	45.8	$Zn(PO_4)_{0.058}(OAc)_{0.250}(OH)_{1.58}\cdot xH_2O$
204	49.8	$Zn(PO_4)_{0.063}(OAc)_{0.267}(OH)_{1.54}\cdot xH_2O$

Table 3: Phosphate uptake due to initial anion exchange and follow-up reaction with zinc acetate hydroxide at room temperature.

Stages of phosphate interaction	Uptake (removal) capacity of phosphate (mg/g)
Initial anion exchange	48.8
Reaction	259[a]

a. reaction of phosphate with zinc acetate yet to reach completion (Figure 1), i.e., the material can remove more phosphate from solution by reacting with phosphate further

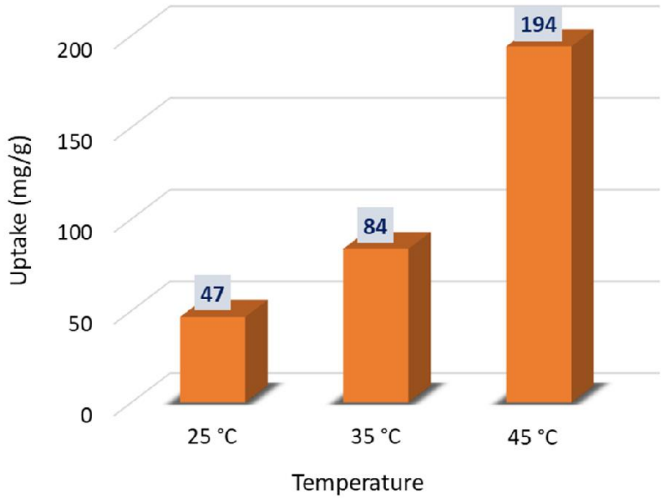

Figure 5: Uptake of phosphate using zinc acetate hydroxide at different temperatures.

Uptake of phosphate at different temperatures such as 25, 35, and 45 °C was investigated for 48 hours using 539 ppm of phosphate solution. It was found that the uptake increased as temperatures were raised, as shown in Figure 4. A 10 °C increase from room temperature to 35 °C increased the uptake to 37 mg/g, while the rise of 10° C from 35 to 45 °C raised the uptake to 110 mg/g. This suggests that the uptake increased exponentially. The exponential increase of uptake

further establishes that phosphate uptake occurs by a reaction between phosphate and zinc acetate hydroxide after the initial acetate exchange step.

The uptake (removal by reaction) of phosphate using zinc acetate hydroxide at room temperature was 259 mg/g after 7 days. While heating speeded up the process since at 45 °C for two days, the uptake was 194 mg/g. The material even can react with more phosphate, as was clear from the uptake vs. time plot (Figure 1). Because zinc acetate hydroxide will be transformed to $Zn_2(PO_4)(OH)$ or $Zn_3(PO_4)_2$ when the reaction reaches completion, which will remove approximately 396 and 527 mg/g of phosphate, respectively. In other words, it can remove more phosphate from water than the above-mentioned experimental uptake value of 259 mg/g. Further experiments treating high concertation phosphate solution at 45 °C for 7 and 15 days determined phosphate uptake as 356 and 452 mg/g, respectively (Table 4). This confirms that the material reacted with more phosphate and exceeded the expected value of 396 mg/g if it were to transform into a $Zn_2(PO_4)(OH)$ phase. These are very high phosphate uptake (removal) quantities compared to frequently reported literature values for phosphate uptake/removal by other materials such as layered double hydroxides, mesoporous metal oxides, and even a few metal-organic frameworks. Table 5 presents a comparative value of phosphate uptake capacities of various materials.

Table 4: Phosphate uptake amounts in treatment of 539 ppm phosphate solution with zinc acetate hydroxide after 7 and 15 days at 45 °C.

Time (days)	Initial concentration of phosphate (ppm)	Concentration of phosphate in the treated solution (ppm)	Uptake of phosphate (mg/g)	Correspnidng materials (claculated)
7	539	298	356	$Zn(PO_4)_{0.46}(OH)_{0.62}\cdot xH_2O$
15		233	452	$Zn(PO_4)_{0.58}(OH)_{0.26}\cdot xH_2O$

Table 5: Comparison of phosphate uptake capacities of various materials reported in the literature with the present work.

Material	Uptake capacities (mg/g)	Reference
Iron based MOF, MIL-101(Fe)	107.7	Reference[22]
Mesoporous Ce/Zr binary oxide, $Ce_{0.8}Zr_{0.3}O_2$	112.2	Reference[23]
Zn-Al layered double hydroxide	68.4	Reference [24]
Calcium rich Sepiolite	98.1	Reference[25]
Mesoporous ZrO_2	91.1	Reference[26]
Fe-Mn binary oxide	33.2	Reference[27]
Zeolite/Lanthanum hydroxide	71.9	Reference[28]
Fe Zeolite A	18.2	Reference[29]
$NaLa(CO_3)_2/Fe_3O_4$	120.2	Reference[30]
Zn-Fe layered double hydroxide	~36	Reference[31]
Al-based metal organic framework	79.4	Reference[32]
$Zn(OAc)_{0.33}(OH)_{1.67}\cdot 0.50H_2O$	259 (24°C, 7 days) 356 (45 °C, 7 days)	This work

Investigation of arsenate uptake:

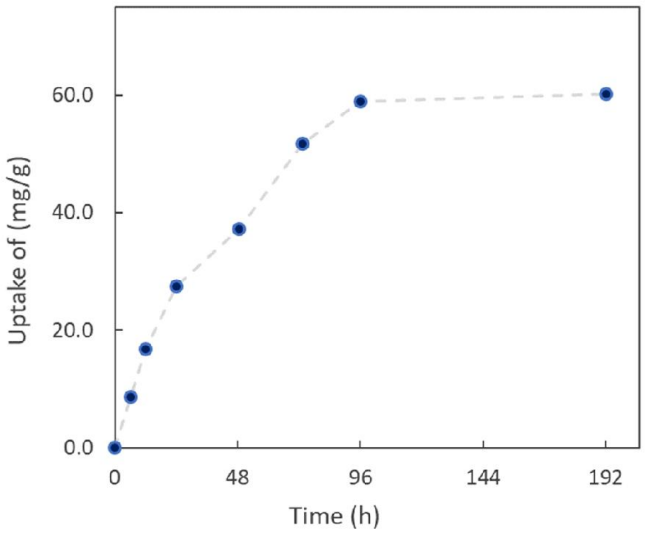

Figure 6: Arsenate uptake vs. time at room temperature during the interaction of 220 ppm arsenate solution and zinc acetate hydroxide.

Arsenate uptake against time using zinc acetate hydroxide was also investigated, as showcased in Figure 6. It turned out that, unlike phosphate, 220 ppm arsenate solution reached equilibrium in 4 days (96 hours) as it was found that at 8 days, the amount of uptake was almost the same as the uptake of 4 days. The uptake at 4 days is 58.9 mg/g corresponding to 0.424 mmol of arsenate for 1g (8.18 mmol) of zinc acetate hydroxide, i.e., 0.052 mmol of arsenate was removed by 1 mmol of zinc acetate hydroxide. By considering the structure of the layered zinc acetate hydroxide, to replace all the acetate groups in $Zn(OAc)_{0.33}(OH)_{1.67}\cdot 0.50H_2O$ (like the phosphate species as elaborated earlier), 0.33 arsenate ($HAsO_4^{2-}$) would be required. Therefore, the uptake around 60 mg/g at the equilibrium corresponds to $Zn(AsO_4)_{0.05}(OAc)_{0.28}(OH)_{1.57}\cdot xH_2O$. This shows that the material at equilibrium has a considerable amount of acetate leftover, meaning all the intercalated acetate groups were not entirely replaced by adsorbed arsenate ions. FTIR spectrum of arsenate treated zinc acetate hydroxide for 8 days (Figure 9, discussed later) shows symmetric and asymmetric stretching bands of acetate groups, further supporting that acetate groups were not

replaced by adsorbed arsenate species. Therefore, unlike phosphate, the arsenate uptake occurs due to adsorption. The adsorption accompanies a slow OH^- release from the layered hydroxide, possibly due to incorporating the adsorbed arsenate in the solid. The release of OH^- during uptake of arsenate is supported by the corresponding pH vs. time plot (Figure 7). The release of OH^- may involve a tiny fraction of acetate replacement during the incorporation of adsorbed arsenate within the layered structure of zinc acetate hydroxide. Therefore, the uptake of arsenate can be presented as follows.

$$Zn(OAc)_{0.33}(OH)_{1.67\,(s)} + HAsO_4^{2-}{}_{(aq)} \rightleftharpoons Zn(OAc)_{0.33}(OH)_{1.67}\ldots.(HAsO_4^{2-})_{x\,(ads)}$$

$$Zn(OAc)_{0.33}(OH)_{1.67}\ldots.(HAsO_4^{2-})_{x\,(ads)} \longrightarrow Zn(OAc)_{0.33}(OH)_{1.67-x}\text{–}(AsO_4^{2-})_x + xH_2O$$

$$Zn(OAc)_{0.33}(OH)_{1.67}\text{–}(AsO_4^{2-})_x \longrightarrow Zn(AsO_4)_x(OAc)_{0.33-y}(OH)_{1.67-2x} + y\ OAc^- + (2x-y)\ OH^-$$

Scheme 2: Adsorption and follow-up fraction of anion exchange and OH^- release during arsenate uptake onto zinc acetate hydroxide. Where "ads" stands for adsorption and y is a tiny fraction.

The pH vs. time plot (Figure 7) exhibits that during the initial 24 hours, the pH change from initial 7.8 to 7.9 was minimal, supporting the initial adsorption stage of arsenate. Afterward, as with increasing arsenate uptake, the pH increased from 7.9 to 9.1, and with further uptake, it reached 9.4. This pH increase confirms the release of OH^- ions from the zinc acetate hydroxide due to the increasing uptake of arsenate. This establishes the adsorbed arsenate spices ($–AsO_4^{2-}$) involve a slow interaction with neighboring OH^- groups in the zinc acetate hydroxide, which results in the release of OH^- to maintain the overall charge neutrality of the solid. Therefore, the observed pH during the interaction of arsenate with zinc acetate hydroxide excellently supports Scheme 2, presenting the adsorption of arsenate species and the follow-up interaction with the zinc acetate hydroxide.

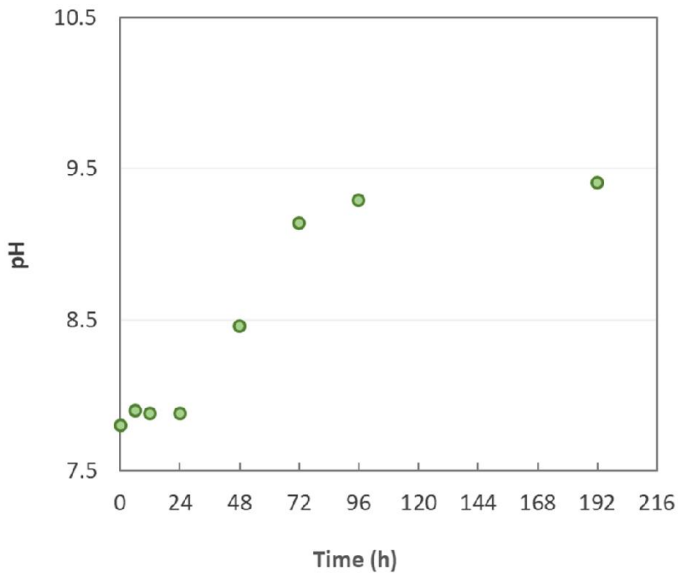

Figure 7: pH of 220 ppm arsenate solution during the interaction with zinc acetate hydroxide at room temperature.

Unlike phosphate, the arsenate uptake reaches an equilibrium at 4 days, i.e., the material cannot remove more arsenate from the solution. This can be attributed to any of the following possibilities—(i) all the active sites in the material that adsorb arsenate species ($HAsO_4^{2-}$) are occupied, meaning the active sites become saturated with adsorbed arsenate species. This saturation of active sites may stop adsorbing more $HAsO_4^{2-}$ or (ii) the inability of the adsorbed arsenate species ($–AsO_4^{2-}$) to replace intercalated-acetate groups. Because if adsorbed arsenate substituted acetate groups, it would follow up with replacing an additional OH^- groups to maintain the charge neutrality and coordination of the arsenate in the layered structure. This likely would facilitate the material to absorb/interact with more arsenate species. Nevertheless, the uptake is around 60 mg/g at the plateau from 4-8 days (at equilibrium), ruling out the possibility of the continuous reaction well beyond the initial adsorption stage to form a zinc arsenate hydroxide, $Zn_2(AsO_4)(OH)$ type material that is a well-known mineral, adamite[33]. Because to produce a zinc arsenate hydroxide type, $Zn(AsO_4)_x(OH)_{2-3x}\cdot nH_2O$ material, the uptake needs to be much higher than the 60 mg/g.

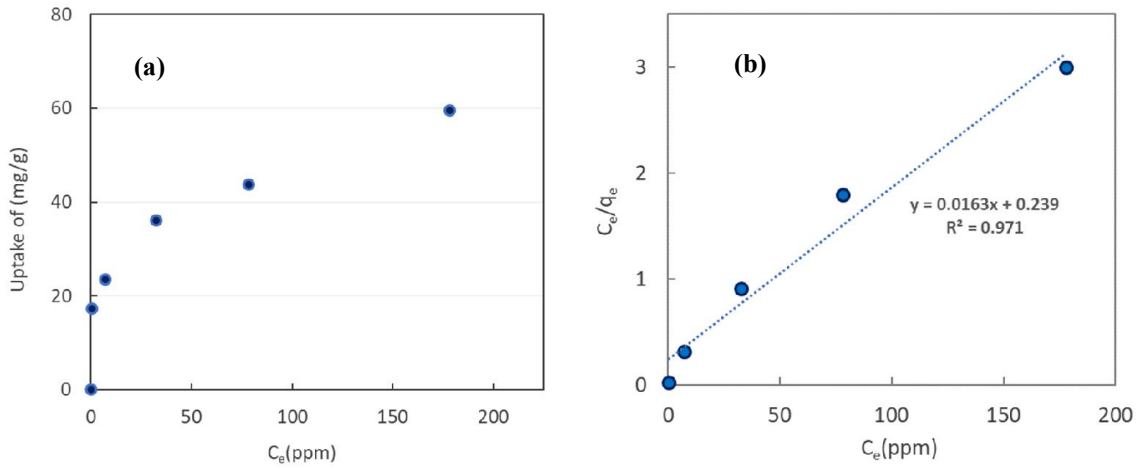

Figure 8: (a) Uptake vs. equilibrium concentrations in treating arsenate solutions with zinc acetate hydroxide at room temperature and (b) its corresponding linear Langmuir isotherm plot.

Isotherm plot was developed by treating zinc acetate hydroxide using 11, 24, 58, 109, and 220. ppm arsenate solutions for 96 hours at room temperature (Figure 8a). The corresponding Langmuir isotherm plot (Figure 8b) shows a slope of 0.0163 that calculates the uptake capacity as 61.35 mg/g, very close to the experimental value of 60.2 mg/g. The intercept of the linear Langmuir plot is 0.239, which determines the Langmuir constant as 0.0706. While in the Langmuir liner plot for the initial anion exchange stage during phosphate uptake, the intercept was 0.0056 with an uptake capacity of 48.8 m/g (Figure 4b). These values calculate the Langmuir constant as 3.66. The Langmuir constant values of 0.0706 and 3.66 for uptake of arsenate and phosphate, respectively, may suggest that the interaction of arsenate with the zinc acetate hydroxide is weaker than that of phosphate

Attenuated total reflectance FTIR spectra of the starting zinc acetate hydroxide and phosphate treated zinc acetate hydroxide are shown in Figures 5(a) and 5(b), respectively. The FTIR spectrum of zinc acetate hydroxide is explained in detail in Chapter VII. Briefly, the strong bands of symmetric and asymmetric peaks (1392 and 1546 cm^{-1}) of acetate confirm the acetate-intercalation in the layered zinc hydroxide. After treating with 550 ppm phosphate solution for 7

days, the intense acetate peaks disappeared (the tiny peaks in the range of 1390 to 1680 cm^{-1} should be due to surface adsorbed acetate and water scissoring bands). This shows that phosphate entirely replaced the acetate groups of zinc acetate hydroxide and produced a zinc phosphate hydroxide material. The peaks at 579, 604, and 1001 excellently agree with a known zinc mineral Tarbuttite, $Zn_2(PO_4)(OH)$.[34] This confirms that the phosphate treated material is a phase of zinc phosphate hydroxide. Additionally, the uptake value (259 mg/g) determines the formula of the material as $Zn(PO_4)_{0.33}(OH)_{1.01}\cdot xH_2O$, which further establishes the formation of a zinc phosphate hydroxide type material.

While after treating zinc acetate hydroxide with 220 ppm arsenate for 8 days, the FTIR spectrum showed peaks of the acetate group, as presented in Figure 5(c). This established that all the acetate groups were not replaced by arsenate during the uptake process even after 8 days. The difference between symmetric and asymmetric stretching bands of acetate groups got smaller than the starting materials suggesting that the coordination modes of acetate may change from pseudo-bridging to bridging. The new intense peak at 825 cm^{-1} arises due to As-O starching vibration, confirming the arsenate incorporation in the layered zinc hydroxide.[15, 35, 36]

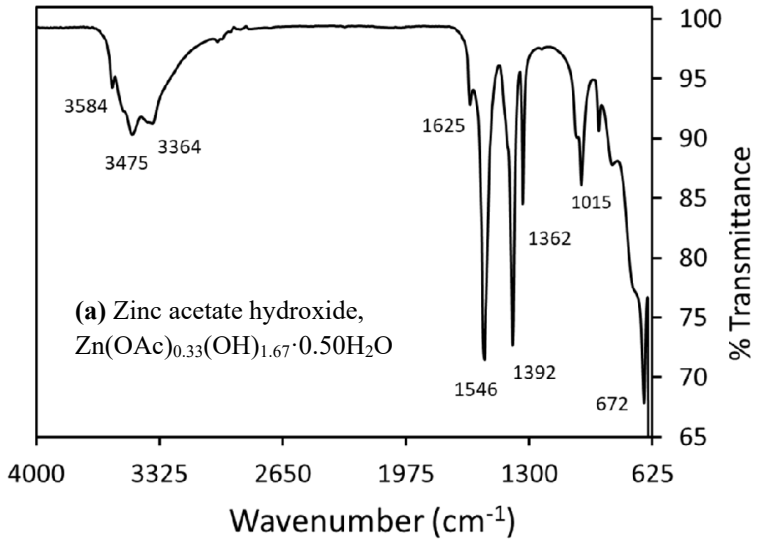

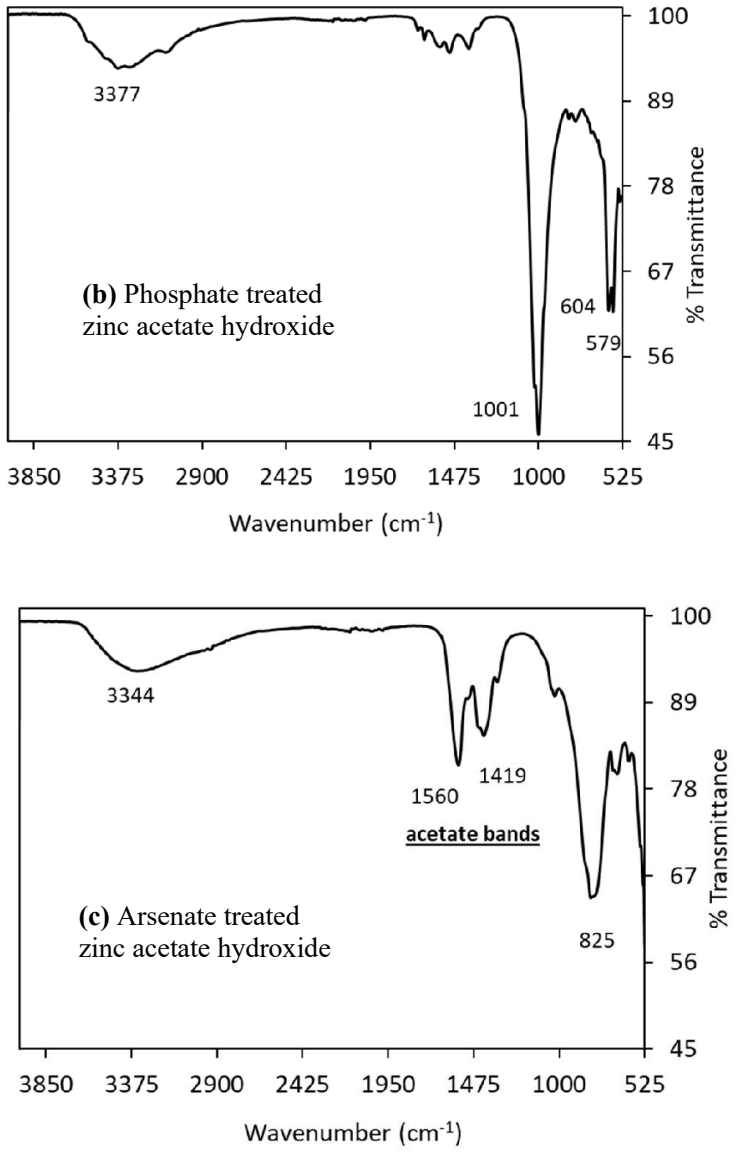

Figure 9: ATR-FTIR spectra of (a) starting material, zinc acetate hydroxide, $Zn(OAc)_{0.33}(OH)_{1.67}\cdot 0.50H_2O$, (b) phosphate treated zinc acetate hydroxide (calculated formula of the treated material is $Zn(PO_4)_{0.33}(OH)_{1.01}\cdot xH_2O$), and (c) arsenate treated zinc acetate hydroxide (calculated formula of the material is $Zn(AsO_4)_{0.05}(OAc)_{0.28}(OH)_{1.57}\cdot xH_2O$).

■ Conclusion:

This investigation established that Zinc acetate hydroxide, $Zn(OAc)_{0.33}(OH)_{1.67}\cdot 0.50H_2O$ underwent a dual process for uptake of hydrogen phosphate (HPO_4^{2-}) from water– initial anion

exchange followed by reaction, which resulted in superior uptake/removal capacity of phosphate from water compared to other layered hydroxides, porous metal oxides, and even some metal-organic frameworks. It showed phosphate uptake as 259 mg/g in 7 days at room temperature, while at 45 °C, the phosphate uptake was 194 mg/g in two days, and in 7 days, it was 356 mg/g. However, it could potentially uptake even more phosphate as these values were not at the completion of the reaction between phosphate and zinc acetate hydroxide. Unlike phosphate, arsenate interaction with zinc acetate hydroxide was limited surface adsorption. However, the adsorption of arsenate resulted in a release of OH^- from the zinc acetate hydroxide, which may involve a very tiny fraction of acetate exchange. At equilibrium, the arsenate uptake was 60 mg/g, which is excellent as it is a better or comparable uptake of arsenate species from water compared to other metal oxides, hydroxides, and layered double hydroxides to remove arsenate. In both uptake cases, the slow release of OH^- groups from zinc acetate hydroxide due to the incorporation (reaction) of phosphate or arsenate in the layered structure was experimentally corroborated by the observed increased pH with the increase of uptake. The superior phosphate uptake capacity and excellent arsenate uptake capacity, inexpensive and scalable synthesis, and environmental beingness render the acetate-intercalated zinc hydroxide an attractive material for remediating phosphate and arsenate pollution in the real-world applications. The present work's findings also invite the idea of investigating the prolonged interaction of phosphate and arsenate and other hazardous metal oxyanions with other benign layered metal hydroxides for treating polluted water.

■ References:

(1) EPA; The Effects: Dead Zones and Harmful Algal Blooms. https://www.epa.gov/nutrientpollution/effects-dead-zones-and-harmful-algal-blooms

(2) Oklahoma State University; Phosphorus and Water Quality. https://extension.okstate.edu/fact-sheets/phosphorus-and-water-quality.html

(3) Kapaj, S.; Peterson, H.; Liber, K.; Bhattacharya, P., Human health effects from chronic arsenic poisoning--a review. *J Environ Sci Health A Tox Hazard Subst Environ Eng* **2006,** 41, (10), 2399-428.

(4) Karagas, M. R.; Gossai, A.; Pierce, B.; Ahsan, H., Drinking Water Arsenic Contamination, Skin Lesions, and Malignancies: A Systematic Review of the Global Evidence. *Curr Environ Health Rep* **2015,** 2, (1), 52-68.

(5) Minnesota Department of Health; Arsenic in Drinking Water. https://www.health.state.mn.us/communities/environment/water/contaminants/arsenic.html#HeatlhEffects

(6) EPA; Arsenic Compounds. In https://www.epa.gov/sites/default/files/2021-04/documents/arsenic_april_2021.pdf.

(7) Pei, J.; Zuo, J.; Wang, X.; Yin, J.; Liu, L.; Fan, W., The Bioaccumulation and Tissue Distribution of Arsenic Species in Tilapia. *Int J Environ Res Public Health* **2019,** 16, (5).

(8) Garelick, H.; Jones, H.; Dybowska, A.; Valsami-Jones, E., Arsenic Pollution Sources. In *Reviews of Environmental Contamination Volume 197: International Perspectives on Arsenic Pollution and Remediation*, Springer New York: New York, NY, 2008; pp 17-60.

(9) Seftel, E. M.; Ciocarlan, R. G.; Michielsen, B.; Meynen, V.; Mullens, S.; Cool, P., Insights into phosphate adsorption behavior on structurally modified ZnAl layered double hydroxides. *Applied Clay Science* **2018,** 165, 234-246.

(10) Bagherifam, S.; Komarneni, S.; Lakzian, A.; Fotovat, A.; Khorasani, R.; Huang, W.; Ma, J.; Wang, Y., Evaluation of Zn–Al–SO_4 layered double hydroxide for the removal of arsenite and arsenate from a simulated soil solution: Isotherms and kinetics. *Applied Clay Science* **2014,** 95, 119-125.

(11) Kozai, N.; Mitamura, H.; Fukuyama, H.; Esaka, F.; Komarneni, S., Synthesis and characterization of nickel–copper hydroxide acetate, $NiCu(OH)_{3.1}(OCOCH3)_{0.9}\cdot 0.9H_2O$. *Microporous and Mesoporous Materials* **2006,** 89, (1-3), 123-131.

(12) Yamanaka, S.; Sako, T.; Hattori, M., Anion-Exchange in Basic Copper Acetate. *Chemistry Letters* **1989,** 18, (10), 1869-1872.

(13) Newman, S. P.; Jones, W., Comparative Study of Some Layered Hydroxide Salts Containing Exchangeable Interlayer Anions. *Journal of Solid State Chemistry* **1999,** 148, (1), 26-40.

(14) Almasri, D. A.; Essehli, R.; Tong, Y.; Lawler, J., Layered zinc hydroxide as an adsorbent for phosphate removal and recovery from wastewater. *RSC Advances* **2021,** 11, (48), 30172-30182.

(15) Ohe, K.; Tabuchi, R.; Oshima, T.; Hara, T.; Shimazu, S., Adsorptive Removal of Arsenic(III) and Arsenic(V) from Aqueous Solution using Nickel–Zinc Hydroxyl Double Salts. *KAGAKU KOGAKU RONBUNSHU* **2019,** 45, (2), 80-85.

(16) Reinoso, D. M.; Fernandez, M. B.; Damiani, D. E.; Tonetto, G. M., Study of zinc hydroxy acetate as catalyst in the esterification reaction of fatty acids. *International Journal of Low-Carbon Technologies* **2012,** 7, (4), 348-356.

(17) Sø, H. Adsorption of arsenic and phosphate onto the surface of calcite as revealed by batch experiments and surface complexation modelling, p 10. Ph.D. Thesis, Technical University of Denmark 2011.

(18) Miao, J.; Xue, M.; Itoh, H.; Feng, Q., Hydrothermal synthesis of layered hydroxide zinc benzoate compounds and their exfoliation reactions. *J. Mater. Chem.* **2006,** 16, (5), 474-480.

(19) Kandare, E.; Hossenlopp, J. M., Hydroxy Double Salt Anion Exchange Kinetics: Effects of Precursor Structure and Anion Size. *The Journal of Physical Chemistry B* **2005,** 109, (17), 8469-8475.

(20) Rojas, R.; Barriga, C.; Angeles Ulibarri, M.; Malet, P.; Rives, V., Layered Ni(ii)-Zn(ii) hydroxyacetates. Anion exchange and thermal decomposition of the hydroxysalts obtained. *Journal of Materials Chemistry* **2002,** 12, (4), 1071-1078.

(21) midat.org; Tarbuttite. https://www.mindat.org/min-3892.html

(22) Xie, Q.; Li, Y.; Lv, Z.; Zhou, H.; Yang, X.; Chen, J.; Guo, H., Effective Adsorption and Removal of Phosphate from Aqueous Solutions and Eutrophic Water by Fe-based MOFs of MIL-101. *Sci Rep* **2017,** 7, (1), 3316.

(23) Su, Y.; Yang, W.; Sun, W.; Li, Q.; Shang, J. K., Synthesis of mesoporous cerium–zirconium binary oxide nanoadsorbents by a solvothermal process and their effective adsorption of phosphate from water. *Chemical Engineering Journal* **2015,** 268, 270-279.

(24) Yang, K.; Yan, L.-g.; Yang, Y.-m.; Yu, S.-j.; Shan, R.-r.; Yu, H.-q.; Zhu, B.-c.; Du, B., Adsorptive removal of phosphate by Mg–Al and Zn–Al layered double hydroxides: Kinetics, isotherms and mechanisms. *Separation and Purification Technology* **2014,** 124, 36-42.

(25) Yin, H.; Yun, Y.; Zhang, Y.; Fan, C., Phosphate removal from wastewaters by a naturally occurring, calcium-rich sepiolite. *J Hazard Mater* **2011,** 198, 362-9.

(26) Liu, H.; Sun, X.; Yin, C.; Hu, C., Removal of phosphate by mesoporous ZrO_2. *J Hazard Mater* **2008,** 151, (2-3), 616-22.

(27) Zhang, G.; Liu, H.; Liu, R.; Qu, J., Removal of phosphate from water by a Fe-Mn binary oxide adsorbent. *J Colloid Interface Sci* **2009,** 335, (2), 168-74.

(28) Xie, J.; Wang, Z.; Fang, D.; Li, C.; Wu, D., Green synthesis of a novel hybrid sorbent of zeolite/lanthanum hydroxide and its application in the removal and recovery of phosphate from water. *J Colloid Interface Sci* **2014,** 423, 13-9.

(29) Saifuddin, M.; Bae, J.; Kim, K. S., Role of Fe, Na and Al in Fe-Zeolite-A for adsorption and desorption of phosphate from aqueous solution. *Water Res* **2019,** 158, 246-256.

(30) Hao, H.; Wang, Y.; Shi, B., $NaLa(CO_3)_2$ hybridized with Fe_3O_4 for efficient phosphate removal: Synthesis and adsorption mechanistic study. *Water Res* **2019,** 155, 1-11.

(31) Gupta, N. K.; Saifuddin, M.; Kim, S.; Kim, K. S., Microscopic, spectroscopic, and experimental approach towards understanding the phosphate adsorption onto Zn–Fe layered double hydroxide. *Journal of Molecular Liquids* **2020,** 297.

(32) Liu, R.; Chi, L.; Wang, X.; Wang, Y.; Sui, Y.; Xie, T.; Arandiyan, H., Effective and selective adsorption of phosphate from aqueous solution via trivalent-metals-based amino-MIL-101 MOFs. *Chemical Engineering Journal* **2019,** 357, 159-168.

(33) mindat.org Adamite. https://www.mindat.org/min-21.html

(34) RRUFF™ Tarbuttite R050621. https://rruff.info/Tarbuttite

(35) Carabante, I.; Grahn, M.; Holmgren, A.; Kumpiene, J.; Hedlund, J., Influence of Zn(II) on the adsorption of arsenate onto ferrihydrite. *Environ Sci Technol* **2012,** 46, (24), 13152-9.

(36) Solís–Rodríguez, R.; Pérez–Garibay, R.; Alonso–González, O.; Mendieta–George, D., Enhancing the arsenic adsorption by controlling the zeta potential of Zn(OH)2 flocs. *Journal of Environmental Chemical Engineering* **2021,** 9, (5).

CHAPTER IX

Conclusions, Findings, and Scientific Impacts

Later 3d transition metal (cobalt, nickel, copper, and zinc) layered hydroxides or hydroxides and their corresponding oxides are essential and valuable materials for many necessary and emerging technologies (briefly discussed in the introduction). Developing straightforward, inexpensive, and green processes for accessing their nano-/micro-structures decorated substrates or supports, preparation of their films and membranes, and improved synthesis routes for their powders are critically important to meet the never-ending demand for materials to continue our present-day technology-dependent era. The dissertation's accomplished research developed such processes for deposition nano-/micro-structures on substrates and porous/non-porous supports, producing thick films and membranes, and advanced syntheses for powder in high yields of layered hydroxides or hydroxides of the later 3d transition metals. The conclusions, findings, and scientific impacts of the accomplished research of the dissertation are as follows.

Discovery of hydrolysis of later 3d transition metal acetates for deposition of nano-/micro-structures of corresponding layered metal hydroxides and metal hydroxides

The dissertation presented a discovery of nickel acetate hydrolysis (hydrothermal) reaction at 90 °C without any additional reagent or reactant to deposit web-like interconnected nanowalls

as thin films of nickel acetate hydroxide, $Ni(OAc)_{0.28}(OH)_{1.72}\cdot 0.25H_2O$, which is an acetate-intercalated layered nickel hydroxide. The thin films of nickel acetate hydroxide were readily converted to NiO thin films by pyrolysis with identical nanomorphology. Exploration of the effect of nickel acetate concentration revealed that a 0.2 M nickel acetate solution deposited web-like interconnected nanowalls with open spaces among the nanowalls, forming a porous-like structure. High concertation such as 0.5 M generated more populated interconnected nanowalls, but the morphology had almost no open areas between the nanowalls. The hydrolysis process was reproducible and deposited robust nanostructured nickel acetate hydroxide films and NiO films upon pyrolysis. Hence the discovered hydrolysis of nickel acetate is a straightforward route to access web-like nanostructured films of layered nickel hydroxide and NiO. The web-like nanostructured layered nickel hydroxide or NiO with open spaces among nanowalls (a porous-like nanomorphology) is a valuable feature and can be exploited for myriad applications of nanostructured films of layered nickel hydroxide or NiO.

The dissertation also showed that hydrolysis of copper acetate aqueous solution at 90 °C deposited micron size sphere-type particles of CuO. Further investigation of the hydrolysis reaction during the initial hours was provided isolation of the initially formed bluish-green crystalline product, which was copper acetate hydroxide, $Cu(OAc)_{0.41}(OH)_{1.59}\cdot 0.40H_2O$, an acetate-intercalated layered copper hydroxide. Unlike nickel acetate hydroxide, the copper acetate hydroxide decomposed to CuO under the hydrothermal condition. While interestingly, hydrolysis of ~ 0.2M copper formate aqueous solution at 90 °C deposited a two-phase crystalline material of copper (I) oxide/copper formate hydroxide, $Cu_2O/Cu_2(OOCH)(OH)_3$. The particles were grown as two types of morphologies, octahedra- and rectangular bar-type particles. However, the ~ 0.5M copper formate deposited crystalline copper (I) oxide/copper (II) oxide, Cu_2O/CuO. Additionally, hydrolysis of copper acetate aqueous solutions (without any second reactant/reagent) and silica pellets or mesoporous silica produced blue silica pellets or blue mesoporous silica. These blue

materials were effortlessly converted to CuO decorated corresponding support and porous materials by pyrolysis.

In continuation of the investigation of discovered hydrolysis process of metal acetates, the present dissertation further established that reaction only zinc acetate with water deposited nanosphere-type $ZnO/Zn(OH)_2$, whereas cobalt acetate generated cobalt hydroxide, $Co(OH)_2$ with dual-morphology of web-like nanowalls and sphere-type nanoparticles onto glass substrates. Investigation of hydrolysis of zinc acetate with gold-pallidum coated substrates also produced the nanosphere-type particles as films with a larger average size of particles. These $ZnO/Zn(OH)_2$ nanostructured films can be readily converted into ZnO films upon pyrolysis. Cobalt hydroxide nanostructured films can easily be transformed into cobalt oxyhydroxide (CoOOH) or cobalt oxide (Co_3O_4) films depending on the pyrolysis temperatures.

The key aspect of the hydrolysis of metal acetates process is that it deposited nano-/micro-structured materials as very robust films (on glass) and decorated supports/mesoporous materials (silica). This feature is expected to be maintained in other types of substrates and supports. The robustness is a critical property of films and nanostructures decorated support materials for real-world applications for various essential technologies, including electro-/photo-/thermal-catalysis, sensors, fuel cells, photoelectrochemical processes, wastewater treatment, and metal oxide-based semiconductor applications. The significance of the discovered hydrolysis reactions of metal acetates is that it has opened a new avenue for preparing nanostructured later 3d transition metal layered hydroxides/hydroxides and their oxides. The hydrolysis route has also opened the idea of exploring hydrolysis of metal acetates and other transition and lanthanide metals to find out what type of nanomaterials and nanostructures their hydrolysis will generate. Another significant feature of the developed hydrolysis process is that the reaction solutions after deposition leave only aqueous solutions of metal acetates and acetic acid. Therefore, recrystallizing the rest of the metal acetates from the reaction solutions after the hydrolysis process can be effortlessly done to recover

the unused metal acetates for reuse. Additionally, the hydrolysis reactions of transition metal acetates with porous and non-porous support materials and conductive porous substrates (porous carbon) can readily be employed for the commercialization of transition metal hydroxides/oxides decorated-corresponding support and substrate materials due to the simplicity of the hydrolysis process, full potential for scalability, and straightforward recovery of unused metal acetates in the process that will lead to no chemical waste generation.

Unusual trends of nickel-copper contents in bimetallic nickel-copper layered double hydroxides synthesized by hydrolysis of nickel acetate and copper acetate mixtures

The present dissertation extensively explored the hydrolysis of nickel acetate and copper acetate mixtures (without additional reactant/reagent) that produced novel bimetallic nickel-copper layered hydroxides (LDHs) with acetate intercalation as crystalline and non-crystalline powders. The chapter explored a series of reactions that led to the discovery of unusual trends of nickel-copper content in the nickel-copper LDHs to ratios of nickel and copper ions in the starting reaction solutions. The nickel-copper LDHs were markedly copper-rich within 1:1 to 6:1 of nickel acetate to copper acetate. However, a ratio of 7:1 of nickel acetate to copper acetate produced almost a 1:1 nickel-copper LDH. A ratio higher than 7:1 generated nickel-rich LDHs. The morphologies of two of the nickel-copper LDHs were nano-/micro-square plates.

Hydrolysis reactions of nickel acetate and copper acetate mixtures that generate acetate-intercalated bimetallic nickel-copper LDHs have never been investigated extensively like the present study. Only one article in the literature studied one reaction of a mixture of nickel and copper acetate hydrolysis that produced a nickel-copper acetate LDH and CuO (Kozai et al., Reference 3, Chapter IV). While the present investigation showed that the hydrolysis process generated pure nickel-cooper LDHs without forming CuO due to the use of a lower temperature. Further, the dissertation showed no need for the unnecessary addition of hydrogen peroxide in the

hydrolysis reaction to prevent CuO formation for accessing a pure phase of a nickel-copper LDH. As a result, the present investigation has advanced the hydrolysis route to synthesize nano-/micro structured acetate-intercalated bimetallic nickel-copper layered double hydroxides. Further, hydrolysis of mixtures of other transition metal acetates has never been explored. Hence, the present work of the dissertation has opened the door for investigating mixtures of other transition and lanthanide metal acetates for the synthesis of pure phases acetate-intercalated layered double hydroxides of corresponding transition or lanthanide metals.

Development of a novel and green process for β-nickel hydroxide films and aluminum substituted α-nickel hydroxide membranes

The dissertation research also developed a novel, simple, and green process for converting commercial nickel hydroxide powder into β-nickel hydroxide films and aluminum substituted α-nickel hydroxide membranes. The investigation utilized the solubility of nickel hydroxide in a concentrated aqueous ammonia solution. In aqueous ammonia, nickel hydroxide forms hexamine nickel(II) hydroxide, $Ni(NH_3)_6(OH)_2$ complex. Evaporation of ammonia from solutions of the $Ni(NH_3)_6(OH)_2$ complex deposited crystalline β-$Ni(OH)_2$ films. While the addition of sodium aluminate to the nickel-ammonia complex facilitated the growth of aluminum-substituted α-$Ni(OH)_2$ membranes, which formed at the solution's water/air interface.

The deposition or growth method using $Ni(NH_3)_6(OH)_2$ does not leave any waste chemical behind, making it a green process. Depending on the solubility in the aqueous ammonia solution, the developed approach can readily be employed for converting other transition metal hydroxides into their films. Additionally, the process would be excellent for recovering nickel and cobalt from spent batteries that use nickel or cobalt hydroxide as electrodes. The process has the full potential to be employed industrially for recovering ammonia.

Development of propylene oxide-assisted hydrolysis process to synthesize layered hydroxides, hydroxides, and bimetallic hydroxides of later 3d transition metals

The dissertation also established a new hydrolysis route for synthesizing acetate-intercalated layered copper hydroxide and layered zinc hydroxide in high yields. Copper acetate aqueous solution with propylene oxide at a low temperature of 40 °C produced crystalline layered copper acetate hydroxide with a yield of 100%. Zinc acetate and propylene oxide in water generated layered zinc acetate hydroxide with ~94% yield. While the reactions of cobalt and nickel acetates and propylene oxide yielded β-$Co(OH)_2$ and β-$Ni(OH)_2$ instead of their acetate-intercalated layered hydroxides. A reaction of 1:2 nickel acetate and cobalt acetate produced stochiometric bimetallic nickel-cobalt hydroxide that can easily be transformed into a stoichiometric nickel-cobalt oxyhydroxide, $NiCo_2O_x(OH)_{6-x}$ or nickel cobaltite, $NiCo_2O_4$ by pyrolysis. The propylene oxide-assisted hydrolysis process exploited the fact that propylene oxide will attack one of the water molecules of $[M(H_2O)_6]^{2+}$ spices that produce $[M(OH)(H_2O)_6]^{2+}$ complex. This hydroxide aqua complex, $[M(OH)(H_2O)_6]^{2+}$ is the key species to generate metal acetate hydroxide, $M(OAc)_x(OH)_{2-x}\cdot nH_2O$ or metal hydroxide $M(OH)_{2-x}\cdot nH_2O$ depending on the metal ions.

Literature investigation shows that single crystals of copper acetate hydroxide $Cu_2(OAc)(OH)_3$ were prepared by hydrolysis of copper acetate under reflux conditions (Švarcová et al. Reference 1, Chapter I). However, the yield of the reaction is expected to be very low as an investigation of a reaction of 10.0 mmol copper acetate in 50 g of water at 90 °C after 3 hours in a closed system produced 0.201 g of $Cu(OAc)_{0.41}(OH)_{1.59}\cdot 40H_2O$ (Chapter III). While the direct precipitation with NaOH produces copper acetate hydroxide as a powder – which is the often reported process used in literature to prepare this material in high yield. Similarly, zinc acetate hydrolysis with polyene oxide has never been investigated before to produce acetate-intercalated layered zinc hydroxide. Literature study shows that zinc acetate hydroxide is also widely prepared by direct precipitation of zinc acetate. Therefore, the scientific impact of the developed hydrolysis

reaction of copper or zinc acetate aqueous solutions with propylene oxide in the dissertation is that it has established a novel route for synthesizing layered materials of crystalline copper acetate hydroxide with a yield of 100% and powder zinc acetate hydroxide with ~94% yield.

While propylene oxide-assisted hydrolysis was investigated for the first time for a mixture of nickel and cobalt acetate that produced stoichiometric bimetallic nickel-cobalt hydroxide with a 99% yield. The bimetallic nickel-cobalt hydroxide is an excellent precursor for accessing technologically valuable nickel-cobalt oxyhydroxide and nickel cobaltite materials. Therefore, the developed propylene oxide-assisted hydrolysis process established a new route for preparing stoichiometric bimetallic nickel-cobalt hydroxide for accessing nickel-cobalt oxyhydroxide and nickel cobaltite. The route can easily be used for synthesizing other bimetallic cobalt-based hydroxides to prepare other transition metal cobaltites. Additionally, the propylene oxide hydrolysis reaction of mixtures of transition metal acetates has also opened the idea of exploring the syntheses of bimetallic manganese- and iron-based hydroxides/layered hydroxides for accessing valuable materials of metal-manganates and metal-ferrites, respectively for various necessary technologies.

Investigation of prolonged interaction of phosphate or arsenate with zinc acetate hydroxide: A new finding in the uptake of phosphate vs. arsenate using zinc acetate hydroxide

Due to the excellent anion exchange-ability of the acetate-intercalated layered zinc hydroxide (zinc acetate hydroxide), the dissertation was promoted to investigate phosphate and arsenate uptake using the zinc acetate hydroxide synthesized by the propylene oxide-assisted hydrolysis method. An exploration of prolonged interaction of a high ppm of phosphate revealed that phosphate species underwent an anion exchange with acetate followed by a slow reaction with the zinc acetate hydroxide. The reaction stage led to a very high phosphate uptake that was superior to other studied layered hydroxides or layered double hydroxides, porous metal oxides, and even

some metal-organic-frameworks. While, unlike phosphate, arsenate interaction with the zinc acetate hydroxide was limited to adsorption with a possibly a very minimal acetate exchange. The uptake capacity of arsenate was much lower than phosphate uptake but comparable to other studied sorbents such as metal oxides, hydroxides, and layered hydroxides.

Up to date, no article has been reported so far on the reaction of phosphate with zinc acetate hydroxide during uptake from water; therefore, the current study has established for the first time that zinc acetate hydroxide can react with a high concentration phosphate ion in water that leading to the formation of a zinc phosphate hydroxide type material. As zinc acetate hydroxide showed a very high uptake capacity of phosphate, it will be an excellent material for uptake of phosphate from a high concentration of phosphate contaminated water such as industrial and municipal phosphate wastewater. While point sources release a low phosphate concentration, the zinc acetate hydroxide can outperform other sorbents as it will have a long lifetime for uptake. Additionally, zinc acetate hydroxide exhibited excellent uptake of arsenate species from water comparable with existing materials to remove arsenate, making it to be employable for removing arsenate from industrial wastewater sources that may contain low or high arsenate before releasing to surface water bodies. Therefore, the dissertation has established that layered zinc acetate hydroxide and other similar environmentally benign layered hydroxides can be directly used to uptake phosphate and arsenate from water to remediate their hazardous pollution for a safer water environment for aquatic species, birds, mammals, and humans.

VITA

Dewan Russel Rahman

Candidate for the Degree of

Doctor of Philosophy

Thesis: NOVEL SYNTHESES AND APPLICATIONS OF LAYERED TRANSITION METAL HYDROXIDES

Major Field: Chemistry

Biographical:

Education:

Completed the requirements for the Doctor of Philosophy in Chemistry at Oklahoma State University, Stillwater, Oklahoma, July 2022.

Completed the requirements for the Master of Science in Chemistry at University of Dhaka, Dhaka, Bangladesh, July 2014.

Completed the requirements for the Bachelor of Science in Chemistry at University of Dhaka, Dhaka, Bangladesh, September 2012.

Experience:
Graduate Research Assistant Oklahoma State University, May 2016 – July 2022
Research Assistantship, XploSafe, Summer 2020 & 2021, Spring 2021, Fall 2021, and Spring – Summer 2022
Teaching Assistant at Oklahoma State University, August 2015 – December 2020
Lecturer, Regent College Dhaka, September 2014 – December 2014

Publication & Presentations:

1. Vecoven, A.; Rahman, D. R.; Apblett, A. W., Green Process for Preparation of Nickel Hydroxide Films and Membranes. *Journal of Materials Engineering and Performance* **2020**, 29, (9), 5602-5608.
2. Deposition of Web-Like Structures with Nanometric Walls of Nickel Acetate Hydroxide and Cobalt Hydroxide and Their Conversion to Oxides
   ACS Midwest Regional Meeting, MO, USA, October **2021**
3. Synthesis of Acetate-Intercalated Nickel-Copper Layered Double Hydroxides
   ACS National Meeting, San Diego, CA & Virtual, March **2022**

Professional Membership:
American Chemical Society